Doctoral thesis

Synthesis, physicochemical characterization and computational studies of selected lanthanide-doped luminophores

by

Andrii Shyichuk

The thesis was prepared
at the Department of Rare Earth,
Faculty of Chemistry,
Adam Mickiewicz University

Supervisor: Prof. Stefan Lis

Poznań
2015

Acknowledgments

I wish to thank my supervisor, Prof. Stefan Lis, for his help, support and guidance during my DSc studies, for his advice and hard work on our research and this thesis.

My gratitude goes to Prof. Oscar L. Malta for being a generous host during my stay in Brazil, and for our fruitful scientific cooperation.

I am much indebted to Marcin Runowski, Albano N. Carneiro Neto, Sarita S. Câmara, Ingrid T. Weber, Luiz A. O. Nunes and Ricardo. L. Longo, for their contributions to our common research.

My thanks are extended to Tomasz Grzyb and Agata Szczeszak, for their professional advice.

I am much grateful to my parents, Alexander and Iryna Shyichuk, for their support and encouragement.

I wish to acknowledge the National Centre of Science (NCN, Poland) for the financial support within Etiuda project, 2013/08/T/ST5/00490, 2013-2014.

Poznan Supercomputer and Networking Center (PCSS, Reef supercomputer) and Wroclaw Center for Networking and Supercomputing (WCSS, Supernova supercomputer) are acknowledged for the provided computational resources and software.

Freely-available software was used in preparation of this thesis, in particular, LibreOffice (http://libreoffice.org), GNOME Image Manipulation Program, GIMP (http://www.gimp.org/), Python (https://www.python.org/), CodeCogs Online LaTeX editor (http://www.codecogs.com/latex/eqneditor.php).

Table of Contents

List of abbreviations and contractions

Spectral ranges:

IR – infrared, electromagnetic radiation range, 700 nm – 1 mm

NUV, UV – (near) ultraviolet, electromagnetic radiation range, 100(300) – 400nm

Vis. – visible range of electromagnetic radiation, light, 400 – 700 nm

Phenomena:

CT – charge transfer, a Ln^{3+} excitation phenomenon

DC – dynamic coupling, one of the Ln^{3+} photoluminescence mechanisms

ET – energy transfer, a phenomenon of transferring excitation energy between ions or molecules

ETU – energy transfer upconversion, an upconversion mechanism

FED, ED – (forced) electric dipole

MD – magnetic dipole

Compounds:

Ln^{3+} – a trivalent cation of the lanthanide series (La-Lu)

RE – rare earth (element or ion, Sc, Y, La-Lu)

BGB – barium-gadolinium borate, $Ba_3Gd_2(BO_3)_4$

CGB – calcium-gadolinium borate, $Ca_3Gd_2(BO_3)_4$

SGB – strontium-gadolinium borate, $Sr_3Gd_2(BO_3)_4$

SLB – strontium-lanthanum borate, $Sr_3La_2(BO_3)_4$

SYB – strontium-yttrium borate, $Sr_3Y_2(BO_3)_4$

Research techniques and devices:

CCD – charge-coupled device, a digital semiconductor light sensor device

FTIR – Fourier-transformed infrared (spectroscopy), a instrumental analysis technique

MRI – magnetic resonance imaging, an instrumental analysis and diagnostics technique

TEM – transmission electron microscopy, an instrumental analysis technique

XRD – x-ray diffraction, a research technique (particularly in this work – a powder XRD)

Quantum-mechanical methods:

ab initio – a first-principles, from-scratch approach, that uses only (or mostly) basic definitions and not (semi-)empirical corrections

ADF – Amsterdam density functional software

AM – Austin model 1, a semi-empirical quantum mechanics method

BFGS – Broyden-Fletcher-Goldfarb-Shanno algorithm, an iterative method for non-linear optimization problems, named after its authors

BLYP – a combination of Becke exchange and Lee-Yang-Parr correlation functionals, a DFT method

CAS – complete active space, a multi-configurational post-HF *ab initio* method

CC – coupled clusters, a multi-configurational post-HF *ab initio* method

CI – configuration interaction, a multi-configurational post-HF *ab initio* method

CIS – a CI method with single-electron excitations only

DFT – density functional theory, a quantum-mechanical method

ECP – effective core potential, can be used to substitute inner shell elections in *ab initio* calculations

GGA – generalized gradient approximation, a method in DFT

HF – Hartree-Fock, a quantum-mechanical method, named after its authors

ISIF – a keyword of VASP software

MRCI – multi-reference configuration interaction, a multi-configurational post-HF *ab initio* method

NDO – neglect of diatomic overlap, a semi-empirical approach in quantum mechanics

PAW – projector augmented wave, a method within DFT, a plane wave DFT

PBC – periodic boundary condition, a technique of treating finite systems as infinite by replication

PBE – Perdew-Berke-Ernzerhof, an exchange-correlation DFT functional, named after its authors

PM* – Parameterization Model *, a family of semi-empirical quantum mechanics methods by J.J.P. Stewart

RM – Recife model 1, an extension of AM1

SCF – self-consistent field - iterative energy minimization procedure, used in most of quantum software

SD – steepest descent, in this work – a custom method of partial geometry optimization

SO – separate optimization, a custom method of partial geometry optimization

STO – Slater-type orbital, a set of Slater-type basis functions for quantum mechanical calculations

TZ2P – triple-zeta double polarization basis set

VASP – Vienna *ab initio* Simulation Package, quantum-mechanical DFT software

ZORA – zeroth order regular approximation to the Dirac equation, a relativistic quantum mechanical method

Other:

CIE – Commission internationale de l'éclairage, The International Commission on Illumination

FWHM – full-width at half-maximum, a spectral peak characteristic

ICDD – The International Center for Diffraction Data

LED – light electric diode

NLO – non-linear optics

NTSC – National Television Standards Committee

Summary – Streszczenie

W ramach przedstawionej pracy doktorskiej zrealizowano kilka zadań badawczych obejmujących syntezę i charakterystykę fotofizyczną oraz badania obliczeniowe wybranych luminoforów nieorganicznych domieszkowanych jonami lantanowców, Ln^{3+}. Przeprowadzono syntezę kilku materiałów luminescencyjnych opartych o mieszane borany metali (II) oraz pierwiastków ziem rzadkich, domieszkowane luminezującymi Ln^{3+}. Badania te dotyczyły mianowicie materiałów o ogólnym wzorze $M_3RE_2(BO_3)_4{:}Ln^{3+}$ (gdzie: M = Ca, Sr, Ba; RE = Y, La, Gd oraz $Ln^{3+} = Eu^{3+}, Tb^{3+}, Dy^{3+}$). Materiały tego typu nie były wcześniej badane w postaci nanoluminoforów. Jak wykazały wyniki badań, tego typu nanomateriały mogą być efektywnie otrzymywane za pomocą metody zol-żelowej Pechini'ego (z dodatkiem kwasu cytrynowego oraz etylenoglikolu). Wprowadzanie do badanych materiałów jonów Eu^{3+}, Tb^{3+} lub Dy^{3+} w formie domieszek, po wzbudzeniu promieniowaniem z zakresu nadfioletu, UV, prowadzi do intensywnej emisji światła czerwonego, zielonego lub białego. Widma wzbudzenia takich luminoforów wykazują różne pasma, takie jak: związane z przeniesieniem energii (związki domieszkowane Eu^{3+}) w zakresie 200-300 nm, pasmo odpowiadające wysokospinowemu przejściu f-d elektronowemu (Tb^{3+}) w zakresie 200-260 nm, oraz liczne pasma charakterystyczne dla przejść f-f elektronowych. Pasma odpowiadające przejściom f-f w badanych układach domieszkowanych Tb^{3+} lub Dy^{3+} mogą służyć do pobudzania tych luminoforów za pomocą diod elektroluminescencyjnych (LED) emitujących w zakresie niebieskim lub nadfioletowym. Kolor emisji luminoforów opartych o mieszane borany może ulegać pewnej modyfikacji w wyniku zmiany składu chemicznego materiału-matrycy.

Kolejna ważna część niniejszej pracy była poświęcona badaniom obliczeniowym, które obejmowały mało dotychczas zbadane aspekty strukturalne wybranych luminoforów ($Sr_3La_2(BO_3)_4{:}Tb^{3+}$, $CeF_3{:}Tb^{3+}$, $YVO_4{:}Eu^{3+}$) opartych o pierwiastki ziem rzadkich. Badania dotyczyły mianowicie wpływu domieszkowania na budowę krystaliczną materiału-matrycy, wpływu budowy krystalicznej matrycy na procesy przeniesienia energii oraz na tworzenie się aglomeratów powodowanych jonami domieszki. Metody kwantowo-mechaniczne pół-empiryczne oraz DFT były zastosowane do badania wpływu ilości domieszki na wymiary komórki podstawowej. Materiał domieszkowany jonami $'Ln^{3+}$ przedstawiono za pomocą superkomórki zbudowanej z wielu elementarnych komórek krystalicznych, zgodnie z budową krystaliczną materiału. Procentowa zawartość jonu domieszki została odtworzona poprzez podstawienie odpowiedniej liczby jonów lantanowca matrycy w początkowej strukturze jonami domieszki ($'Ln^{3+}$). Podstawiane poszczególne pozycje wybierano losowo, przy czym, dla każdej ilości domieszki wygenerowano dziesięć różnych losowo podstawionych struktur.

Struktury te poddano następnie minimalizacji energii całkowitej układu. Wyniki badań wykazały, że zwiększenie ilości domieszki Tb^{3+} w układach CeF_3 i $Sr_3La_2(BO_3)_4$ skutkowało zmniejszeniem wymiarów komórki. Jest to powodowane najprawdopodobniej wynikiem różnicy promieni jonowych jonów Ce^{3+}, La^{3+} i Tb^{3+}. Zarówno obliczenia pół-empiryczne jak również DFT wykazały dobrą zgodność przewidywanych wartości wymiarów komórek z danymi doświadczalnymi (błędy nie przekraczały kilku procent). Identyczne badania obliczeniowe przeprowadzono celem dokonania analizy dwóch nieidentycznych położeń krystalicznych jonów La^{3+} (La1 i La2, symetria punktowa C_1 w obu przypadkach) w układzie $Sr_3La_2(BO_3)_4$, różniących się geometrią otoczenia koordynacyjnego. W wytworzonej z badanego materiału superkomórce jony La^{3+} zastępowano jonami Tb^{3+}, jak opisano wyżej, tj. poprzez losowe podstawienie. Różnica polegała na tym, że w każdej oddzielnej strukturze podstawiane pozycje wybierano w taki sposób, aby jony domieszki podstawiały wyłącznie jedno z dwóch możliwych miejsc krystalograficznych. Obliczenia dowiodły, że umieszczenie domieszki w miejscu koordynacyjnym (La1) prowadzi do tworzenia się układu o niższej energii całkowitej niż w wypadku podstawienia odpowiednio w miejscu La2, dla każdej zbadanej ilości domieszki. Dowodzi to, że umieszczenie jonów domieszki w miejscu krystalograficznym La1 umożliwia powstanie struktury bardziej trwałej termodynamicznie. Wniosek ten jest zgodny z wynikami spektroskopii luminescencyjnej, uzyskanymi dla układu $Sr_3La_2(BO_3)_4:Tb^{3+}$. Analiza widm wzbudzenia dla $Sr_3La_2(BO_3)_4:Tb^{3+}$ umożliwiła określenie dwóch pasm w zakresie przejścia f-d, istotnie różniących się intensywnościami. Ze wzrostem stężenia domieszki, obserwowano wzrost intensywności mniej intensywnego pasma. Obserwacja ta sugeruje obecność dwóch centrów emisji; przy czym obsadzenie jednego z nich bardziej wzrasta wraz ze zwiększeniem ilości jonów domieszki, co prowadzi do wniosku o preferowanym obsadzaniu jednego z tych centrów. Małe ilości domieszki prowadzą do preferowanego sposobu obsadzenia, podczas gdy przy większych stężeniach domieszki o obsadzaniu decydują względy statystyczne, co prowadzi do wzrostu obsadzenia mniej preferowanego centrum emisyjnego.

Ważnym osiągnięciem tej dysertacji jest opracowanie metody obliczenia szybkości przeniesienia energii pomiędzy wieloma jonami Ln^{3+} w ciele stałym, z uwzględnieniem wielu możliwych odległości pomiędzy cząsteczkami donora i akceptora. Bezpromieniste przeniesienie energii skutecznie wpływa na wydajność emisji luminoforów opartych o jony lantanowców, zwłaszcza materiałów wykazujących konwersję energii w górę (ang. *upconversion luminescence*). Dla kryształu, który jest (teoretycznie) układem nieskończonym, istnieje wiele możliwości umieszczenia jonów domieszki, oraz wiele możliwych odległości pomiędzy nimi. Opracowane podejście polega na zastosowaniu superkomórki przedstawiającej układ krystaliczny, celem uzyskania zestawu możliwych odległości pomiędzy jonami domieszki w układzie, oraz liczby każdej z tych odległości. Dane te zostały następnie użyte do obliczenia efektywnej szybkości przeniesienia energii z uwzględnieniem wielu możliwych dróg. Tego typu podejście zostało zastosowane do teoretycznego modelowania dynamiki procesów przeniesienia energii w układzie YVO_4:Yb^{3+},Er^{3+}, wykazującym zjawisko upkonversji. Luminofor ten został opisany za pomocą układu równań różniczkowych, uwzględniających zmiany w czasie obsadzeń poszczególnych poziomów energetycznych układu. Do rozwiązywania układu równań zastosowano metodę Runge-Kutta. Procesy przeniesienia energii poddano modelowaniu dla przypadków wzbudzenia impulsowego oraz ciągłego. Scharakteryzowano, obliczono i porównano z danymi doświadczalnymi obsadzenie poziomów energetycznych, luminescencyjne czasy życia oraz liczbę fotonów wzbudzenia biorących udział w emisji jednego fotonu. Dobra zgodność uzyskanych wyników potwierdza skuteczność przyjętego modelu. Opisywana metoda modelowania może być zastosowana nie tylko do opisu układów upkonwersyjnych, ale też dla innych wykazujących przeniesienie energii.

Badania uwzględniały również analizę (za pomocą obliczeń kwantowo-mechanicznych) możliwości tworzenia klasterów jonów lantanowców w matrycach nieorganicznych. W rzeczywistości mało wiadomo o odległościach dotyczących wzajemnego rozmieszczenia jonów domieszki (położone blisko siebie czy maksymalnie oddalone, czy/lub losowo?). Mała liczba tego typu badań uniemożliwia wyjaśnienie kluczowego znaczenia i pełnego zrozumienia procesów przeniesienia energii, które zawsze uzależnione są od odległości pomiędzy biorącymi udział w tym procesie cząstkami. Badania w tym zakresie polegały na umieszczeniu kilku jonów domieszki (Eu^{3+}) w superkomórkach YVO_4 (zamiast jonów Y^{3+}) oraz analizie wpływu odległości pomiędzy tymi jonami na energię układu. Początkowa budowa krystaliczna nie ulegała zmianom, natomiast wymiary komórki ulegały relaksacji. Badania wykonane z użyciem obliczeń metodami pół-empirycznymi oraz DFT prowadzą do wniosku wskazującego, że ułożenie jonów domieszki blisko siebie w YVO_4 prowadzi do zmniejszenia energii całkowitej układu. Inaczej mówiąc, geometria układu odpowiadająca bardziej skupionemu ułożeniu jonów domieszki jest bardziej preferowana termodynamicznie, a więc możliwa jest tendencja do tworzenia aglomeratów jonów domieszki.

1. Aim of the study

The aim of the study presented was twofold. One aim was to obtain photoluminescence powder materials of a particular class of rare earth compounds, i.e. borates. The borate-based photoluminescence materials are known for their efficiency and stability and the demand for the new photoluminescence materials of potential application in light sources remains high. The double (mixed) borates of rare earth and alkaline earth metals such as Ca, Sr and Ba have been scarcely investigated as powder phosphors, although they offer more possibilities of photoluminescence tuning via materials composition. Thus, the experimental part concerned optimization of the synthesis of the mixed borates in a powder (nanocrystalline) form and characterization of their physicochemical properties that is structure and photoluminescence.

The other aim of the study was to provide theoretical descriptions of properties of the obtained materials in order to find out the effect of the structure of luminophores on their photoluminescence properties such as transition intensities and energy transfer processes. Generally, the effects of geometry on photoluminescence are described within the crystal field theory. On the other hand, some aspects such as the effects of doping on crystal structure have not been well understood as yet. The studies reported were focused on structural changes in selected doped materials, including the obtained mixed borates, and their effect on the photoluminescence properties (down- and upconversion). The intention of the study was to develop a set of computational tools to be used as extensions to the classical approaches for modeling and prediction of photoluminescence properties of the lanthanide-based inorganic solid luminophores on the basis of their composition and crystal structure.

2. Introduction

2.1. Lanthanides: general characterization

Lanthanides [1] are heavy transition metal elements of the first f-block. They are located in the sixth period of the periodic system. The series starts with lanthanum and ends with lutetium (atomic numbers 57 through 71). The fourteen elements after lanthanum are named lanthanides, while the lanthanides plus lanthanum together are referred to as lanthanoids, although often lanthanum is treated as one of the lanthanides. The lanthanoids together with scandium and yttrium are referred to as rare earth elements.

The most important electronic characteristic of the lanthanides it the presence of the unfilled 4f electron shell (except for the $4f^{14}$ Lu^{3+}). General configuration of neutral lanthanide atoms is [Xe] $6s^2$ $4f^n$. For some elements, the configuration is [Xe] $6s^2$ $5d^1$ $4f^{n-1}$ (La, Ce, Gd, Lu). The 3+ cations of lanthanides (Ln^{3+}) lack the 6s electrons. The occasional 5d electron or one of the 4f electrons are also missing in Ln^{3+}. As the ions are heavy, the relativistic effects and spin-orbit interactions are intense and important for them. These interactions (as well as numerous other factors) result in unique photoluminescence properties of Ln^{3+}, which make it attractive for various current and potential applications that explains much research interest in them.

Another characteristic feature of lanthanides is lanthanide contraction. The nature of 4f electrons results in their weak shielding of nuclear attraction that affects the electrons of 5s, 5d and 6s configurations. In the lanthanide series, the increase in the 4f orbitals population increases the shielding. However, as the shielding effect is weak, it cannot compensate the increasing attraction by the nucleus which results in reduction in the ionic radius. In particular, the ionic radii of Ln^{3+} cations decrease from 1.216 Å for La^{3+} down to 1.032 Å for Lu^{3+} (coordination number of 8) [2]. Due to this effect, La^{3+} is characterized by maximal possible coordination number of 12, while this number is only 9 for Lu^{3+}. In summary, chemical and stereochemical properties of lanthanides are similar but not identical.

The 4f configuration of Ln^{3+} is screened from chemical environment by the electrons of 5s and 5p configurations. All Ln^{3+} are hard Lewis acids and have a tendency to complex formation. However, as the 4f orbitals are screened, their overlap with the bonding orbitals of ligand atoms is low. Consequently, 4f electrons poorly affect the coordination geometry.

Ln^{3+} cations have very similar chemical properties and can replace each other in compounds. Therefore, the phenomenon of doping is common among the lanthanide-based materials: a small amount of 'Ln is added to the main Ln/RE-based compound (matrix). It is very probable that a mixture of Ln and 'Ln reagents would form a single compound containing both lanthanides rather than two separate compounds. In doped materials, in which rare earth trications of matrix material are substituted by the dopant Ln^{3+}, the doping itself may cause changes in crystal cell dimensions. In complexes, substitution of one Ln^{3+} by another Ln^{3+} would cause just a linear size change rather than significant geometry changes. Another manifestation of this is that naturally occurring lanthanide ores always contain more than one lanthanide elements in a single compound, and their separation can be troublesome. However, the doping is used in Ln^{3+}-based photoluminescent materials in which only small amounts of activator ions are sufficient. High concentrations of activator usually result in quenching, which limits the acceptable doping rates [3].

2.2. Photoluminescence of lanthanide ions

One of the most prominent (and also important for practical application) features of Ln^{3+} is their photoluminescence properties. The Ln^{3+} ions capabilities of absorption and emission of light in ultraviolet, visible and infrared ranges of spectrum are direct consequence of numerous energy levels originating from 4f electron configuration (Fig. 1). In particular, such ions as Ce^{3+}, Pr^{3+}, Sm^{3+}, Eu^{3+}, Tb^{3+}, Dy^{3+}, Ho^{3+}, Er^{3+} and Tm^{3+} can produce emission of light in the visible range. The colors can be red (Sm^{3+}, Eu^{3+}, Er^{3+}), green (Pr^{3+}, Tb^{3+}, Ho^{3+} Er^{3+}), blue (Tm^{3+}), yellow (Ce^{3+}, Ho^{3+}, Er^{3+}, Dy^{3+}) or white (Dy^{3+}). Ce^{3+} and Gd^{3+} are characterized by efficient absorption in the UV range and are capable of non-radiative energy transfer to other Ln^{3+} ions. Thanks to the latter feature, Ce^{3+} and Gd^{3+} are commonly used as co-activators/sensitizes (co-dopants). The transition lines of Ln^{3+} ions are sharp and similar to those in the atomic spectra unlike those from organic molecules. The emission and excitation spectra are different and unique for each of the lanthanide trivalent cations. Ln^{3+} luminescence is resistant to photobleaching as the transitions occur within a single electronic configuration of a single ion – unlike those of organic molecules. Moreover, the Ln^{3+} photoluminescence is predictable to a large extent. While the excitation and emission intensities can differ over quite a large range, the wavelengths of the bands of the same Ln^{3+} in different compounds can differ only by as much as several nanometers (except for Ce^{3+}). The photoluminescence of each lanthanide can be tuned within some range, but the tunable aspects are limited to intensities of absorption/emission lines and lifetimes of emission. To sum up, Ln^{3+} are useful luminescence centers which find different applications in lasers, scintillators, light sources, nonlinear optical devices and biotechnology [4,5]. That is why it is important to know the dependence of lanthanide luminescence properties on the type of material used, from both application and cognitive point of view.

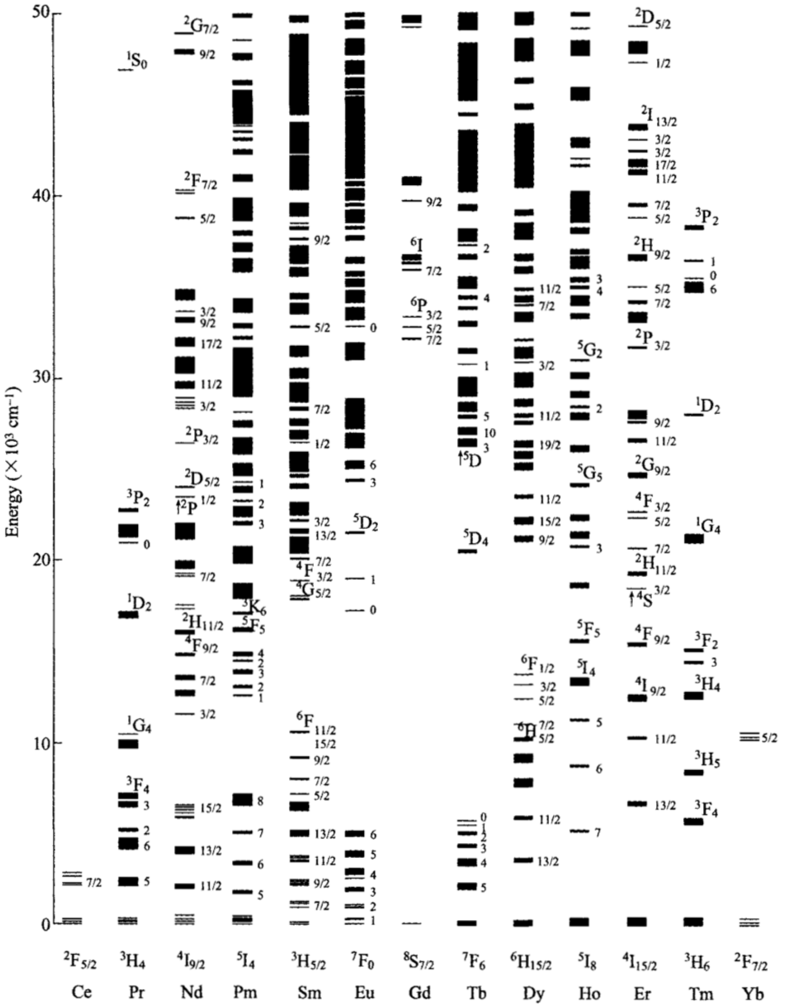

Fig. 1. The diagram of Ln^{3+} energy levels [5]

2.2.1. Photoluminescence spectroscopy

Photoluminescence spectroscopy is a common name to a number of research techniques based on measurements of photoluminescence features of a material studied. Luminescence is a property of material to emit electromagnetic radiation other than thermal (blackbody) radiation. A material capable of light emission is called luminophore. Photoluminescence is a phenomenon of electromagnetic radiation (light) emission under excitation by light (usually, the emission and excitation wavelengths differ). The quantum nature of matter is responsible for the luminescence properties. In particular, a transition between a pair of electronic levels of the luminophore corresponds to a specific type of luminescence. Other processes (*e.g.* vibronic, plasmonic, excitonic etc.) can participate in the luminescence process. In separate ions and molecules the photoluminescence-active levels are atomic orbitals and molecular orbitals, respectively. In solid state, the transitions usually occur between the electronic bands. Electronic structure of Ln^{3+} is a special case. The photoluminescence levels of Ln^{3+} originate from a single 4f configuration and behave similarly to the electronic states of a free ion - either in solution, in complexes or in a solid state.

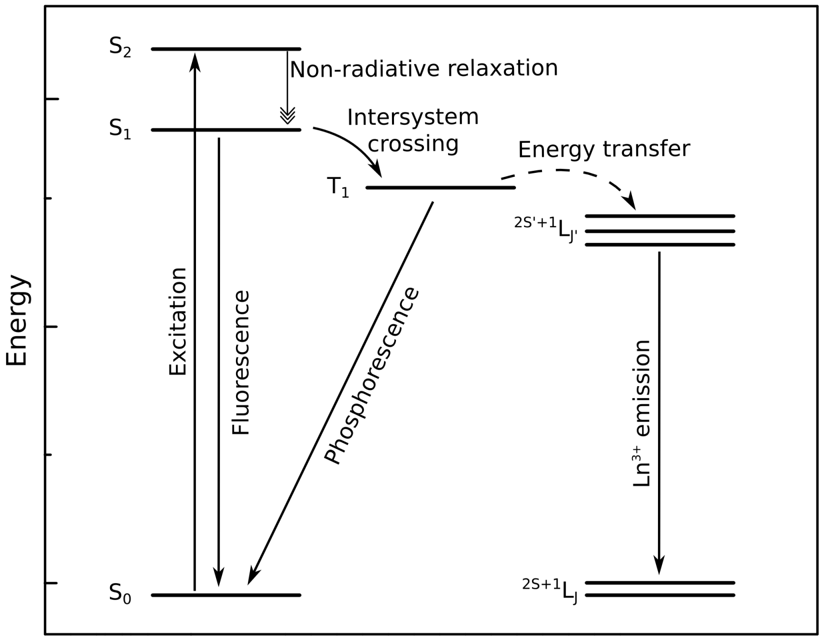

Fig. 2. A simple Jablonski diagram of exemplary complex of Ln^{3+} with an organic ligand

The process of luminescence and the related processes can be illustrated using a simple Jablonski diagram (Fig. 2) that is named after its author, Aleksander Jabłoński. As an example, a diagram of a complex of Ln^{3+} with an organic ligand will be considered (singlet ($S_{0,1,2}$) and triplet (T_1) spin states correspond to the ligand). In a diagram of this type the ordinate axis represents the energy of a level. The energy levels corresponding to the states of the same multiplicity are displayed above each other, in a single column. The states corresponding to other spin multiplicities are displayed in the following columns. There can be as many columns as are there different kinds of species (atoms, molecules) and the corresponding multiplicities. Vertical arrows indicate transitions that do not cause spin multiplicity changes. These transitions include the absorption/excitation processes, in which the system gains energy. Consequently, the corresponding arrows are pointed up. The other "vertical" processes include nonradiative and radiative relaxation processes corresponding to energy decrease. Radiative transitions correspond to the emission of photons. The energy of the emitted photon should be equal to the transition energy. As the energy of the system is decreased in such process, the corresponding arrow points down. Such processes are spin-allowed (spin multiplicity change is zero) and are characterized by high values of the oscillator strength. The emission intensities and transitions rates of such processes are high while the lifetimes are short (nano- to picoseconds). The emission of this type in organic molecules is called fluorescence. The non-radiative relaxation might occur via vibronic processes i.e. via coupling of the electronic transition to a molecular vibrations or phonons. In such processes, the transition energy is lost in the form of heat. The transition rates depend strongly on the amount of vibration quanta/photons. The other processes include intersystem crossing and energy transfer processes. In the former, a transition to an energy level of different multiplicity occurs. As the energies of the initial and the final states are not equal, such processes are usually assisted by the vibronic processes, showed as wavy lines on the diagram. The emission processes from triplet levels usually result in the relaxation to the singlet ground state, that is, another change in spin occurs. As the spin multiplicity change of the transition is non-zero, the transitions of that kind are spin-forbidden and are characterized by low rates and intensities, while the lifetimes (micro- to nanoseconds) are longer that those of fluorescence processes. The emission from triplet states is called phosphorescence. The transitions of Ln^{3+} cations are special because of the strong spin-orbit coupling. Consequently, total spin momentum quantum number S and total orbital momentum L are not good quantum numbers. In other words, the states of different multiplicity are not purely spin states (still, the $^{2S+1}L_J$ notations is used). Consequently, the lanthanide 4f levels of a single ion are displayed in a single column, no matter of S and L. Also, the terms of fluorescence and phosphorescence do not apply to Ln^{3+} ions. A more general term of luminescence is commonly used.

2.2.2. Sensitization of lanthanide ions emission

The excitation of Ln^{3+} ions can occur via the 4f-4f or 4f-d5 electronic excitations or via charge transfer processes. The 4f-5d transitions are allowed and characterized by high intensities. However they occur only in several Ln^{3+} cations, such as Ce^{3+} or Tb^{3+}. One of the ways of improving photoefficiency of a Ln^{3+}-based material is to use these ions as co-activators. As Ln^{3+} ions are capable of non-radiative energy transfer, the excitation energy can be transmitted from co-activator to the emitter.

The 4f-4f transitions are forbidden and result in very weak intensities of Ln^{3+} optical transitions, unless an appropriately strong and non-centrosymmentric crystal or ligand field is provided. This applies to both emission and absorption intensities. Consequently, in order to create a light-converting material based on Ln^{3+}, the absorption efficiency must be increased. In the complexes of Ln^{3+} with organic ligands, the ligands are usually the sensitizers. There are numerous organic compounds that absorb light efficiently. In a complex, the excitation energy can be transferred to the central ion via ligand-to-metal energy transfer process. Both efficient absorption of organic part and the energy transfer result in high efficiency of photoluminescence of Ln^{3+} complexes. This effect has been called the *antenna effect* or *light harvesting* [6,7]. In solid inorganic Ln^{3+}-based luminophores the role of sensitization remains important. However, it can be achieved in several ways different from that of addition of organic complexes.

Another option of sensitization includes charge transfer processes. In such processes, absorption of a photon excites an electron from the top of the materials valence band [8]. The electron can bind to an Ln^{3+} ion forming a Ln^{2+} ion (most likely, in its ground state). Still, such state is excited in respect to the initial electron equilibrium and the electron can relax back to the valence band. The released energy can promote the restored Ln^{3+} ion to one of its high-lying excited states. However, in order to make this kind of excitation feasible, the ground state of Ln^{2+} must be located above the valence band and below the conduction band [8]. The information required to predict the location of Ln^{2+} in the band structure of particular material providing opportunities for design of a material of desired properties is given in [8].

2.2.3. Energy transfer processes

Important elements of photoluminescence-related processes are non-radiative energy transfer processes. In processes of this type at least two different species must be involved. The relaxation of an excited state may not necessarily result in photon or phonon emission. The corresponding energy can be transferred non-radiatively to another species resulting in increase in its electronic energy. Such processes are possible via electric multipole interaction [9]. The first theoretical quantum-mechanical treatment of this problem has been provided by Förster [10], who has taken into account only the dipole-dipole interaction. For the ligand-to-metal or metal-to-metal energy transfer cases, higher-order interactions such as dipole-quadruple and quadruple-quadruple should be also considered, as proposed later by Dexter [11]. The energy transfer according to the above mechanisms decreases strongly with increasing donor-acceptor distance, and usually becomes irrelevant at 10-20 Å. The energy difference between the energy donor and acceptor transitions should be as small as possible. In particular, the energy transfer rate is a linear function of the so-called spectral overlap factor F. The latter is an overlap between the donor emission peak and the acceptor absorption peak, both corresponding to the transitions participating in the energy transfer process.

Several types of energy transfer processes involve Ln^{3+} ions. The initial excitation energy can correspond either to an excited state originating from the matrix compound itself (*e.g.* V-O bond absorption in vanadates) or the excited state of another Ln^{3+}. In some cases, virtual state can be the energy donor. For instance, in Yb^{3+}-doped compounds, a virtual state of energy double that of Yb^{3+} excited state is observed [12]. The non-radiative energy transfer between Ln^{3+} ions is actually a very important feature. It can result in both useful and useless processes. An example of a useful process is the upconversion emission. In this kind of process the energy of excitation photon is lower than the energy of the emission photon. For instance, the same Ln^{3+} can be excited from the ground state by one photon, then re-excited to higher levels by the following photon(s) [12]. The energy from excitation source is thus accumulated within a given Ln^{3+} leading to the emission of a photon of higher energy. Such a process can occur in Er^{3+}-doped materials. Alternatively, an Yb^{3+} co-dopant can be used. The absorption of Yb^{3+} in the infrared is very efficient. The energy from Yb^{3+} excited state is then transferred non-radiatively to the activator ions (Ho^{3+}, Tm^{3+}, Er^{3+}) promoting them to high excited levels. The occurrence and efficiency of these processes depends to a large extent on the energy transfer efficiency. The energy transfer processes can also lead to quenching. The most common is the concentration quenching which occurs at higher amounts of dopant ions. The mechanism is referred to as a cross-relaxation: the energy is transferred from high-lying levels of one Ln^{3+} to the low-lying levels of another Ln^{3+} ion, which undergoes a relaxation [13]. Additionally, the energy can migrate from one Ln^{3+} to another before it is finally turned into the emission photon [14]. Another pathway of quenching of the Ln^{3+} emission is through the vibronic processes. The excited levels of Ln^{3+} can couple to both phonons and molecular vibrations. As a result, the excitation energy is converted to heat instead of light. The efficiency of quenching depends on the energy of the coupled oscillator. The dependence is described by the energy gap law [15]. Generally, the smaller the energy of the quenched transition is, the smaller the oscillation energy is required to quench it. Therefore, the energy of phonons of the matrix compound can significantly affect the photoefficiency of the doped material. Additionally, the OH oscillators are very efficient quenchers [4,7] because of their high oscillation energy of more than 3000 cm^{-1} (for comparison – the most important Ln^{3+} transition energies range from several thousands to tens of thousands cm^{-1}).

2.2.4. Upconversion emission

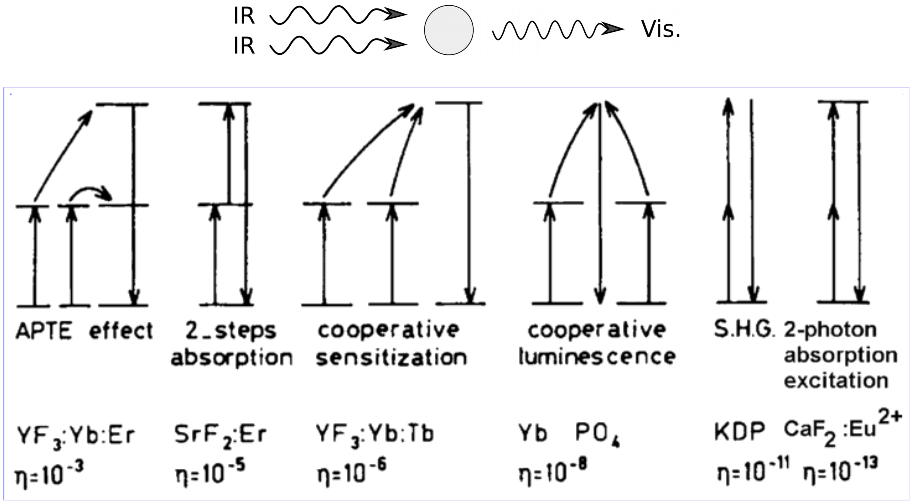

Fig. 3. General scheme of upconversion and various upconversion mechanisms and their efficiency [12]

Regular singe-photon luminescence processes follow the Stokes law which says that the energy of emitted photon is always lower than the energy of the excitation photon. Some exceptions to the rule are the cases in which a level right above the excitation level is efficiently thermally populated. If so, the energy of emitted photon can be slightly higher than the excitation photon energy. This type emission is called anti-Stokes emission as it violates the Stokes law. The upconversion, however, is a kind of anti-Stokes emission in which more than one excitation photons are involved in order to produce a single emission photon. Consequently, the emission photon energy is rather lower than the sum of the excitation photons energies, while it is much higher than the energy of a single excitation photon. The term of *upconversion* refers to the fact the emission photon energy is increased in respect to the excitation photon energy. Several mechanisms can be responsible for the upconversion emission. A single-ion mechanism is called *excited state absorption*. In this mechanism, the activator ion in one of its excited states absorbs another excitation photon and gets promoted to the higher-lying excited state. The energy difference between the states should correspond to the absorbed photon energy. This kind of excitation can be followed by the upconversion emission of a higher-energy photon. More than two excitation photons can participate. Other mechanisms are based on energy transfer processes (Fig. 3). In the *energy transfer upconversion*, the sequential excitations of the activator ion occur via portions of energy transferred from the sensitizer ions. Such process requires the activator ion of energy levels such that energies of the first, second and following excitation steps would match the energy of the sensitizer (energy donor) transition. An alternative mechanism of *cooperative sensitization* involves two ions of the sensitizer and a virtual state of energy twice as large as that of the sensitizer excited state. The virtual state can relax via both upconversion emission (radiative process) or an energy transfer to an activator level of the matching energy. The mechanisms are characterized by different yields. The most efficient is the energy transfer upconversion, next is the excited state absorption while the cooperative sensitization and other mechanisms are even less efficient.

2.3. Lanthanide photoluminescence: theory

Photoluminescence properties of lanthanide ions such as spectroscopic energy levels, emission lifetimes and absorption/emission intensities strongly depend on the number of 4f electrons and on the chemical nature and structure of the compound, containing the Ln^{3+} emission center. The optically active transitions occur between the energy levels produced by the 4f electron interactions within the 4f subshell. The interactions, however, involve both lanthanide ion itself and the atoms around it. Coulomb interaction splits the energy levels of the 4f configuration into terms, the terms are split into manifolds as a result of spin-orbit coupling, while the manifolds are split into Stark levels by the crystal field. The transitions between these levels are forbidden, but they can be allowed by means of admixing higher $4f^{n-1}$ 5d configurations into $4f^{n}$ configuration. The most prominent works on the task were published in 1937 by J.H. Van Vleck [16] and in 1940s by G. Racah [17], which made a background for B.R. Judd [18] and G.S. Ofelt [19] publications in 1962 [20]. The theory describing the intensities of the Ln^{3+} transitions is known now as the Judd-Ofelt theory. It can be used in the form of full solution to calculate transitions between individual Stark levels. However, more often it is used in approximate form for the calculations of manifold-to-manifold transitions [20]. In this case, almost all properties of the emission center and its surrounding are represented by three parameters Ω_λ (λ=2,4,6), which can be either calculated from first principles (*ab initio*) or fitted to experimental data. The Ω_λ parameters link the emission intensities and geometry. In particular, the integrated coefficient of spontaneous emission of a transition between two manifolds J and J' is given by [6]:

$$A_{JJ'} = \frac{4e^2\omega^3}{3\hbar c^3}\left(\frac{n(n^2+2)^2}{9}S_{ED} + n^3 S_{MD}\right) \tag{2.3.1}$$

$$S_{ED} = \frac{1}{2J+1}\sum_{\lambda=2,4,6}\Omega_\lambda \left\langle J'||U^{(\lambda)}||J\right\rangle^2 \tag{2.3.2}$$

$$S_{MD} = \frac{\hbar^2}{4mc^2}\left\langle J'||L+2S||J\right\rangle^2 \tag{2.3.3}$$

Where J and J' are the total angular momenta of the initial and final states, respectively, *e* is the electronic charge, *m* is the electron mass, ω is the angular frequency of the transition, $\hbar$ is Planck’s constant over 2π, *c* is the speed of light, and *n* is the refractive index of the medium [6].

2.3.1. Wavefunctions, coupling schemes and matrix elements

As mentioned above, the Ln^{3+} emission intensity is defined by the strength of electric and magnetic dipoles assigned to the transition states. The dipoles are described by the respective matrix elements (the terms in the ⟨⟩ brackets in Eq. 2.3.1-3). The matrix elements are the integrals of electric or magnetic dipole operators between the lower and upper wavefunctions of the transition, integrated by the volume of the central atom [20]. The electron-unique wavefunction is described by the series of quantum numbers, namely α, L, S, J and M, where S is a spin angular momentum, L is orbital angular momentum, J is total angular momentum, $M = M_J$ = -J, -J+1,. J-1, J arises from the angular momentum coupling and α represents other quantum numbers required to define a state. S, L and J are used to label the corresponding states as spectroscopic terms of $^{2S+1}L_J$. Although in both spectroscopy and theory of lanthanide photoluminescence, the $^{2S+1}L_J$ notation is used, these states are not pure and have some admixture of other states. The degeneracy of the $^{2S+1}L_J$ terms is 2J+1. The 2J+1 Stark levels are split by the crystal filed and give separate spectroscopic signals. The full solution of Judd-Ofelt theory applies to these levels. Application of a spherical tensor operator $\mathbf{T}_q^{(\lambda)}$ corresponding to a transition between two states would result in matrix elements of the form $\langle \alpha LSJM \mid \mathbf{T}_q^{(\lambda)} \mid \alpha' L' S' J' M' \rangle$. If, however, one wants to analyze manifold-to-manifold transitions (the most popular case), many matrix elements describe a single transition [21]. Thus, a simplification by Wigner-Eckart theorem can be applied in order to obtain a set of reduced matrix elements (independent of M), connected to the original set of matrix elements by a 3-j symbol. Similarly, another simplification step would introduce a 6-j symbol and doubly reduced matrix elements [21].

In the free-ion approximation used in the Judd-Ofelt theory, the matrix elements are obtained within the intermediate coupling scheme, which is based on the LS (Russell-Sanders) coupling scheme [21]. If, however, the electron-electron repulsion is of the same order of magnitude as the spin-orbit coupling [20], the LS coupling is not good any more as different terms start to mix up with one another. Thus, the intermediate coupling is applied and describes the $|f^n \alpha [SL] J\rangle$ states as a linear combination of the $|f^n \alpha SLJ\rangle$ free-ion LS wavefunction, which can be obtained from literature [21].

$$|f^n \alpha [SL] J\rangle = \sum_{S,L} C\,(S,L) |f^n \alpha SLJ\rangle \tag{2.3.4}$$

The linear combination (coupling) coefficients *C(S,L)* are found by diagonalization of combined electrostatic, spin-orbit and configuration interaction energy matrices [20]. Such task requires a prominent computational effort and had not been made until the first electronic computers became available in the 1960s. As the crystal field effects are added as small perturbations, the matrix elements are almost the same for Ln^{3+} in different materials. Thus, the pre-obtained tabulated values are most commonly used.

The mentioned coupling coefficients from the intermediate coupling scheme as well as the intermediate-coupled wavefunctions $|f^n [SL] J\rangle$ are also used to calculate magnetic dipole strength of the transition. The details of such calculations are provided elsewhere [22].

2.3.2. Judd-Ofelt theory and its extensions

The problem resolved by the Judd-Ofelt theory concerns the intensities of Ln^{3+} electron excitation and emission transitions in the optical range [20]. The sharp lines of such transitions, similar to the free-ion spectral lines, suggested that the transitions occur within the

4f subshell. The problem was to find out the mechanism responsible for the transition intensities. On the one hand, the electric dipole mechanism was feasible. However, according to the Laporte selection rules, the electric dipole transitions cannot occur between the states of the same parity (even or odd). As both states belong to the 4f configuration, they are of the same parity. The respective electric dipole transitions are forbidden and thus their intensity is very low. On the other hand, such transitions by the magnetic dipole or electric quadruple are allowed. The problem here is that the magnetic dipole mechanism cannot be responsible for all of the lines, while the electric quadruple mechanism is unsuitable, as follows from the intensities of the transitions. This puzzle has been finally resolved independently by B.R. Judd and G.S. Ofelt [18,19], on the basis of previous theories and mathematical tools. The main idea was that the transitions are actually electric dipole, but the states are not purely single-configurational. As a result of the crystal field effect, some of the 5d and higher states is admixed to the 4f states. Consequently, the states are characterized by a mixed parity and the selection rules are relaxed, increasing the transition intensities. However, the effect vanishes in a centrosymmetric crystal field. As the selection rules relaxation is forced by the crystal field, the mechanism is commonly referred to as forced electric dipole mechanism.

Judd-Ofelt theory is based on several approximations. The static approximation postulates that the central ion is located in the static electric field produced by the surrounding ions. The field can be a crystal field (in solids) or a ligand field (in complexes). Next, the free-ion approximation is applied, that is, the central ion is described by a free-ion (ion in vacuum) Hamiltonian operator, while the static crystal field is applied as perturbation. Finally, by the single-configuration approximation, the interactions between configurations are neglected, although they are mixed with each other.

$$\langle\psi_a| = \langle\phi_a| + \sum_{\beta} \frac{\langle\phi_a|V|\phi_\beta\rangle}{E_a - E_\beta}\langle\phi_\beta| \tag{2.3.5}$$

$$|\psi_b\rangle = |\phi_b\rangle + \sum_{\beta} \frac{\langle\phi_\beta|V|\phi_b\rangle}{E_b - E_\beta}|\phi_\beta\rangle \tag{2.3.6}$$

where $\langle\psi_a|$ and $|\psi_b\rangle$ are the initial and final mixed parity states, respectively, $\langle\phi_a|$ and $|\phi_b\rangle$ are the initial and final states of single parity (the $|4f^n\alpha[SL]JM\rangle$ states), while $|\phi_\beta\rangle = |nl\,\alpha''[S''L'']J''M''\rangle$ are the states of higher configuration and opposite parity, V is a crystal field operator and $E_{a,b,\beta}$ are the energies of the respective configurations. The electric dipole matrix elements D can be found by applying the electric dipole operator **P** to the $\langle\psi_a|$ and $|\psi_b\rangle$ states [20,21]:

$$\mathbf{P} = -e\sum_i \mathbf{r}_i \tag{2.3.7}$$

$$D = \langle\psi_a|\mathbf{P}|\psi_b\rangle = \sum_\beta \left(\frac{\langle\phi_a|V|\phi_\beta\rangle\langle\phi_\beta|\mathbf{P}|\phi_b\rangle}{E_a - E_\beta} + \frac{\langle\phi_a|\mathbf{P}|\phi_\beta\rangle\langle\phi_\beta|V|\phi_b\rangle}{E_b - E_\beta}\right) \tag{2.3.8}$$

At this point, the tensor forms of the operators are applied [20,21]. It is assumed that the higher configuration energy takes a particular value, E_β, and that the $E_a - E_\beta$ and $E_b - E_\beta$ energy differences are the same. The higher configuration states ϕ_β are considered completely degenerate in J. Next, the closure of $|\phi_\beta\rangle\langle\phi_\beta| = 1$ is used meaning that the higher configuration states form a complete orthonormal set of wavefunctions [20]. After that, the equation can be simplified according to the Wigner-Eckart theorem, and the angular parts of the electric dipole and crystal field operators (in tensor form) can be combined. The following simplification produces an equation with effective tensor operator $\mathbf{U}^\lambda_Q$. Further simplification allows elimination of the dependence of the wavefunctions on M and produces the full solution of the Judd-Ofelt theory with the $\mathbf{U}^\lambda$ tensor operator. It is important that the separation of geometry and physics takes place at the tensor operator combination stage. The physics is contained in the reduced matrix elements of the $\mathbf{U}^\lambda$ tensor operator. As the physics part (represented by the matrix elements of $\mathbf{U}^\lambda$) does not contain geometry, the matrix elements should be the same (to some extent) in any material. While further simplifications are applied to obtain a more commonly used short version of the theory, these matrix elements remain the essential part of it.

However, the static crystal field model was not enough. In particular, it did not explain the behavior of some transitions, which were called hypersensitive. Thus, a dynamic coupling model was introduced by Jørgensen and Judd in 1964 [23]. In general, the idea was that ligand atoms actively participate in the transitions between the central Ln^{3+} ion 4f states. Unlike in the crystal field model, in which the ligated atoms produce a static filed, in the dynamic coupling model the atoms surrounding the central (activator ion) can be polarized by the incident radiation. Thus induced oscillating dipoles interact with the central ion and can increase the transition intensities of the latter. The induced dipoles strengths depend on isotropic dipolar polarizabilities of the surrounding atoms [24]. The dynamic coupling Hamiltonian must be added to the interaction which results in forced electric dipole mechanism. The solution is similar to the original Judd-Ofelt theory. This model brings another contribution to the intensity parameters, besides the crystal field contribution.

$$\Omega_\lambda = (2\lambda + 1)\sum_{t,p}\frac{|B_{\lambda tp}|^2}{(2t+1)} \tag{2.3.9}$$

$$B_{\lambda tp} = B_{\lambda tp}^{FED} + B_{\lambda tp}^{DC} \tag{2.3.10}$$

$$B_{\lambda tp}^{FED} = \frac{2}{\Delta E} \left\langle r^{t+1} \right\rangle \Theta(t, \lambda) \gamma_p^t \tag{2.3.11}$$

$$\gamma_p^t = e^2 \left(\frac{4\pi}{2t+1} \right)^{1/2} \sum_j \left(\rho_j (2\beta_j)^{t+1} g_j \frac{Y_p^{t*}(\Theta_j, \phi_j)}{R_j^{t+1}} \right) \tag{2.3.12}$$

$$B_{\lambda tp}^{DC} = -\left(\frac{(\lambda+1)(2\lambda+3)}{(2\lambda+1)} \right)^{1/2} \left\langle r^{\lambda} \right\rangle (1-\sigma_\lambda) \left\langle 3 \left\| C^{(\lambda)} \right\| 3 \right\rangle \Gamma_p^t \delta_{t,\lambda+1} \tag{2.3.13}$$

$$\Gamma_p^t = \left(\frac{4\pi}{2t+1} \right)^{1/2} \sum_j \left(\alpha_j \frac{Y_p^{t*}(\Theta_j, \phi_j)}{R_j^{t+1}} \right) \tag{2.3.14}$$

Here, the coordination geometry is stored in the spherical coordinates R_j, Θ_j, ϕ_j and belongs to the input data. The other variables according to [6] are: ΔE is the energy difference between the barycenters of the excited $4f^{n-1}$ $5d^1$ and ground $4f^n$ configurations, $\langle r^x \rangle$ is a 4f radial integral, $\Theta(t, \lambda)$ is a numerical factor, $(1-\sigma_\lambda)$ is a screening factor, $\langle || C^{(\lambda)} || \rangle$ is the Racah tensor operator of rank λ, $\delta_{t,\,\lambda+1}$ is the Kronecker delta function, ρ is the central ion-ligand overlap integral, $\beta_i = (1+\rho_i)^{-1}$, e is the elementary charge and Y_p^{t*} are the spherical harmonics. The FED and DC abbreviations stand for the forced electric dipole mechanism, as expressed by the average energy denominator method, and the dynamic coupling mechanism within the point dipole isotropic ligand polarizability approximation [6]. Odd-rank ligand field parameters γ_p^t are provided within the simple overlap model.

The isotropic polarizability of ligated atom or group of atoms [6] α is not computed directly and is a fit parameter. The charge factor g can be a fit parameter too, or may be calculated from the chemical bond overlap [25]. Alternatively, ligated ion valence can be used as g, while the values of α can be obtained from literature data.

2.4. Quantum-chemical computational methods

Following the advances in digital computing, computational techniques have been found increasingly useful and applied along with the experimental studies. On the one hand, the theory and calculations can provide more information about the system studied and thus improve the understanding of the subject. On the other hand, the computations can predict the results of yet unperformed experiments and help reducing the experimental effort expenses. There are, basically, two types of approach, namely the *ab initio* methods and semi-empirical ones. In the former, every modeled aspect is calculated from scratch, while in the latter some diatomic integrals are replaced with pre-obtained experimental or computational values

[26,27]. Consequently, the *ab initio* methods offer precise results of good agreement with the experiment, but are usually time-costly. Meanwhile, semi-empirical methods are known to produce some errors in exchange for very short calculation times.

2.4.1. Hartree-Fock self-consistent field approach and later extensions

The Hartree-Fock method [28], which is used in most of the modern quantum-chemical software, is an approximation to a solution of a many-body electron system. In this approach, the electrons are located in the central field of other electrons. In other words, the electron-electron repulsion is integrated, and the average effect of the repulsion is taken into account [26]. Additionally, the approach separates a many-electron wavefunction into single-electron wavefunctions which are called spin-orbitals or just orbitals. The single-electron wavefunction, which depends on spatial coordinates, is represented in the spherical coordinate system of distance R and angles Θ and φ. Next, the radial and angular parts are separated. The angular part, responsible for the orbital symmetry, is given by a special set of functions called spherical harmonics. The exact radial function is unknown and is usually expanded in a set of basis functions. A basis function is most commonly a Gaussian function or, less commonly, a Slater function. A single-electron wavefunction can contain one or more basis functions, weighted by particular coefficients. The multi-electron wavefunction is a linear combination of the single-electron wavefunctions [29]. The single-electron wavefunctions must satisfy the Pauli exclusion principle, that is, the electrons should be indistinguishable. In order to achieve this goal, the multi-electron wavefunction is represented as a determinant, in which columns are vector representations the singe-electron wavefunctions. If any two columns of the determinant are interchanged, the determinant changes its sign, which represents the antysymmetricity of a multi-fermion wavefunction in respect to interchange of any two particles. The determinant of that kind is called the Slater determinant. One Slater determinant represents one state of a multi-electron system. In the Hartree-Fock computation, the single determinant is assumed to represent the ground state. After the determinant is formed, a variational method [30] is applied to the set of the linear combination coefficients in order to minimize the energy. The procedure is called the self-consistent field (SCF) and is continued until the energy and the coefficients remain unchanged between the iterations (converge).

The presented concept is used in most of the computation methods, including semi-empirical and DFT computations. Most of them use basis sets, Slater determinants and the SCF procedure.

2.4.2. Semi-empirical NDO methods

As noted before, the general strategy of the semi-empirical calculations is the same as that of the Hartree-Fock method. The essential difference is in the computation of the energy of the system. In order to save computational power and reduce the computation time, some properties (two-electron integrals) are totally neglected (not calculated) while some others are replaced by the pre-calculated or experimental values. Some parameters may be added in order to compensate for the errors introduced by the simplifications. The set of parameters and not-calculated values is called parameterization. Additionally, core electrons might be omitted and small (single-function) basis sets are used.

In the studies presented in this thesis, only two groups of semi-empirical methods were applied. They are, namely, the AM1[31] model and its extension – the RM1 [32] model, and the PM3 [33–36], PM6 [37,38] and PM7 [39] methods which are the consequent extensions of each other.

In the PM* methods, the two-center two-electron integrals are neglected. However, a one-electron two-center integral is calculated. A full description of the parameters used in the methods is given in [40].

Another semi-empirical model used was the Sparkle model [41–44] chosen to represent the Ln^{3+} cations in the semi-empirical computations. The Sparkle model is essentially important for modeling lanthanide compounds by semi-empirical methods as the other kinds of semi-empirical parameterization representing Ln^{3+} are usually missing. In this model, Ln^{3+} are represented as point charges with no electrons. These point charges are supplied with a bonding radius and the diffuse functions. Thus, the Sparkle Ln^{3+} "ion" is not just a point charge, but rather a charge delocalized over a sphere [41]. Although they are rather crude approximation, Sparkle computations are characterized by acceptable agreement of theoretical geometries with the experiment [6,45,46]

2.4.3. Density functional theory

Density functional theory, commonly abbreviated as DFT, is based on a concept different from those applied in the Hartree-Fock and post-HF methods. That is, in HF, the properties are calculated on the basis of the wavefunction, while in DFT, the properties are calculated on the basis of electron density [47,48]. The wavefunction and the energy that is minimized in the variational procedure are both functionals of electron density. The wavefunction is composed of numerous orthonormal electron orbitals and is thus multidimensional. The electron density of a molecule as a whole (in the stationary case) depends only on the three spatial coordinates. Thus, the minimization procedure is much simpler and faster in DFT. The most important question in DFT is the density functional itself, which must correctly reproduce electron exchange and correlations. The exact functional remains unknown so far, while all existing DFT functionals are approximations to the exact functional [49,50].

An important variant of the DFT method is the Projector Augmented Wave approach [51], which is commonly called a plane-wave DFT. In regular DFT, the computation is based on (most-commonly) Gaussian type basis functions used to construct the orbitals. It has been shown that it is possible to use a function describing a plane wave. The basis size in this case is defined by the amount of plane waves in question, which in turn is defined by the plane wave cutoff energy [52]. This approach works only with periodic boundary conditions. That is, the defined volume of space that is modeled is treated as an element repeated infinitely in three dimensions. The disadvantage of the approach is that the vacuum (if any) in the periodic box consumes the computational power, unlike the approaches with Gaussian-type or Slater-type basis functions.

Both semi-empirical and *ab initio* methods can be applied to isolated species (a non-periodic, molecule-in-vacuum approach) or continuous systems (a periodic, infinite-space approach).

2.4.4. Computational studies in the field of lanthanide-based luminophores

The name of computational studies of lanthanide-based photoluminescent compounds can refer to a few different fields. One of them is related to crystal field calculations [53], usually based on the phenomenological approach to the problem. That is, a crystal field Hamiltonian is constructed as a sum of crystal field parameters (geometry-based symmetry restrictions apply). Diagonalization of such a Hamiltonian produces a set of energy levels. Then, a variational method is applied to the crystal field parameters in order to match the resulting theoretical energy levels with the experimental ones. Crystal field parameters are used as a universal description of spectroscopic properties and that is why their use permits comparative analysis of results from different methods and different experimental data. Similarly, Judd-Ofelt intensity parameters are often treated phenomenologically (are fitted to the experiment) and then used for interpretation of the experimental results.

Another field concerns the computations of the crystal field and intensity parameters using the conventional quantum-chemistry software. There are two main problems in this area. The first one concerns the computation itself, that is, the representation of solids in different ways, the computational methods and their quality and the agreement with experiment. The other problem concerns the extraction of the crystal field parameters data from such computations [54–56]. This task is important as the crystal field parameters can be easily compared to the huge amount of the other results available in literature, both experimental and theoretical. In this way the quality of the computational results can be evaluated.

The computational studies concerning complexes are usually simpler as a complex is a separate molecule. Its geometry and the excited states of the organic part can be properly predicted even with the semi-empirical quantum-chemical methods. This fact has resulted in a set of methods [6,57] providing full description of the photoluminescence properties of Ln^{3+} complexes with organic ligands. The tools for analysis of excitation and emission energy levels, transition probabilities, energy transfer pathways and dynamics as well as photoluminescence lifetimes and quantum yields were developed. All of the mentioned parameters be calculated and compared with experiment.

In the field of solid state, the question is a bit more complicated. On the one hand, it is possible to represent an infinite solid crystal by a piece of solid repeated infinitely (the unit cell principle) [58–60]. On the other hand, the periodic box should be large enough to contain the central ion and its surrounding. The bigger the system is, the greater are the computation expenses. The workarounds include the embed cluster method (a coordination complex in a box of point charges [61,62] or in a model potential [63–65]). Another problem originates from the nature of 4f electrons. The spin-orbit interactions and relativistic effects are strong and must be taken into regard if a good result is to be obtained. Advanced DFT methods might be required [66]. Alternatively, multi-configuration methods such as complete active space (CAS) [65], coupled clusters (CC) [67] configuration interaction [68] or a multi-reference configuration interaction (MRCI) [69] should rather be used.

The presence of non-valence (inner shell) electrons is important for Ln^{3+}-related calculations. On the one hand, those electrons are not required for chemistry, spectroscopy or magnetism computations. On the other hand, these electrons still interact with the 4f and higher configurations. Keeping them in the calculations means time and computational power expenses. Alternatively, the effective core potentials (ECP) [70] can be used to substitute the core electrons (shells 1-3) with a potential, simulating their presence.

2.5. Lanthanide-based inorganic photoluminescence materials

The most common way to produce a lanthanide-based inorganic photoluminescence material is via the matrix-dopant principle. The matrix is usually a transparent inorganic insulator.

Transparency is required so that the excitation light would reach the sensitizer ions and so that the emission of the material would not be reabsorbed by the matrix. Large bandgap of the matrix compound prevents quenching and trapping processes, which are usually undesirable.

Both crystalline or amorphous (glass) materials can be used. The matrix material affects the overall luminescence intensity of Ln^{3+} ions introduced into it (they are commonly referred to as dopant), the spectral pattern and the photoefficiency. The 4f-4f transitions of Ln^{3+} are forbidden unless a non-centrosymmetric crystal field is provided. Thus, the matrix material must offer an appropriate crystallographic site lacking the inversion symmetry. The relaxation of selection rules forbidding the transitions depends on the crystal field, thus the intensities are affected. The crystal field conditions in some materials (*e.g.* LaF_3) result in high intensity of 4f-4f absorption and emission [71]. Consequently, no other sensitization is required. In the crystalline matrix material, the Ln^{3+} sites are mostly the same all over the material and rather not change in most conditions, resulting in a stable spectral pattern. The pattern can be characteristic of a particular matrix-dopant pair in some cases. The matrix material also defines the quenching processes and thus the efficiency. Typically, the matrix materials are composed of metal cations and inorganic anions. A common practice is to use a matrix based on non-luminescent rare earth ions such as Y, La or, less commonly, Lu. Alternatively, Gd- or Ce-based compound can be used. The most studied classes of matrix compounds (according to the anions) include oxides, borates, fluorides, vanadates, phosphates, aluminates (garnets) tungstates and other.

2.5.1. Bulk solid and nanocrystalline materials

Solid photoluminescence materials can be obtained in the form of both monocrystals and powders. Different forms can have different applications. For instance, monocrystals are used in lasers and scintillators, while the powder materials are used in light sources and for bioapplications. Over the last decade, the study area of nanomaterials based on lanthanides has developed significantly [72]. Most of the methods for nanoparticle synthesis are controlled syntheses. That is, the particle size, morphology and crystal phase can be controlled precisely. The main advantage of nanophosphors is increased number of potential applications. Nanoparticles can form stable colloids and maintain their photoluminescence properties in water and other solvents. Nanomaterials can be added to fibers maintaining their photoluminescence [73]. Nanoparticles can be introduced into biological tissues for the purposes of photodynamic therapy, bioimaging, biolabeling [74–77] or as MRI contrast agents [78–80]. However, the toxicity of nanoparticles requires further studies. Finally, the nanosize can have a direct effect on photoluminescence lifetimes and spectra [81–83].

2.5.2. Recent advances in rare earth borate luminophores

Rare earth borates are relatively new and promising class of inorganic photoluminescence materials [84]. These compounds are characterized by high chemical and photolytic stability [85] as well as high bulk modulus [86]. As rare earth borates are transparent in the UV and visible range [87], they can be used to make phosphor materials for applications in both Hg- and non-Hg luminescence lamps and plasma display panels [88]. Other potential applications of borate phosphors include LEDs, neutron detectors, non-linear optics (NLO) and lasers [89–93]. Yttrium borate and yttrium-gadolinium borate of the general formulas YBO_3 and $(Y_xGd_{1-x})BO_3$ doped with Ln^{3+} [94–96] are the most commonly studied borate materials. It has been reported that the morphology of $GdBO_3:Eu^{3+}$ can affect its photoluminescence spectrum [97]. The phenomenon of quantum cutting in $GdBO_3:Ce^{3+},Yb^{3+}$ system has been reported [98]. There is information about the possibility of application of RE borates as laser-stealth coatings [99]. RE borates, co-doped with $Ce^{3+}/Mn^{2}+$ or Eu^{2+}/Mn^{2+} are rather typical phosphor materials for white-emitting light electric diodes [100,101]. The most common borate matrices are $REBO_3$ (where RE = Y, Gd, La, also Y_xGd_{1-x}) [85,102–108] and garnet-like borates $REAl_3(BO_3)_4$ (RE=Y, Gd) [109–114]. Borate phosphors are mainly doped with Eu^{3+} and Tb^{3+}, while the former is sometimes used as a structural probe [115,116]. Lanthanide-doped borate materials are relatively simple to obtain and can be synthesized with a variety of methods. For nanoscaled borates, hydrothermal route is often used [85,117–119], but also sol-gel [120–123] and microemulsion [95,124,125] methods look quite promising. Mixed borates such as $M_3RE_2(BO_3)_4$ (M=Ca, Sr, Ba, RE=Y, La, Gd) have been mostly studied in the form of monocrystals [126–134] and micro-scaled luminophores [135], but not as nanophosphors.

2.5.3. Rare earth fluoride luminophores

Another important class of Ln^{3+}-based phosphors are doped rare earth fluorides REF_3 [136–138]. These materials are characterized by low phonon energy [71] which results in high efficiency of such phosphors. Both downconversion and upconversion Ln^{3+}-doped REF_3 systems can be prepared. The materials can be obtained in the form of crystalline nanoparticles using various methods without any post-calcination required [139]. Consequently, Ce^{3+} (which tends to oxidize to Ce^{4+} upon calcination) can be used as a co-activator or CeF_3 can serve as matrix compound.

2.5.4. Rare earth vanadate luminophores

Rare earth vanadates can also be used as host compounds for Ln^{3+} dopant ions [140]. YVO_4 is a commonly studied laser host material [15,141,142]. Vanadate-based Ln^{3+}-doped materials can be obtained as (nano)powders for various application [143–147]. Hybrid antiferromagnetic photoluminescence materials can be prepared by doping of $GdVO_4$ with

Eu^{3+} ion [140]. The most prominent feature of $REVO_4:Ln^{3+}$ phosphors is the excitation band of $(VO_4)^{3-}$ group located at 250-350 nm [148–150]. After the excitation, the energy can be efficiently transferred to the Ln^{3+} dopant. The phonon energy of the rare earth vanadate compounds is a bit higher than that of REF_3 [151].

2.6.1. Most common routes of lanthanide phosphors synthesis

In general, the synthesis of lanthanide-based luminophores consists of two steps. In the first, raw powder material is obtained, and in the second, the powder is annealed at high temperatures (400-1300 °C) for several hours. The calcination is required in order to improve crystallinity and phase purity. The purity and crystal quality are important for luminescent materials because defects and additional phases can cause emission quenching and crystal lattice distortions. The disadvantage is that the pre-obtained nanoparticles tend to agglomerate during the second stage, which results in a wide size distribution, improper shape of the particles and increased particle size.

2.6.1.1. Solid-state synthesis

Solid-state process is the simplest way to obtain luminophores using rare earth oxides and alkali and alkaline earth metal carbonates [152–157] or nitrates [158] as the reagents. RE components are usually used in the form of oxides while alkali and alkali earth components are used in the forms of carbonates. The method does not require any complicated facilities, extreme conditions or additional compounds like pH controllers or chelating agents. Material preparation is simple and easily reproducible, so the solid state process is widely used. In a typical process, raw materials are mixed in stoichiometric amounts, and ground. In the synthesis of borate phosphors, solid boric acid is added with a small excess to compensate for evaporation [158]. The mixture is calcined at 1000-1300 °C [159–162] for several hours. Sometimes, the reaction mixture is pre-heated at lower temperatures (400-600 °C) [161,162] and reground before the final calcination. If Ce^{3+} or Pr^{3+} are used as dopants, a neutral (N_2, Ar) or reductive (CO) atmosphere is used in order to control the oxidation state of the dopant ions. The obtained material is bulk (macro- or microcrystalline) and has to be ground down to a desired dispersity [163]. Thus obtained powder is inherently polydispersed with the average size varied from millimeter to several micrometers and rarely reaching hundreds of nanometers. Usually, the obtained particles have irregular shapes.

2.6.1.2. Hydrothermal synthesis

In the process of hydrothermal synthesis, the solution of raw compounds in water is kept under increased temperature (~150-300 °C) and pressure (20 bar and higher) for some time ranging from 3 [164] to 72 hours [165] and more. The synthesis is performed in an autoclave filled up to 70-100% of its volume. Heating of the autoclave causes a dramatic pressure increase. Raw compounds can be solved (salts, acids, bases) or suspended (oxides) in water. There are reports that metal acetates [85] are better precursors for borate phosphors obtained by the hydrothermal route. The pH value of the raw solution is usually adjusted [165,166]. Chelators [167] can be also used for additional control of the goal material properties. The hydrothermal route can be followed for both target material synthesis and micro-precipitated rare earth hydroxide precursor preparation [168,169]. Sometimes, the hydrothermally-obtained materials are subsequently subjected to calcination [170]. Calcination temperature may affect the photoluminescence of the product [171]. At this stage microcrystalline material can melt [172] which may change its crystallographic and luminescent properties to be similar to those of the materials obtained by the solid state process.

Generally, the hydrothermal method allows controlling the size, phase and morphology of the products through the use of appropriate precursor composition and modifications of the reaction parameters, such as time and temperature. It should be mentioned that highly pure and homogeneous materials can be obtained without any subsequent calcination [169].

Morphology of HT-obtained materials depends on the temperature and time of synthesis, the solution pH and the presence of additional components (chelators etc.) In most cases, hydrothermal synthesis results in round microplates of 1-10 μm in diameter and several ten nanometers in thickness. These microplates tend to agglomerate forming spherical associates or cylindrical packs of co-axially agglomerated microplates. Those microplates of μm size are composed of nanocrystals (~50-100nm) of irregular shape which can be observed by means of electron microscopy [118,169]. Particle morphology does not depend directly on the metal ion. Different rare earth compounds are composed of similar microplates and their agglomerates, if obtained under the same conditions [118,169].

There is a variation of the hydrothermal route called the solvothermal route [173]. The latter uses solvents other than water and is very similar to the hydrothermal route in its principles.

2.6.1.3. Sol-gel route

Unlike the solid state and the hydrothermal routes, there are lots of quite different methods with different precursors and conditions under the common name "sol-gel route" [174]. Generally, a sol-gel synthesis is performed in the following way. At first, the initial sol (true solution) of raw compounds is obtained. The sol contains the solvent, rare earth ion sources, anions and linking agents. Linking agents (usually polycondensable molecules or their oligomers) are used to form a polymer network (gel) [175,176]. Additional components such as chelating agents, stabilizers and emulsifiers may be applied [122]. Chelating agent forms complexes with metal ions in solution to prevent precipitation [177]. In some cases, chelator may take part in gel formation [177]. The initial sol is placed into conditions favorable for gel formation and then the obtained gel is dried, forming a xerogel [178]. Alternatively, electrospinning technique can be applied to the precursor gel [179,180]. After the fibered precursor calcination, a nanofiber product is obtained. The xerogel is calcined after drying. Microwave heating can also be used [181]. During the calcination step, the organic part is removed (so the method is sometimes called "sol-gel combustion" [182]). The xerogel prevents agglomeration of the formed inorganic particles resulting in the formation nanoparticles as small as tens of nanometers.

2.6.1.4. Combustion route

The combustion synthesis is a wet process involving nitrate salt precursors and fuel components in the raw solution. Usually, fuels are flammable organic compounds like amino-acids, organic acids, urea, hydrazides etc. [92,112,183,184]. On the one hand, the metal nitrate (RE source) is a satisfactory oxidizer. On the other hand, additional oxidizer can be used [107] as well. Nanoparticles are obtained during combustion of raw solution, usually initiated by calcination. The characteristic feature of the method is fast removal of organic components together with solvent. The method gives a product in the form of very small crystalline particles.

2.6.1.5. Co-precipitation route

To obtain nanoparticles via the co-precipitation route, a mixture of raw materials is treated with alkali solution until the pH of the mixture is alkaline (about 7-9) [104,185,186]. Aqueous ammonia is commonly used as it can be easily made volatile by heating and thus removed. The pH value increase causes precipitation of partially amorphous rare earth compound and subsequent calcination results in a crystalline product. Alternatively, applying the appropriate conditions, it is possible to obtain crystalline product directly by co-precipitation [139]. This kind of synthesis is sensitive to pH of the solution. Highly-alkaline conditions as well as rapid increase in pH might trigger the unwanted reactions of rare earth hydroxide formation. The latter would not necessarily react with the anion required for formation of the goal compound. The method is capable of production of nanoparticles as small as several nanometers [80]. The size is strongly dependent on the use of surfactant which provides a wide range of synthesis control options.

2.6.1.6. Microemulsion route

Microemulsion method is an extension of the co-precipitation method [187]. Typically, two water-in-oil emulsions are prepared – one containing metal ions and the anion solution in water phase and the other containing an alkali element [95]. Mixing these two solutions results in a co-precipitation reaction inside the microdroplets of water phase. Emulsion micelles confine particle growth so the obtained particles are spherical. The size is controlled by the size of droplets, depending on surfactant type and portion as well as stirring speed [124].

3. Research techniques

3.1. Powder X-ray diffraction

After the experimental samples were synthesized, the first step was to check their composition and structure, which was made by means of the powder X-ray diffraction, abbreviated as XRD [188]. The technique is nondestructive, that is the analyzed samples can be recovered after the XRD pattern is recorded. The method is based on diffraction of waves. Crystal lattice is a periodic structure and thus may cause a diffraction of wave of appropriate length. In particular, by the Bragg's law, positive interference condition is:

$$2d \sin \Theta = \lambda \tag{3.1.1}$$

where d is a distance between the atomic planes, Θ is the incidence angle and λ is a wavelength.

The interatomic distances are of the order of magnitude of several angstroms. Thus, the radiation of a wavelength of that order is required to obtain a diffraction pattern. The Cu K_{α_1} X-ray radiation is commonly used. K_α is a kind of electromagnetic emission produced by the electron transition from 2p level to the ground shell, while K_{α_1} is the emission accompanying the transition from a $^2p_{3/2}$ state to the 1s ground state. In copper (Cu), the transition energy is 8047.82 eV, which corresponds to wavelength of about 1.541 Å [189]. This wavelength is of the order of magnitude of atomic radii of all of the atoms. It is also comparable to the distances between the atomic planes in crystals. Consequently, irradiation of a crystalline material by this kind of radiation causes diffraction of the incident waves on the atomic planes. If a monocrystal is irradiated, the diffraction pattern is three-dimensional. In a powder sample in which (ideally) all of the possible crystal orientations are present, a diffraction pattern can be represented as a plot of intensity as a function of incident angle: $I = f(\Theta)$. The pattern is characteristic of the material analyzed and can be used for identification by the fingerprint principle. First of all, however, it is used for calculation of the crystal structure of a given material.

In the kind of analysis used in this work, a diffractometer of Bragg-Brentano $\Theta - 2\Theta$ configuration was used. In this kind of setup, the powder sample is located on a round rotating holder. The holder is put on the axis of the diffractometer and is tilted (the tilt angle is Θ). The holder rotates in the plane perpendicular to the tilt plane. Meanwhile, either the X-ray source or the detector are rotated on an arm (in a plane of the tilt) by the angle of 2Θ. The diffraction pattern is recorded as $I = f(2\Theta)$. In particular, a Brucker D8 Advance Diffractometer with a Johansson monochromator and a LynxEye linear X-ray was used. The patterns were recorded with Cu K_{α_1} radiation.

3.2. XRD pattern analysis

A simple pattern analysis can be performed by the Scherrer equation [190]. The equation provides data on the average size of particles in the powder sample, on the basis of FWHM of a diffraction peak:

$$d = \frac{K\lambda}{\beta \cos \Theta} \tag{3.2.1}$$

where *d* is average nanopartcile size, *K* is a shape factror, λ is a wavelength, β is a FWHM of a corresponding diffraction peak and Θ is a Bragg angle. In this work, the shape factor of 0.9 [191] was used.

Another interesting and important technique based on XRD is Rietveld refinement [192] and its extensions [193–195]. Numerous factors affect the XRD pattern of a particular material, including: present crystal phases, crystallite size and distribution, particle orientation, strain and defects, crystal lattice distortions as well as instrumental effects (*e.g.* lack of monochromaticity of the incident X-ray radiation, peak broadening). These factors influence the shape of peaks, their widths and positions. Rietveld refinement uses various techniques in order to simulate these properties of a powder sample and represent them in a series of numerical parameters. The parameters are then varied in order to minimize the mismatches between the theoretical diffraction pattern, produced with the parameters, to the experimental one. In practice, all these procedures are carried out automatically by the appropriate software [193]. The experimenter is free to select, which properties should be included in the model, and which should not, as well to define the sets of varying and restricted parameters. For instance, it does not make sense to use automatic Cu K_{α_2} removal, if a monochromatic Cu K_{α_1} radiation was applied. The method is also very useful to detect additional phases. The theoretical diffraction pattern may be composed of as many single-phase patterns as necessary, and the mentioned structural effects can be applied to any of them individually. As the percentage of the particular phase is also a fitting parameter, the refinement would show - in a quantitative way – which theoretical pattern (i.e. single-phased or multi-phased) is a better match to the experimental one. For multi-phased patterns, the best-fitting contribution of each of them is provided as a result. In the present study, MAUD software [193] was used in order to perform the refinement.

3.3. Transmission electron microscopy

The detection limit of a classical optical microscope is the wavelength of light. Objects comparable to the wavelength (hundreds of nanometers) cannot be observed. Thus, a kind of radiation with a much shorter wavelength is required. In electron microscopy, the wave-particle dualism of electrons is exploited [188]. A relativistic electron moving through the space with appropriate energy would behave like a ray of light. As the moving electron is charged, it can be tilted by the electromagnetic field. Considering these facts, the electron microscope is similar to a regular microscope as it has a tube, a radiation source and a set of electromagnetic lenses to focus it. The beam is transmitted through the analyzed sample, which gives the technique its name. The electrons are focused to project the image onto a detector plane. Historically, the detector was a photographic film. Now, CCD cameras are used. The tube must be empty (that is, must contain vacuum). High voltage (hundreds of kV) is applied to accelerate the electrons. The images in this work were obtained using a JEM 1200 EXII device

3.4. Fourier-transform infrared spectroscopy

Every compound at temperature above 0 K is characterized by the vibrational motion of its atoms around their equilibrium position. The thermal energy of a compound is stored in the form of its atomic vibrations. The vibrations are characterized by particular frequencies that depend on the atomic mass, molecular geometry of the compound and its electronic structure. Vibration modes are characterized by the respective energies. As the electron density of the atoms and molecules is altered during the vibrations, electromagnetic waves can couple with this kind of oscillations. Consequently, a photon can be absorbed or emitted on the transitions between the energy levels, if the electric dipole is altered during the transition. The corresponding wavelength are in the range infrared light, that is 700 nm and higher.

Every compound is characterized by a particular spectrum of vibrations. They include various lengths and angles changes in molecules. In solid state, it is rather spoken about oscillations of atoms around the equilibrium. The oscillations of this type can result in collective effects known as phonons. Phonons are virtual particles that can be interpreted as quanta of sound waves in a crystal. Both molecular vibrations and phonons can be detected by means of absorption spectroscopy in the infrared range of wavelengths.

The IR spectrum can be matched as a whole (to some reference spectrum) in order to identify the compound by the fingerprint principle. Alternatively, particular vibrations can be identified by their characteristic wavelengths. Thus, the presence of a certain group can be deduced by the occurrence of a corresponding peak in the spectrum. In this thesis, this method was used in order to check the phase purity of the obtained samples. As the crystal structure of the target compound is known, the list of atomic groups in the structure is known as well. The corresponding IR peak positions can be found in literature. Then, it is possible to find out, if the groups of the target compound are present and if other groups (from impurity phases) are present.

Fourier-transformed IR spectroscopy is a kind of spectrum measurement technique. A conventional spectroscopy uses a monochromatic incident beam of gradually changing wavelength. The intensity of transmitted light in respect to the incident intensity is recorded as a function of wavelength. Such a setup requires a monochromator of the excitation beam. In the FTIR setup, the excitation light is polychromatic. Excitation beam is split at a beam splitter (half-transparent mirror) into two perpendicular beams. Both are reflected by mirrors back to the beam splitter. The mirror in line with the excitation source can be moved so that the distance between it and the beam splitter can be changed. As the mirror moves, interference pattern (which depends on the path of light reflected by the moving mirror) at the beam splitter is changed. The sample is radiated by the beam reflected through the beam splitter by the non-moving mirror. The raw spectrum is recorded as intensity of light transmitted through the sample as a function of the moving mirror position. The Fourier transform of the raw spectrum results in a regular IR absorption-as-a-function-of-wavenumber spectrum.

3.5. UV-Vis luminescence spectroscopy

Luminescence spectroscopy is used to study the energy conversion processes in the compound studied. The most basic luminescence spectroscopy techniques include measurements of excitation and emission spectra of the studied compound as well as photoluminescence lifetimes measurements. In a typical setup, monochromatic excitation light is used. The resulting emission light can be analyzed either with a monochromator plus a photomultiplier setup or using a multi-wavelength CCD detector. The sample can be in the form of solution or solid state. In the former case (provided that the scattering can be neglected), the excitation beam goes through the cuvette while the emission is collected in a direction perpendicular to the excitation. If the sample is solid, its surface is irradiated with the excitation beam and the scattered emission is collected. It is important to avoid direct reflections of the excitation beam into the emission collection setup. Additionally, filters on both excitation and emission beams can be used to avoid second (and higher) harmonic bands. For instance, in the presented studies, a filter blocking the radiation below 395 nm was used to cover the emission collector. As the typical excitation range was 200-400 nm, while the emission range was 400-700 nm, it was probable to obtain a second harmonics line in the emission spectrum without such a filter (*e.g.* $\lambda_{ex.} = 250$ nm, thus $\lambda_{2nd.h.} = 500$ nm).

Two kinds of spectra in this spectroscopic method can be recorded, namely, excitation and emission spectra. During the excitation spectrum measurement, the wavelength of the excitation light is altered gradually while the emission is collected at one particular wavelength. The spectrum obtained is the dependence of emission intensity (at a particular wavelength) as a function of excitation wavelength. The emission spectrum is recorded using fixed excitation wavelength, while the collected emission wavelength is changed gradually. Consequently, the emission spectrum (under particular excitation wavelength) is a dependence of emission intensity on the emission wavelength. Actually, a two-dimensional scan can be performed, producing a three-dimensional (surface) spectrum, where emission intensity is a function of both emission and excitation wavelengths.

After the spectra are recorded, the peak positions, widths and intensities are analyzed. These data can be used to deduce the phase purity of the compound, its consistence with the XRD and database structure, the amount of photoemission sites, the wavelengths that can be used to excite potential phosphor, the emission color etc. Shortly speaking, the spectra of this kind are the main source of information on photoluminescence properties of the materials studied.

A subsection of the luminescence spectroscopy is photoluminescence lifetime measurements. In this kind of experiment, the material is excited by a very short pulse of radiation (the shorter the better). Right after the pulse, the evolution of emission intensity in time is recorded. In the simplest experiment, the emission is observed at a single wavelength. Alternatively, the evolution of the whole emission spectrum in time after the pulse can be recorded using the appropriate facility. The obtained decay pattern is usually fitted to an exponential decay function, $I_t = I_0 \mathrm{e}^{-t/\tau}$, where I_0 and I_t are the emission intensities are time 0 and t, respectively.

The decay constant τ is referred to as a photoluminescence lifetime. More complicated patterns are possible, including multi-exponential decays and increase-plus-decay patterns. Such patterns can provide important information on the energy transfer and quenching processes. A radiative transition between a pair of levels is usually characterized by a single-exponential decay patter. If the emission originates from an activator ion (*e.g.* Ln^{3+}), the corresponding lifetime would depend on the coordination geometry of the ion. Different geometries would result in different decay dimes. Thus, the amount of exponential decay components can give the information about the number of different coordination geometries (different crystallographic sites) of the activator ions. The lifetimes of the components can provide information about their origin. For instance, in nanoparticles, surface sites are efficiently quenched by the surface water and are characterized by higher decay rates than the sites inside the particle.

In this work, the Hitachi 4500 spectrofluorimeter was used to record the specta. Luminescence decay curves of the prepared samples were measured using a QuantaMasterTM 40 spectrophotometer equipped with Opolette 355LD UVDM tunable YAG:Nd laser as an excitation source and a Hamamatsu R928 photomultiplier as a detector.

3.6. Chromaticity coordinates

The physical color of light can be described by its spectrum. However, in some applications, it is important to know, how the light of a particular spectrum would be perceived by the human eye. CIE color spaces are the tools that provide a mathematical description of color perception for a given spectrum. CIE is the abbreviation of the French name (Commission internationale de l'éclairage) of The International Commission on Illumination, which has introduced the methods.

A particular set of light-sensitive cells (cone cells) in the retina is responsible for color vision. There are three kinds of cone cells sensitive to red, green and blue light respectively. Each of them is characterized by a wavelength of peak sensitivity. According to the sensitivity spectra of each type of cone cells and the data on average cone cell density in the retina of the human, the so-called color matching functions were developed. A particular set of functions is called a standard observer. There are several different standard observes.

In order to characterize a color of light, the set of so-called tristimulus values X, Y and Z are calculated by the Eq. 3.6.1. Next, they can be decomposed into chromaticity coordinates x and y:

$$X, Y, Z = \int_{380}^{780} I(\lambda) \cdot \overline{x}, \overline{y}, \overline{z}(\lambda) d\lambda \tag{3.6.1}$$

$$x = \frac{X}{X + Y + Z} \tag{3.6.2}$$

$$y = \frac{Y}{X + Y + Z} \tag{3.6.3}$$

where $\overline{x}(\lambda), \overline{y}(\lambda), \overline{z}(\lambda)$ are the color matching functions of the standard observer. One of the idea behind the method was to separate the chromaticity and brightness. The color matching functions were developed in such a way that the Y tristimulus value would contain the brightness data. After the coordinates are calculated, the color can be represented as a point on a chromaticity diagram (Fig. 4, left). Fig. 4, right shows the color matching functions.

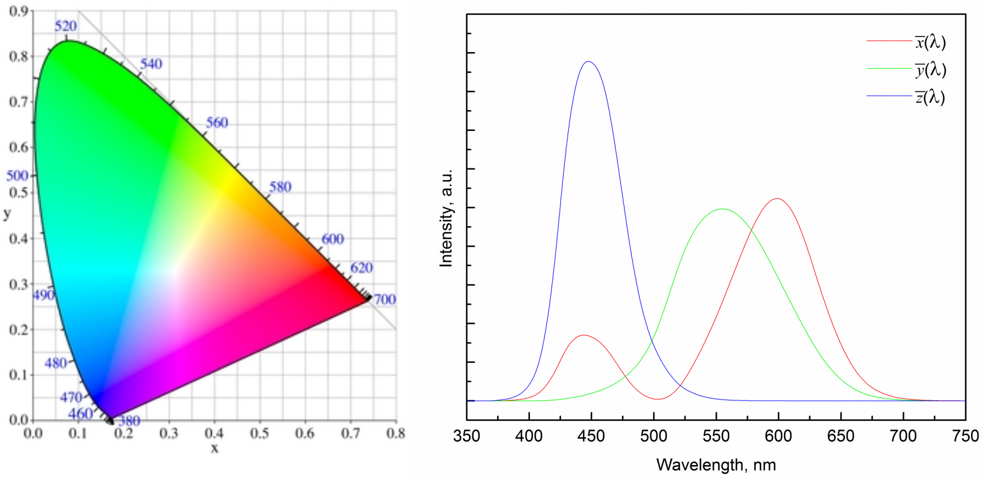

Fig. 4. The CIE 1931 color space (left), the corresponding color matching functions (right)

4. Experimental studies

4.1. Optimization of synthesis procedure of mixed borates

The studied borate materials were obtained via sol-gel technique. According to it, the initial crystallization takes place in the viscous gel phase. A thermally-degradable gel is used to prevent small particles from agglomeration, which takes place upon crystallization and high-temperature calcination at the final stage of the synthesis. Moreover, the reagents used to prepare mixed borates, such as boric acid, metal(II) nitrates and rare earth nitrates can precipitate into compounds other than double borate. For instance, MB_2O_4 and/or $REBO_3$ or other mono-cation borates might be formed. However, the stoichiometry is different in formation of different phases. Consider the following example (the thermal decomposition of HNO_3, which happens upon heating is omitted for simplification):

$$M(NO_3)_2 + 2\ H_3BO_3 = MB_2O_4 + 2\ H_2O + 2\ HNO_3 \tag{4.1.1}$$

$$RE(NO_3)_3 + H_3BO_3 = REBO_3 + 3\ HNO_3 \tag{4.1.2}$$

$$3\ M(NO_3)_2 + 2\ RE(NO_3)_3 + 4\ H_3BO_3 = M_3RE_2(BO_3)_4 + 12\ (HNO_3) \tag{4.1.3}$$

where M is a metal(II) cation.

In order to get mixed borate according to reaction (4.1.3), it is required to have 4 parts of boric acid, 3 parts of metal(II) nitrate and 2 parts of rare earth nitrate at the site of crystallization. Alternatively, if there was the right proportion of metal nitrates, but the wrong amount of boric acid at the crystallization site (for instance, tree parts of metal(II) nitrate, two parts of rare earth nitrate and $3\times2 + 2 = 8$ parts of boric acid), the resulting process would rather go via reactions (4.1.1) and (4.1.2) then reaction (4.1.3). Moreover, if the proportion of metal nitrates was wrong, the formation of the mixed borate would be even less likely. As the solution is a dynamic object, any proportion of the reagents might happen to be in a small volume where the initial crystallization occurs, even though the general stoichiometry in the reactor is correct. Instead, if the reagents are put into gel, which is then dried, the proportions of the reagent will be fixed all over the reaction mixture. Consequently, it would be more likely that the desired phase is obtained. This might explain why it was possible to obtain mixed borate materials via sol-gel route, while the attempts to get it via the traditional wet-chemistry precipitation route failed.

The particular sol-gel method used was a modification of the Pechini method [196]. The procedure was originally developed for deposition of nanocrystalline thin films on a glass substrate surface. In this route, citric acid and ethylene glycol (ethane-1,2-diol) are added to the rest of the reagents. Citric acid acts both as chelating and polymerizing agent. It undergoes polycondensation with ethylene glycol forming a gel. Drying of the gel turns it into a xerogel. Finally, a high-temperature calcination results in xerogel combustion and formation of the product. The method is known to work well to obtain $REBO_3$ nanomaterials [122,179,197]. After a series of modifications and tests, the resulting methodology allowed the formation of mixed borates [198].

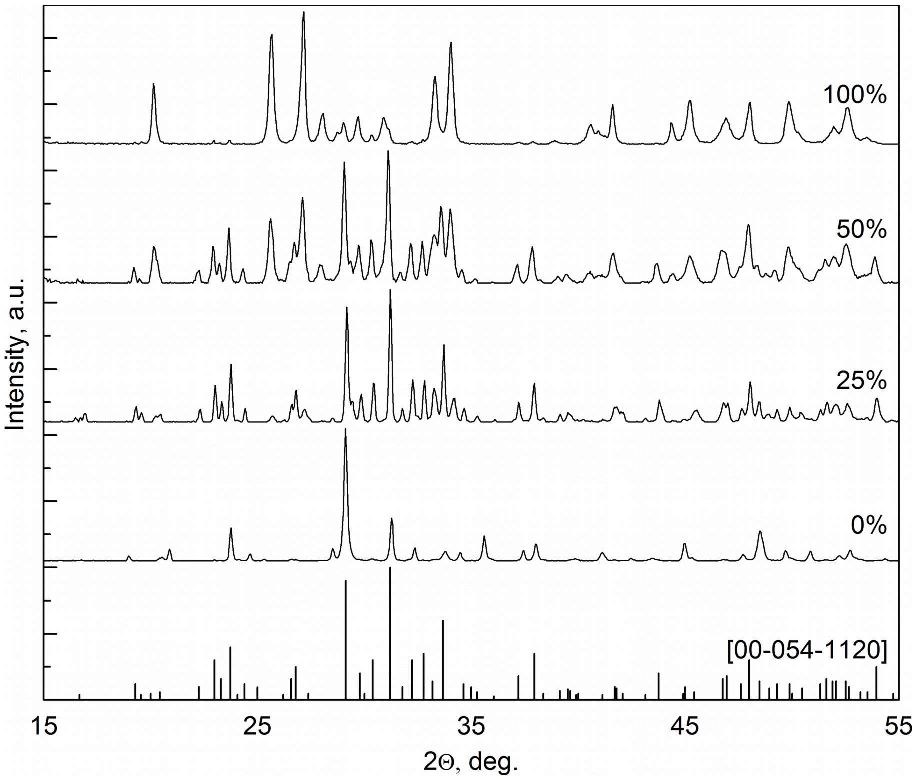

Fig. 5. The effect of boric acid excess (marked in %) on the product of the synthesis (XRD data)

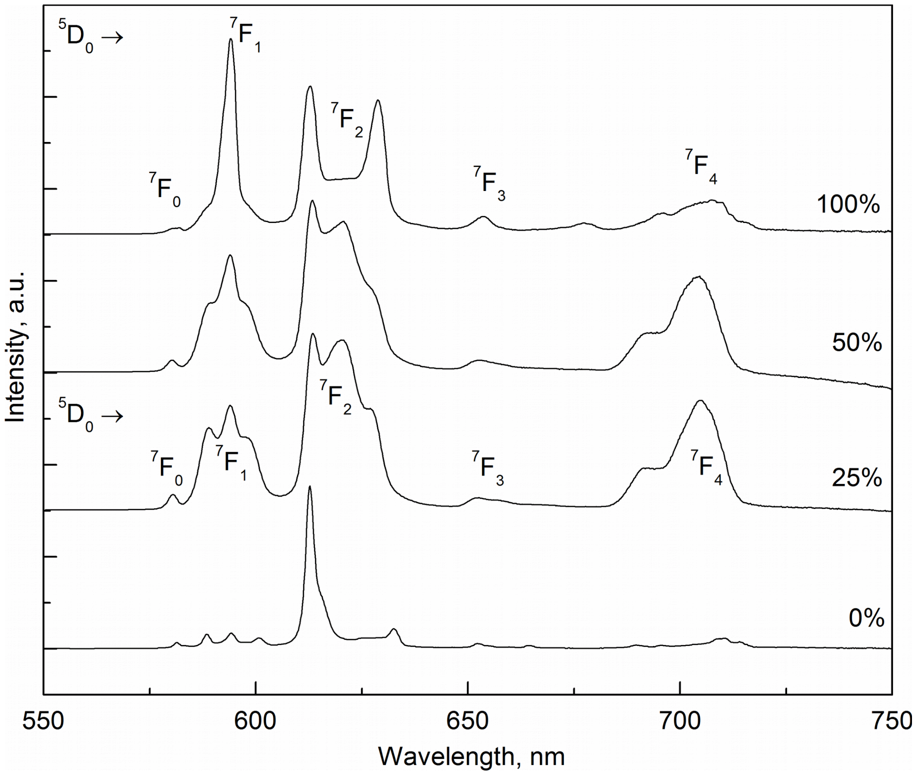

Fig. 6. The effect of boric acid excess (marked in %) on the product of the synthesis (photoemission data)

The proportional amounts of both boric acid and citric acid were optimized per 0.0004 mol of the $Sr_3Y_2(BO_3)_4$ product. Some excess of boric acid over its stoichiometric amount was used [198]. The optimization began with initial guess values of both citric acid amount and boric acid excess. After a trial and effort procedure, the excess rate of 25% and the ratio of 30 mol of citric acid per 1 mol of the product was found to be optimal. The amount of ethylene glycol was kept proportional to the amount of citric acid. The particular volume of 1 ml of ethylene glycol per 12 g of citric acid was originally proposed by Szczeszak *et al.* for the synthesis of $REBO_3$ [197] and was found to work well for mixed borates as well. This value corresponds to 0.314 mol of ethylene glycol per 1 mol of citric acid. In order to prove these values to be correct, a control series of syntheses was performed. The first series was made in order to check the optimal excess of boric acid. The amounts of 0, 25, 50 and 100 mol % were used. The amount of citric acid was kept as 30 mol per 1 mol of the borate [198]. The products were analyzed by means of XRD and the patterns were compared to the database reference pattern (ICDD: 00-54-1120). The results are shown in Fig. 5. The reference patterns of the impurities are not shown.

According to the XRD patterns, the sample with 0% excess of boric acid is mostly composed of cubic yttrium oxide Y_2O_3. The XRD pattern of the sample prepared with the excess of 25% matched the reference pattern. The XRD pattern of the sample prepared with the excess equal to 50% was characterized by an apparent content of impurity phases. A 100% excess of boric acid resulted in a mixture of mainly YBO_3 and SrB_2O_4. This latter case illustrates the model given at the beginning of the section: most of the crystallization has occurred according to reaction (4.1.1) and (4.1.2) instead of reaction (4.1.3). The same conclusions about the presence of the impurity phases can be drawn from the spectroscopic data. In particular, the photoemission spectra of the samples described were measured and analyzed. As the Eu^{3+} ion is highly sensitive to the symmetry of its coordination surround, the shape of the emission spectrum is often used to obtain information about the material's structure.

According to the spectroscopic results, the shape of the emission spectrum corresponding to 100% excess of boric acid looked typical of vaterite-type $YBO_3:Eu^{3+}$ [81]. The excitation wavelength was selected to match the $O^{2-} \rightarrow Eu^{3+}$ charge transfer band (200-250 nm). The sample corresponding to 0% excess was characterized with a cubic $Y_2O_3:Eu^{3+}$ spectrum [199]. The other two spectra were characteristic of the $SYB:Eu^{3+}$. See Fig. 6 for details.

Another series of SYB samples was obtained in order to check the effect of the amount of citric acid on the product. The products were also analyzed by means of XRD. As seen from Fig. 7, a change in the amount of citric acid from 40 mol through 25 mol per 1 mol of SYB resulted in notable changes in the XRD pattern, which indicated changes in the composition and crystallographic phase(s) of the samples (the excess of boric acid was kept as 25 mol per 1 mol [198]). A decrease in the amount of citric acid led to a decrease in the Y_2O_3 phase content and to an increase in $Sr_3Y_2(BO_3)_4$ The amounts of citric acid lower that 25 mol per 1 mol of the target borate resulted in the appearance of impurities [198].

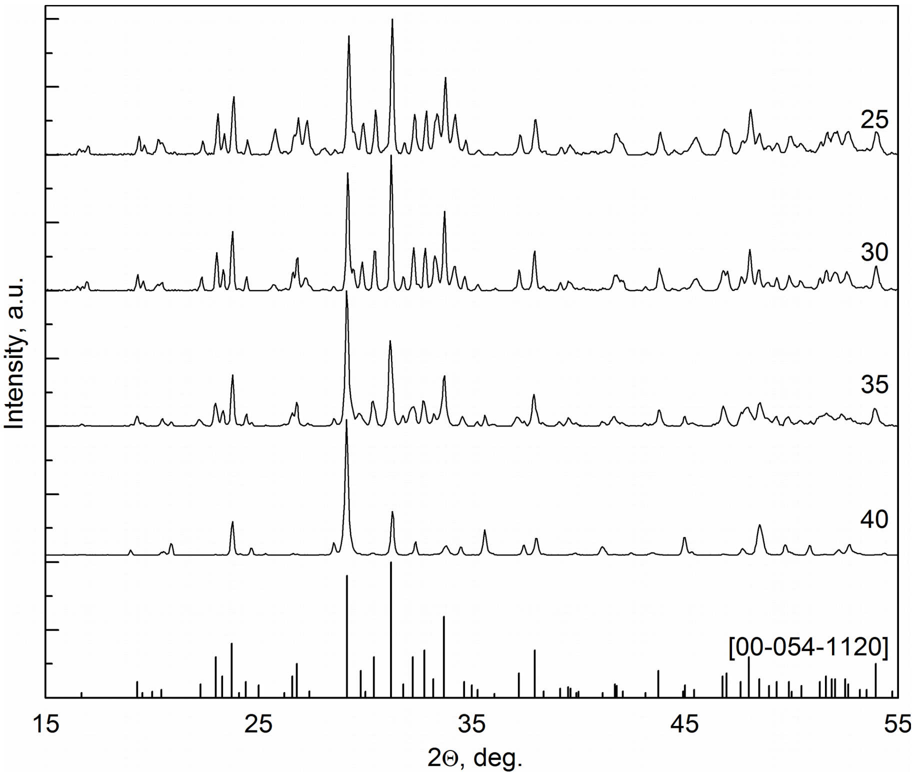

Fig. 7. The effect of citric acid excess (marked on the right side of the graphs, mol per 1 mol of SYB) on the product of the synthesis (XRD data)

Additional confirmation was provided by the emission spectra of the samples, excited into the charge transfer band. The results are shown in Fig. 8, where the upper two spectra are rather typical of Y_2O_3:Eu^{3+}, while the other represent the SYB:Eu^{3+} emission. Thus, the most suitable value was found to be 30 mol of citric acid per 1 mol of the borate. All of the following photoluminescence measurements were performed on samples obtained with optimal amounts of boric (25% excess) and citric (30 mol per 1 mol of the goal borate) acids [198].

After the optimal conditions leading to $Sr_3Y_2(BO_3)_4$ product were found, a typical procedure followed the description provided [198]. The pre-determined volumes (corresponding to 0.0004 mol of the SYB compound) of aqueous solutions of $Sr(NO_3)_2$, $Y(NO_3)_3$, $Ln(NO_3)_3$ (Ln=Eu, Tb) and boric acid as well as ethylene glycol (0.0038 mol) were consecutively added to a weighed amount of solid citric acid (0.012 mol) and mixed in a beaker. The indicated sequence of additions of components was the same for all the samples. The obtained transparent solution (sol) was mixed with 10 ml of distilled water and heated up to 80 °C, which allowed water evaporation and gel formation. The obtained gel was aged in a dryer at 80 °C until a white and almost hard foam was formed. The formed xerogel was slowly heated (at the temperature increase rate of 10 °C/min) up to 900 °C, then kept for 3 h at this temperature and left to cool down in a furnace. The composition of the samples formed was $Sr_3Y_{2-x}Eu_x(BO_3)_4$. The x values ranged from 0.01 to 0.4, corresponding to 0.5 to 20 mol.% of Eu^{3+}.

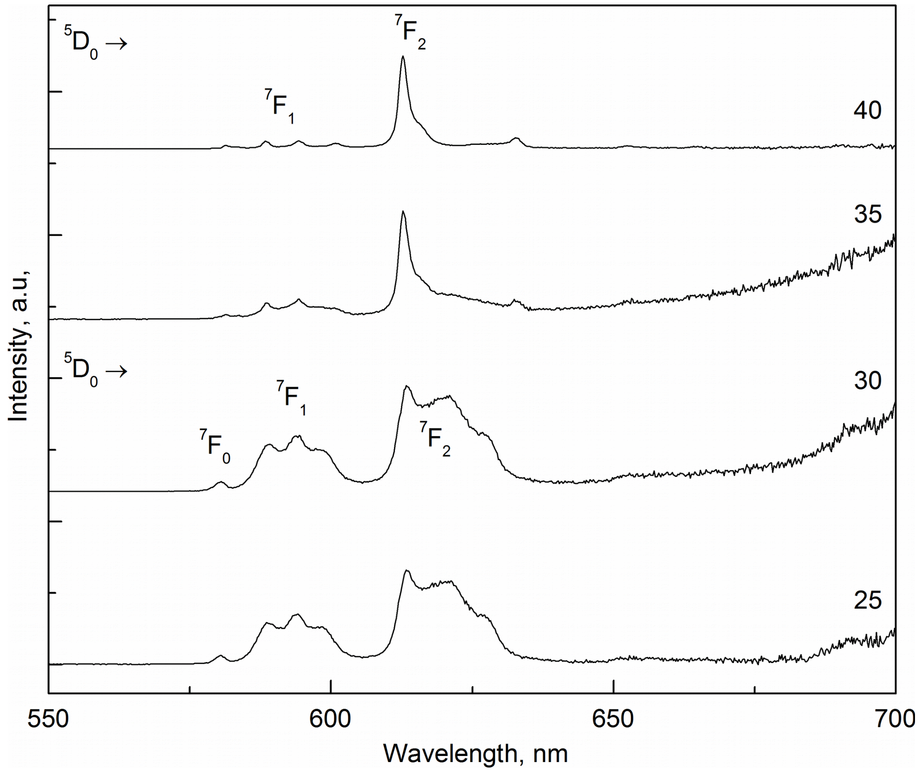

Fig. 8. The effect of citric acid excess (marked on the right side of the graphs, mol per 1 mol of SYB) on the product of the synthesis (photoemission data)

In order to obtain another mixed borate, namely $Sr_3Gd_2(BO_3)_4$, the synthesis procedure was modified. In particular, the 25% excess of boric acid was found to be ineffective for the synthesis of strontium-gadolinium borate. This value was slightly changed and a reoptimization of the excess was performed, the new value of 20% excess was applied. The same synthesis procedure also worked well for $Sr_3La_2(BO_3)_4$, SLB and $Ba_3Gd_2(BO_3)_4$, BGB.

The final synthesis procedure for $M_2M'Gd_2(BO_3)_4$ (M, M' = Ca, Sr, Ba) was the following. The amounts of reagents per 0.0004 mol of the product were: 0.012 mol of citric acid (30:1 ratio), 0.0038 mol of ethylene glycol, 0.00192 mol of boric acid (20% excess). The rest of the compounds were taken in stoichiometric amounts for 0.0004 mol of the target borate. The reagents were added to the mixture one by one in the following sequence: citric acid (Hempur, pure p.a.), $Sr(NO_3)_2$,H_3BO_3, $Y(NO_3)_3$/$La(NO_3)_3$/$Gd(NO_3)_3$, $Tb(NO_3)_3$, ethylene glycol (Hempur, pure p.a.), 10 ml of distilled water.

4.2. Morphology and photoluminescence properties of $Sr_3Y_2(BO_3)_4$:Eu^{3+}

The XRD patterns of the prepared materials were in a good agreement with the reference pattern obtained theoretically on the basis of ICDD database 00-54-1120 structure ($Sr_3Y_2(BO_3)_4$, SYB). The patterns are presented in Fig. 9.

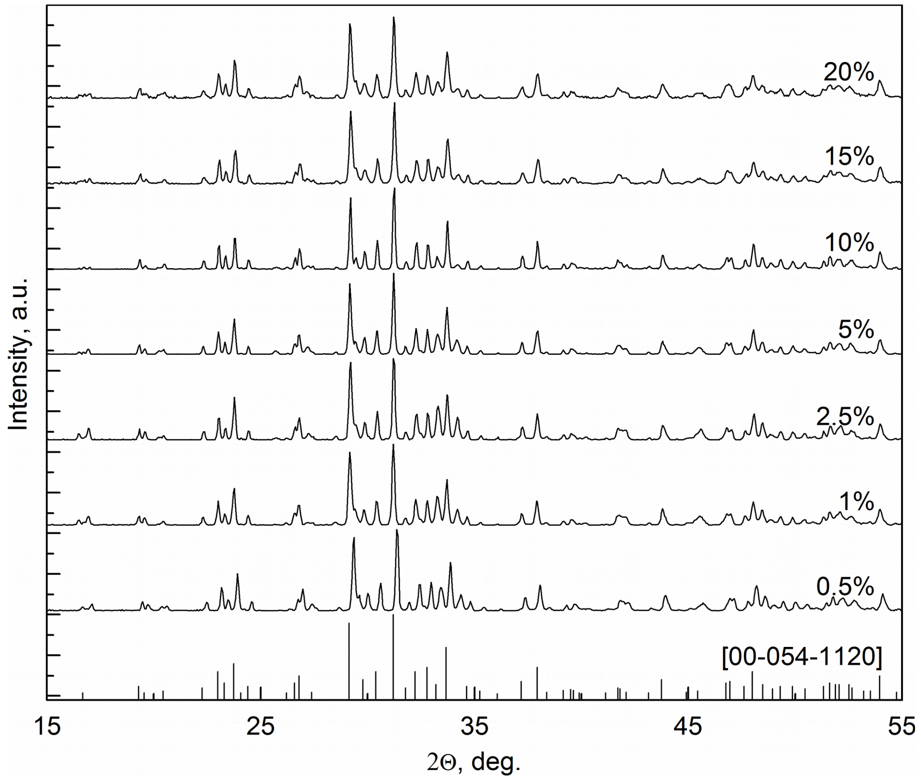

Fig. 9. The XRD patterns of SYB:Eu^{3+} samples

The analysis of XRD patterns confirmed that the composition of the samples obtained was $Sr_3Y_2(BO_3)_4$. The material crystal symmetry belongs to $Pc2_1n$ space group [126]. Two inequivalent crystallographic positions of yttrium ions are present in the structure. Both are eight-coordinated by oxygen ions. Additionally, there are three inequivalent strontium ion positions. In this case, the surrounding is more complex, that is the Sr1 ion is characterized by coordination environment of ten oxygen ions, the Sr2 ion is nine-coordinated, and the Sr3 ion is eight-coordinated [126]. In the following sections it is suggested that Ln^{3+} cations occupy the sites of rare earth ions, substituting them. There are several arguments supporting this idea. The first is that such a substitution is suggested by the stoichiometry: the sum of all rare earth ions, both matrix and dopant (Y^{3+} and Eu^{3+} in this case, respectively), was two molar parts per three molar parts of metal(II), which in this case is Sr^{2+}. The second is that there is no problem of charge compensation in the described substitution: a 3+ ion replaces another 3+ ion. The third is that the ionic radii, in this case, of Y^{3+} and Eu^{3+} are very similar (1.019 Å and 1.066 Å respectively, both 8-coordinated) [2]. Considering the radii of 8- and 9-coordinated Sr^{2+} ion (0.126 nm and 0.131 nm, respectively) and a 9-coordinated Eu^{3+} ion (0.112 nm) [2], it is most probable, the Eu^{3+} would occupy Y^{3+} sites. And finally, the XRD pattern of strontium-yttrium borate doped by Eu^{3+} at as much as 20% ratio still matched the reference pattern, even though some shift of peaks was noted.

The transmission electron microscopy images (Fig. 10) present the morphology of the obtained product. The product consisted of micro-particles rather than nanoparticles. On the other hand, nanosized particles were clearly present in the product. Their approximate size was 10-40 nm. The large particles were most likely a result of nanoparticle agglomeration upon the high-temperature calcination. The agglomerates were of about 100–300 nm in size.

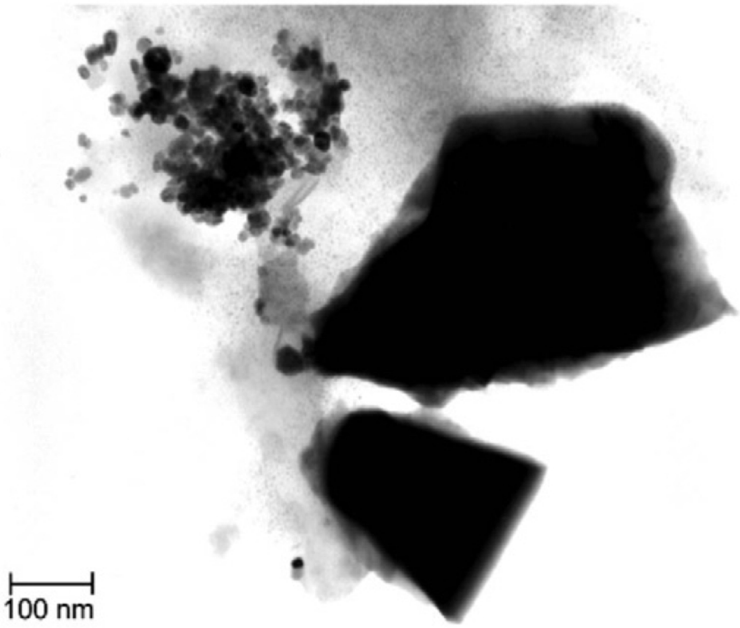

Fig. 10. TEM image of the SYB:5%Eu^{3+} sample [198]

The excitation spectra of the samples obtained are shown in Fig. 11, left. Both wide $O^{2-} \rightarrow Eu^{3+}$ charge transfer band (maximum at 257 nm) and bands of interconfigurational 4f-4f transitions of Eu^{3+} were present in the spectra [198]. The 4f-4f, or simply f-f excitation bands were represented by the transitions from the ground state of Eu^{3+} ions ($^7F_0$) to their excited states, namely $^5H_{5\text{-}7}$ (317–318 nm), $^5D_4$ (361–362 nm), $^5G_{4\text{-}6}$ (375–384 nm) and $^5L_6$ (392–402 nm) [198], with the most intense excitation band of $^7F_0 \rightarrow {}^5L_6$ transition (393 nm). A significant broadening of the peaks was observed. The centroid positions of the peaks depended slightly on the amount of dopant. Both phenomena might be caused by lattice distortions, which, in turn, originate from the addition of Eu^{3+} dopant. The details are given in the following section of this discussion. The increase in the amount of dopant ions also resulted in an increase in the intensities of both CT and f-f bands [198].

The emission spectra (Fig. 11, right) consisted of bands of transitions from the lowest excited manifold of Eu^{3+}, namely $^5D_0$, to its ^7F_J levels: $^5D_0 \rightarrow {}^7F_4$ (687–714 nm), $^5D_0 \rightarrow {}^7F_3$

(648–659 nm), $^5D_0 \rightarrow {}^7F_2$ (608–633 nm), $^5D_0 \rightarrow {}^7F_1$ (583–605 nm), $^5D_0 \rightarrow {}^7F_0$ (580–581 nm). No emission from the manifolds above $^5D_0$ was observed. Similar emission patterns were observed on excitation into CT band or $^7F_0 \rightarrow {}^5L_6$ band, both of much higher energy than the $^5D_0$ level. Apparently, the energy was cascading down in the Eu^{3+} ion, being lost in non-radiative way, until the system reached the $^5D_0$ level. At this point, visible emission occurred. The most intense band in the emission spectra was the one corresponding to the $^5D_0 \rightarrow {}^7F_2$ transition. Relatively high intensity of the $^5D_0 \rightarrow {}^7F_4$ band is rather unusual for borate phosphors. The resulting emission color was red.

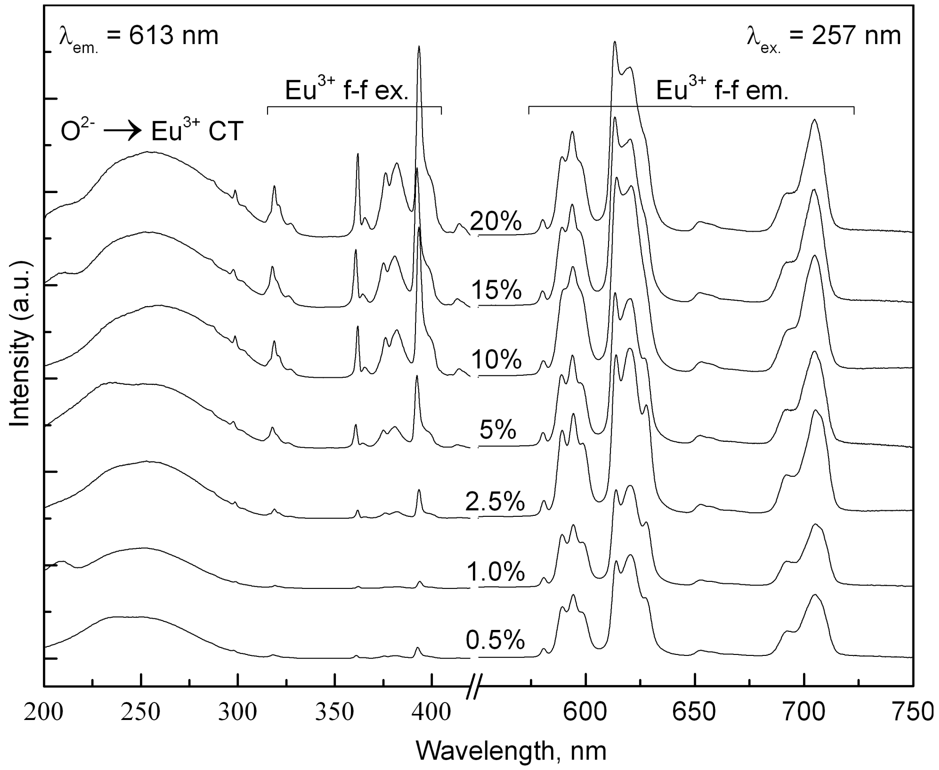

Fig. 11. The excitation and emission spectra of the SYB:Eu^{3+} samples

Photoluminescence spectra of lanthanide ions usually consist of narrow peaks similar to atomic spectral lines [4]. In Fig. 11, an apparent broadening of both excitation and emission spectra of $Sr_3Y_2(BO_3)_4:Eu^{3+}$ is present. The band broadening can be explained by a disorder in the material's crystal structure [200]. In a disordered crystalline structure the local symmetries of crystallographic sites, interatomic distances and angles as well as the electronic structure of the emission centers are quite similar all over the structure but not exactly the same. This results in some rather randomly-distributed changes in band wavelengths and intensities. Consequently, the cumulative peaks are broadened. One might try to estimate this effect quantitatively. The Eu^{3+} $^5D_0 \rightarrow {}^7F_0$ emission band has a one-site-one-peak property [4]. This transition occurs without angular momentum change (ΔJ is equal to zero) and thus does not undergo any crystal field splitting. On the other hand, it is sensitive to coordination geometry, as any other Ln^{3+} transition. As a result, the number of $^5D_0$-$^7F_0$ peaks in the emission spectrum is equal to the number of unequal coordination geometries in the studied system [4]. The emission spectra in Fig. 11 contain only one $^5D_0$-$^7F_0$ peak each. The full width at half maximum, FWHM of the $^5D_0$-$^7F_0$ bands is more than 2 nm, while the emission peak positions of the Eu^{3+} ions at two different sites should differ by about 0.4 nm [81]. This shows clearly, that the broadening of the peaks in the SYB:Eu^{3+} samples obtained was significant. Consequently, it is rather impossible to find out the true number of emission-active Eu^{3+} sites in the studied samples. One cannot say if there was only one disordered emitting site of Eu^{3+} in the structure, or if there were several slightly different sites. The photoluminescence properties seem to imply the presence of only one site of such a kind. One can speak about an "average site" in this case. Additionally, the photoluminescence decay data can be fitted with a single-exponential function (Fig. 12). Such a decay dynamics is typical when only one kind of emission site is present in the material. Similarly, one might speak about "average site symmetry" [198].

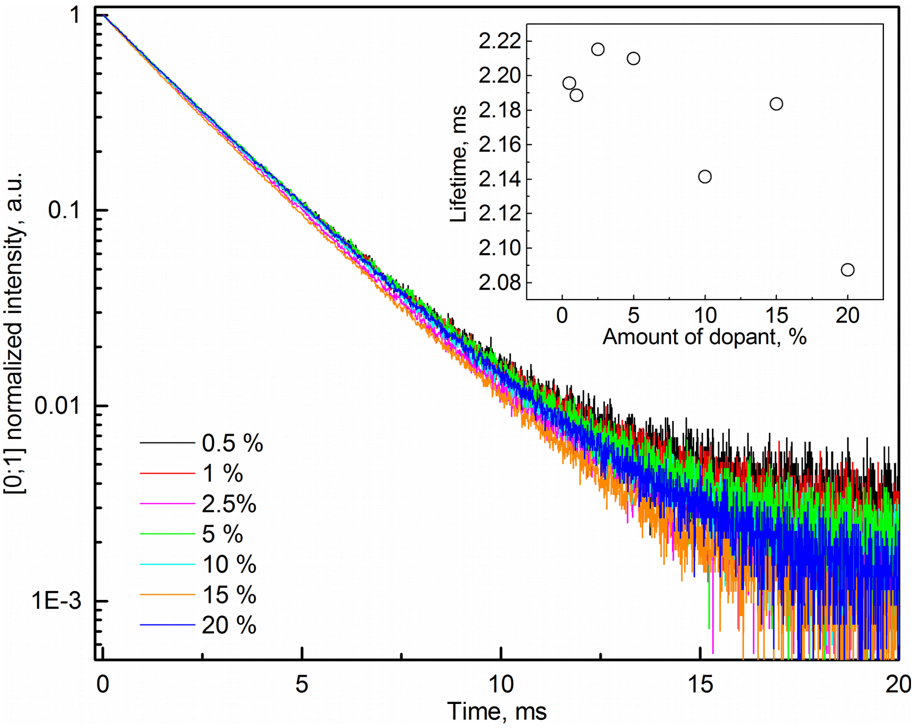

Fig. 12. The photoluminescence decay curves of SYB:Eu^{3+} samples

The local site symmetry of Eu^{3+} ion was analyzed on the basis of the number of particular peaks in the excitation [201] and emission [116] spectra [198]. Using the approach proposed by Binnemans and Görller-Walrand [201] one can deduce the site symmetry of Eu^{3+} to be D_2 from the number of peaks in $^7F_0 \rightarrow {}^5D_1$ and $^7F_0 \rightarrow {}^5D_2$ transition manifolds. On the other hand, the local symmetry of Y^{3+} sites is C_1 [126], and it should be the same for Eu^{3+} at these sites. The approach by Jia et al. [116] provides the possible site symmetry of the C group.

Comparing the experimental emission spectra to those described by Ruan et al. [202], one can conclude that the local site symmetry of Eu^{3+} ion is C_1 or C_2 group [198].

Judd-Ofelt theory in its simplified form [20] is a useful tool if one needs a compact and general quantitative description of Ln^{3+} photoluminescence properties. In particular, the asymmetry of the coordination geometry, covalency and polarizability of the environment as well as density of electrons on the dopant ions can be described by means of three Ω_λ parameters. They are called the Judd-Ofelt parameters or the intensity parameters. For Eu^{3+}, one does not need a full fitting procedure typical of the other lanthanides. Thanks to the nature of $^5D_0$-$^7F_1$ transition, its intensity can be used as a reference. Thus, the intensity parameters can be derived as a function of the integrated intensity of $^5D_0$-$^7F_{2,4,6}$ emission peaks. This approach was proposed by Kodaira and coworkers [203] and was used in the presented study. The results are presented in Table 1. Clearly, both parameters Ω_2 and Ω_4 increased with increasing amount of the dopant. Increase in average polarizability of coordination medium and decrease in the average symmetry with increasing amount of the dopant can be deduced from this trend [198]. This conclusion agrees with an increase in the matrix distortion caused by introduction of relatively larger Eu^{3+} ions into the Y^{3+} sites [198]. The latter substitution would also lead to a decrease in the average distance between the baricenters of the dopant Eu^{3+} and O^{2-} of coordination surrounding, which results in an increased covalency of Eu-O bonds. On the other hand, introduction of Eu^{3+} ions into more roomy Sr^{2+} sites should result in an increase in the average distance and a decrease in the covalency of Eu-O bonds [198]. The increase in Ω_4 parameter might be related to a decrease in the electron density on the coordination oxygen ions, which agrees with the increase in the covalency of Eu-O bonds [198].

Table 1. The photoluminescence lifetimes of the SYB:Eu^{3+} samples and the calculated Judd-Ofelt intensity parameters and quantum yields

Amount of dopant, %	Lifetime, ms	Ω_4, $\times 10^{-20}$ cm^2	Ω_2, $\times 10^{-20}$ cm^2	Quantum yield, %
0.5	2.20	16.8	11.8	54.7
1	2.19	16.8	11.9	54.8
2.5	2.22	17.6	12.1	56.8
5	2.21	17.8	12.5	58.1
10	2.14	18.0	12.9	56.9
15	2.18	18.8	13.1	59.4
20	2.09	18.5	13.5	57.4

4.3. Photoluminescence properties of $M_3Gd_2(BO_3)_4$:Dy^{3+} phosphors

This section describes a series of phosphors, for which an attempt at tuning the photoluminescence properties via changes in chemical composition was made. Dysprosium(III) was selected as a dopant ion because of its white emission. Dy^{3+} cations in a solid matrix can be excited with NUV LED chips and thus can be applied in light sources [100,101] (Gd^{3+} of the matrix provides additional excitation bands). The f-f transitions are not that much sensitive to the material temperature and can possibly provide a phosphor with a temperature-stable emission color [100]. And, as will be shown, the emission color can be tuned (within some range) via chemical composition.

The composition of the materials was kept as $M_2M'Gd_{2-x}Dy_x(BO_3)_4$, where M and M' are ether Ca, Sr or Ba, including the cases when M=M'. The *x* value is equal to 0.1 so the materials are doped with dysprosium at 5% of gadolinium content.

The XRD patterns of the studied materials are shown in Fig. 13-15. The patterns of the studied compounds matched the related entries of ICDD database noted in the figure. Although in the case of different M and M', the peaks in XRD patterns were located between the peaks of appropriate references, it was possible to fit the initial reference pattern to the experimental one and thus check if the patterns are match. The Scherrer XRD analysis showed the particles size of 53±9 nm.

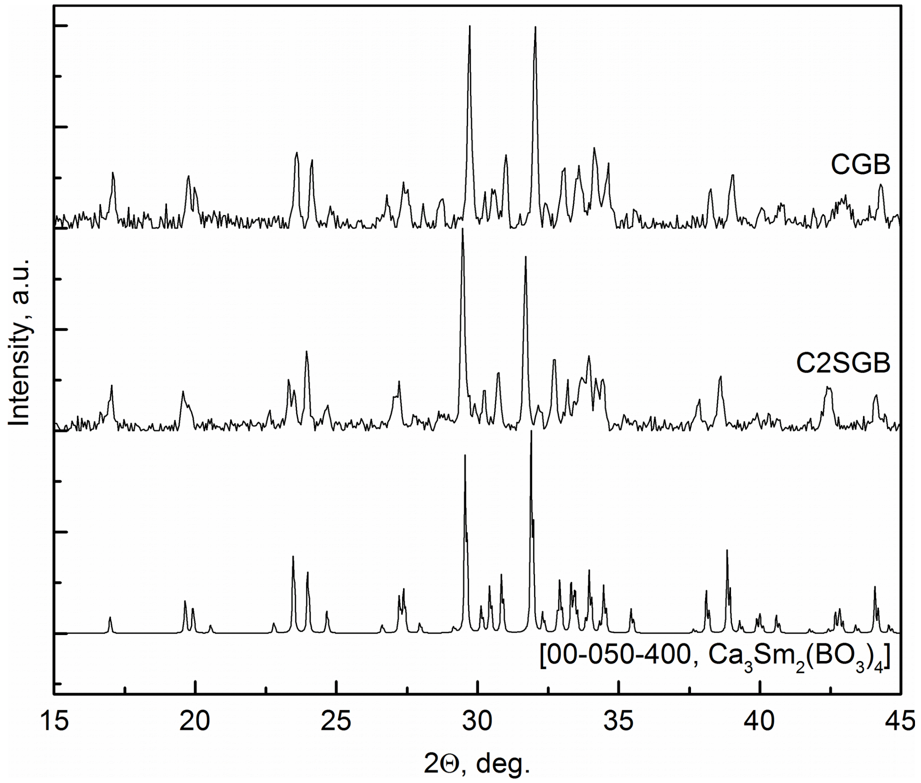

Fig. 13. The XRD patterns of CGB:Dy^{3+}, C2SGB:Dy^{3+}, and a calculated reference pattern

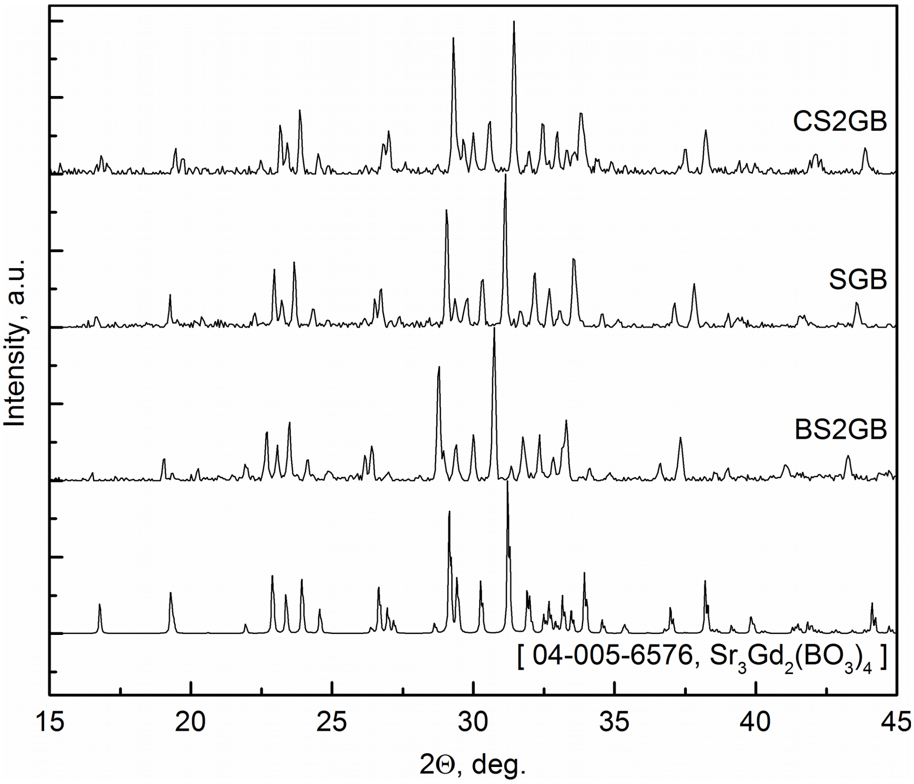

Fig. 14. The XRD patterns of CS2GB:Dy^{3+}, SGB:Dy^{3+}, BS2GB:Dy^{3+} and a calculated reference pattern

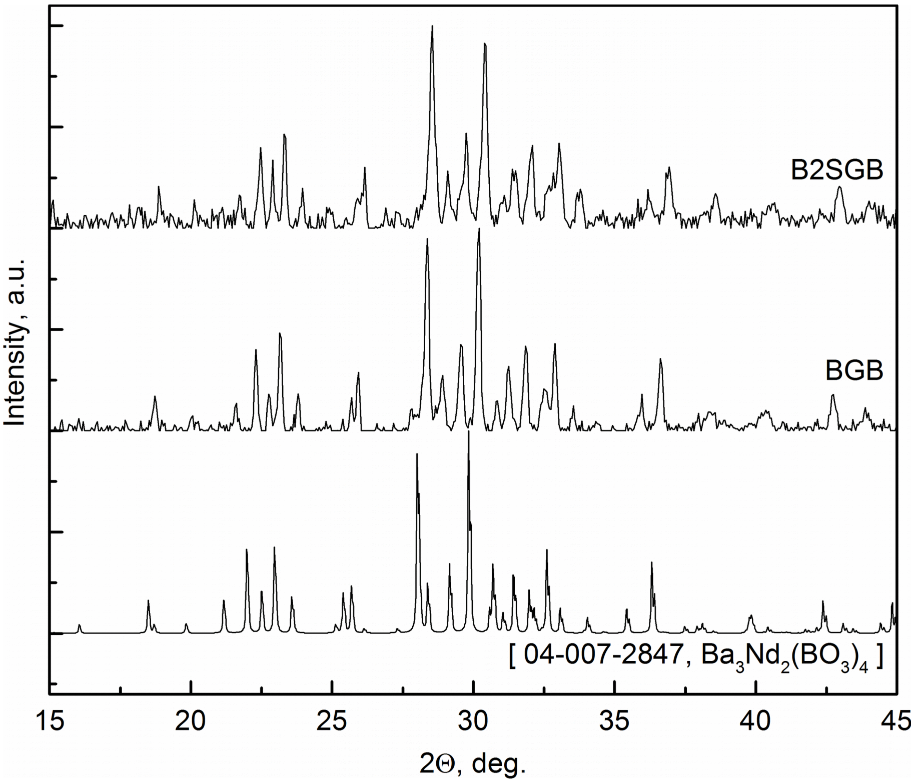

Fig. 15. The XRD patterns of B2SGB:Dy^{3+}, BGB:Dy^{3+}, and a calculated reference pattern

The photoluminescence properties of the materials were studied by analysis of their excitation and emission spectra recorded in near-UV and visible range. Both excitation and emission spectra consist of 4f-4f transitions in Dy^{3+} only. They are shown in Fig. 16 and 17.

The excitation spectra of the samples (Fig. 16) in the spectral range of 330-400 nm show characteristic maxima corresponding to 4f-4f transitions from the ground state of $^6H_{15/2} \rightarrow {}^4F_{7/2}$, $^6F_{9/2}$, $^4G_{21/2}$, $^4H_{15/2}$, $^4K_{15/2}$, $^4P_{3/2}$, $^4P_{7/2}$ levels of Dy^{3+}. Additional excitation bands arising from the ground state transitions of $^8S_{7/2} \rightarrow {}^6I_{15/2}$, $^6P_{7/2}$ level of Gd^{3+} were present in the spectra of Gd-based compounds. These bands were located at 272.8 and 310 nm, respectively. No emission from Gd^{3+} was observed, confirming the presence of an efficient energy transfer from Gd^{3+} to Dy^{3+} ions.

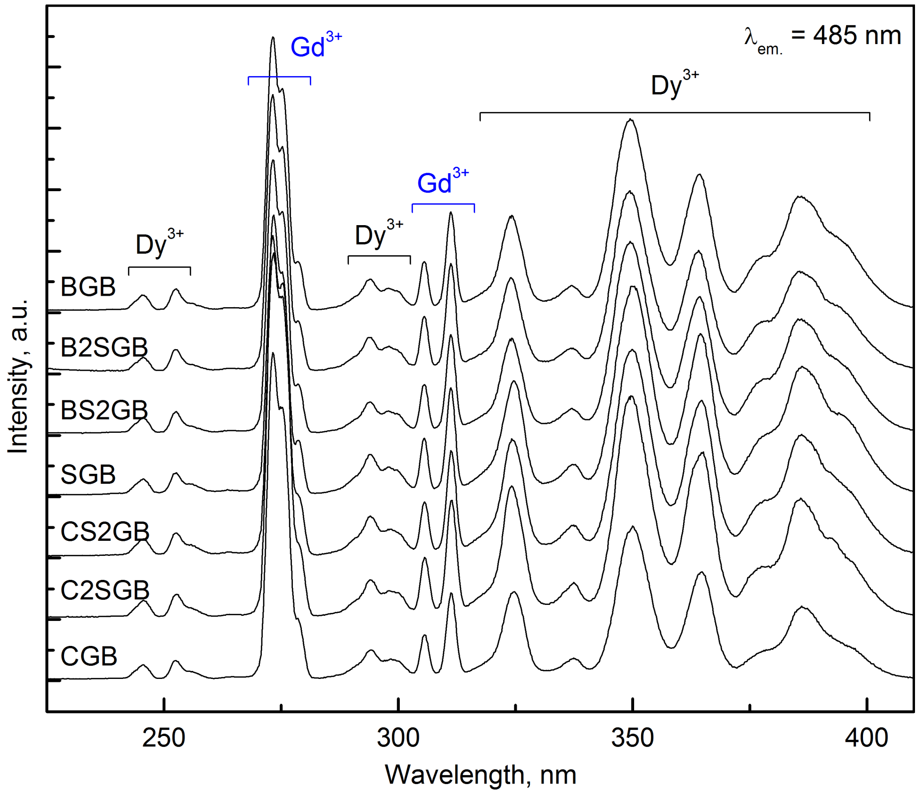

Fig. 16. The excitation spectra of MGB:Dy^{3+}

The emission (Fig. 17) was represented by two main bands at 485 and 577 nm corresponding to the transitions from $^4F_{9/2}$ Dy^{3+} level to $^6H_{15/2}$ and $^6H_{13/2}$ levels, respectively. Relative intensity of the emission peaks depends both on the composition of materials studied and their excitation wavelength. The changes in the shape are most likely attributed to the effect of the matrix material structure on the dopant ions. The peak shapes were similar and the energy levels were similar as well (at least, from as much information as the spectra can provide). This means that the materials were indeed isostructural. On the other hand, the non-systematic changes illustrate the fact that lots of distortions took place.

The effect of structure on the photoluminescence of $M_3Gd_2(BO_3)_4$:Dy^{3+} phosphors also manifests in the ratio of the two main emission peaks. In the series of $Ba_3Gd_2(BO_3)_4$, $Ba_2SrGd_2(BO_3)_4$, $BaSr_2Gd_2(BO3)_4$, $Sr_3Gd_2(BO_3)_4$, $CaSr_2Gd_2(BO_3)_4$, $Ca_2SrGd_2(BO_3)_4$ and

$Ca_3Gd_2(BO_3)_4$ the $^4F_{9/2} \rightarrow {}^6H_{13/2}$ peak gradually increases, while the $^4F_{9/2} \rightarrow {}^6H_{15/2}$ peak decreases. The plots of the ratio of the peaks are shown in Fig. 18.

The luminescence decay curves were two-exponential with the first component within the range of 0.5-1.0±0.2 ms and the second of 0.2-0.4±0.1 ms. As this photoluminescence lifetimes are of a similar order of magnitude, they most likely correspond to the two different luminescence sites. As noted at the beginning of section 4.2, the crystal structure of mixed borates provides two sites of RE ions and tree sites of metal(II) ions (the substitution of the latter by the dopant ions, although unlikely, cannot be 100% disproved).

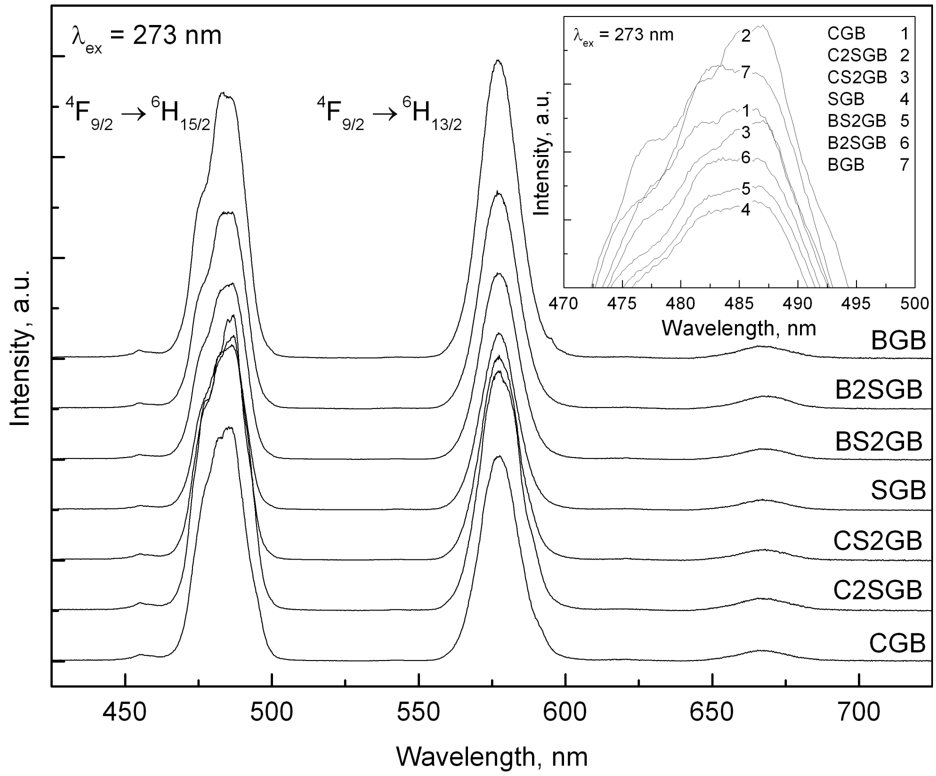

Fig. 17. The emission spectra of MGB:Dy^{3+}

The color of emission (characterized by CIE 1931 color coordinates) linearly changed in the series of $Ba_3Gd_2(BO_3)_4$, $Ba_2SrGd_2(BO_3)_4$, $BaSr_2Gd_2(BO3)_4$, $Sr_3Gd_2(BO_3)_4$, $CaSr_2Gd_2(BO_3)_4$, $Ca_2SrGd_2(BO_3)_4$ and $Ca_3Gd_2(BO_3)_4$ from yellowish-white to bluish-white being very close to pure white (D65 standard source).

A quantitative description of the emission colors was given by means of CIE1931 chromaticity diagram using a 2-degree standard observer. The results are shown in Fig. 19, the white point is at x=0.33, y=0.33.

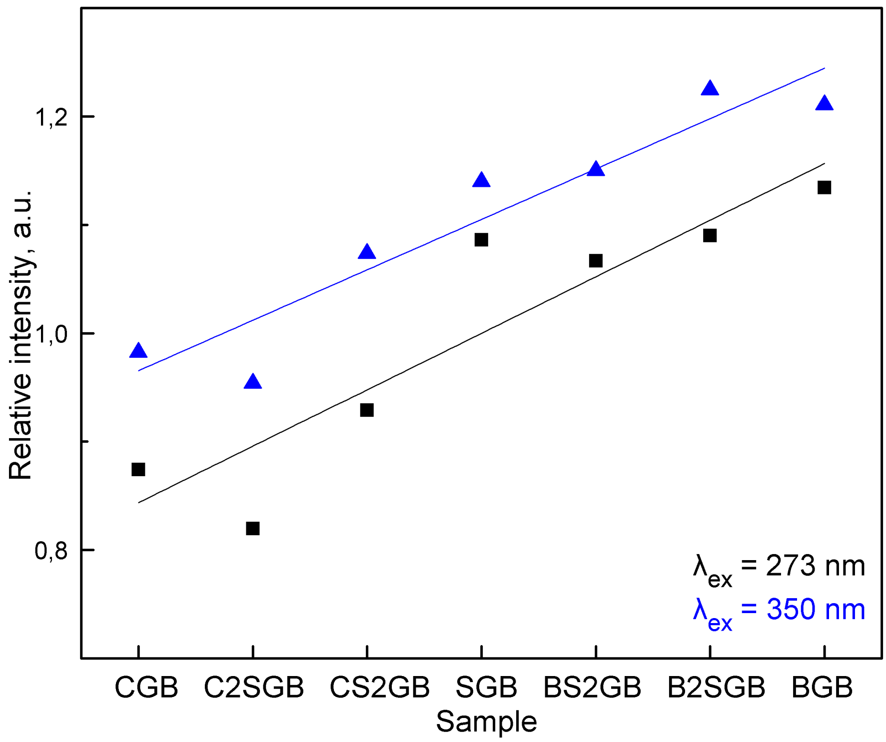

Fig. 18. The ratios of the I($^4F_{9/2} \rightarrow {}^6H_{13/2}$)/I($^4F_{9/2} \rightarrow {}^6H_{15/2}$) Dy^{3+} emission peaks

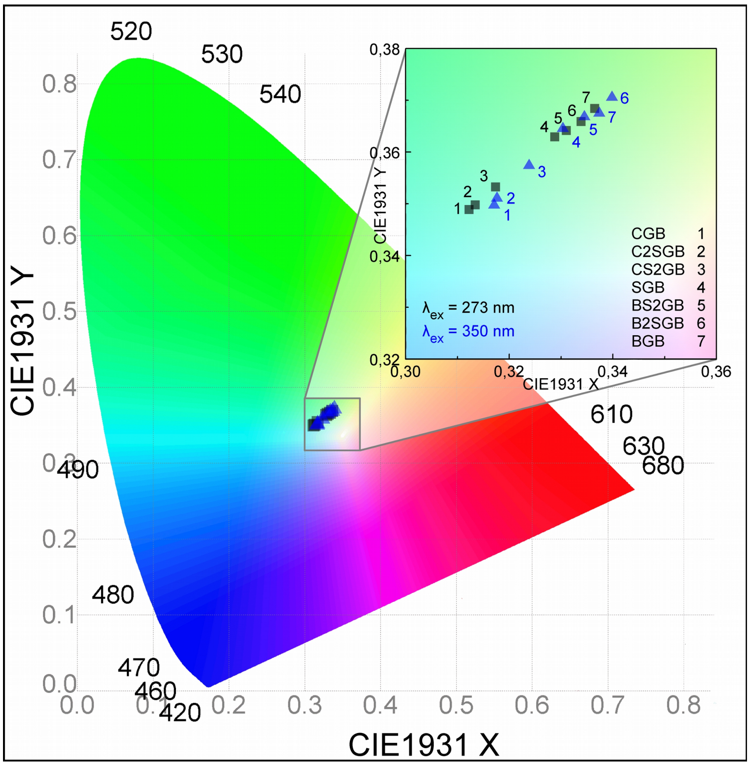

Fig. 19. The chromaticity diagram of MM'GB:Dy^{3+} emission color

4.4. Morphology and photoluminescence properties of the $Sr_3RE_2(BO_3)_4$:Tb^{3+}

The next step of the study was to prepare Tb^{3+}-doped strontium-lanthanum borate ($Sr_3La_2(BO_3)_4$, SLB) and strontium-gadolinium borate ($Sr_3Gd_2(BO_3)_4$, SGB), as well as SYB:Tb^{3+}. As described in section 4.1, it was found that an improvement in the synthesis procedure was required to obtain SGB and SLB. After the optimal conditions were found (namely, the required excess of boric acid was 20%), three series of samples doped with Tb^{3+} were obtained, namely SYB:Tb^{3+}, SLB:Tb^{3+} and SGB:Tb^{3+}.

In Fig. 20, 21 and 22 the XRD patterns of the prepared $Sr_3RE_2(BO_3)_4$:Tb^{3+} materials are presented with the respective theoretical reference patterns and the database codes of the reference structures. It can be clearly seen that the patterns are in agreement with reference data and that the doping did not have any significant effect on the matrix structure. The structures of Tb^{3+}-doped SYB, SLB and SGB samples were consistent with those from ICDD database (cards no. 00-054-1120, 04-005-6578 and 00-058-0627, respectively). On the basis of the presented X-ray analysis and comparison with the reported data, it has been verified that in all samples the major phase comprises the primitive orthorhombic cell of $Pc2_1n$ symmetry [204].

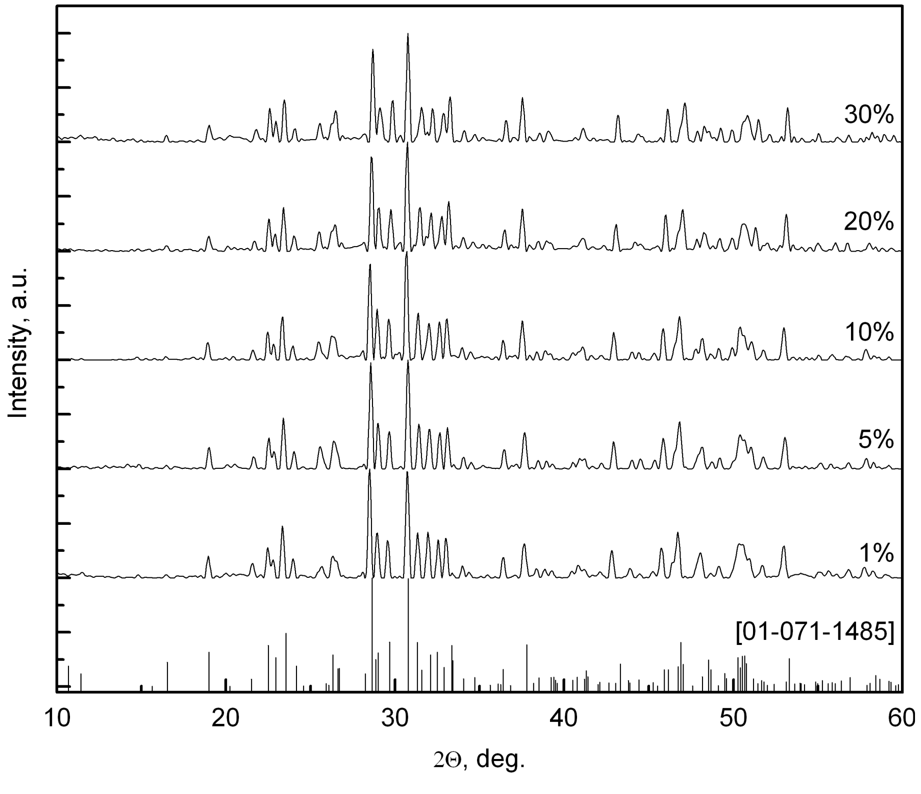

Fig. 20. The XRD patterns of SLB:Tb^{3+} samples

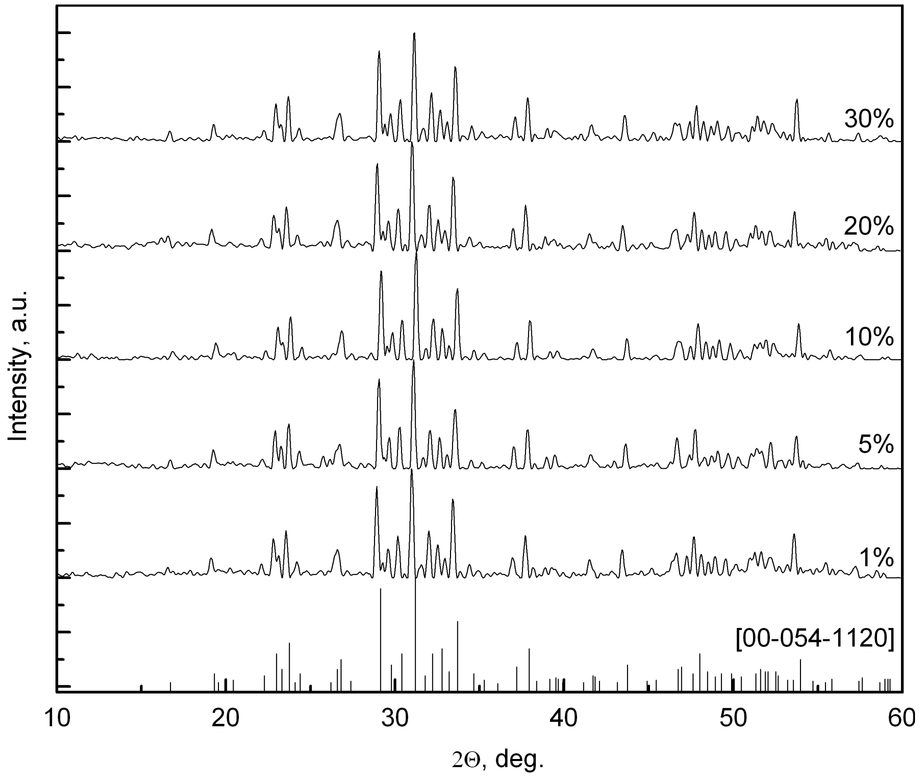

Fig. 21. The XRD patterns of SGB:Tb^{3+} samples

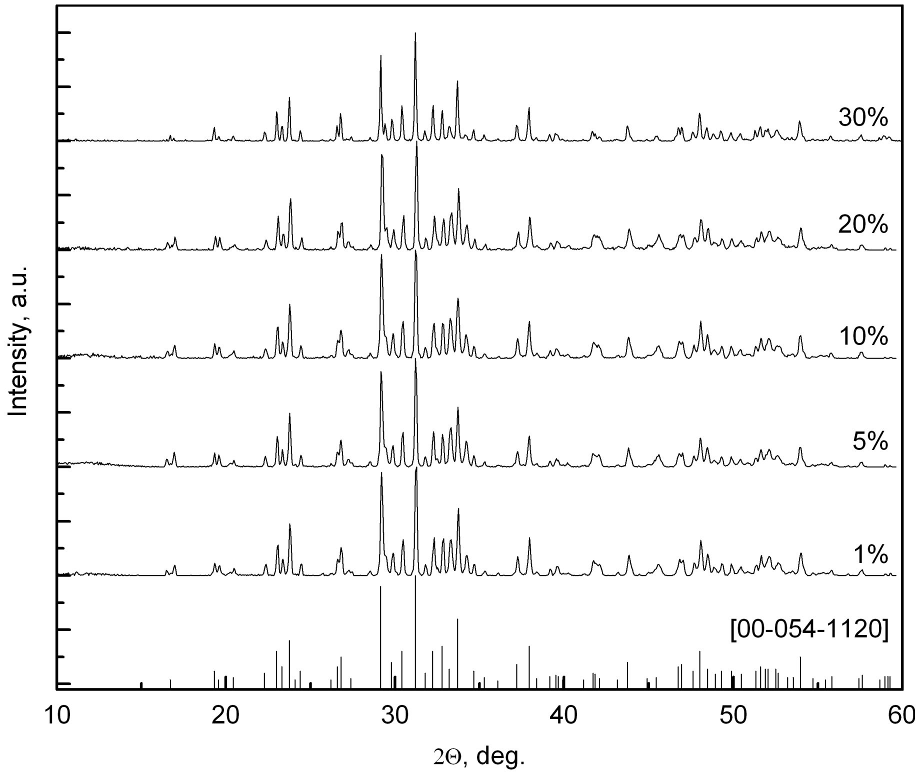

Fig. 22. The XRD patterns of SYB:Tb^{3+} samples

The images obtained by means of transmission electron microscopy are shown in Fig. 23. for the 5% Tb^{3+}-doped SYB, SLB and SGB respectively. Comparing to the previous results for SYB:Eu^{3+}, the presented samples were characterized by a higher content of nanoparticles and smaller content of micrometer-scaled agglomerates (although the latter were still present). In SYB, the size of particles varied between 25 and 40 nm; the particles in SLB:Tb^{3+} sample were of 20-30 nm in size and particles in SGB:Tb^{3+} sample were of 20-40nm in size. The particles were the most agglomerated in the latter sample, while some inclusions of smaller particles and larger agglomerates could be found in all samples. TEM images confirmed that nanoparticles were obtained in all samples [204]. The analysis with the help of the Scherrer formula indicated that all samples contained nanoparticles of the size of 40±10 nm, which was a bit inconsistent with the TEM data. The inconsistency originates from the Scherrer method itself: it gives the average particle size, while the presented simple formula does not contain any corrections for the texture and other properties of the materials.

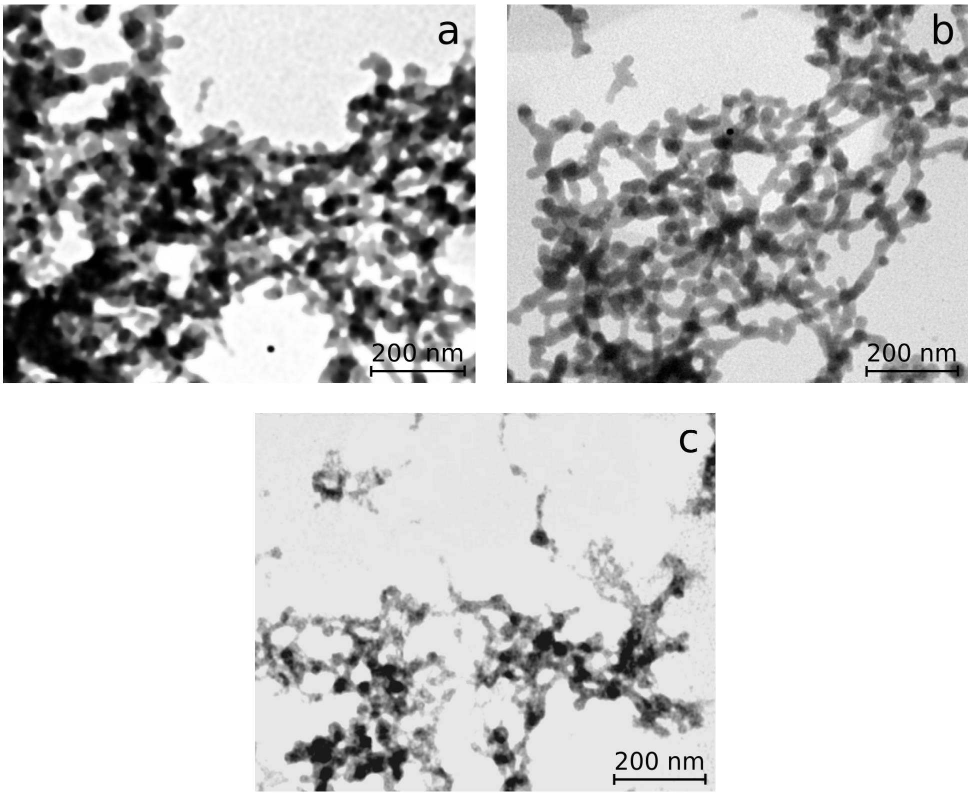

Fig. 23. TEM images of SGB:Tb^{3+} (a), SLB:Tb^{3+} (b) and SYB:Tb^{3+} (c) samples

Rietveld refinement was used to determine the phase purity of the samples [204]. The samples were mostly composed of the respective mixed borates (95-98%). Some amounts of SrB_2O_4, $REBO_3$ and/or RE_2O_3 appeared as impurities [204].

More insights into the composition of the samples were obtained using Fourier-transform infrared spectroscopy. The respective spectra are presented in Fig. 24. It was found that, for the same compound, the amount of dopant does not affect the pattern of the spectra. On the other hand, the spectra were a bit different for different borates.

Although different matrices were characterized by a slightly different FTIR spectra, most of the peaks were located at similar wavenumbers, but had different intensities. The peaks can be attributed to the vibrations of BO_3 triangle borate groups of $Sr_3RE_2(BO_3)_4$ [204]. The details are given in Table 2.

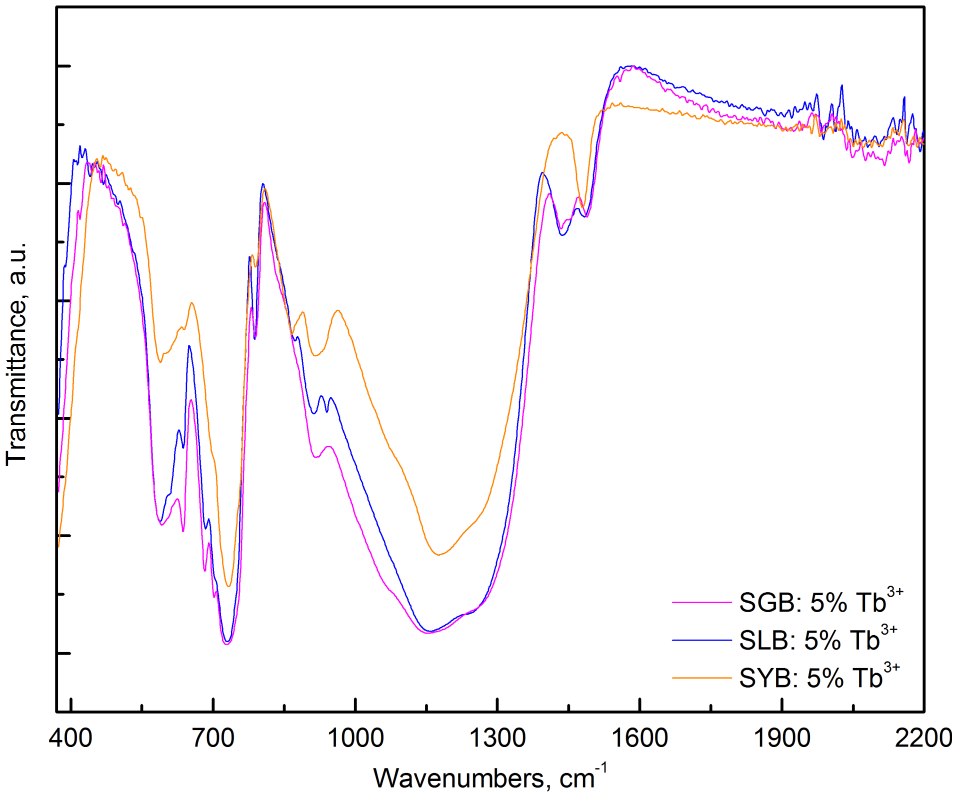

Fig. 24. The FTIR spectra of SGB:Tb^{3+}, SLB:Tb^{3+} and SYB:Tb^{3+} samples

Table 2. The FTIR analysis of the prepared Tb^{3+}-doped mixed borates

Compound	Group	Vibration	Wavenumber, cm^{-1}
$Sr_3RE_2(BO_3)_4$	BO_3 triangle	asymmetric stretching symmetric stretching out-of-plane stretching asymmetric bending symmetric bending triangle bending	1260 914 790 590-640 757, 732 720
	B-O	bond stretching	1478
Impurity, see the discussion below	BO_4 tetrahedron	B-O-B triangle bending	693
	B-O	bond stretching	1068, 867

Some bands in the FTIR spectra (Table 2) could be attributed to impurities [205,206]. For example, BO_4 tetrahedral groups are the essential part of vaterite-type YBO_3 [207]. The presence of some amount of impurities is consistent with the results of Rietveld analysis [204].

The mixed borate materials doped with Tb^{3+} produced bright green emission under the excitation by ultraviolet (UV) radiation. The excitation spectra of the samples are presented in Fig. 25-27, left. The spectra were obtained by excitation in the 200-450 nm range (λ_{em} = 544 nm, Tb^{3+} $^7F_6 \rightarrow {}^5D_5$). The excitation spectra consisted of 4f-5d high-spin band and 4f-4f bands of Tb^{3+}. In the spectrum of SGB, the 4f-4f bands of Gd^{3+} appeared. The broad band corresponding to the $^7F_6 \rightarrow {}^7D$ (f-d) transition of Tb^{3+} was located at 238-250 nm [204]. At higher doping rates, a bathochromic shift of this band was observed. The bands of transitions from Tb^{3+} ground level $^7F_6$ to the $^5G_{5,6}$, $^5H_{6,7}$, $^5I_8$, $^5L_{7\text{-}10}$ levels were located at 290-400 nm. See Fig. 25 for details. In the spectrum of SGB, the peaks corresponding to the $^8S_{7/2} \rightarrow {}^6I_{15/2}$ and $^8S_{7/2} \rightarrow {}^6P_{5/2,\,7/2}$, transitions of Gd^{3+} appeared at 272.8, 304.9 and 310.7 nm, respectively. As the intense Gd^{3+} excitation bands were present in the spectra of SGB:Tb^{3+}, one can conclude that efficient Gd-to-Tb energy transfer occurred in the system. The increase in the dopant amount resulted in a consequent increase in the excitation transition intensities. At the doping rates of 10% and more, the intensity of the f-f transitions of Tb^{3+} was high enough to be used for excitation of phosphors, in potential practical application. This feature might be useful for excitation by means of near-UV or blue light electric diode, NUV-LED. From the practical point of view, this is a characteristic feature required by the phosphors for light source applications [100]. Additionally, excitation with a high-pressure Hg UV lamp into the f-d band is possible.

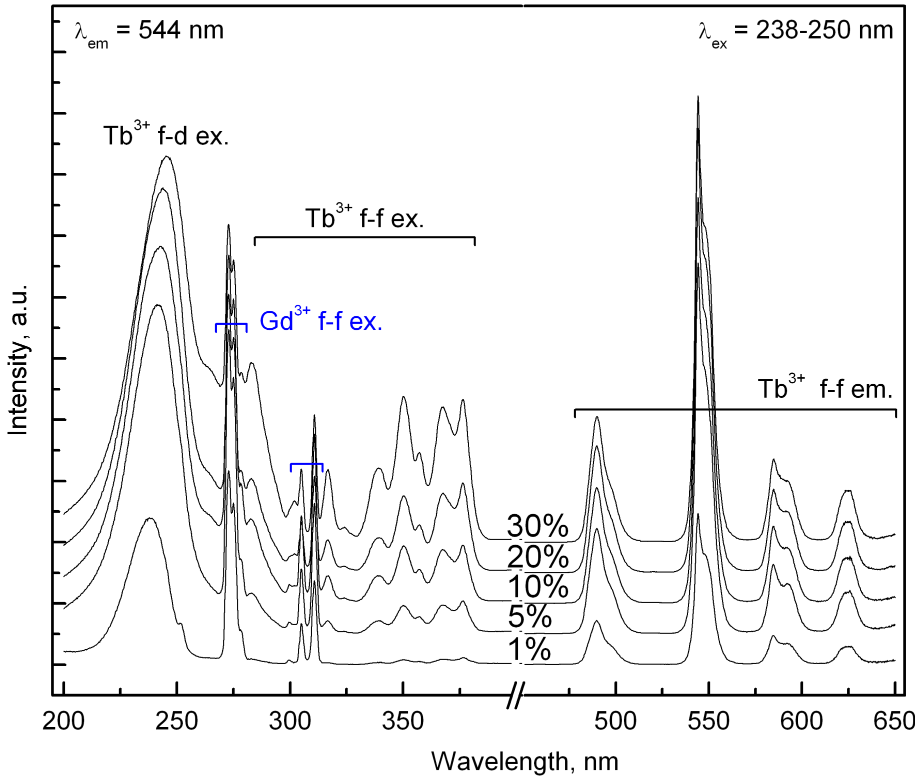

Fig. 25. The excitation (left) and emission (right) spectra of SGB:Tb^{3+} samples

In order to get deeper understanding of the photoluminescence of the materials studied, the number of peaks in the f-d excitation band was established. This task was resolved via peak search and fitting procedure. The simplest way to find peak positions analytically is to apply differentiation to the spectrum. This particular step was coupled to the problem of noise in the spectrum. The attempt to obtain a second derivative of the spectra numerically from the raw spectrofluorimetric data resulted in a differentiated spectrum composed mostly of a strongly amplified noise. Thus, a smoothing procedure was applied before differentiation.

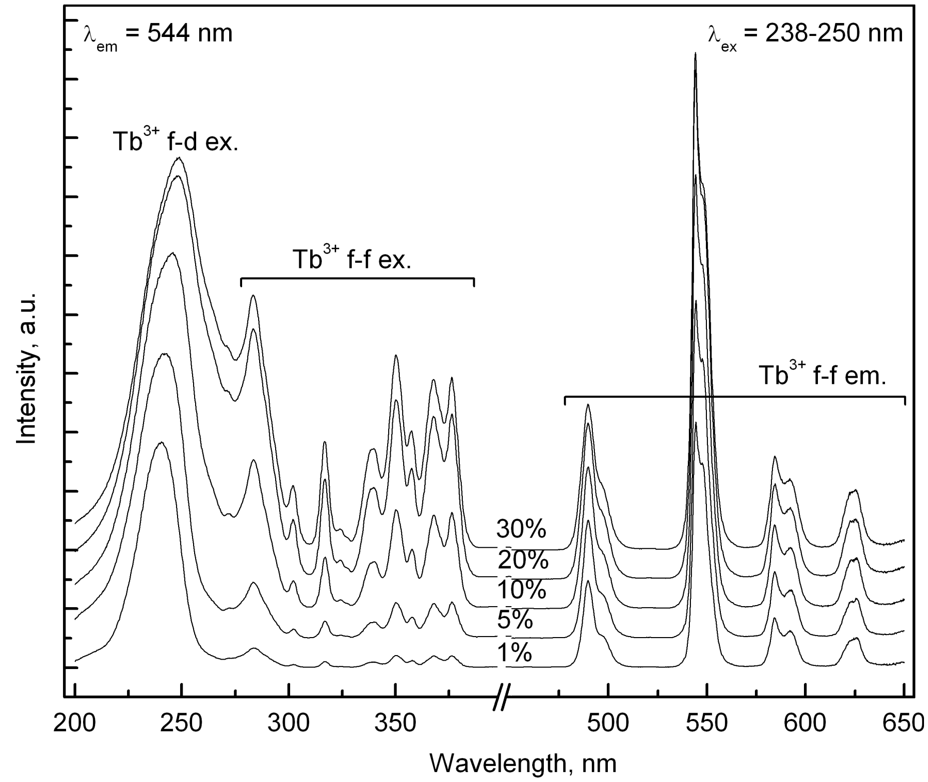

Fig. 26. The excitation (left) and emission (right) spectra of SLB:Tb^{3+} samples

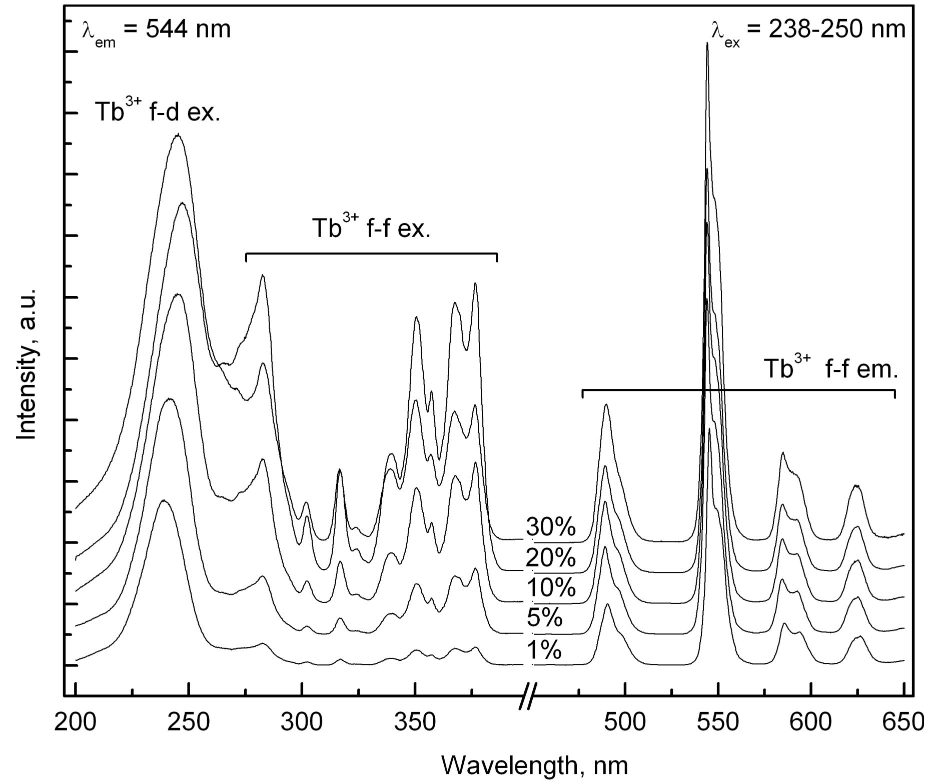

Fig. 27. The excitation (left) and emission (right) spectra of SYB:Tb^{3+} samples

In particular, Savitzky-Golay smooth with polynomial order of 5 was used [204]. The first step was a 20-point smoothing; the second and the third steps were 50-point and 20-point smooth, respectively [204]. The last smoothing step was included into the differentiation procedure, as the feature is available in the OriginPro software used for the task. As the smoothing might have removed some low-intensity peaks, the average of absolute difference between the original and smoothed spectra for every data point of the spectra was found [198]. In 1% doped SLB it was equal to 0.03% and 0.08% for the first and the second step, respectively, whereas for 30%-doped SLB these values were equal to 0.004%. These values were compared to the error of the measurements. The spectra were recorded thrice under the same conditions and the average deviation was calculated at every wavelength of the spectra. The average value of the deviation (0.6%) clearly shows that the error introduced by the smoothing procedure is negligible. After the two-step smoothing, a second-order differentiation with additional smoothing step was applied (as mentioned above). The positions of peaks in the resulting differentiated spectra were used as the initial guess in the peak fitting procedure [204]. The fit peaks were produced by the Gaussian function. See Fig. 28 and 29 for the details (the second derivatives are presented as solid lines).

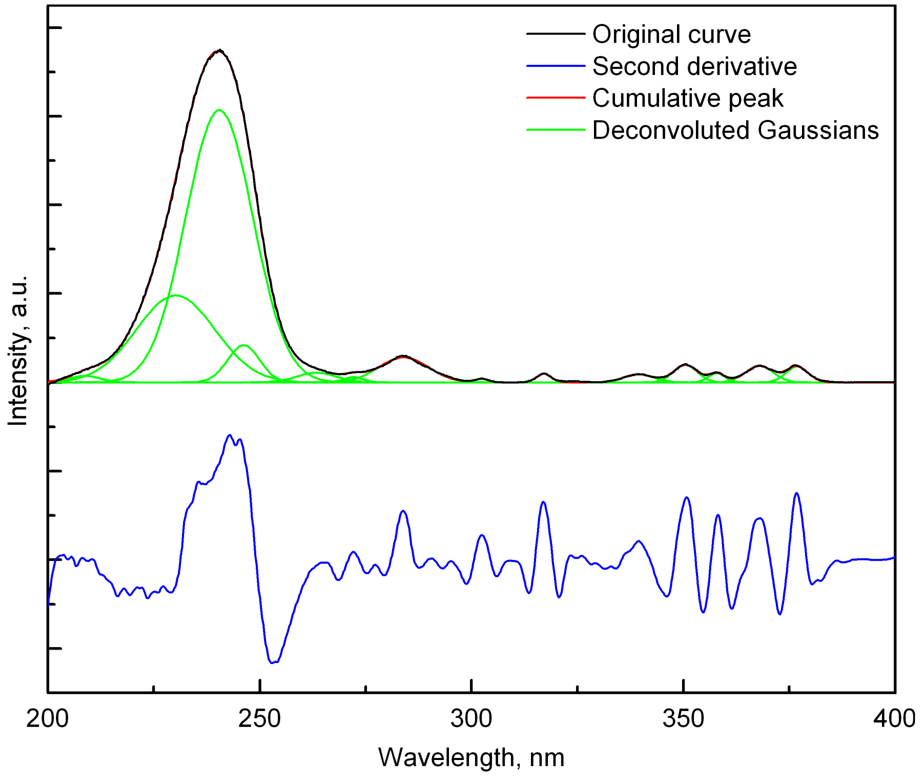

Fig. 28. The second derivative and the deconvolution of the excitation spectrum of SLB:1%Tb^{3+}

As it can be seen in Fig. 28 and 29, the f-d excitation peaks contained more than one Gaussian peak. The two main peaks were located around 235 and 251 nm [204]. Comparison of the spectra of SLB:Tb^{3+} samples doped by 1% or 30% clearly shows, that the peak at higher wavelength has a significantly higher intensity in the case of 30%-doped sample. Thus, the total shift of the f-d excitation peak might be attributed to the changes in relative intensity of its component peak at 251 nm. However, the f-d transition of Tb^{3+} in this range should contain only one peak. The presence of two peaks suggests the presence of two different photoluminescence centers.

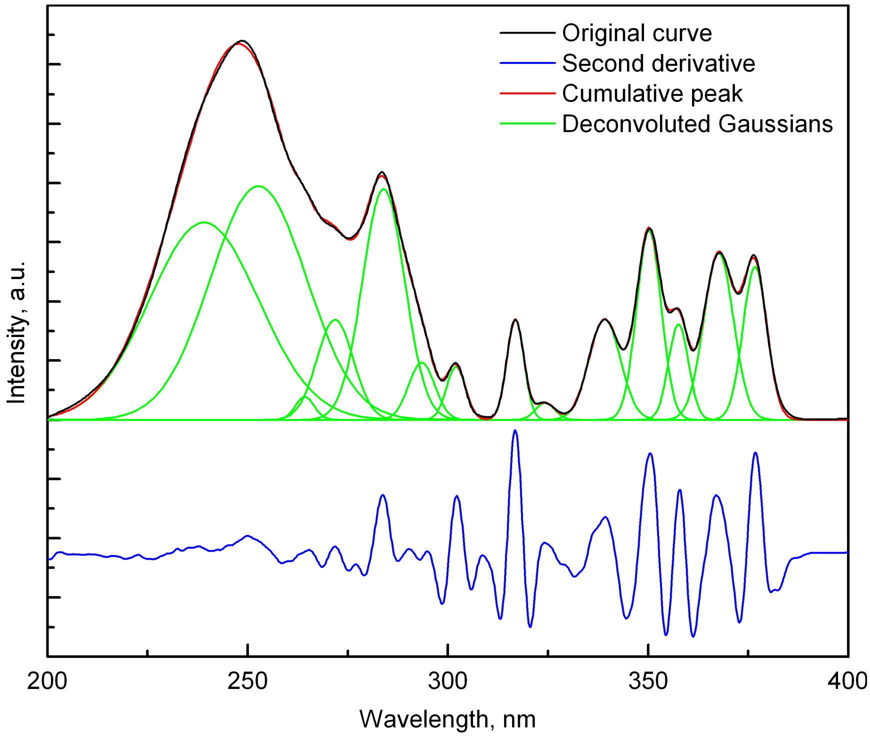

Fig. 29. The second derivative and the deconvolution of the excitation spectrum of SLB:30%Tb^{3+}

According to their crystalline structure, the mixed borates of the type presented contain two different sites of rare earth ions [204]. The dopant ions might occur at any of those two. The coordination geometry of these sites is not the same. It might happen that, for some reason, there is a preference in site occupation by the dopant ions. When the amount of dopant is small, the preferred site is occupied. When the number of dopant ions increases, the possibility for the dopant ions to occupy the preferred sites decreases. Thus, the probability of occupation of the less preferred site increases. This would produce two photoluminescence sites giving bands of similar band shape and slightly different energies. The data on the photoluminescence lifetimes of the 1%-doped sample measured under excitation into these two bands (235 and 251 nm) support this idea [204]. Both decay curves are single-exponential. The fitting procedure results in the lifetimes of 3.45 ± 0.02 ms and 2.26 ± 0.03 ms, respectively. The "±" values are standard deviations of three measurements. This also supports the idea of two different photoluminescence sites.

The emission color of the obtained phosphors was green under both UV or NUV excitation. The main peaks originate from $^5D_4 \rightarrow {}^7F_{6,5,4,3}$ transitions of Tb^{3+} ions with the most intense peak of $^5D_4 \rightarrow {}^7F_5$ transition at 545 nm in the case of SYB:Tb^{3+}, and 544 nm in the cases of SGB:Tb^{3+} and SLB:Tb^{3+} [204]. The emission spectra of the samples collected under the f-d band peak wavelength excitation are shown in Fig. 25-27, right.

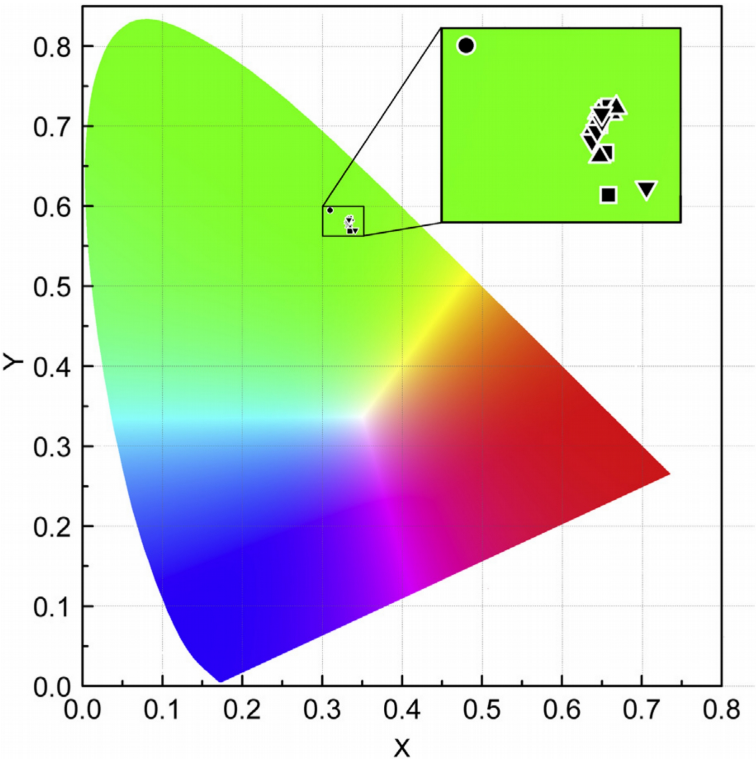

Fig. 30. The chromaticity diagram of SGB:Tb^{3+} (■), SLB:Tb^{3+} (▲) and SYB:Tb^{3+} (▼) emission color, and NTSC standard of green (●) [204]

In order to give a quantitative characterization of the emission color, the CIE1931 color space [204] was used. The CIE chart is shown in Fig. 30, together with the National Television Standards Committee (NTSC) standard [208] of green [204].

The effect of excitation wavelength on the emission pattern was checked to be found insignificant. The emission intensity depended strongly on the excitation wavelength as it can be deduced from the form of the excitation spectra.

Fig. 31 presents the dependence of the emission intensities at 544 nm on the amount of Tb^{3+} dopant. The vertical error bars on these data points were supposed to be about 0.6%, but they were not shown since they overlapped the data points. The emission intensities of the samples were increased in the range of the dopant amounts from 0.5% through 20% [204]. The cross-relaxation processes increase strongly at high amounts of dopant such as 10-20%. The overall trend in Fig. 31 strongly suggests a saturation (a slight decrease in the intensity is observed for 30%-doped SLB:Tb^{3+}). The amount of dopant of 10% seems to be optimal, since further increase in the dopant amount did not increase the emission significantly. On the other hand, the f-f excitation transitions were intense enough to excite the phosphor in the NUV range. The Tb^{3+} emission was the most intense in the SLB matrix (under other conditions unchanged) [204].

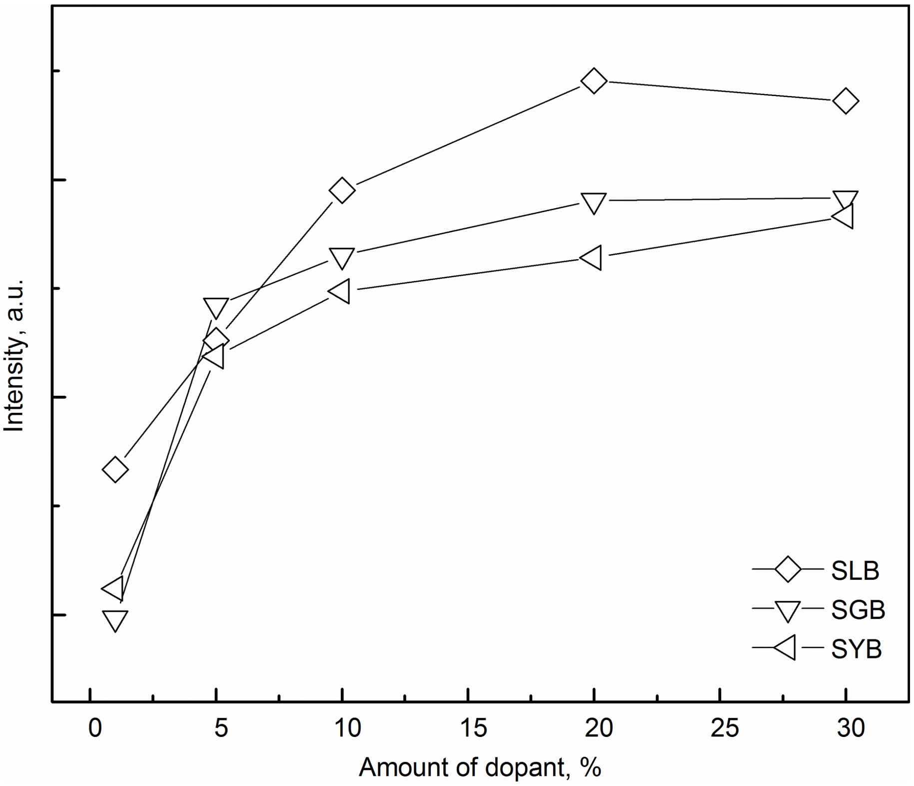

Fig. 31. The dependence of the 544 nm emission intensities of SGB:Tb^{3+}, SLB:Tb^{3+} and SYB:Tb^{3+} on the amount of Tb^{3+} dopant

The photoluminescence decay curves of the studied samples are presented in Fig. 32-34. The decay curves were fitted to a single exponential decay function, the R^2 factor was 0.997-0.998 [204]. The type of dependence of the photoluminescence lifetimes on the amount of dopant was not the same for different matrices. In SLB:Tb^{3+}, no significant dependence was observed [204] and the lifetimes did not change much. In SGB:$^{3+}$, the lifetime changes were a bit higher, but lacked any informative trend. In SYB:Tb^{3+}, the changes in lifetimes were significant: the emission lifetime decreased from 2.65 to 2.4 ms, with the dopant amount increased from 1 to 30% [204]. Unlike other matrices, a clear linear dependence was observed (Fig. 32). As indicated above, the cross-relaxation efficiency is similar for all three matrices (Fig. 31). Consequently this special behavior of the photoluminescence lifetimes of SYB:Tb^{3+} should be attributed to some feature characteristic of SYB. Definitely, the matrices differ in ionic radii of the rare earth ions [204]. In SGB:Tb^{3+} and SLB:Tb^{3+} the dopant ions substitute ions of almost the same or larger size. In SYB:Tb^{3+}, Tb^{3+} ions substitute a bit smaller Y^{3+} ions, thus, the effect of crystal field on the dopant ions should be stronger.

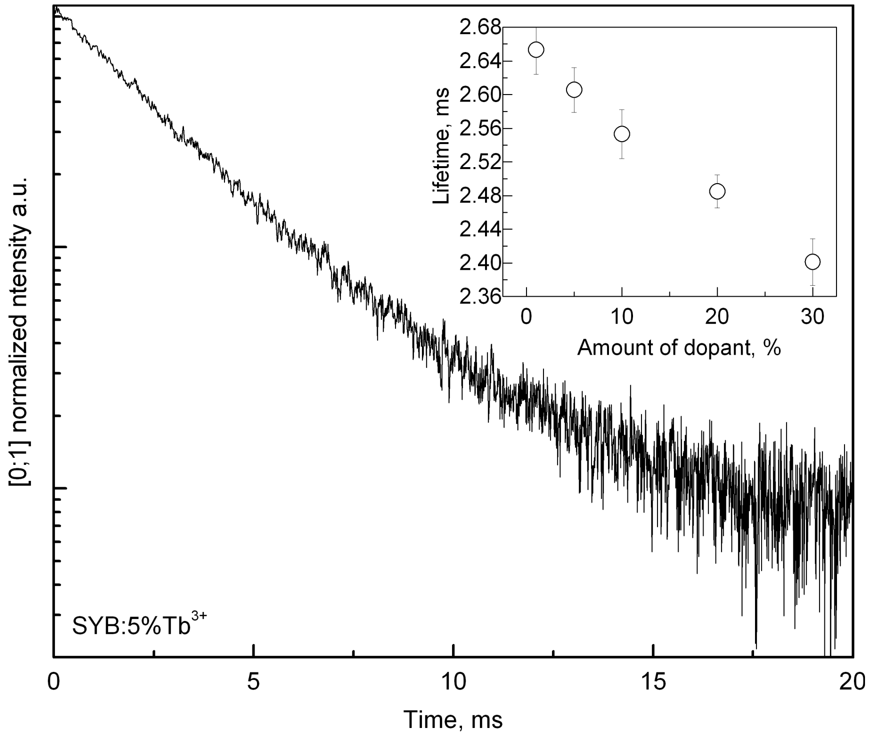

Fig. 32. Decay of SYB:1%Tb^{3+} sample photoluminescence; the inset depicts the dependence of the emission lifetime of the other samples on the amount of dopant

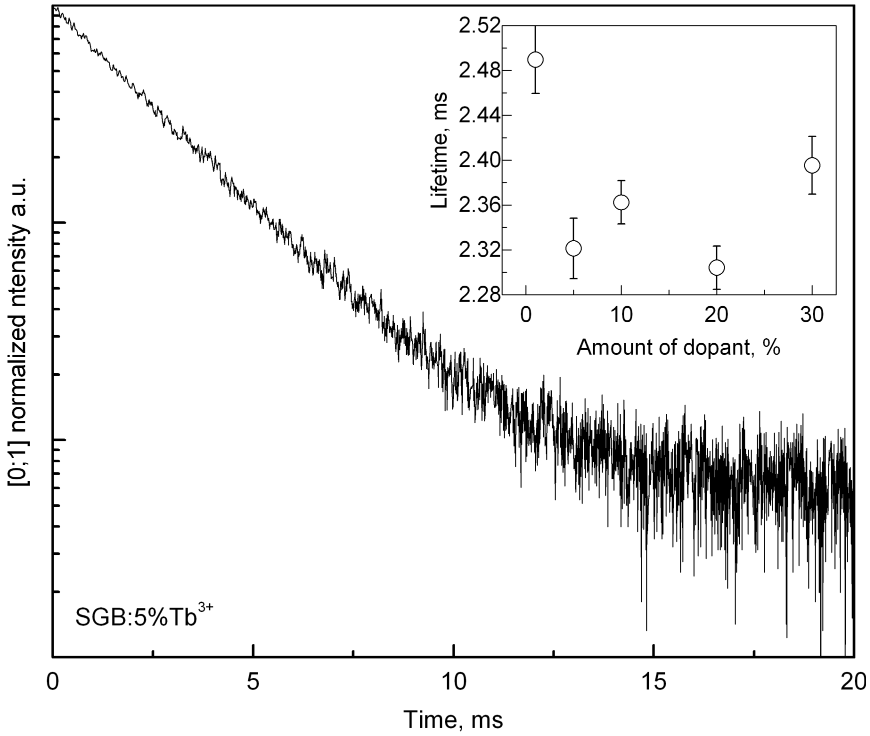

Fig. 33. Decay of SGB:1%Tb^{3+} sample photoluminescence; the inset depicts the dependence of the emission lifetime of the other samples on the amount of dopant

The emission lifetimes of SGB:Tb^{3+} emission did not depend on the kind of excitation band, that is, the Tb^{3+} f-d or f-f bands band or the Gd^{3+} f-f transitions. This feature clearly shows that strong Gd-to-Tb energy transfer must have occurred in the system. The rate of the process can be deduced to be high enough not to affect the single-exponential character of Tb^{3+} decay of about 2.3-2.5 ms lifetime.

The lifetimes of the phosphors are short enough for them to be used in plasma display panels capable to screen more than 30 frames per second (i.e. those supporting 3D standard) [204,209].

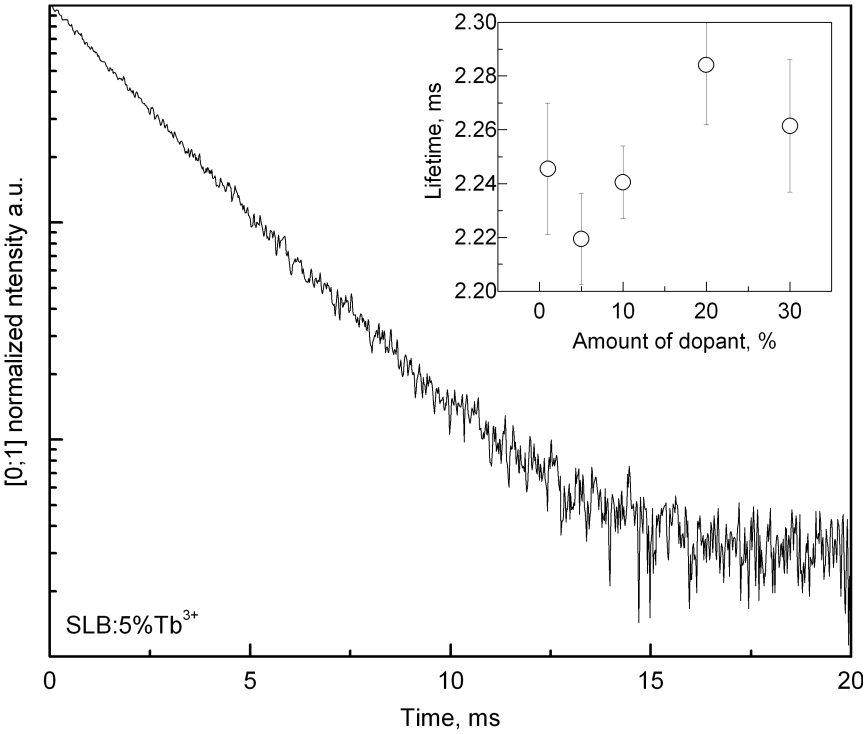

Fig. 34. Decay of SLB:1%Tb^{3+} sample photoluminescence; the inset depicts the dependence of the emission lifetime of the other samples on the amount of dopant

5. Theoretical and computational studies

5.1. Computational studies on the effect of doping on the crystal structure of $CeF^3:Tb^{3+}$

The experimental results obtained for $Sr_3La_2(BO_3)_4:Tb^{3+}$ strongly suggest that one of the two La^{3+} sites in the structure might be preferably occupied by the dopant ions. Such preference is most likely caused by the structural properties of the material. Substitution of La^{3+} by Tb^{3+} in either of the sites should have some thermodynamic effect on the system and this might be the cause of the preference. A quantum chemical computational study is required to investigate this aspect. Moreover, the ionic radii of Ln^{3+} ions decrease with increasing atomic number of the ion, which is known as lanthanide contraction. Thus, substitution of a La^{3+} ion with a Tb^{3+} ion should cause some changes in the whole structure. Among the other properties, crystal lattice vectors might be affected. This effect can be manifested in the X-ray diffraction patterns of the materials studied. In particular, the more dopant is in the matrix, the more lattice parameters of the doped material should differ from those of the non-doped structure. This effect can also be studied using computations. Both the preferred occupation and the effect on the lattice vectors are important from the spectroscopic point of view as the photoluminescence properties of lanthanide ions strongly depend on their coordination geometry [20].

The initial crystal lattice should undergo energy minimization. It is important to preserve the principal crystallographic positions of the atoms (because the crystal structure of a model should be the same as the one of the compound studied and thus match both database reference and XRD data) while the lattice parameters of the cell can be changed. It is to be noted here that changes in lattice parameters cause changes in the dopant ions surrounding (as well as changes in the vicinity of the other ions) even if all of the fractional coordinates are constrained, as the Cartesian coordinates are the products of the fractional coordinates and the respective lattice vectors. On the other hand, the changes are exactly the same as those in coordination geometry of any other RE atom in the structure. In order to get dopant-specific changes in the surrounding geometry, the fractional coordinates of the respective atoms must be allowed to change (unconstrained).

Strontium-lanthanum borate is a relatively complicated system. Thus, it is better to use a simpler material in order to find out the optimal computational procedure. Still, it should be a system somehow related to SLB (that is, to be a Ln-based compound), and the study must remain scientifically interesting. Cerium fluoride was selected as a model system. It is much easier to model (simple structure, only one Ln site, only two elements, small amount of electrons on non-lanthanide atoms). Besides, it is a known luminophore matrix and its modeling is both interesting and important.

There are various computational methods that might be applied in order to model a CeF_3 crystal. The basic choice was between semi-empirical and *ab initio* methods. The preliminary tests have shown that semi-empirical methods offer very short computation time and thus, they were the starting point. In order to give the computations an experimental reference, a series of CeF_3:Tb^{3+} samples was obtained by two methods, namely co-precipitation and hydrothermal. The details of the synthesis procedure can be found in [27,210].

The ionic radii of Ce^{3+} and Tb^{3+} differ slightly (1.196 Å and 1.095 respectively, coordination number of 9) [2]. The difference is small, though and thus it is suggested that Tb^{3+} ions substitute Ce^{3+} ions without any defects in the crystal structure. At least, no other phases were detected by means of XRD and the pattern matched that of the reference. The database structure ICDD #155555 was used as a source of both reference XRD pattern and input geometry. Some of Ce^{3+} ions in the input structures were substituted by Tb^{3+} ions, according to the desired stoichiometry. Usually, the optimal dopant concentration for CeF_3:Tb^{3+} is several % [27]. The unit cell of CeF_3 (P-3c1, z = 6) contains 6 cerium atoms. Substitution of any one of them would represent 1/6 = 0.1(6) = 16.6% of the dopant. Thus, a larger system with more Ce ions is required. Replication of the unit cell twice along each of the lattice vectors would form a 2×2×2 supercell containing 8 unit cells and 8×6 = 48 Ce positions. In such a system, substation of one Ce^{3+} ion would correspond to 1/48=2.08(3)% of dopant [27]. The supercell is shown in Fig. 35.

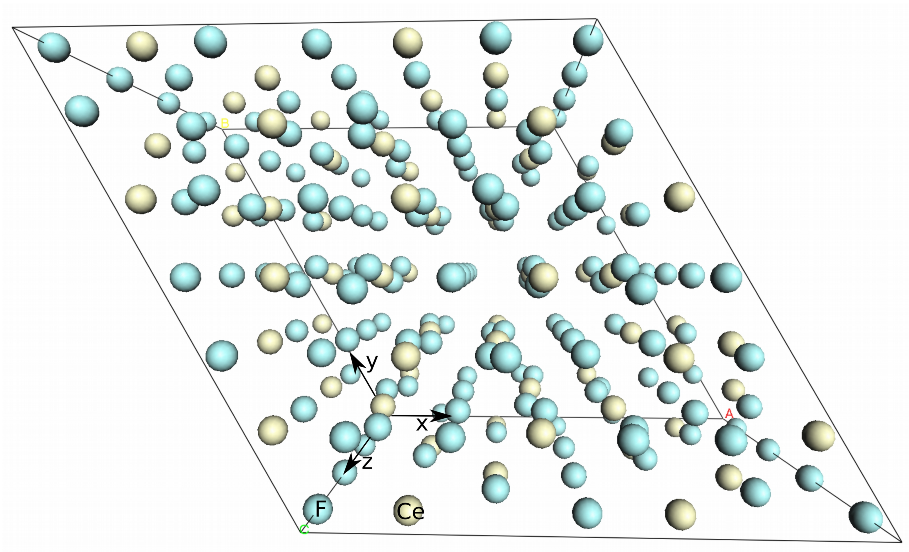

Fig. 35. The 2×2×2 supercell of CeF_3

As the usual amount of a dopant in the matrix compound is much lower than 100%, only some of the positions available in the supercell can be substituted. The total amount of doping options equals $N!((N-n)!\ n!)^{-1}$, where N is the number of positions in the supercell available for doping and n is the number of dopant ions in the supercell. It is obviously too big effort to perform the computations for all of them. For this reason, a random selection of substitution positions was used in order to form the input structures containing the dopant ions. Ten different random inputs for semi-empirical calculations were made for each studied amount of the dopant, with the doping rates from 0 to 6 Tb ions per supercell [27,210]. The corresponding percentage of the dopant was between 0 and 12.5% (0.0, 2.08, 4.17, 6.25, 8.33, 10.42 and 12.5%). In order to generate the input structure and perform the substitution, a script in Python [211] language was developed.

5.1.1. Details of semi-empirical computation on CeF_3:Tb^{3+}

Semi-empirical computations were performed with the methods AM1 [31], RM1 [32], PM3 [33–35], PM6 [37,38] and PM7 [39]. All of the methods were used with the appropriate Sparkle models [42,43,212–214] applied to represent the Ln^{3+} ions, as the original methods do not have parameterizations for these ions. The methods are parametrized, among the others elements, for fluorine, and thus, can be used in calculations of CeF_3:Tb^{3+} properties. The studied systems were treated as continuous periodic solids. The periodical boundary conditions were set by addition of transition vectors to the studied structures [37,38]. Another script in Python was used to perform the relaxation procedure. The script used MOPAC2012 [215,216] software with default convergence and integral cutoff settings to calculate singe point energies at relaxation steps. The relaxation was performed via step-by-step scaling of the lattice vectors of the optimized structure. The optimization was performed as a search for minimum energy as a function of the length of one of the lattice vectors. During the procedure, the other vectors were kept at their initial values. Only cell dimensions were relaxed, the fractional coordinates of atoms underwent no changes, as well as no cell angles were modified [27]. At a particular iteration i, the current value of a modified cell dimension was defined as its initial value times a multiplier m_i corresponding to the iteration (the initial value of the multiplier was 1). For the next i+1 iteration, the m_{i+1} multiplier was defined as:

$$m_{i+1} = m_i + s \tag{5.1.1}$$

where $|s| < 1$ was the current optimization step. If the energy of the modified structure corresponding to the $i+1$ iteration was lower than the previous (i^{th}) step energy, the current change was accepted. Else, the value of s was multiplied by –0.5 and a new modification (applied to the i^{th} iteration geometry, $m_i + s$) was tested. If the absolute value of s went below 0.0001, the relaxation was considered complete. The sign of s was defined in the initial guess and was changing during the relaxation procedure.

Crystal cell dimensions were optimized via a two-stage procedure [27]. In the first stage, the initial lengths of lattice vectors were equal to the database values (ICDD code 155555). In the second stage, the initial values were the ones found in the first stage [27]. A two-step procedure of this type was found to result in better agreement with the experiment.

It must be noted, that the *a* and *b* lattice vectors of CeF_3 must have the same length because of the symmetry of the system (space group P-3c1). Thus, they were relaxed simultaneously at both stages [27].

5.1.2. Details of ab initio computation on $CeF_3:Tb^{3+}$

Analysis of the results obtained by the semi-empirical computations has shown that the total energies of structures containing the same amounts of dopant and differing in particular locations of dopant ions, were very similar. As the *ab initio* computations are time-consuming, it was decided to use only one input structure per each amount of dopant. Moreover, the 2×2×2 supercell of CeF_3 was found to be insufficiently large for the computations using Vienna *ab initio* Simulation Package (VASP) [217–220] code. Thus, a unit cell was used.

The projector augmented wave (PAW) method [51] was applied in the computations. The generalized gradient approximation with Hubbard U (the so-called GGA+U method) [221] exchange-correlation functional by Perdew, Becke and Ernzerhof, abbreviated as PBE [222], was used. The values of U and J parameters were: U_{Tb}=7.7 eV, U_{Ce}=6.7 eV and J=0.7 eV [223]. Brillouin zone integration was performed by using a Γ-centered 8×8×8 k-point grid and Gaussian smearing of 0.05 eV [27]. The kinetic energy cutoff of 520 eV and the total energy convergence threshold of 10^{-6} eV were used [27]. The system was relaxed in a ferromagnetic state, according to normal ferromagnetic occurrence of both CeF_3 and TbF_3 [223]. One, two or three cerium atoms were substituted in the unit cell (16.67%, 34.33% and 50% of the dopant, respectively). An undoped system was modeled as well [27]. Two kinds of relaxation were performed: a full relaxation of crystal cell shape and atom positions (ISIF=3) or a relaxation of cell dimensions only (ISIF=7) [27].

5.1.3. The experimental samples of $CeF_3:Tb^{3+}$

Two methods, namely the hydrothermal one and co-precipitation were used to prepare the samples [27]. The details of their synthesis procedure can be found in [71,224]. The amount of dopant in both hydrothermal and co-precipitation samples varied as 0.00, 4.17, 8.33 and 12.5%.

Fig. 36 presents the powder X-ray diffraction patterns of the obtained $CeF_3:Tb^{3+}$ materials. They match the reference pattern obtained from the database. Rietveld refinement was used to analyze the data. The procedure was finished with the R_w value of 3-4% for hydrothermally obtained materials and 9-12% for co-precipitation products [27]. The patterns were consistent with P-3c1 CeF_3 phase. Although no impurity phases were detected, a shift of the pattern toward higher values of 2Θ was noticed. The shift increased with increasing amount of the dopant. On the other hand, the peaks in the XRD patterns of both doped and non-doped samples were of the same width [27], thus, the doping did not cause their broadening. It can be concluded, that Tb^{3+} ions enter the main phase and do not form a separate compound. Moreover, they have a direct effect on crystal structure of the matrix compound. The refinement provided the values of lattice vectors of the samples. The peaks in the XRD patterns of the samples obtained via co-precipitation route were noticeably broader than those in the patterns of the hydrothermally obtained samples. The respective widths at half-maximum for the two methods were about 0.5-0.8° and 0.1° of 2Θ [27].

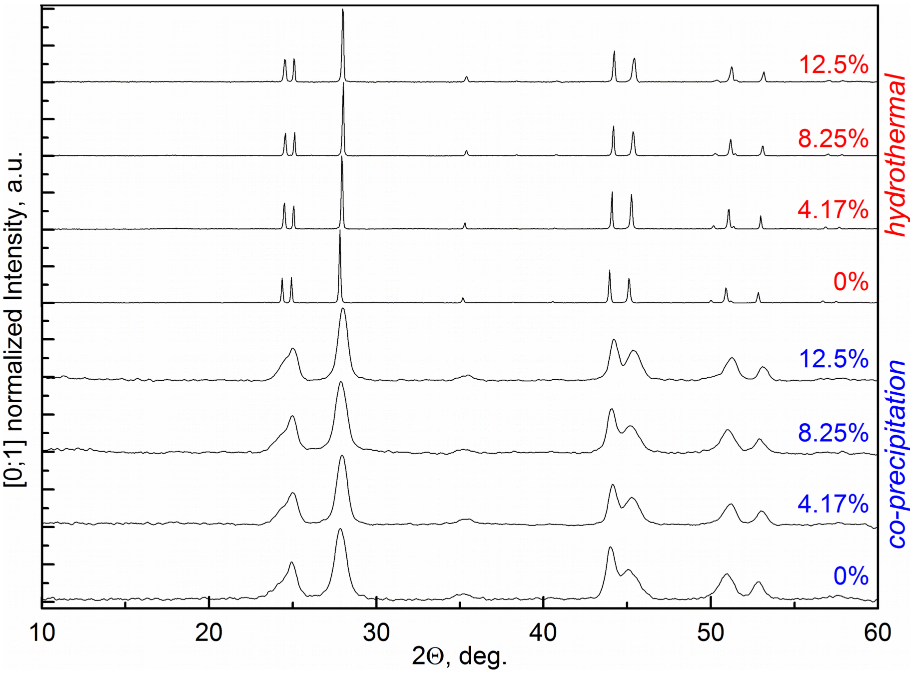

Fig. 36. XRD patterns of the CeF_3:Tb^{3+} samples obtained by the hydrothermal (top) and co-precipitation (bottom) methods

As the ionic radii of Ce^{3+} and Tb^{3+} are not the same [2], some distortions in proximity of the dopant ions might occur. The distortions did not seem significant according to XRD, and were neglected in the semi-empirical computations [27]. In contrast, the DFT computations were performed either with or without constrains on atom positions [27]. The latter option should have reproduced the changes in the coordination geometry of Tb^{3+} ions, in relation to the original geometry. This option had some effect on the lattice parameters as well. Although the effect was small, relaxation of the lattice vectors only resulted in lower error (0.91% vs. 1.16%) [17]. Thus, it was reasonable to neglect the distortions in the coordination geometry. The DFT results presented in section 5.1 were obtained via relaxation of the lattice vectors only.

5.1.4. Spectroscopy features of the of CeF_3:Tb^{3+} samples

Detailed descriptions of photoluminescence properties of CeF_3:Tb^{3+} phosphors can be found in the following references: [71,224]. Here, a brief description is provided.

The excitation spectra of the CeF_3:Tb^{3+} samples consisted mostly of Ce^{3+} f-d bands (225-300 nm). Thus, the excitation energy absorbed by Ce^{3+} ions was transferred to Tb^{3+} ions (Fig. 37, left). The bands of Tb^{3+} f-f transitions were relatively weak and almost unnoticeable [27].

Excitation of the CeF_3:Tb^{3+} phosphors in the ultraviolet region results in bright emission of the visible light. The emission color is green. The emission spectra are shown in Fig. 37, right. The peaks bands of $^5D_4 \rightarrow {}^7F_{6,5,4,3}$ transitions of Tb^{3+} can be noticed at 490, 544, 585 and 624 nm respectively.

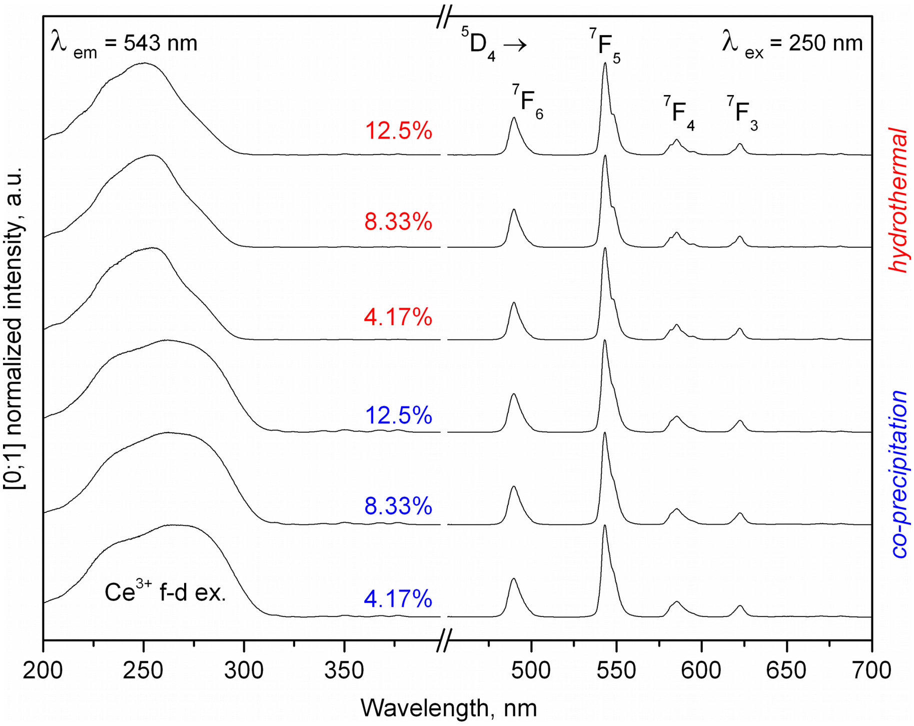

Fig. 37. Excitation (left) and emission (right) spectra of CeF_3:Tb^{3+} obtained by hydrothermal or co-precipitation methods

The amount of dopant had a small effect on the spectral shape of both excitation and emission of the samples. On the other hand, the spectra of the samples obtained by co-precipitation and hydrothermal methods are apparently not the same. In particular, the relative intensities of the f-d excitation bands were not the same and depended on the synthesis procedure. The band component at about 250-260 nm was apparently more intense for the CeF_3:Tb^{3+} samples obtained by the co-precipitation route. As a result, the shape of the f-d band was different. The samples were characterized by the same crystal structure and differed significantly in the particle size. Thus, most likely, one may speak of the effect of nanocrystallinity on photoluminescence in this case.

The photoluminescence decay curves (not shown) were obtained under the conditions of 250 nm excitation and 543 nm emission. As the amount of dopant increases, the photoluminescence lifetimes decrease from 4.90 to 4.29 ms for the hydrothermal products, and from 5.35 to 5.04 ms for the samples obtained by co-precipitation [27]. Most probably, the cross-relaxation decay processes are responsible for this phenomenon. However, the intensity of cross-relaxation remains low: the decay curves remain mono-exponential for all samples [27].

5.1.5. The computational results

The electronic structure of the studied CeF_3:Tb^{3+} materials is not discussed in this section. On the one hand, this section is strictly focused on the structural aspects. On the other hand, semi-empirical methods are not a good tool for electronic structure analysis, even provided that the geometry is represented correctly.

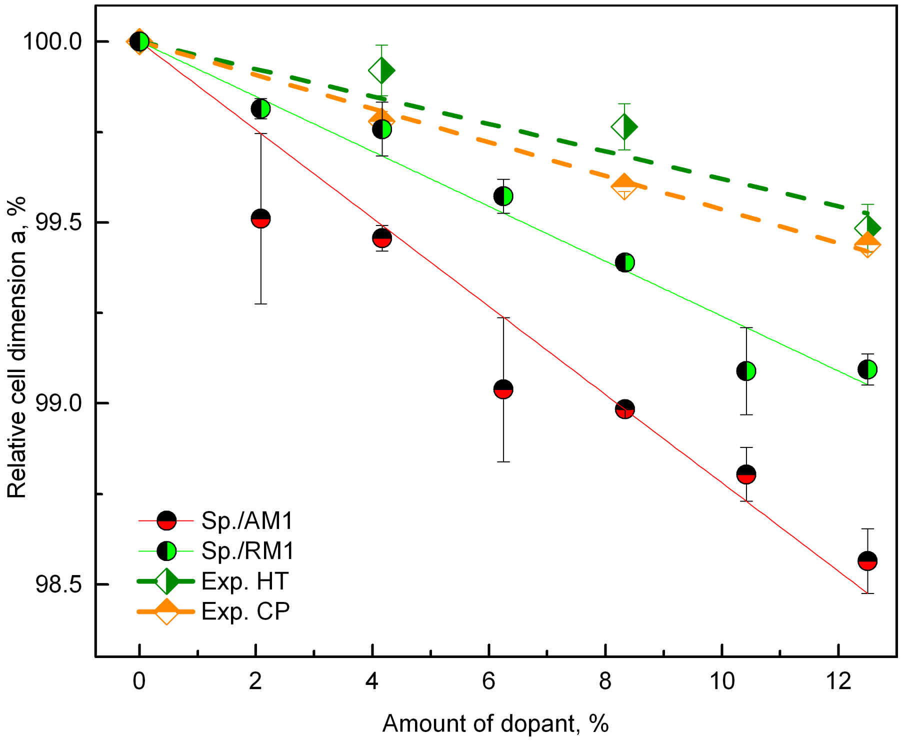

Fig. 38. Changes in the cell dimension *a*, experimental and computed by Sparkle/AM1, and Sparkle/RM1 semi-empirical methods; "Sp." stands for "Sparkle

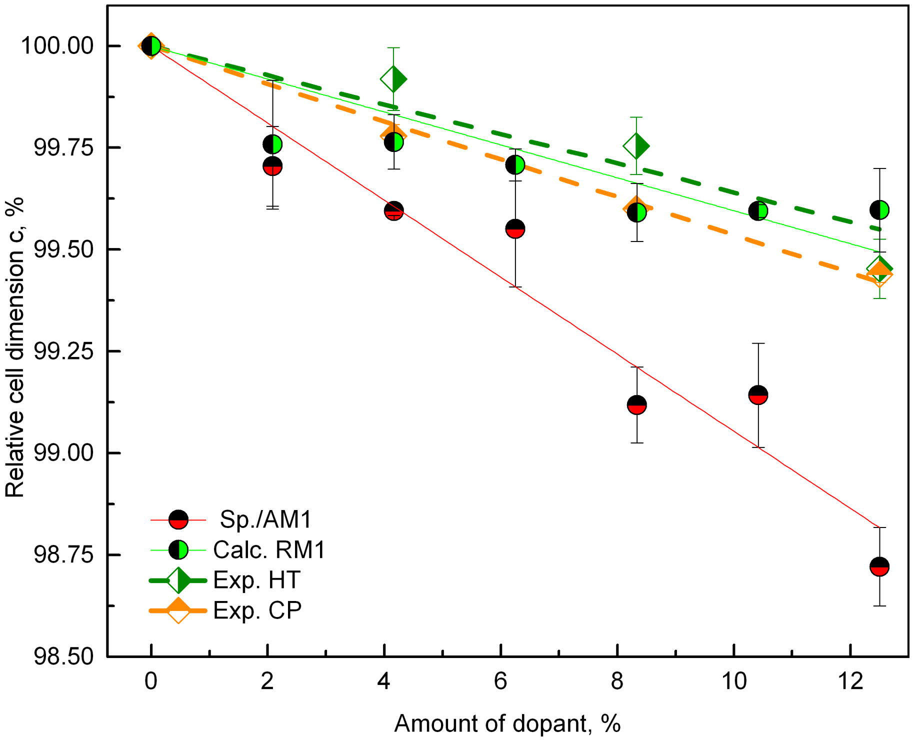

Fig. 39. Changes in the cell dimension *c*, experimental and computed by Sparkle/AM1, and Sparkle/RM1 semi-empirical methods; “Sp.” stands for “Sparkle

The optimization of structures with the same amount of the dopant and different particular locations of the dopant ions resulted in the same length of the lattice vectors. The energies of these structures were very similar. The differences in these energies are three orders of magnitude lower than those caused by the change in the doping rate [27]. In other words, the crystal cell dimensions depended mostly on the amount of the dopant, while the particular locations of the dopant ions cause only slight differences in total energy and heat of formation of the system [27].

The values of the lattice vectors were expressed in percent: the values of lattice vectors of the dopant-free samples was taken as 100%. Both experimental and computational data points are supplied with linear fits. The intercepts of the fit lines were set to 100% [27].

According to both experimental and theoretical results, an increasing amount of dopant caused a decrease in the cell dimensions (Fig. 38-43). It was not surprising, as the radius of the dopant ion (Tb^{3+}) is smaller than the radius of the lanthanide ion of the matrix (Ce^{3+}) [2]. Different computational methods provided results characterized by different degree of agreement with the experiment for CeF_3:Tb^{3+}.

In the figures, the computational methods were grouped according to their origins. The PM3, PM6 and PM7 methods were all developed by J.J.P. Stewart and the newer versions are the extensions and revisions of the older. The RM1 method is a modern modification of the AM1 method. All of the methods were used in combination with the Sparkle model providing

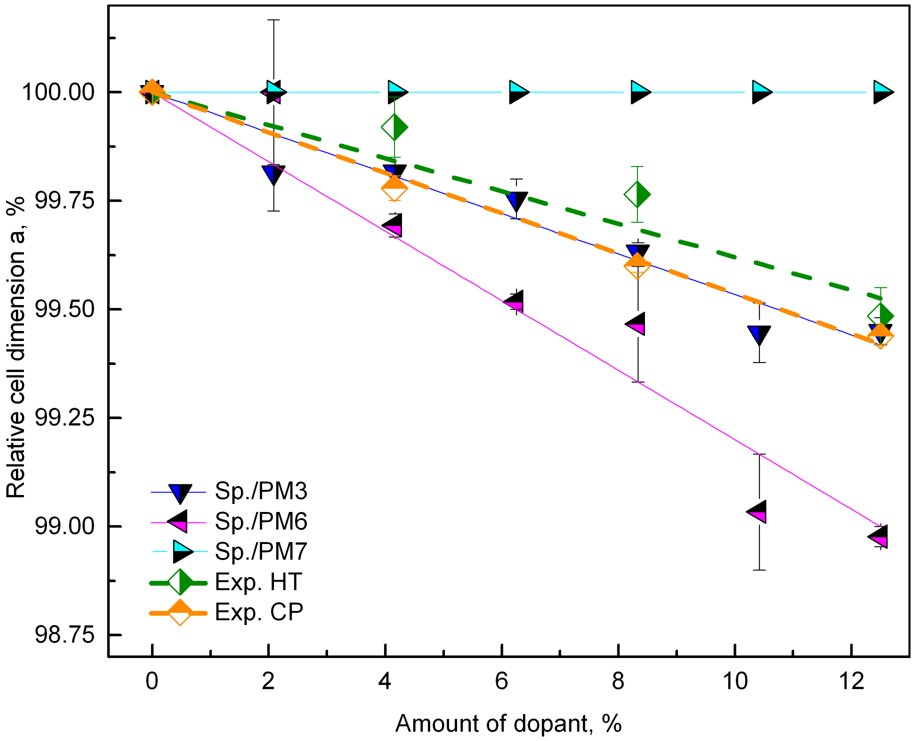

Fig. 40. Changes in the cell dimension *a*, experimental and computed by Sparkle/PM3, Sparkle/PM6 and Sparkle/PM7 semi-empirical methods; "Sp." stands for "Sparkle

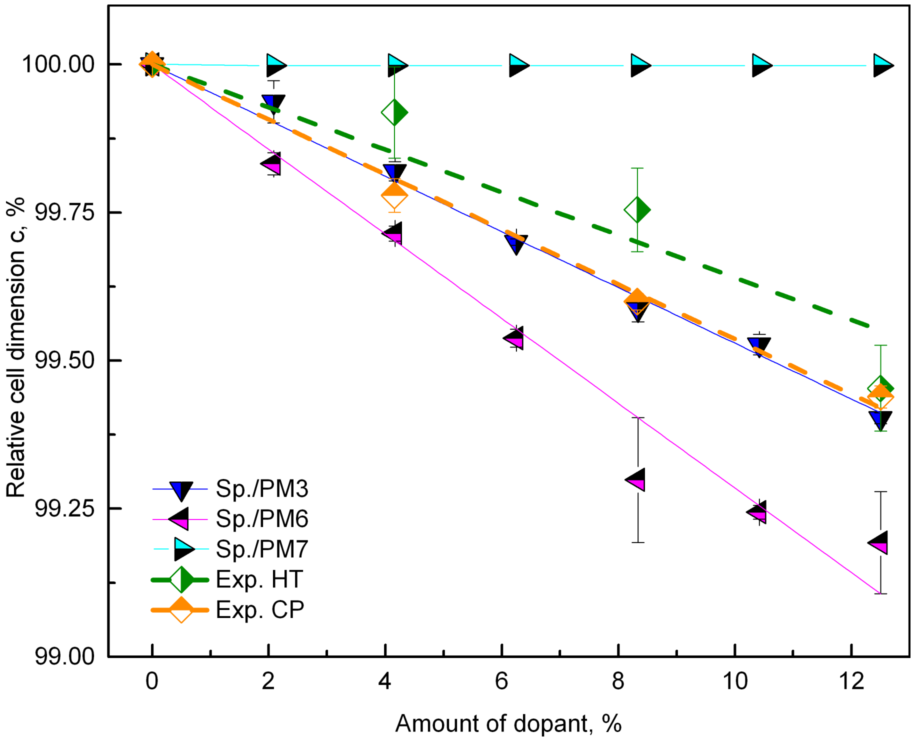

Fig. 41. Changes in the cell dimension *c*, experimental and computed by Sparkle/PM3, Sparkle/PM6 and Sparkle/PM7 semi-empirical methods; "Sp." stands for "Sparkle"

parameterization for Ln^{3+} ions. As the Sparkle models for all of the methods originate from the same research group, the errors introduced by the model should be similar in all of the computations by the semi-empirical methods. Thus, the quality of results would depend mostly on the respective semi-empirical method and not on the Sparkle model.

Comparison of the results obtained with the use of PM models shows that those based on Sparkle/PM3 model gave results in the best agreement with the experiment (Fig. 40-41) [27]. All of the other methods resulted in rougher trends as well as higher deviations from the experiment. Although the Sparkle/RM1 results were not as good as those of Sparkle/PM3, the improvement of RM1 over AM1 method is clear. The same observations are confirmed with the values of absolute error of prediction of cell dimensions (in relation to the experiment) collected in Table 3 below.

Among the semi-empirical methods applied, the computations by Sparkle/PM7 resulted in the lowest error [27]. On the other hand, the results suggested that cell dimensions of $CeF^3:Tb^{3+}$ did not change, no matter how many Tb^{3+} ions were added. The latter conclusion is apparently incorrect, indicating a problem with the Sparkle/PM7 method. Presumably, the origin of the error might be PM7 parameterization: Sparkle model works well with all other methods [27].

Quality of the computational results was estimated on the basis of the absolute deviation of the calculated lattice vector values from those obtained in the experiment. Although there were two experimental references obtained by two methods, the values of lattice vectors from the two were very close (for the same doping rate). The mean values of the lattice vectors for the samples doped by 0.00, 4.17, 8.33% and 12.5% Tb^{3+} were used as a reference. In DFT computation, the minimal amount of dopant was 16.(6)%, thus the appropriate values for comparison were found as points on the fit line (Fig. 41-42) [27]. The obtained values of absolute errors are shown in Table 3.

Table 3. Mean deviations of the calculated absolute values of cell dimensions of $CeF_3:Tb^{3+}$ from the experimental ones (averaged by the amounts of dopant)

	a err., %	*c* err., %	mean err., %
GGA+U/PAW/PBE	1.09	0.72	0.91
Sparkle/AM1	3.34	3.38	3.36
Sparkle/RM1	2.49	3.13	2.81
Sparkle/PM3	1.17	1.76	1.46
Sparkle/PM6	4.14	4.01	4.08
Sparkle/PM7	1.84	0.30	1.07

According to the data from Table 3, the error provided by Sparkle/AM1 and Sparkle/PM6 methods was rather high, while the error in Sparkle/PM3 calculations was relatively small. Sparkle/PM3 computations were in the best agreement with the experiment from among the data provided by all semi-empirical methods applied (average deviation for two axes of 1.46%), while the error was comparable to that of the DFT computations (deviation of 0.91%).

Using the obtained data, it was possible to describe the dependence of cell dimensions (in percentage of the value for non-doped system) of $Ce_{(1-x)}Tb_xF_3$ on the value of x [27] (the values in brackets are the Pearson correlation coefficients):

$$a'_x = 100 - 4.124 \cdot x \ (0.79677) \tag{5.1.1}$$

$$c'_x = 100 - 4.375 \cdot x \ (0.79657) \tag{5.1.2}$$

$$a'_x = 100 - 4.658 \cdot x \ (0.89062) \tag{5.1.3}$$

$$c'_x = 100 - 4.707 \cdot x \ (0.89049) \tag{5.1.4}$$

where Eqs. 5.1.1-2 represent the GGA+U/PAW/PBE results, while Eqs. 5.1.3-4 represent the Sparkle/PM3 results; a'_x and c'_x are relative dimensions (in %) at the amount of dopant x [27]. The equations were obtained from the linear fits mentioned above.

Table 4. Cell dimensions of non-doped CeF_3 samples, both experimental and calculated

	Cell dimension *a*, Å				Cell dimension *c*, Å			
Amount of dopant, %	0.00	4.16	8.32	12.5	0.00	4.16	8.32	12.5
Experimental HT	7.14	7.13	7.12	7.10	7.30	7.29	7.28	7.26
Experimental CP	7.14	7.13	7.12	7.11	7.30	7.28	7.27	7.26
GGA+U/PAW/PBE	7.22	7.21	7.20	7.18	7.35	7.34	7.33	7.31
Sparkle/AM1	7.42	7.38	7.34	7.31	7.58	7.54	7.51	7.48
Sparkle/RM1	7.33	7.32	7.29	7.27	7.53	7.51	7.50	7.50
Sparkle/PM3	7.23	7.21	7.20	7.19	7.43	7.42	7.40	7.39
Sparkle/PM6	7.45	7.43	7.41	7.38	7.61	7.59	7.55	7.55
Sparkle/PM7	6.99	6.99	6.99	6.99	7.26	7.26	7.26	7.26

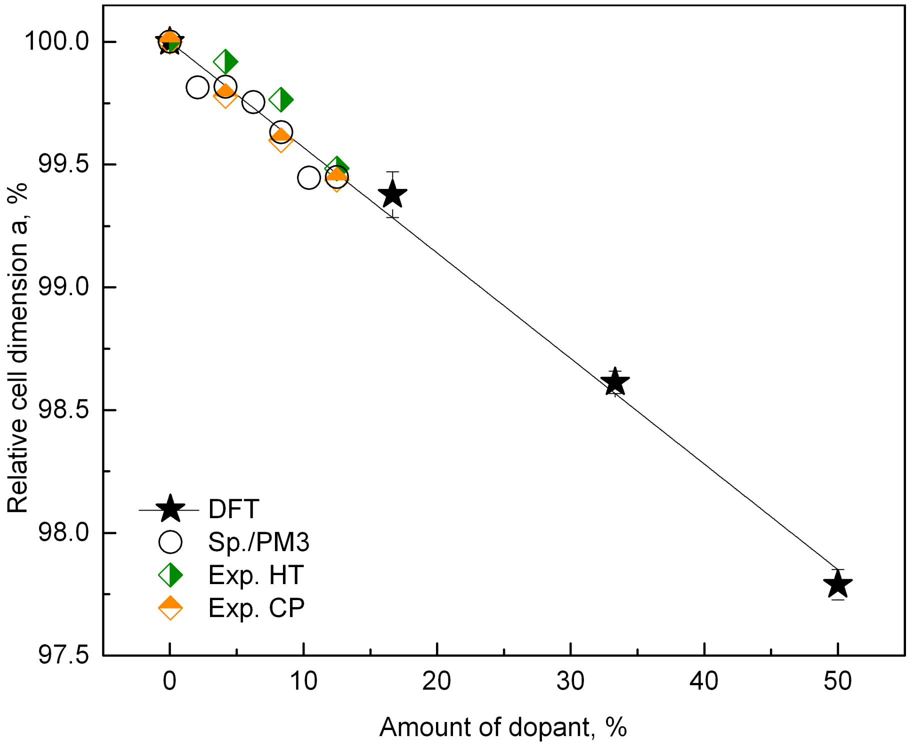

Fig. 42. Changes in the cell dimension *a*, both experimental and computed (Sparkle/PM3, DFT); “Sp.” stands for “Sparkle

The computations using semi-empirical methods required significantly shorter computation times. In particular, the relaxation of a unit cell of $CeF_3:Tb^{3+}$ in VASP via GGA+U/PAW/PBE lasted about a day, while the relaxation of any of the 2×2×2 supercell of $CeF_3:Tb^{3+}$ using Sparkle/PM3 was completed within minutes to tens of minutes. Both kinds of computations were performed on modern supercomputers and applying a comparable computational power per task. Considering the agreement of the result obtained by this method, Sparkle/PM3 is a reasonable choice when large lanthanide fluoride systems are to be modeled [27].

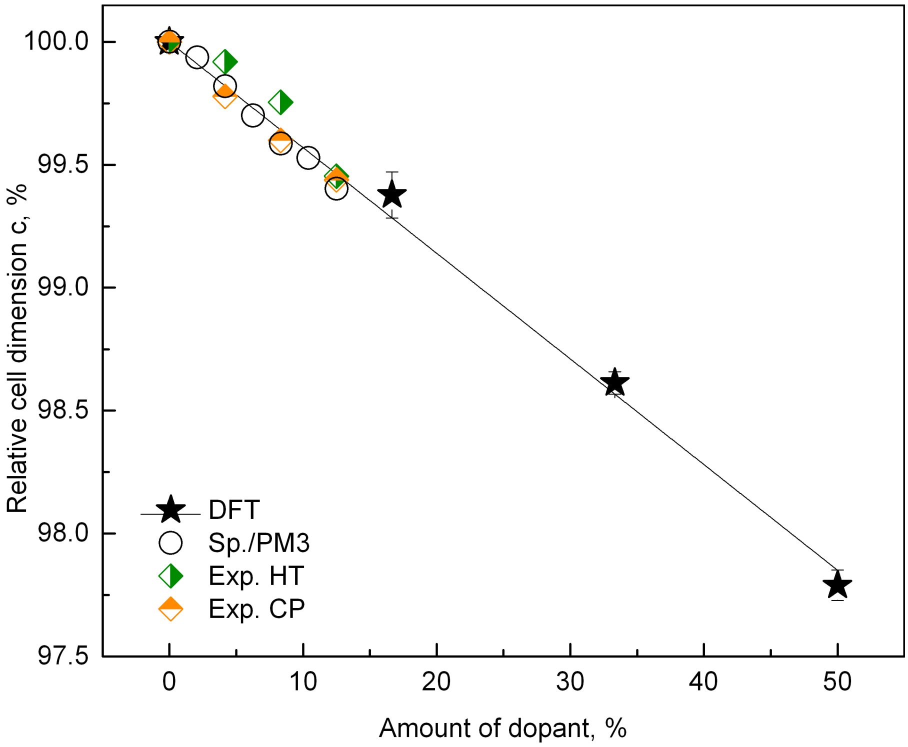

Fig. 43. Changes in the cell dimension *c*, both experimental and computed (Sparkle/PM3, DFT); "Sp." stands for "Sparkle

5.2. Computational studies on the effect of doping on crystal structure of $Sr_3La_2(BO_3)_4$:Tb^{3+}

In order to compare the computational and the experimental results of the studies of the effect of dopant concentration on the SLB:Tb^{3+} system, a new series of samples was synthesized. The series was required to provide the samples with the amounts of Tb^{3+} dopant matching those in the computations. The particular dopant contents were dictated by the used supercells sizes. See the following sections for details.

The samples of $Sr_3La_{2-x}Tb_x(BO_3)_4$ were obtained as described in Section 4.1.

The values of x were 0.125 (6.25%), 0.25 (12.5%), 0.5 (25%, 0.75 (37.5%) and 1 (50%). As the synthesis of 50%-doped sample failed repeatedly without obvious reason, this sample was not included in measurements. However, it was taken into account in computations. The samples were characterized by means of X-ray diffraction, spectrofluorimetry under continuous lamp excitation and photoluminescence decay measurements under pulsed laser excitation.

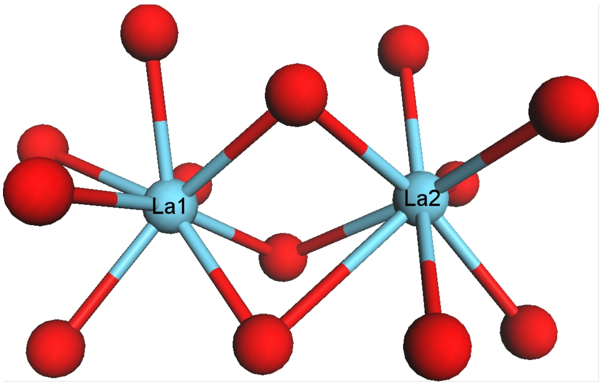

Fig. 44. The coordination geometries of the two La sites in SLB

5.2.1. Details of computational studies on $Sr_3La_2(BO_3)_4$:Tb^{3+}

As Sparkle/PM3 method was found optimal in the previous section, it was applied for a computational study on SLB:Tb^{3+}. Again, MOPAC2012 was used as a subroutine. The initial geometry was acquired from the ICDD database. A supercell of two unit cells of SLB was the structure studied. An attempt to use a 2×2×2 supercell was made and resulted in much too long time of a single point calculation, lasting about tens of hours. There were three options of constructing a supercell of two unit cells as the unit cell can be replicated along *x, y* or *z* axis. All three options were tested. The respective structures were labeled SLB-x, SLB-y or SLB-z. Each of them contains 16 La^{3+} ions that can be substituted, so the possible amounts of dopant were the multiples of 100%/16. The lowest possible doping rate was 6.25%. The experimental samples were prepared with matching percentage contribution of dopant. Moreover, from among the 16 La positions, 8 corresponded to a crystallographic site named La1 and another 8 to the site La2. Both are 8-coordinated low-symmetry sites and are not identical. The coordination geometries of these positions are shown in Table 5. See Fig. 44 for the visualization of the structure.

Table 5. The Cartesian coordinates of La coordination surround in SLB, ICDD

	La1 site, x, y, z, Å			La2 site, x, y, z, Å		
La	0.000	0.000	0.000	0.000	0.000	0.000
O	0.055	-2.299	-0.764	-2.526	0.348	0.868
O	0.206	2.614	-0.460	1.104	0.348	-2.842
O	-0.386	0.000	-2.486	1.440	-1.571	-1.573
O	2.213	-0.992	0.245	-1.212	-2.100	-0.690
O	2.432	1.340	0.341	1.414	-1.240	1.618
O	-0.895	-1.142	2.122	-1.054	1.655	-1.833
O	-0.974	1.241	1.825	-0.369	1.655	1.877
O	-2.450	0.099	-0.579	2.055	1.505	0.045

Similarly as for CeF_3, it does not make sense to perform the calculations for all possible structures produced by various combinations of dopant ion positions. A random substitution procedure was applied producing ten randomly substituted input structures of each amount of the dopant. It should be emphasized that two groups of structures were produced. In the structures of one of the groups the dopant ions were at La1 sites only, while in the structures of the other group only La2 positions were substituted. For one dopant ion per supercell (6.25% Tb^{3+}) there was no need for randomization: there were only 8 available options of locating one Tb^{3+} ion at La1 site and another 8 for La2 site. Similarly, for 50% doping rate (8 Tb^{3+} ions per a supercell) there was only one option where all La1 positions contain Tb^{3+}, and another one of La2 positions filled with Tb^{3+}.

5.2.2. Optimization of the lattice vectors of $Sr_3La_2(BO_3)_4$:Tb^{3+} supercells

In order to optimize the dimensions of the supercells, two different procedures were applied: the one used for CeF^3:Tb^{3+} and a new one. In both methods, the cell dimensions were modified in order to minimize the total energy of the system. In one of the methods, the optimization of the three lattice vectors was performed via three independent relaxation sequences, all starting with the same initial geometry. The optimization was performed in two stages, like previously. In the first stage, the initial values of cell dimensions were those provided by the crystallographic database. In the second stage, the results of the first stage were used as the initial data. The method was called “separate optimization”, SO. In the new procedure, all three lattice dimensions were optimized in parallel, at the same iteration. A simple steepest-descent (SD) algorithm of lattice dimensions optimization was used. The procedure started with a user-defined initial descent step, which was decreased during the optimization as the relaxation process approached the energy minimum. The system was pushed towards its lowest energy according to the negative gradient at a particular state. The algorithm, however, does not have any local minimum detection and would converge to the first minimum found. The optimization software (Python script) used MOPAC2012 as a subroutine to calculate the energy of the system. In the following section, the energy of a system would mean its total energy (electronic energy plus nuclei repulsion energy) calculated by MOPAC2012 (with default settings, as previously). None of the fractional coordinates of atoms were changed.

The geometry of a periodic structure can be separated into fractional coordinates and lattice vectors. In the present study, only the cell linear dimensions were optimized, while the angles were not. In other words, only the length of the lattice vectors was changed. Thus, if the initial geometry is known, all of the following changes can be represented in the form of three lattice vector multipliers m_0, m_1 and m_2, (of coordinates x, y and z respectively) that can be expressed in the vector:

$$\mathbf{M} = \begin{pmatrix} m_0 \\ m_1 \\ m_2 \end{pmatrix} \tag{5.2.1}$$

It should be noted that the multipliers were applied directly to Cartesian coordinates. As the SLB structure is orthorombic, the lattice vectors are mutually orthogonal and co-linear with the principal coordinate axes. Thus, a multiplication of a lattice vector by a scalar is identical to multiplication of every respective Cartesian coordinate by this scalar. Although in its present form the optimization script would work with any orthorhombic system, it can be easily extended to optimize any system. The mathematical procedures would remain the same, with just one exception: the $m_{0,1,2}$ multipliers would apply to lattice vectors (before the conversion of the fractional coordinates to Cartesian).

The optimization goal was to find a set of m_j, j=0,1,2 corresponding to minimal possible total energy of the system. The goal was reached via step-by-step modifications of m_j, so that every step would result in some energy decrease. Here, such modification is referred to as iteration.

The optimization started with the calculation of energy for the input geometry, $\mathbf{M}_0$ = [1, 1, 1]. Then, the so-called cube operation was performed. Its aim was to find out if a particular multiplier m_j should be increased or decreased in order to reach an energy decrease. For this purpose, each m_j was changed consequently by $\pm s$ (where $s \in (0;1)$ was a step in the current iteration) and the energies were collected. The cube procedure can be expressed as a cube matrix $\mathbf{M}_{\text{cube}}$, in which every line describes a separate cube geometry. The respective energies are stored as elements of the $\mathbf{E}_{\text{cube}}$ vector:

$$\mathbf{M_{cube}} = \begin{pmatrix} m_0+s & m_1 & m_2 \\ m_0-s & m_1 & m_2 \\ m_0 & m_1+s & m_2 \\ m_0 & m_1-s & m_2 \\ m_0 & m_1 & m_2+s \\ m_0 & m_1 & m_2-s \end{pmatrix}, \mathbf{E_{cube}} = \begin{pmatrix} E_{m_0+s} \\ E_{m_0-s} \\ E_{m_1+s} \\ E_{m_1-s} \\ E_{m_2+s} \\ E_{m_2-s} \end{pmatrix} \tag{5.2.2}$$

Here, the values of $m_{0,1,2}$ represent the geometry that was an input to the cube operation. The corresponding energy (E_r) is a reference in the cube operation:

$$\Delta\mathbf{E_{cube}} = \mathbf{E_{cube}} - E_r = \begin{pmatrix} E_{m_0+s} - E_r \\ E_{m_0-s} - E_r \\ E_{m_1+s} - E_r \\ E_{m_1-s} - E_r \\ E_{m_2+s} - E_r \\ E_{m_2-s} - E_r \end{pmatrix} = \begin{pmatrix} \Delta E_{m_0+s} \\ \Delta E_{m_0-s} \\ \Delta E_{m_1+s} \\ \Delta E_{m_1-s} \\ \Delta E_{m_2+s} \\ \Delta E_{m_2-s} \end{pmatrix} \tag{5.2.3}$$

$\Delta\mathbf{E}_{\text{cube}}$ contained six elements. The smaller of every two $\Delta E_{m_j \pm s}$ defined the change that was applied to m_j. That is, if $\Delta E_{m_j - s}$ was smaller (more negative) than $\Delta E_{m_j + s}$, $-s$ was applied to m_j at next iteration, or $+s$ if the opposite was true. If the two were equal or positive (that is, no energy-decreasing move was available) m_j remained unchanged. These values formed the iteration vector **I** returned by the cube operation.

$$\mathbf{I} = \frac{1}{\max\left(\left|\Delta E_{s_{0,1,2}}\right|\right)} \begin{pmatrix} \Delta E_{s_0} \\ \Delta E_{s_1} \\ \Delta E_{s_2} \end{pmatrix} \tag{5.2.4}$$

Thus, vector **I** contained three values in the range of [-1; 1], proportional to the energy decreases caused by changes in each m_j multiplier by the value of the step s. It can be said that vector **I** contained the normalized negative gradient of the $E = f(m_j)$ function at $\mathbf{M}_i$ point. The geometry at i+1 (next) iteration was defined as:

$$\mathbf{M}_{i+1} = \mathbf{M}_i + s\mathbf{I}_i \tag{5.2.5}$$

Note that vector $\mathbf{I}_i$ remained unchanged until the next cube operation.

The iterations continued like this until the total energy increased at particular i-th iteration: $E_i > E_{i-1}$. If the energy increased, the geometry was rolled back to the i-1 state, the step s was decreased by half and the cube operation was called with E_{i-1} as a reference energy and the $\mathbf{M}_{i-1}$ input geometry. If there was an energy-decreasing path with the new value of s, it was found by the cube operation and the optimization proceeded to the next iteration. If, however, all of the cube steps resulted in no energy decrease, the step was again reduced by half and another cube operation was called. The overall process continued until s dropped below some predefined limit, or when the iteration count reached a predefined maximum. The energy difference was assumed zero if it was lower than a predefined degree of accuracy. The optimization stopped if the absolute value of the iteration energy change was lower than a particular user-defined value, or if the optimization step was lower than a particular user-defined value.

The optimization of SLB:Tb^{3+} samples was performed with the step limit of 0.0001 and the initial step of 0.005.

5.2.3. The experimental samples of $Sr_3La_2(BO_3)_4$:Tb^{3+}

The powder X-ray diffraction patterns of the obtained materials were consistent with that presented in the database (ICDD card 10213) [210]. Rietveld refinement was applied to the XRD data in order to check the phase purity and obtain the unit cell dimensions. The refinement result was characterized by R_w value of 8%–9%. The patterns are displayed in Fig. 45.

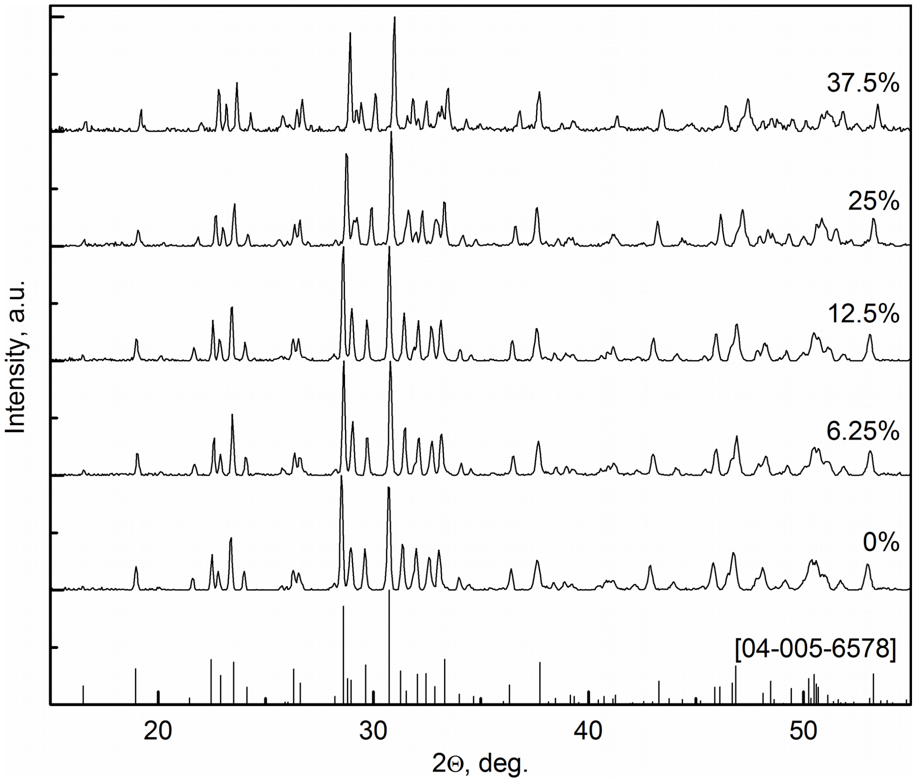

Fig. 45. The XRD patterns of SLB:Tb^{3+} samples

UV-vis excitation spectra of the samples (Fig. 46, $\lambda_{em.}$ = 544 nm, Tb^{3+} $^5D_4 \rightarrow {}^7F_5$ emission peak) indicate the $^7F_6 \rightarrow {}^5G_{5,6}$, $^5H_{6,7}$, $^5I_8$, $^5L_{7\text{-}10}$ f-f transitions of Tb^{3+}. The respective spectral bands were located in the range of 290–400 nm. A band assigned to high-spin f-d transition of Tb^{3+} was located at 220–270 nm and was the most intense. The maximum of the latter shifts from 246 for 6.25% of dopant to 250 nm for 37.5% of Tb^{3+} [210].

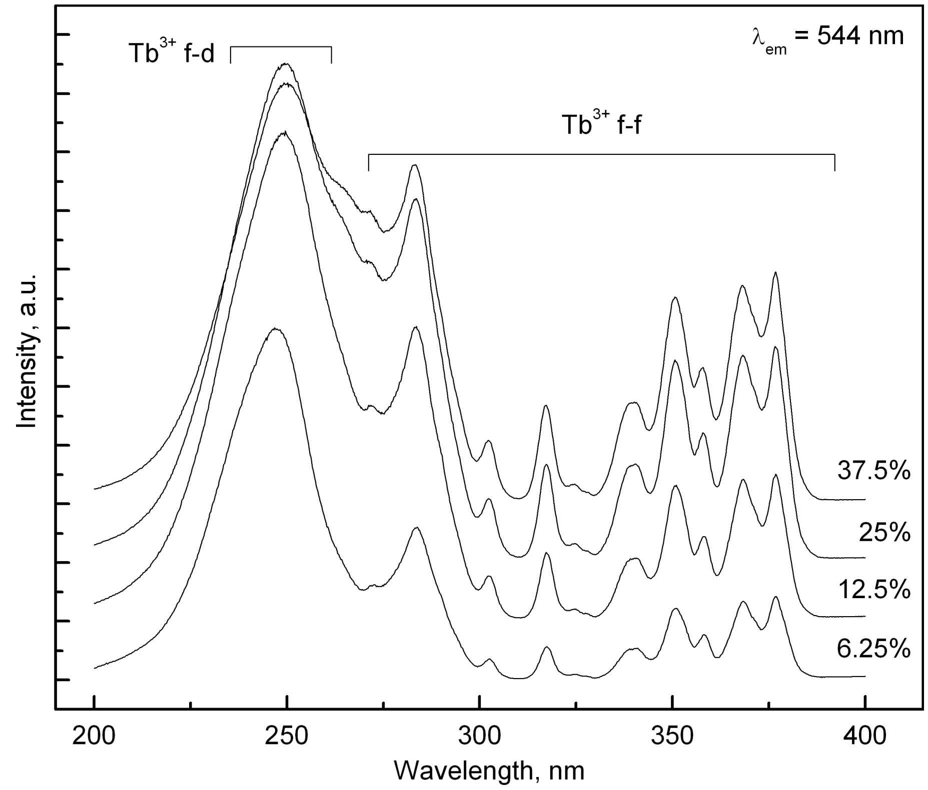

Fig. 46. The excitation spectra of SLB:Tb^{3+} samples

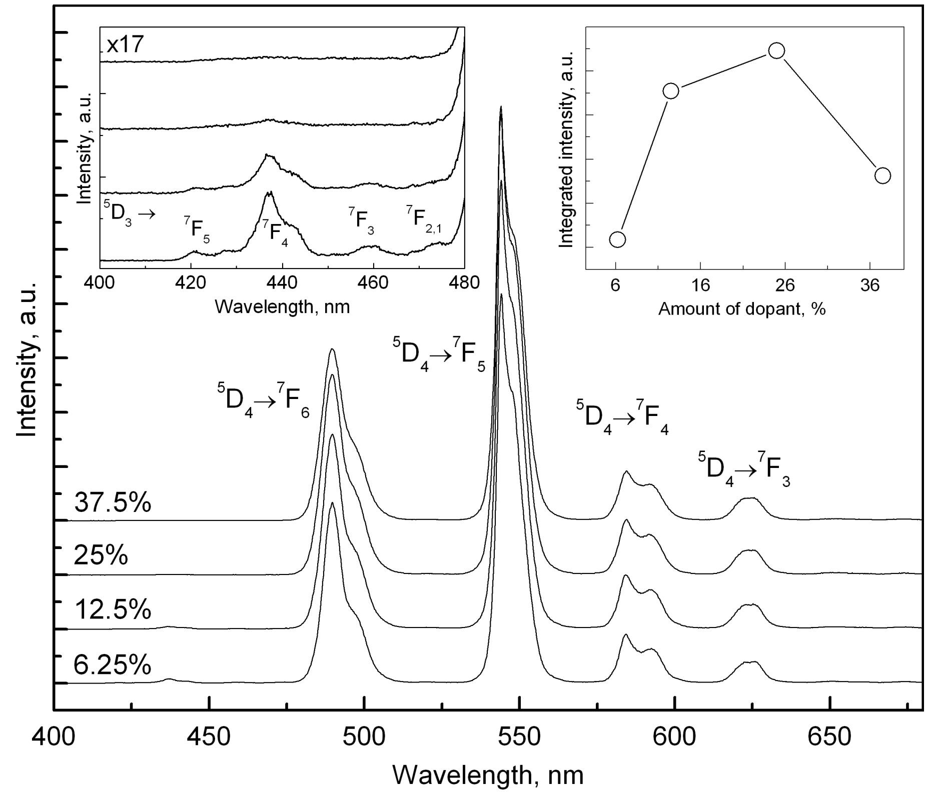

Fig. 47. The emission spectra of SLB:Tb^{3+} samples ($\lambda_{ex.}$ = 248-251 nm)

Excitation of the samples into either f-d band by UV light or into f-f bands (near-UV light) resulted in a bright green emission. The bands of $^5D_4 \rightarrow ^7F_{6,5,4,3}$ transitions of Tb^{3+} were present in the emission spectra (Fig. 47). The dependence of the integrated emission intensity on the amount of dopant [210] is shown on the right inset in Fig. 47. The most intense $^5D_4 \rightarrow ^7F_5$ transition band at 544 nm defined the emission color as green. Very weak emission bands of $^5D_3 \rightarrow ^7F_{5,4,3,2,1}$ transitions were noticeable at 400–450 nm (Fig. 47, left inset). In the spectrum of the sample with 37.5% of dopant the intensity of these bands is comparable with the background noise of the spectrum [210].

The photoluminescence decay curves were obtained via pulsed laser excitation by 250 nm radiation. The emission was collected at 544 nm. The plots are shown in Fig. 48. The curve of 6.25% Tb^{3+}-doped sample can be fitted with a two-exponential relation, while the sample of 37.5% Tb^{3+} with a three-exponential curve [210]. The value of R^2 in both cases is 0.99998. According to the fit results, the evolution of emission intensity in time after the excitation pulse can be expressed as:

$$I = 5.16427 \cdot \exp(-t/\mathbf{1.94076}) + 1.52906 \cdot \exp(-t/\mathbf{0.52192}) + 0.00498 \qquad (5.2.6)$$

$$I = 2.84071 \cdot \exp(-t/\mathbf{1.85217}) + 2.44205 \cdot \exp(-t/\mathbf{0.49684}) + 1.49309 \cdot \exp(-t/0.09155) + 0.00283 \qquad (5.2.7)$$

where t is time and I is the intensity [210]; I_0 was equal to unity as the curves were normalized to the [0;1] range before fitting.

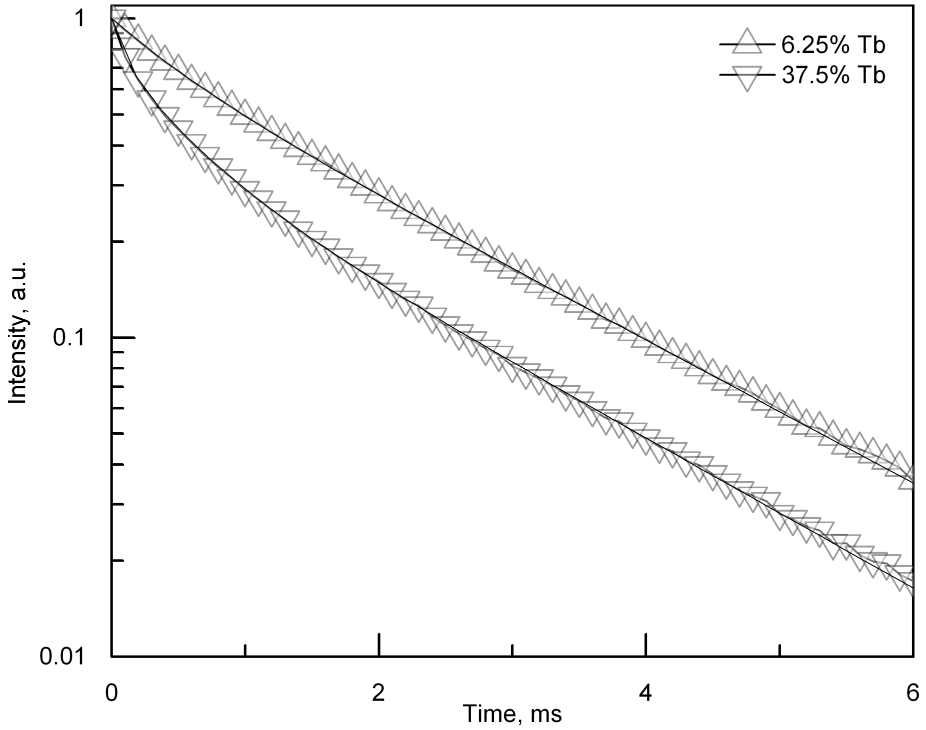

Fig. 48. The emission decay curves of SLB:Tb^{3+} samples

Equations 5.2.6 and 5.2.7 correspond to the 6.25% and 37.5% SLB:Tb^{3+} samples, respectively. Both curves had components of similar lifetimes (shown in bold) while the coefficients before the exponents were different [210]. By assumption, the components of 1.8–1.9 ms represented radiative relaxation of $^5D_4$ level, while those of 0.49–0.52 ms corresponded to the Tb-Tb non-radiative cross-relaxation processes involving higher levels [210]. This idea was supported by the high doping rate of the samples. The third decay component of 91.55 μs lifetime was observed for the 37.5%-doped sample [210]. The lifetime was apparently too short to be a regular radiative f-f transition of Tb^{3+} is SLB. Lifetimes of such an order of magnitude are rather typical of lanthanides in organic complexes in solution. A strong interaction of dopant ions in the near-surface sites with the environment might be responsible for this term. The particles were very likely to contain molecules of adsorbed water, which are known to quench Ln^{3+} emission efficiently [4]. The short-lifetime term was absent in the photoluminescence decay curve of the 6.25%-doped sample, in which the proportional content of dopant ions near surface should be lower and the effect of quenching by particle environment was weaker.

Additionally, an attempt at using the cross-relaxation processes as an indirect luminescence probe was made [210]. It has been found recently [13], that total donor-acceptor energy transfer probability in a solid material depends on the amount of dopant ions, or, more specifically, is a function of donor/acceptor density ρ and the shortest possible donor-acceptor distance R_{min}:

$$P = \frac{4\pi\rho}{3R_{min}^3} \tag{5.2.8}$$

If the amount of dopant is increased from 6.25% to 37.5%, the density should increase appropriately. The increase in the activator density should result in a proportional increase in the cross-relaxation intensity:

$$\frac{P_{37.5}}{P_{6.25}} = \frac{\rho_{37.5}}{\rho_{6.25}} \cdot \frac{R_{min6.25}^3}{R_{min37.5}^3} \tag{5.2.9}$$

Assuming that the dopant ions replace exclusively the La ions (i.e. without inclusions and other defects), the shortest possible distance is defined by the crystal structure (ICDD card 10213) [210]. The database structure lattice vectors should be modified in respect to experimental values of those, so that the changes caused by doping would be taken into account. Next, the changes in the cross-relaxation rate were estimated by the ratio of emission peaks corresponding to transitions from the $^5D_3$ and $^5D_4$ excited states of Tb^{3+} [210]. The transitions from the $^5D_3$ level in SLB:Tb^{3+} were very weak. However, it was possible to make some crude estimation [210]. The relative intensity of transitions from the $^5D_3$ level decreased by the factor of about 14 as a result of the increase in the dopant amount from 6.25% to 37.5%. Only two theoretical values of $P_{37.5}/P_{6.25}$ were close to 14, which corresponded to the occupation of only La1 sites in the sample with 6.25% of dopant, and occupation of La2 or both La1 and La2 in the sample containing 37.5% of dopant [210].

5.2.4. The results of computational studies on $Sr_3La_2(BO_3)_4$:Tb^{3+}

In the following section, the dependence of relative cell dimensions on the amount of dopant is discussed. The relative dimensions show, by how much the linear dimensions of the cell (and the lattice vector length) have changed when particular amount of dopant has been introduced, in respect to the dimensions of the undoped system. The latter has the relative cell dimensions of 100%, by definition. The very same concept of relative cell dimensions has been used previously [27,210].

The experimental data on the cell dimensions of the studied SLB:Tb^{3+} samples are presented in Table 6.

Table 6. Database and experimental data on the cell dimensions of the studied SLB:Tb^{3+} samples

% of dopant	Cell dimensions *a*, *b*, *c*, Å		
ICDD:	8.78	16.54	7.42
Experiment:			
0	8.8947	16.5236	7.4687
6.25	8.8763	16.4875	7.4677
12.5	8.8602	16.4555	7.4697
25	8.8129	16.3375	7.4706
37.5	8.7957	16.2667	7.4711

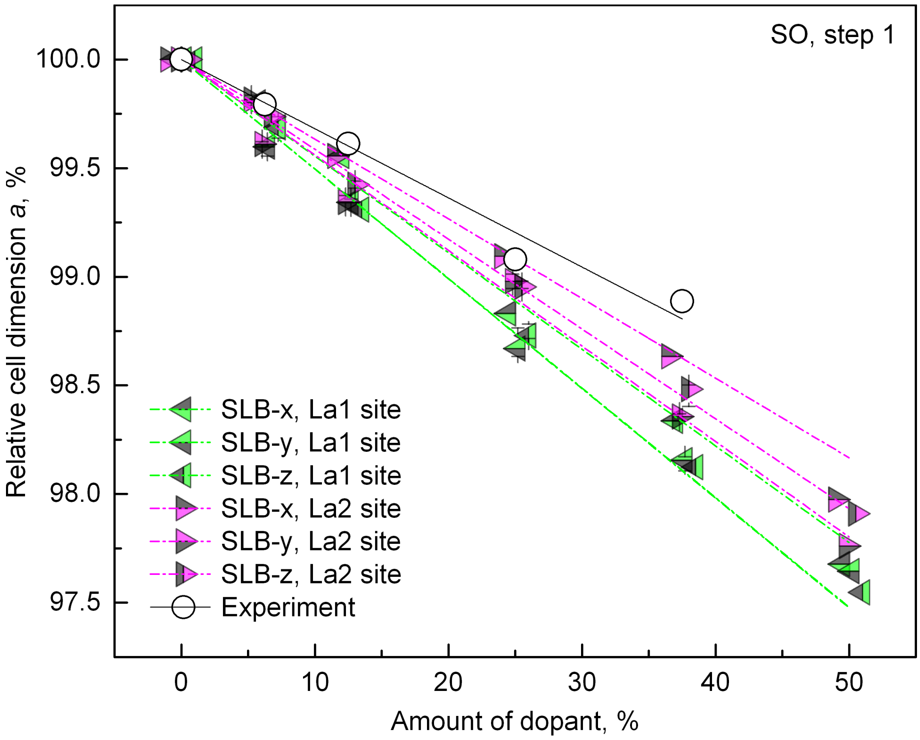

Fig. 49. The effect of the amount of dopant on the cell dimension *a* of SLB-(x,y,z) supercells; single-step SO method; “site” indicates the location of dopant ions

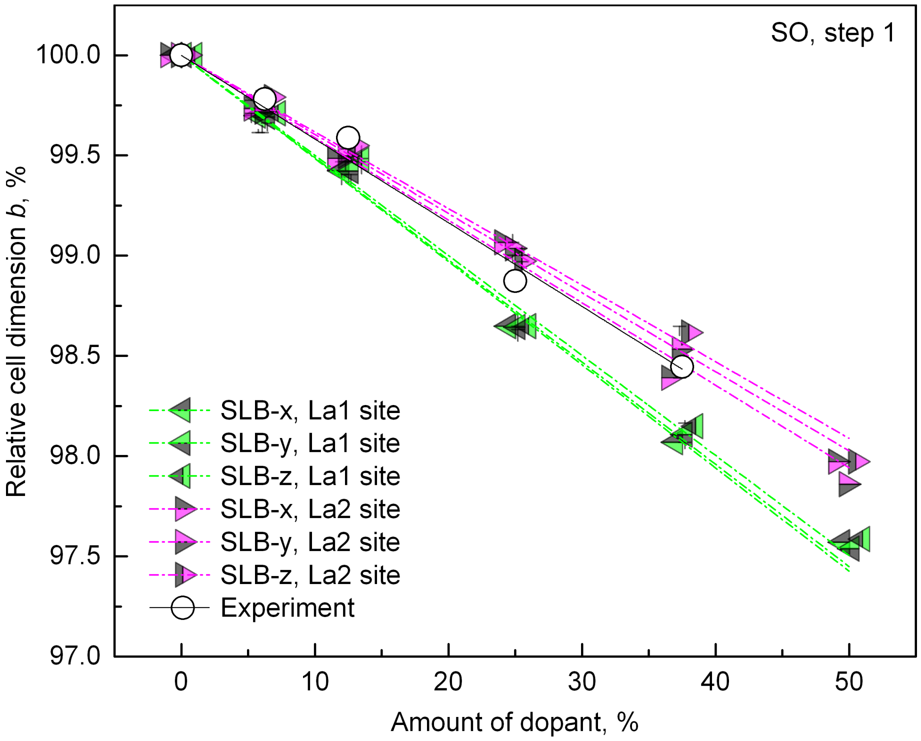

Fig. 50. The effect of the amount of dopant on the cell dimension *b* of SLB-(x,y,z) supercells; single-step SO method; "site" indicates the location of dopant ions

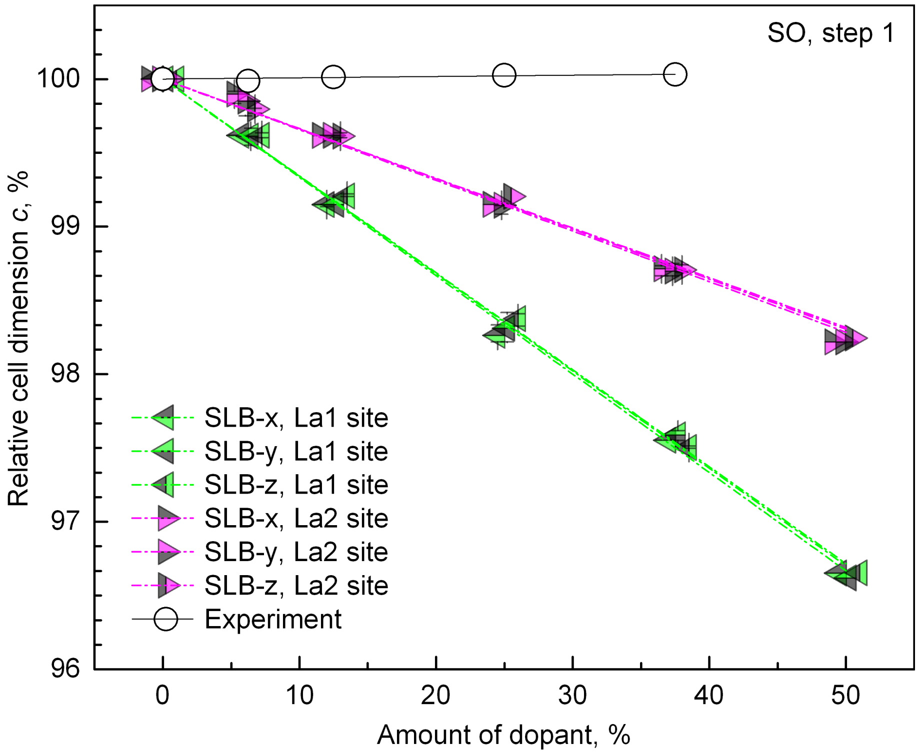

Fig. 51. The effect of the amount of dopant on the cell dimension *c* of SLB-(x,y,z) supercells; single-step SO method; "site" indicates the location of dopant ions

The results obtained by the separate optimization (SO) and steepest-descent (SD) methods are shown in Figures 49-57. In the figures, the data points were supplied with linear fit lines. Small horizontal shifts were applied to the data points. The error bars indicate distributions (minimal and maximal values) of the calculated cell dimensions for the same amount of dopant. The intercepts of the fit lines with the ordinate axis were fixed to 100%. The detailed data on the computed cell dimensions are presented in Tables 7-9.

Apparently, the results provided by both methods agree well with the experiment. The increase in the dopant concentration caused a decrease in the linear dimensions of the supercells, similarly to the CeF_3:Tb^{3+} case. Supposedly, the difference in the ionic radii of La^{3+} and Tb^{3+} [2] is the main cause of this phenomenon. Introduction of dopant exclusively to La1 or La2 sites produces similar but still a bit different changes in the cell dimensions.

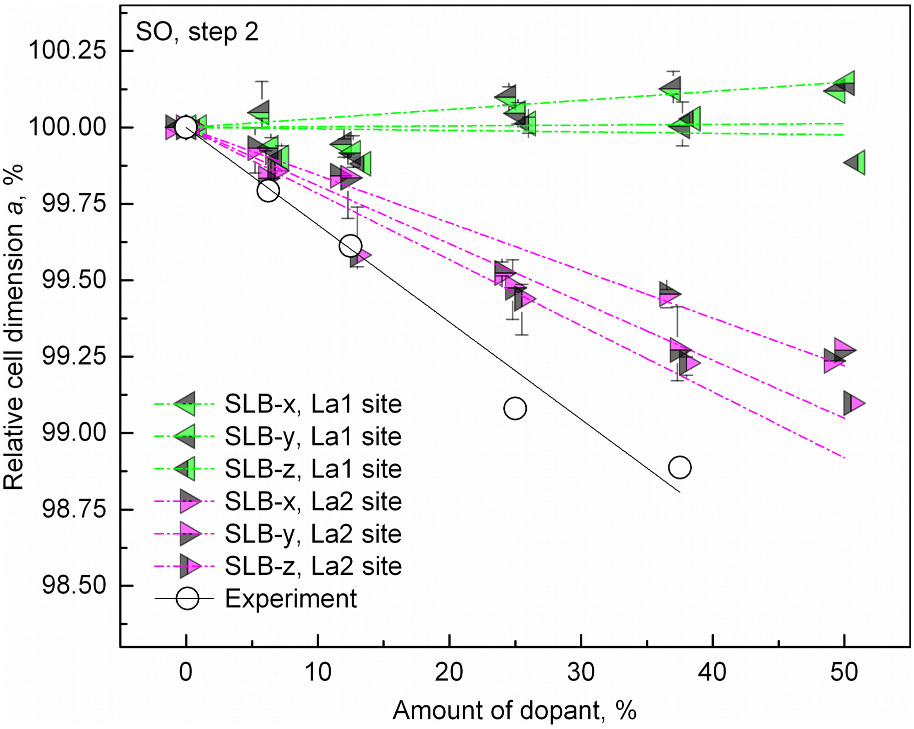

Fig. 52. The effect of the amount of dopant on the cell dimension *a* of SLB-(x,y,z) supercells; double-step SO method; “site” indicates the location of dopant ions

However, some aspects of the results were different. Obviously, the data points produced by the single-step SO method overlap each other very well (for the same amount of dopant). Only several exceptions were found. In other words, the optimization of input structures that differ by particular positions of dopant ions resulted in very similar values of optimized cell dimensions. It can be concluded that in the single-step SO method, the mutual location of dopant ions has had a very small effect on the cell dimensions.

The effect of the different dopant ions locations on the total energy of the samples was negligible. The total energies of the samples containing the same amount of dopant, optimized using single-step SO procedure, varied insignificantly. On the other hand, different random locations of dopant ions provide significant changes to the optimized cell dimensions in both the double-step SO method and the SD method. The results of the latter two methods are much rougher.

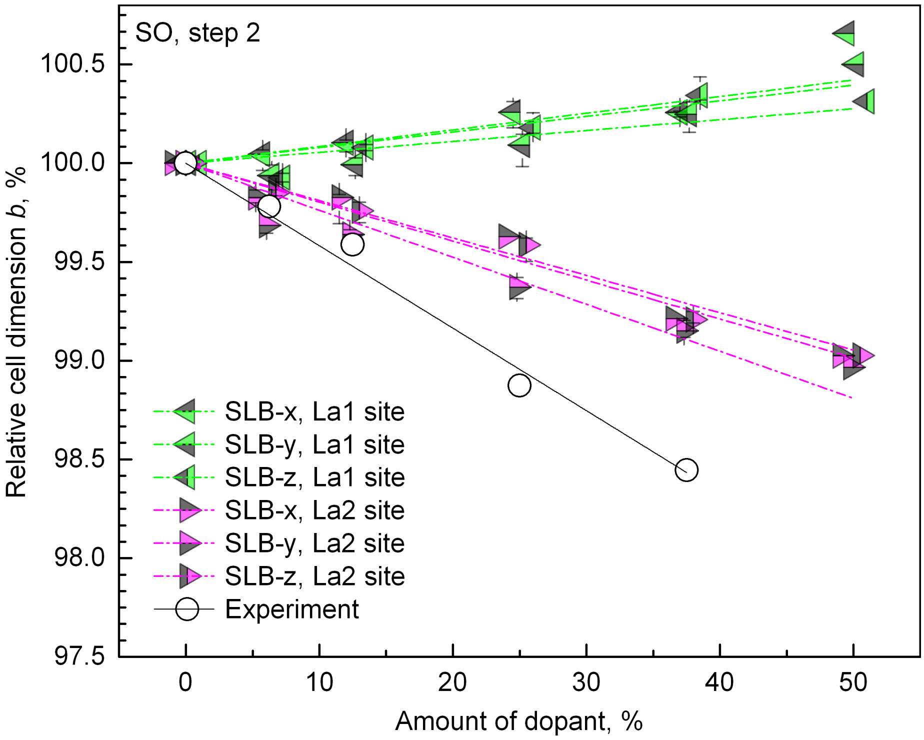

Fig. 53. The effect of the amount of dopant on the cell dimension *b* of SLB-(x,y,z) supercells; double-step SO method; "site" indicates the location of dopant ions

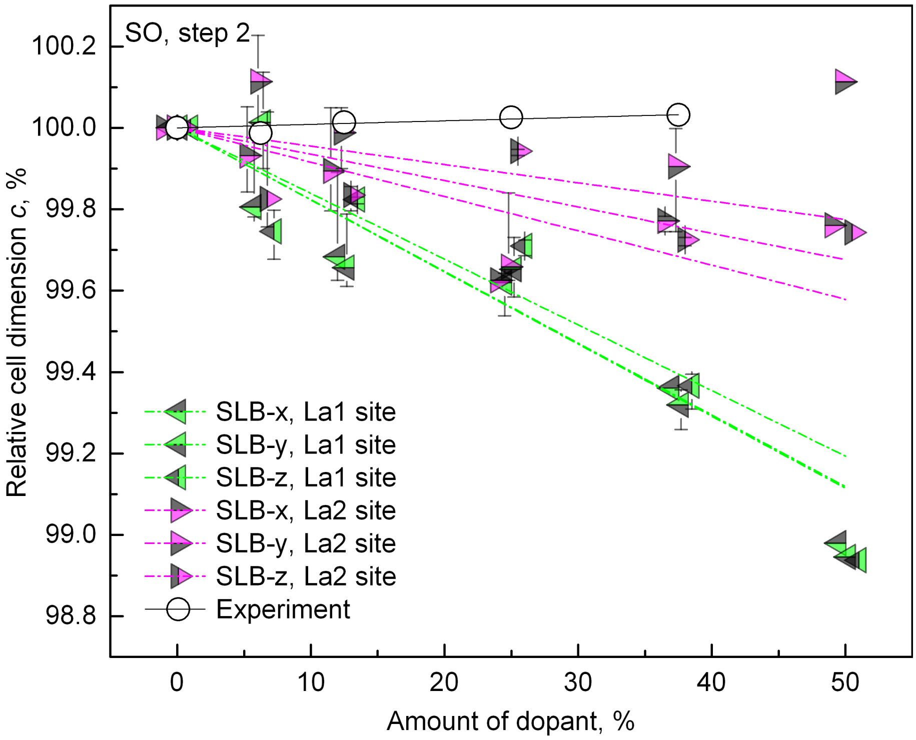

Fig. 54. The effect of the amount of dopant on the cell dimension *c* of SLB-(x,y,z) supercells; double-step SO method; "site" indicates the location of dopant ions

The double-step SO method resulted in better agreement with the experimental data (Tables 7-9). The SD method resulted in an error comparable to that introduced by the single-step SO method. This is an apparent disadvantage of the SD approach. On the other hand, the

SD approach is closer to traditional geometry optimization (*e.g.* BFGS) in which all geometry variables are optimized in parallel. Moreover, the error of about 5% is rather normal and expected for semi-empirical computation. The main advantage of both SO and SD methods is their speed and general agreement of trends. Both are good for basic explanation of the observations and some preliminary general research.

It is obvious, that the computations of structures containing the dopant ions in La2 sites resulted in much better agreement with the experiment than the computations corresponding to the dopant ions in La1 site. Such results suggest a preferred occupation of La2 site by the dopant ions.

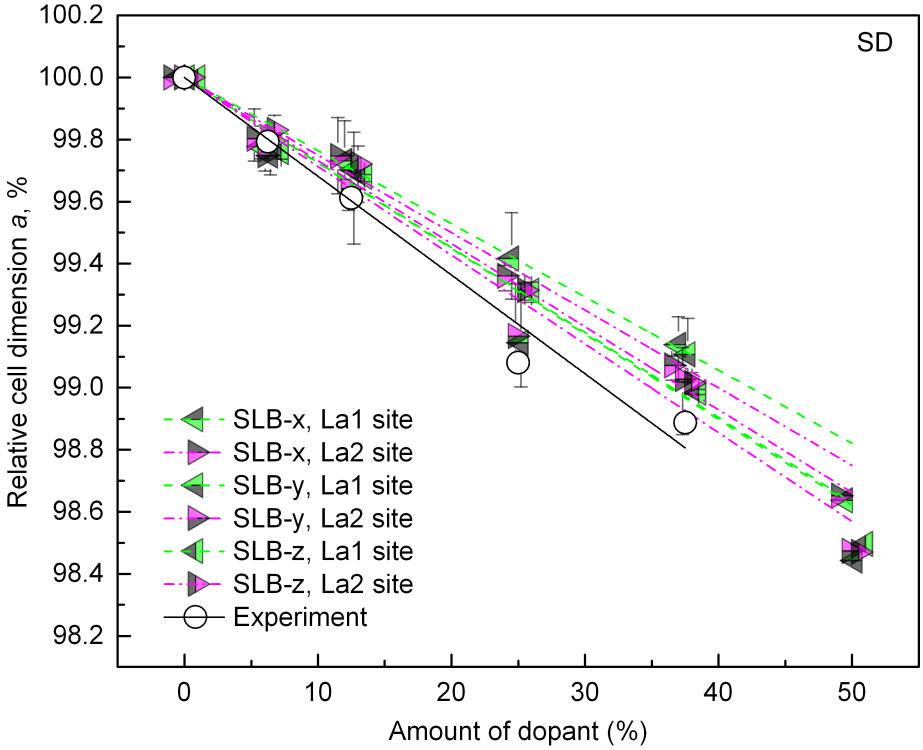

Fig. 55. The effect of the amount of dopant on the cell dimension *a* of SLB-(x,y,z) supercells; SD method; “site” indicates the location of dopant ions

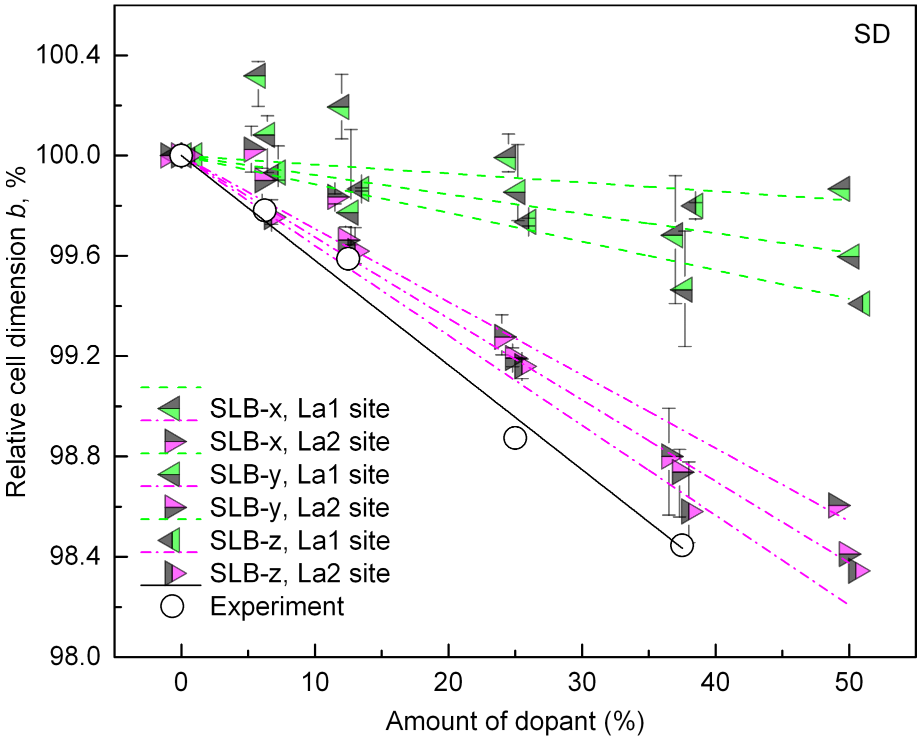

Fig. 56. The effect of the amount of dopant on the cell dimension *b* of SLB-(x,y,z) supercells; SD method; “site” indicates the location of dopant ions

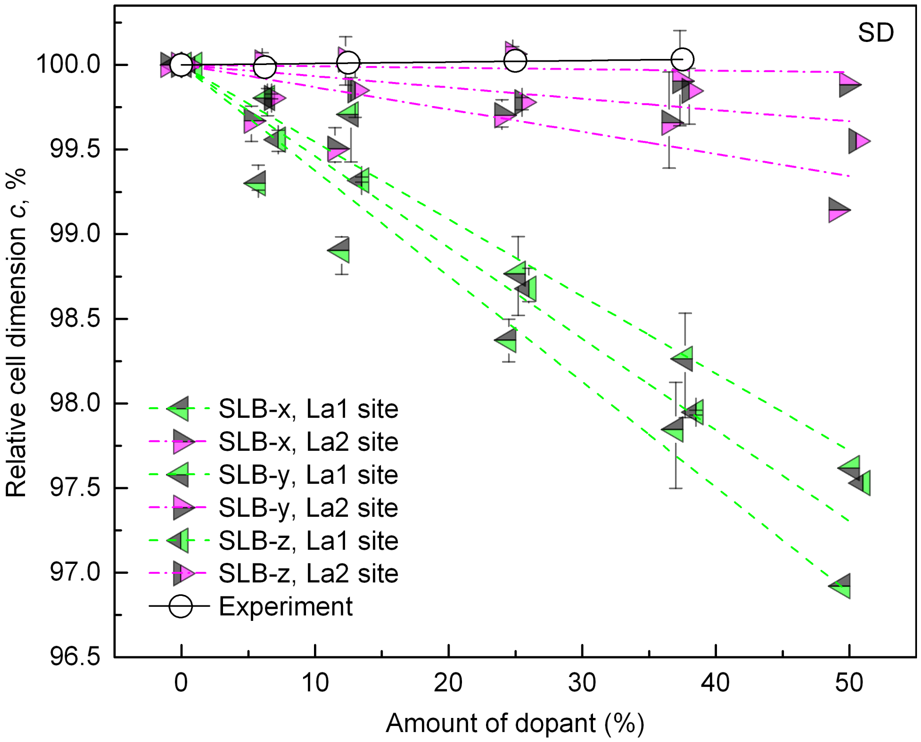

Fig. 57. The effect of the amount of dopant on the cell dimension *c* of SLB-(x,y,z) supercells; SD method; “site” indicates the location of dopant ions

Table 7. The cell dimensions of SLB:Tb^{3+}, obtained by the single-step SO method; SLB-(x,y,z) indicates the type of supercell, La1 and La2 indicate the sites of doping

% of dopant	Cell dimensions *a*, *b*, *c*, Å			Error, in respect to experimental data, %		
SLB-x, La1						
0	8.329	16.054	6.960	-6.364	-2.841	-6.815
6.25	8.312	16.006	6.933	-6.355	-2.922	-7.159
12.5	8.292	15.962	6.900	-6.417	-3.001	-7.620
25	8.231	15.837	6.839	-6.600	-3.063	-8.457
37.5	8.190	15.744	6.789	-6.885	-4.213	-9.126
50	8.135	15.664	6.727	--	--	--
SLB-x, La2						
0	8.329	16.054	6.960	-6.364	-2.841	-6.815
6.25	8.313	16.011	6.953	-6.344	-2.887	-6.897
12.5	8.292	15.971	6.933	-6.417	-2.942	-7.184
25	8.253	15.904	6.901	-6.351	-2.652	-7.630
37.5	8.215	15.796	6.870	-6.605	-2.895	-8.043
50	8.160	15.729	6.836	--	--	--
SLB-y, La1						
0	8.329	16.054	6.960	-6.364	-2.841	-6.815
6.25	8.295	16.005	6.933	-6.546	-2.928	-7.163
12.5	8.274	15.961	6.901	-6.617	-3.003	-7.619
25	8.218	15.836	6.842	-6.753	-3.068	-8.412
37.5	8.175	15.750	6.792	-7.057	-4.175	-9.092
50	8.132	15.659	6.724	--	--	--
SLB-y, La2						
0	8.329	16.054	6.960	-6.364	-2.841	-6.815
6.25	8.296	16.009	6.949	-6.535	-2.903	-6.942
12.5	8.274	15.974	6.933	-6.616	-2.929	-7.184
25	8.244	15.899	6.900	-6.460	-2.682	-7.636
37.5	8.192	15.819	6.869	-6.867	-2.754	-8.058
50	8.142	15.710	6.836	--	--	--
SLB-z, La1						
0	8.333	16.054	6.996	-6.318	-2.841	-6.334
6.25	8.307	16.008	6.969	-6.417	-2.911	-6.680
12.5	8.275	15.970	6.940	-6.603	-2.948	-7.090
25	8.227	15.837	6.882	-6.650	-3.063	-7.878
37.5	8.176	15.757	6.821	-7.041	-4.134	-8.702
50	8.128	15.666	6.761	--	--	--
SLB-z, La2						
0	8.333	16.054	6.996	-6.318	-2.841	-6.334
6.25	8.311	16.021	6.981	-6.371	-2.832	-6.513
12.5	8.285	15.982	6.969	-6.495	-2.879	-6.709
25	8.246	15.889	6.940	-6.438	-2.744	-7.102
37.5	8.206	15.832	6.905	-6.701	-2.673	-7.576
50	8.159	15.729	6.873	--	--	--

Table 8. The cell dimensions of SLB:Tb^{3+}, obtained by the double-step SO method; SLB-(x,y,z) indicates the type of supercell La1 and La2 indicate the sites of doping

% of dopant	Cell dimensions *a*, *b*, *c*, Å			Error, in respect to experimental data, %		
			SLB-x, La1			
0	8.590	16.807	7.270	-3.423	1.713	-2.665
6.25	8.594	16.814	7.255	-4.176	1.981	-2.842
12.5	8.585	16.824	7.247	-4.101	2.240	-2.987
25	8.599	16.850	7.242	-2.431	4.136	-3.060
37.5	8.601	16.850	7.223	-2.214	3.585	-4.318
50	8.600	16.917	7.195	--	--	--
			SLB-x, La2			
0	8.590	16.807	7.270	-3.423	1.713	-2.665
6.25	8.584	16.777	7.265	-4.289	1.758	-2.719
12.5	8.577	16.777	7.262	-4.200	1.957	-2.781
25	8.549	16.744	7.242	-2.991	2.489	-3.055
37.5	8.543	16.674	7.253	-2.869	2.506	-2.919
50	8.525	16.643	7.252	--	--	--
			SLB-y, La1			
0	8.589	16.847	7.270	-3.438	1.956	-2.665
6.25	8.583	16.836	7.271	-4.303	2.115	-2.639
12.5	8.582	16.845	7.245	-4.143	2.370	-3.013
25	8.593	16.862	7.244	-2.497	4.211	-3.028
37.5	8.589	16.888	7.220	-2.347	3.822	-4.359
50	8.601	16.931	7.193	--	--	--
			SLB-y, La2			
0	8.589	16.847	7.270	-3.438	1.956	-2.665
6.25	8.575	16.794	7.278	-4.399	1.857	-2.542
12.5	8.575	16.786	7.269	-4.222	2.008	-2.690
25	8.544	16.741	7.245	-3.053	2.470	-3.022
37.5	8.526	16.704	7.263	-3.063	2.687	-2.789
50	8.526	16.673	7.278	--	--	--
			SLB-z, La1			
0	8.583	16.787	7.305	-3.507	1.592	-2.192
6.25	8.574	16.774	7.286	-3.403	1.739	-2.428
12.5	8.573	16.800	7.292	-4.247	2.093	-2.377
25	8.584	16.817	7.284	-2.599	2.933	-2.501
37.5	8.585	16.844	7.259	-2.393	3.550	-2.843
50	8.573	16.839	7.227	--	--	--
			SLB-z, La2			
0	8.583	16.787	7.305	-3.507	1.592	-2.192
6.25	8.571	16.761	7.292	-3.445	1.662	-2.350
12.5	8.547	16.746	7.293	-3.536	1.766	-2.367
25	8.535	16.717	7.301	-4.158	2.323	-2.273
37.5	8.517	16.654	7.285	-4.173	2.379	-2.492
50	8.505	16.623	7.286	--	--	--

Table 9. The cell dimensions of SLB:Tb^{3+}, obtained by the SD method; SLB-(x,y,z) indicates the type of supercell La1 and La2 indicate the sites of doping

% of dopant	Cell dimensions *a*, *b*, *c*, Å			Error, in respect to experimental data, %		
SLB-x, La1						
0	8.432	16.568	7.097	-5.199	0.267	-4.975
6.25	8.413	16.620	7.047	-5.214	0.806	-5.628
12.5	8.410	16.600	7.019	-5.086	0.877	-6.029
25	8.383	16.566	6.982	-4.877	1.401	-6.545
37.5	8.360	16.515	6.944	-4.958	1.527	-7.052
50	8.317	16.546	6.879	--	--	--
SLB-x, La2						
0	8.432	16.568	7.097	-5.199	0.267	-4.975
6.25	8.416	16.572	7.074	-5.190	0.511	-5.277
12.5	8.411	16.540	7.062	-5.071	0.516	-5.459
25	8.378	16.448	7.076	-4.931	0.675	-5.283
37.5	8.354	16.369	7.073	-5.022	0.628	-5.331
50	8.319	16.336	7.036	--	--	--
SLB-y, La1						
0	8.428	16.611	7.061	-5.248	0.532	-5.463
6.25	8.407	16.625	7.047	-5.291	0.835	-5.636
12.5	8.403	16.574	7.040	-5.163	0.718	-5.752
25	8.356	16.587	6.974	-5.187	1.528	-6.654
37.5	8.353	16.523	6.938	-5.038	1.573	-7.135
50	8.297	16.544	6.892	--	--	--
SLB-y, La2						
0	8.428	16.611	7.061	-5.248	0.532	-5.463
6.25	8.407	16.595	7.062	-5.290	0.652	-5.438
12.5	8.398	16.556	7.063	-5.220	0.608	-5.446
25	8.358	16.477	7.065	-5.166	0.856	-5.427
37.5	8.346	16.402	7.054	-5.114	0.830	-5.584
50	8.299	16.347	7.052	--	--	--
SLB-z, La1						
0	8.421	16.580	7.118	-5.327	0.342	-4.690
6.25	8.401	16.569	7.087	-5.359	0.493	-5.099
12.5	8.394	16.558	7.070	-5.262	0.623	-5.354
25	8.363	16.536	7.024	-5.105	1.217	-5.975
37.5	8.335	16.547	6.972	-5.234	1.722	-6.677
50	8.294	16.482	6.942	--	--	--
SLB-z, La2						
0	8.421	16.580	7.118	-5.327	0.342	-4.690
6.25	8.407	16.539	7.104	-5.291	0.315	-4.864
12.5	8.397	16.517	7.108	-5.223	0.373	-4.847
25	8.363	16.441	7.103	-5.103	0.632	-4.926
37.5	8.338	16.345	7.107	-5.205	0.479	-4.868
50	8.292	16.305	7.086	--	--	--

5.2.5. Identification of crystallographic positions of $Sr_3La_2(BO_3)_4$ occupied by the dopant

According to the crystallographic data, two different crystallographic positions of lanthanum^{3+} ions are present in the structure of SLB [210]. The photoluminescence characteristics of SLB:Tb^{3+} suggests that one of the sites is more likely to get occupied by the dopant ions [27,204].

The possibility of such preference was studied by means of analysis of total energies of the samples containing dopant ions either at La1 or La2 sites. The plots of total energies of the samples as a function of the amount of dopant are shown in Figures 58 and 59. The total energies in the plots correspond to the cell dimension values obtained using single-step SO and SD optimization. As follows from both methods, a clear conclusion about inequality of the two sites can be drawn. Similar conclusion can be also drawn on the basis of data in Fig. 49-57. Location of the dopant ions exclusively at La1 or La2 sites produced the systems of different total energy and the energy corresponding to the system with La1 site doping was lower. Thus, if the total energy was a defining factor, the dopant ions would prefer occupation of La1 sites. This idea is supported by the fact that semi-empirical Parameterization Model 3 (PM3) uses ambient-temperature properties of real molecules and not the 0 K properties [225]. Consequently, unlike *ab initio* calculations, the results obtained with this model correspond to the studied system at ambient temperature state rather then 0 K state, even if the computations were performed for 0 K [225]. From the spectroscopic data it was clear that two sites types of sites are occupied at higher doping rates in SLB:Tb^{3+}.

Summarizing, it is possible, that La1 site is thermodynamically more favorable; however, when the doping ratio is high, the dopant site is selected rather randomly [210]. Considering the total energy of the system, in the case of 37.5%-doping, the La1 site doping is more favorable by only 0.029% (SO) or 0.038% (SD). It might be that the thermodynamic factor is not that much driving force in the process of introduction of dopant atoms into the structure. In other words, when the amount of dopant is small, the probable driving force of the site selection is total energy, thus one of the sites is preferred. At higher doping amounts, the dopant atoms have less choice in selecting the site and thus both La1 and La2 sites are occupied [210].

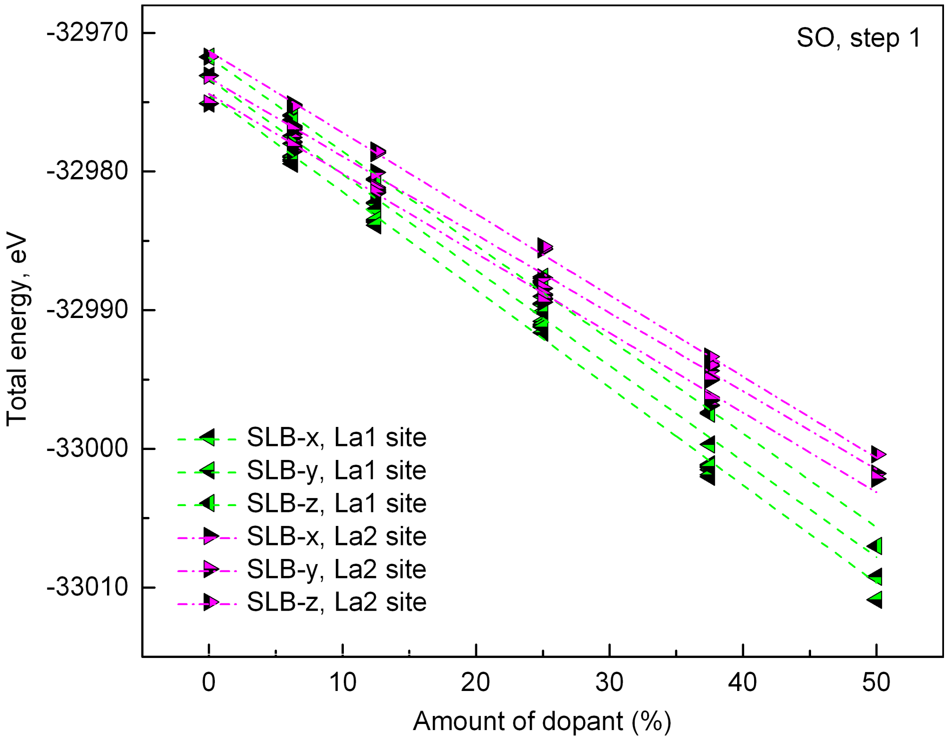

Fig. 58. The total energies of Tb^{3+}-doped SLB-(x,y,z) supercells, obtained by the single-step SO method

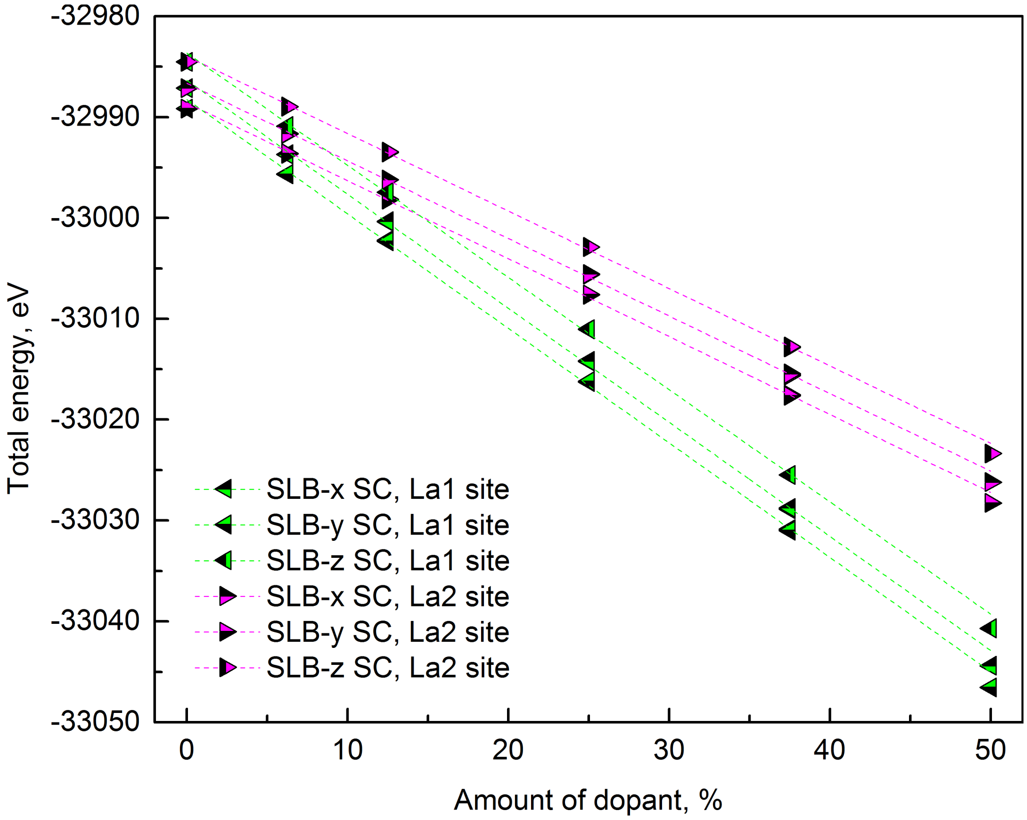

Fig. 59. The total energies of Tb^{3+}-doped SLB-(x,y,z) supercells, obtained by the SD method

5.3. Theoretical studies on upconversion dynamics in $YVO_4:Yb^{3+},Er^{3+}$

Upconversion is a photoemission process characterized by emission photon energy higher than the excitation photon energy. Such processes might occur in a single activator ion (Er^{3+}). For this ion, several infrared photons are sequentially absorbed to produce visible emission. However, Yb^{3+} ion is capable of highly efficient absorption of IR light and the following non-radiative transfer of energy to other Ln^{3+} ions. Consequently, the Yb^{3+}, Er^{3+} upconversion pair is commonly used. The overall efficiency of upconversion emission of the pair is mostly defined by the energy transfer rates, according to the energy transfer upconversion mechanism [12]. Considering this fact, the Yb^{3+}, Er^{3+} pair is a perfect tool to study the effects of energy transfer on photoluminescence.

Another problem was to select an appropriate material for this kind of study. Mixed borates did not seem to be a good choice, for the following reasons. Firstly, two types of crystallographic sites are present in the mixed borate structure. Moreover, one of them seems to be preferred by the dopant ions, but not 100% preferred. This factor rises a question of how to locate the dopant ions – in one site, in two sites and which proportion of the two to use. Next, Yb can have the oxidation state of 2+ and thus can enter Sr^{2+} sites (three of them). Thus, the concentration of Yb^{3+} cannot be exactly defined at the synthesis stage while the location of the ions is even more unclear. Although substitution of Sr^{2+} by Yb^{2+} is not very probable due to highly oxidative synthesis conditions (see Section 4.1), it cannot be excluded. Additionally, the coordination surroundings of the RE ions in mixed borates are low-symmetric while the variety of RE-O bond lengths in the RE coordination geometry is high. This factor makes the calculations of the intensity parameters (Eq. 2.3.9-14) a bit more complicated. If the bond distances are similar, it is possible to simplify the calculations by using the same values of overlap integrals, surrounding polarizabilities, charge and shielding factors for different ions of the coordination geometry. On the other hand, if the ions differ in their crystallographic sites and RE-O distances, such a simplification would introduce additional errors. Considering these factors, tetragonal yttrium vanadate (t-YVO_4) was selected as it is free from the above problems. In particular, its structure is simple and symmetric. Each of Y, O and V atoms is characterized by only one kind of crystallographic site. The Y-O bond distances in the coordination geometry differ only slightly. And finally, the Ln^{3+} materials based on t-YVO_4 have been widely studied and are characterized by stable and efficient photoluminescence.

5.3.1. General characteristics of the upconversion photoemission of $YVO_4:Yb^{3+},Er^{3+}$ samples

The experimental data about the $YVO_4:Yb^{3+}$, $YVO_4:Er^{3+}$ and $YVO_4:Yb^{3+},Er^{3+}$ samples and the details on the synthesis may be found in Ref. [226]. The studied materials contained 2% of

Er^{3+} dopant, while the amounts of Yb^{3+} ions included were 0.5, 1, 2, 4, 6 and 8%. Under 980 nm excitations, the materials exhibited green upconversion emission (Er^{3+}: $^2H_{11/2}$, $^4S_{3/2} \rightarrow {}^4I_{15/2}$). Although the emission in the red range (Er^{3+}: $^4F_{9/2}$, $\rightarrow {}^4I_{15/2}$) was observed, its intensity was very low in comparison to the green emission (Fig. 60). The emission intensities plotted as a function of Yb^{3+} concentration squared were characterized by a linear trend. The studies with variable pump power were performed. The plots of logarithm of intensity as a function of logarithm of pump power were obtained. According to the slopes of these plots [227], both green and red emissions were a result of a two-photon process (Fig. 60).

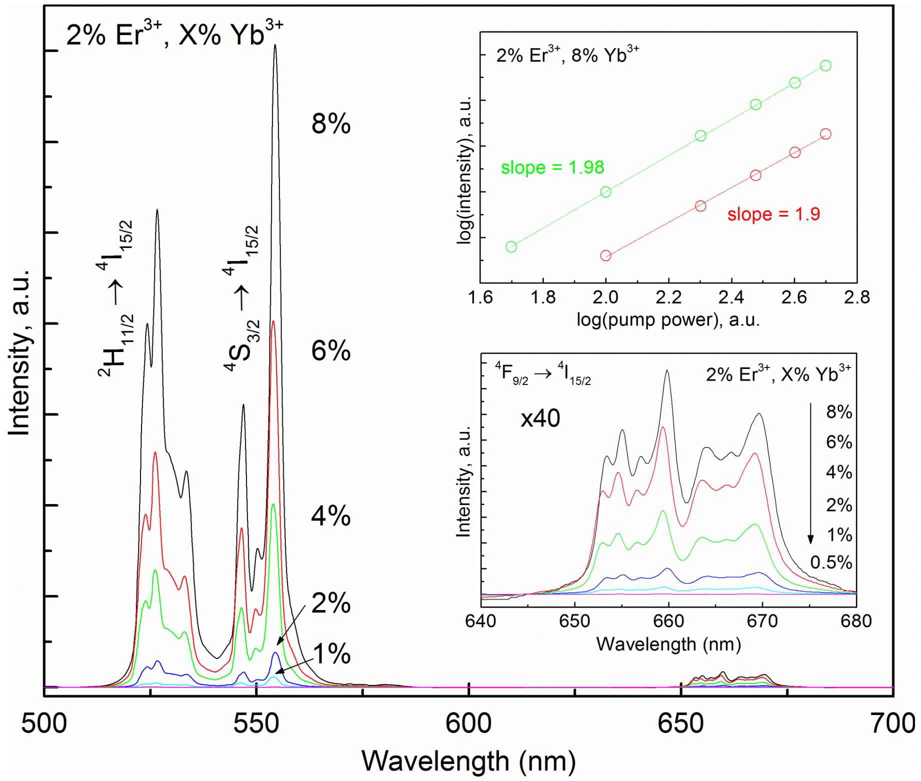

Fig. 60. The upconversion emission of $YVO_4:Yb^{3+},Er^{3+}$ samples; the insets show the double-logarithmic upconversion intensity vs. pump power plots (upper inset) and a closer look on the $^4F_{9/2} \rightarrow {}^4I_{15/2}$ transition manifold (lower inset)

The $YVO_4:Yb^{3+}$ and $YVO_4:Er^{3+}$ samples were used to measure the non-radiative decay rates of energy levels of the respective dopant ions in the YVO_4 matrix. The measurements were performed at room temperature. The excitation was performed into the respective level, while the lifetime of the corresponding emission from the level was measured. The reciprocals of the lifetimes were assumed to be the relaxation rates of the levels.

5.3.2. The theoretical model of upconversion in $YVO_4:Yb^{3+},Er^{3+}$

General strategy of the study in this section was the following. First, the energy level diagram of the Yb^{3+} and Er^{3+} in question was set. Next, probable upconversion mechanism (*energy transfer upconversion*, ETU) was assumed [226]. Then, the possible energy transfer pathways were found with respect to the energy mismatch condition. Every pathway was characterized by a respective energy transfer rate. In order to calculate the energy transfer rates, the approach presented in Ref. [9] was applied. For particular material, interacting ions and their coordination geometries, the energy transfer rate is a function of the donor-acceptor distance [9]. As the matrix material is a crystalline solid with numerous positions suitable for Yb^{3+} and Er^{3+} ions, there are many possible Yb-Er distances and to each distance an elementary energy transfer rate corresponds. These rates must be summed and normalized in order to get the total rate. The summations were made with respect to the occurrence of particular distances in the population. While the energy transfer rates were calculated theoretically, the data on radiative and non-radiative decay rates were collected from the experiment. Finally, the system of rate equations was set and solved numerically [226].

Alternative upconversion mechanisms were also considered. In particular, for the pair Yb^{3+}, Er^{3+}, the upconversion process might involve such mechanisms as *cooperative sensitization* or *excited state absorption*. However, in comparison with the energy transfer upconversion (ETU), these mechanisms are much less likely to take place and thus were neglected to simplify the model. In the latter mechanism, the excitation radiation is absorbed by the Yb^{3+} ions, and the energy is then transferred to Er^{3+} ions in its ground state or in one of the excited configurations.

The ETU mechanism includes Yb-Er energy transfer processes. However, Er-Er processes may also be important. Therefore, two types of simulations were performed. In one of them, only the Yb-Er processes were included. In the other one, both the Er-Er and the Yb-Er energy transfer processes were taken into account.

5.3.3. The energy levels in the model

In the Yb-Er upconversion pair, Er^{3+} is the activator (emitter), while Yb^{3+} is the sensitizer. Yb^{3+} can be excited with infrared radiation (~980 nm). According to the ETU mechanism, Er^{3+} is excited in a step-by-step fashion by the portions of energy transferred from Yb^{3+}. The visible green emission from Er^{3+} is possible from the two levels, namely $^2H_{11/2}$ and $^4S_{3/2}$. The energy of transition from Er^{3+} ground state ($^4I_{15/2}$) to $^4F_{7/2}$ level (right above the green-emitting levels) is about twice as large as the energy of Yb^{3+} excited state ($^2F_{5/2}$). The $^2H_{11/2}$ and $^4S_{3/2}$ levels are located below $^4F_{7/2}$ level and are populated mostly by non-radiative (vibronic) decay from $^4F_{7/2}$ level. As the energy difference between the levels is small, the decay rates are very high. Such properties allow introducing another simplification to the theoretical model. In particular, the three levels can be treated as one effective level [15,82]. Thus, instead of three

Yb-to-Er direct energy transfer pathways and three back-transfers corresponding to the three levels, the model contained only one direct transfer pathway and one back-transfer involving the effective level (marked as level 7 in Fig. 61). According to the model, the direct Yb-to-Er energy transfer involved the high-lying $^4F_{7/2}$ state as the final level of acceptor (Er^{3+}), while the reverse process (Er-to-Yb, back-transfer) involved the Er^{3+} $^4S_{3/2}$ state as the initial level of the donor [226]. The $^4I_{11/2}$ state was the final level of donor in the back-transfer from level 7 [226]. The appropriate doubly-reduced matrix elements obtained by Carnall and co-workers [228] were used in calculations of the corresponding energy transfer rates [226].

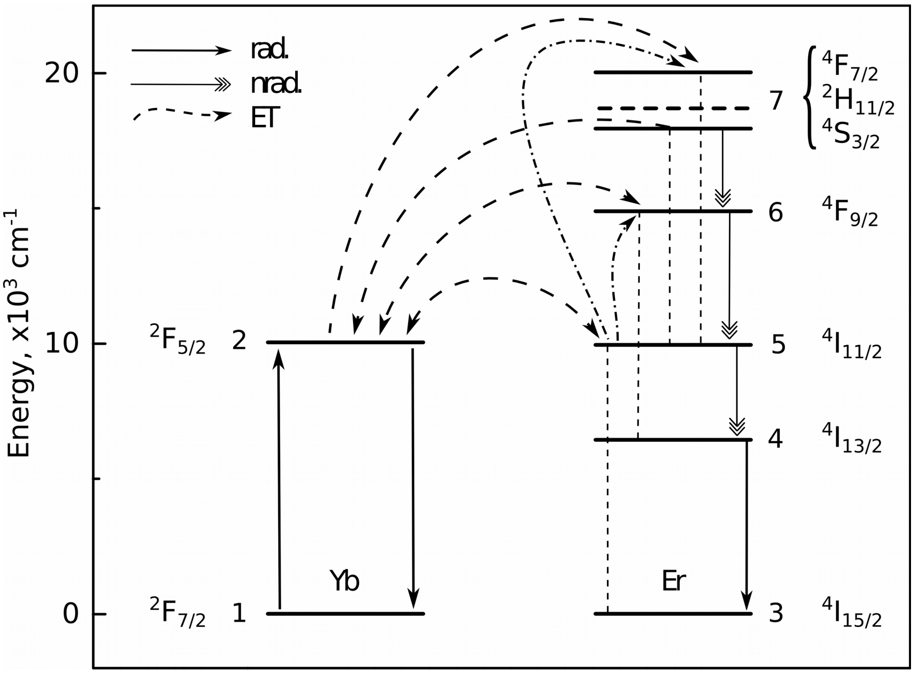

Fig. 61. Energy levels and processes taken into account in the model; *rad.* refers to radiative transition, *nrad.* to non-radiative transition and *ET* to energy transfer process; arrows point at the final levels of the acceptor, while the dash/dash-dot lines between the levels mark the transitions involved in particular energy transfer processes

The $^4I_{9/2}$ level of Er^{3+} was not included in the model. The transitions involving the level do not satisfy the energy mismatch conditions. In other words, the rate of such transitions was vanishingly small.

In the presented model, level 2 of Yb^{3+} ($^2F_{5/2}$) was populated by the excitation source ($^2F_{7/2} \rightarrow {}^2F_{5/2}$) and by the back-transfer processes (Er^{3+}: $^4I_{11/2} \rightarrow {}^4I_{15/2}$, Yb^{3+}: $^2F_{7/2} \rightarrow {}^2F_{5/2}$; Er^{3+}: $^4S_{3/2} \rightarrow {}^4I_{11/2}$, Yb^{3+}: $^2F_{7/2} \rightarrow {}^2F_{5/2}$ and Er^{3+}: $^4F_{9/2} \rightarrow {}^4I_{13/2}$, Yb^{3+}: $^2F_{7/2} \rightarrow {}^2F_{5/2}$). Level 2 was depopulated by a radiative decay to the Yb^{3+} ground state ($^2F_{5/2} \rightarrow {}^2F_{7/2}$) and by direct energy transfer processes to either Er^{3+} ground state (Yb^{3+}: $^2F_{5/2} \rightarrow {}^2F_{7/2}$, Er^{3+}: $^4I_{15/2} \rightarrow {}^4I_{11/2}$) or to Er^{3+} excited states (Yb^{3+}: $^2F_{5/2} \rightarrow {}^2F_{7/2}$, Er^{3+}: $^4I_{11/2} \rightarrow {}^4F_{7/2}$ and Yb^{3+}: $^2F_{5/2} \rightarrow {}^2F_{7/2}$, Er^{3+}: $^4I_{13/2} \rightarrow {}^4F_{9/2}$) [226].

The green-emitting level 7 (Er^{3+} $^4F_{7/2}$, $^2H_{11/2}$, $^4S_{3/2}$) was populated by a direct energy transfer process (Yb^{3+}: $^2F_{5/2} \rightarrow {}^2F_{7/2}$, Er^{3+}: $^4I_{11/2} \rightarrow {}^4F_{7/2}$) and was depopulated by a back-transfer process (Er^{3+}: $^4S_{3/2} \rightarrow {}^4I_{11/2}$, Yb^{3+}: $^2F_{7/2} \rightarrow {}^2F_{5/2}$). The appropriate doubly reduced matrix elements were used to calculate the rates. The energy transfer rate that populates level 7 was calculated using the matrix elements of the Er^{3+} $^4I_{11/2} \leftrightarrow {}^4F_{7/2}$ transition, while the corresponding back-transfer rate was calculated with the matrix elements of the Er^{3+}: $^4I_{11/2} \leftrightarrow {}^4S_{3/2}$ transition [226]. This scheme represents the nature of the effective level and the rapid non-radiative relaxation processes within its components – the high-lying excited levels of Er^{3+}. The energy transfer populates $^4F_{7/2}$ level, the following non-radiative decay populates $^2H_{11/2}$ level and $^4S_{3/2}$ level. The non-radiative relaxation of $^4S_{3/2}$ level to $^4F_{9/2}$ level is characterized by a significantly larger energy gap and much lower rate. Thus, $^4S_{3/2}$ was the lowermost component of the effective green-emitting level. Consequently, this level was the initial one in the back-transfer process from level 7.

An absorption of non-radiative energy transfer from Yb^{3+} was possible at level 4, promoting Er^{3+} ion to level 6 (Yb^{3+}: $^2F_{5/2} \rightarrow {}^2F_{7/2}$; Er^{3+}: $^4I_{13/2} \rightarrow {}^4F_{9/2}$). Alternatively, a radiative decay to level 3 was possible (Er^{3+}: $^4I_{13/2} \rightarrow {}^4I_{15/2}$) [226]. The former process populates the red-emitting level 6 [226]. Level 6 was depopulated by a respective back-transfer (Er^{3+}: $^4F_{9/2} \rightarrow {}^4I_{13/2}$, Yb^{3+}: $^2F_{7/2} \rightarrow {}^2F_{5/2}$). Level 5 was mostly involved in the direct and back energy transfer processes [226]. If the level was the initial level of the process, it was depopulated at a respective rate. Alternatively, it would be populated by the process in which it would be the final level.

A non-radiative (multi-phonon) decay was possible from levels 5, 6 and 7. The non-radiative rate of the transition from level 6 to level 5 was, in fact, the rate of Er^{3+} $^4F_{9/2} \rightarrow {}^4I_{9/2}$ multi-phonon decay. Since the respective energy differences were too high, the $^4I_{9/2}$ level did not participate in any energy transfer processes [226]. If it had been in the model, it would have been populated exclusively by the non-radiative process from level 6 and depopulated exclusively by the non-radiative process to level 5. Thus, the $^4I_{9/2}$ state was the unrequired intermediate of non-radiative process from level 6 to level 5 and was omitted [226]. The energy gap between level 6 and $^4I_{9/2}$ state was larger than the energy gap between $^4I_{9/2}$ state and level 5 [226]. By the energy gap law [15], a smaller gap corresponds to a more efficient multi-phonon relaxation. Consequently, the overall non-radiative rate from level 6 to level 5 through the $^4I_{9/2}$ state would be close to the rate of the less-efficient (slower) process, that is to the rate of non-radiative depopulation of level 6 [226].

Considering the energy gaps between the emitting $^4S_{3/2}$ and $^4F_{9/2}$ states of Er^{3+} and the states right under them ($^4F_{9/2}$ and $^4I_{9/2}$ respectively), only several YVO_4 phonons [151] were enough for the multi-phonon relaxation of the levels. The multi-phonon relaxation rates of the emitting levels agree well with the energy gap law, while the radiative lifetimes of these levels are relatively short [15,226]. Thus, the relaxation of the mentioned levels was predominantly non-radiative. In the model, the processes were either radiative or non-radiative for the sake of simplification. That is, a process was considered a radiative or non-radiative according to the nature of the dominant component. Consequently, the radiative processes responsible for green and red emission from Er^{3+} were omitted [226] as the non-radiative decays of the corresponding emitting levels were much more efficient than the emission processes.

One of the two types of simulations was performed with the Er-Er energy transfer processes included. It was performed without additional Er^{3+} ion. The Er^{3+} levels in the model worked as levels of both donor Er^{3+} and acceptor 'Er^{3+} [226]. It was possible thanks to the fact that the levels in the model represent ensembles of Er^{3+} and Yb^{3+} species, not single ions. For example, consider the situation where one of real Er^{3+} ions underwent a $^4I_{11/2} \rightarrow {}^4I_{15/2}$ (5-to-3) transition and transferred the energy to some other 'Er^{3+} ion which underwent a $^4I_{13/2} \rightarrow {}^4F_{9/2}$ (4-to-6) transition. The model would represent this process as an increase in the population of levels 3 and 6 and a decrease in the population of levels 5 and 4 [226]. The distances between the interacting Er^{3+} ions were taken into account in the same way as the distances between the Yb^{3+} and Er^{3+} ions. The details are given below in this section. Some of the Er-Er energy transfer processes were very weak, despite the satisfactory energy mismatch conditions. Some of the processes were neutralizing each other, for instance, the ones Er^{3+}: $5 \rightarrow 3$, 'Er^{3+}: $3 \rightarrow 5$ [226]. As a result, only two Er-Er processes were included in the model.

The visualization of the transitions in the model and the energy levels is given in Fig. 61.

5.3.4. The calculated energy transfer rates

A theoretical method proposed by Kushida [229] and reviewed by Malta [9] was used to calculate the energy transfer rates. The equations for different energy transfer mechanisms were derived with the lanthanide states in the intermediate coupling scheme, leading to “one level – one manifold” approach. That is, a sum over the levels in a manifold is weighted by the degeneracies of the donor and acceptor initial states [9,226]. Electric dipole-dipole (*dd*), dipole-quadruple (*dq*) and quadruple-quadruple (*qq*) mechanisms of energy transfer were taken into account [226]. Another possible mechanism was the electron exchange mechanism. On the other hand, the exchange part of energy transfer rates was negligibly weak in comparison to that in the multipolar mechanisms [226].

In the original equations, most of the components are material-specific, lanthanide ion-specific or transition-specific constants. The only variable is the distance between the donor and acceptor species. The equations were slightly modified so that the rate components ω_{dd}, ω_{dq}, and ω_{qq}, independent of donor-acceptor distance R, were obtained.

$$W(R) = W_{dd}(R) + W_{dq}(R) + W_{qq}(R) \tag{5.3.1}$$

$$W_{dd}(R) = \omega_{dd} R^{-6} \tag{5.3.2}$$

$$W_{dq}(R) = \omega_{dq} R^{-8} \tag{5.3.3}$$

$$W_{qq}(R) = \omega_{qq} R^{-10} \tag{5.3.4}$$

$$\begin{gathered} \omega_{dd} = e^4 \frac{4\pi}{3\hbar} \frac{(1-\sigma_1^D)^2 (1-\sigma_1^A)^2}{[J_D^*][J_A]} \left(\sum_\lambda \Omega_\lambda^D \left\langle \psi_D J_D \left\| U^{(\lambda)} \right\| \psi_D^* J_D^* \right\rangle^2 \right) \times \\ \times \left(\sum_\lambda \Omega_\lambda^A \left\langle \psi_A^* J_A^* \left\| U^{(\lambda)} \right\| \psi_A J_A \right\rangle^2 \right) F \end{gathered} \tag{5.3.5}$$

$$\begin{gathered} \omega_{dq} = e^4 \frac{2\pi}{\hbar} \frac{(1-\sigma_1^D)^2 (1-\sigma_2^A)^2}{[J_D^*][J_A]} \left(\sum_\lambda \Omega_\lambda^D \left\langle \psi_D J_D \left\| U^{(\lambda)} \right\| \psi_D^* J_D^* \right\rangle^2 \right) \times \\ \times \left\langle r^2 \right\rangle_A^2 \left\langle f \left\| C^{(2)} \right\| f \right\rangle^2 \left\langle \psi_A^* J_A^* \left\| U^{(2)} \right\| \psi_A J_A \right\rangle^2 F \end{gathered} \tag{5.3.6}$$

$$\begin{gathered} \omega_{qq} = e^4 \frac{28\pi}{5\hbar} \frac{(1-\sigma_2^D)^2 (1-\sigma_2^A)^2}{[J_D^*][J_A]} \left\langle r^2 \right\rangle_D^2 \left\langle r^2 \right\rangle_A^2 \left\langle f \left\| C^{(2)} \right\| f \right\rangle^4 \times \\ \times \left\langle \psi_D J_D \left\| U^{(2)} \right\| \psi_D^* J_D^* \right\rangle^2 \left\langle \psi_A^* J_A^* \left\| U^{(2)} \right\| \psi_A J_A \right\rangle^2 F \end{gathered} \tag{5.3.7}$$

The equations include shielding factors $(1 - \sigma_k)$, intensity parameters Ω_λ, doubly reduced matrix elements $\langle \psi^* J^* \| U^{(2)} \| \psi J \rangle^2$, radial integrals of the 4f shell $\langle r^2 \rangle$, one-electron reduced matrix element $\langle f \| C^{(2)} \| f \rangle$, which is -1.366 [230], spectral overlap factor F and donor-acceptor distance R [9,226]. The shielding factors were represented by the equation:

$$(1 - \sigma_k) = \rho \, (2\beta)^{k+1} \tag{5.3.8}$$

Here, ρ is the overlap integral of ligand atom wavefunctions and 4f configuration (averaged by the ligated atoms) and $\beta = (1 + \rho)^{-1}$ [6,226]. As the overlap integrals of Er-O and Yb-O are very similar (0.1214 and 0.1208 respectively), the mean value of the two (0.121) was used for calculation of the shielding factors of both donor and acceptor species [226].

The overlap integral was defined by [226]:

$$S_{ij} = \int A_i B_j d\tau \tag{5.3.9}$$

Here, A_i and B_j are valence atomic spin-orbitals centered on the bound atoms A and B; $d\tau$ is a volume element which includes orbital and spin part[226]. Each spin-orbital can be written as a sum of the basis functions,

$$A_i = \sum_k a_k \phi_k s_k \tag{5.3.10}$$

$$B_j = \sum_l a_l \phi_l s_l \tag{5.3.11}$$

where a_k and b_k are the coefficients of the linear combinations, φ is the spatial part of the spin-atomic orbitals (each function in the basis set) and s is the spin part [226]. From the Eqs. (5.3.9-11):

$$S_{ij} = \int \sum_k a_k \phi_k s_k \cdot \sum_l b_l \phi_l s_l d\tau \tag{5.3.12}$$

$$S_{ij} = \int \sum_k \sum_l a_k \phi_k s_k b_l \phi_l s_l dr ds \tag{5.3.13}$$

$$S_{ij} = \sum_k \sum_l a_k b_l \int \phi_k \phi_l dr \int s_k s_l ds \tag{5.3.14}$$

$$S_{ij} = \sum_k \sum_l a_k b_l \int \underbrace{\phi_k \phi_l dr}_{=O_{kl}} \left[\int \underbrace{s_k(\alpha) s_l(\alpha)}_{=1} + \underbrace{s_k(\alpha) s_l(\beta)}_{=0} + \underbrace{+ s_k(\beta) s_l(\alpha)}_{=0} + \underbrace{s_k(\beta) s_l(\beta)}_{=1} ds \right] \tag{5.3.15}$$

$$S_{ij} = \sum_k \sum_l \left(a_k^\alpha b_l^\alpha + a_k^\beta b_l^\beta \right) O_{kl} \tag{5.3.16}$$

Where a_k^α, b_l^α, b_k^β and b_l^β are the are the coefficients of the basis functions of atoms A and B, in spin states α and β, and O_{kl} is the overlap integral between the pair of basis functions k and l in the valence shell of each atom [226]. These coefficients were computed [226] with ADF [231,232] DFT software package using the BLYP [233,234] functional with TZ2P STO basis set [235–237] and relativistic effects included via relativistic scalar ZORA [238–240].

The radial integrals were provided by [241]. The refraction index of yttrium vanadate equal 2.066 was taken after [242]. The doubly-reduced matrix elements obtained by Carnall and coworkers [228] were used [226].

The intensity parameters for Er^{3+} in YVO_4 were calculated using the following equations [6,226]:

$$\Omega_\lambda = (2\lambda + 1) \sum_{t,p} \frac{|B_{\lambda tp}|^2}{(2t+1)} \tag{5.3.17}$$

$$B_{\lambda tp} = B_{\lambda tp}^{FED} + B_{\lambda tp}^{DC} \tag{5.3.18}$$

As the energy transfer rates are a function of electric dipoles on the interacting ions, the corresponding intensity parameters must contain only the forced electric dipole part. In other words, the dynamic coupling contribution must not be included, that is, the $D_{\lambda tp}^{DC}$ should be zero:

$$\Omega_{\lambda}^{ED} = (2\lambda+1)\sum_{t,p}\frac{\left|B_{\lambda tp}^{FED}\right|^2}{(2t+1)} \tag{5.3.19}$$

$$B_{\lambda tp}^{FED} = \frac{2}{\Delta E}\left\langle r^{t+1}\right\rangle \Theta(t,\lambda)\gamma_p^t \tag{5.3.20}$$

$$\gamma_p^t = e^2\left(\frac{4\pi}{2t+1}\right)^{1/2}\sum_j\left(\rho_j(2\beta_j)^{t+1}g_j\frac{Y_p^{t*}(\Theta_j,\phi_j)}{R_j^{t+1}}\right) \tag{5.3.21}$$

Here, R_j, Θ_j, ϕ_j are the spherical coordinates of coordination surround atoms, in respect to the luminescence center [226]. ΔE is the energy difference between the barycenters of the excited $4f^{n-1}$ $5d^1$ and ground $4f^n$ configurations, $\langle r^{t+1}\rangle$ is a 4f radial integral, $\Theta(t,\lambda)$ is a numerical factor[6]. ρ and β are the overlap integral and shielding factor mentioned above.

One of the key approximations in the Judd-Ofelt theory was the assumption that energy differences between the initial and final states of 4f configuration and the higher excited configuration(s) are the same. Here, a $4f^{N-1}$ $5d^1$ configuration was used. The energy difference was calculated using singlet-excitation configuration interaction (CIS) method implemented in Gaussian03 software [243]. A Stuttgart RSC 1997 effective core potential was used, with the respective basis set [244–246]. Almost one hundred excitations were analyzed [226].

Table 10. The energies and oscillator strengths of the selected 4f-d5 transitions of Er^{3+} [226]

Excited state number	Energy (eV)	Oscillator strengths
17:	21.8792	0.0013
18:	21.8793	0.0013
19:	21.8793	0.0013
39:	24.2723	0.0002
40:	24.2724	0.0002
41:	24.2724	0.0002
47:	24.4816	0.0010
48:	24.4816	0.0010
49:	24.4817	0.0010

From among the excitations, the transitions between 4f and 5d configurations with nonzero oscillator strength were selected. The excitations involving lower configurations were omitted. The energies and the oscillator strength of the selected transitions are provided in Table 10. The final value of $\Delta E = -23.11$ eV was obtained as a mean of the ΔE_i excitation energies weighted by the respective oscillator strengths f_i [226]:

$$\Delta E = \frac{\sum_i \Delta E_i f_i}{\sum_i f_i} \tag{5.3.22}$$

The values of $\langle\|U^{(\lambda}\|\rangle$ matrix element and S_{ED} of Yb^{3+} were obtained from literature [247].

The spectral overlap factor can be estimated from the energy difference Δ between the levels participating in the energy transfer and spectral widths of both of them (γ_D and γ_A) [226,229]:

$$
\begin{aligned}
F = \frac{\ln 2}{\sqrt{\pi}}\,\frac{1}{\hbar^2 \gamma_D \gamma_A} \left\{ \left[\left(\frac{1}{\hbar\gamma_D}\right)^2 + \left(\frac{1}{\hbar\gamma_A}\right)^2 \right] \ln 2 \right\}^{-1/2} \times \\
\times \exp\left(\frac{1}{4}\, \frac{\left(\frac{2\Delta}{(\hbar\gamma_D)^2}\ln 2\right)^2}{\left[\left(\frac{1}{\hbar\gamma_D}\right)^2 + \left(\frac{1}{\hbar\gamma_A}\right)^2\right]\ln 2} - \left(\frac{\Delta}{\hbar\gamma_D}\right)^2 \ln 2 \right)
\end{aligned}
\tag{5.3.23}
$$

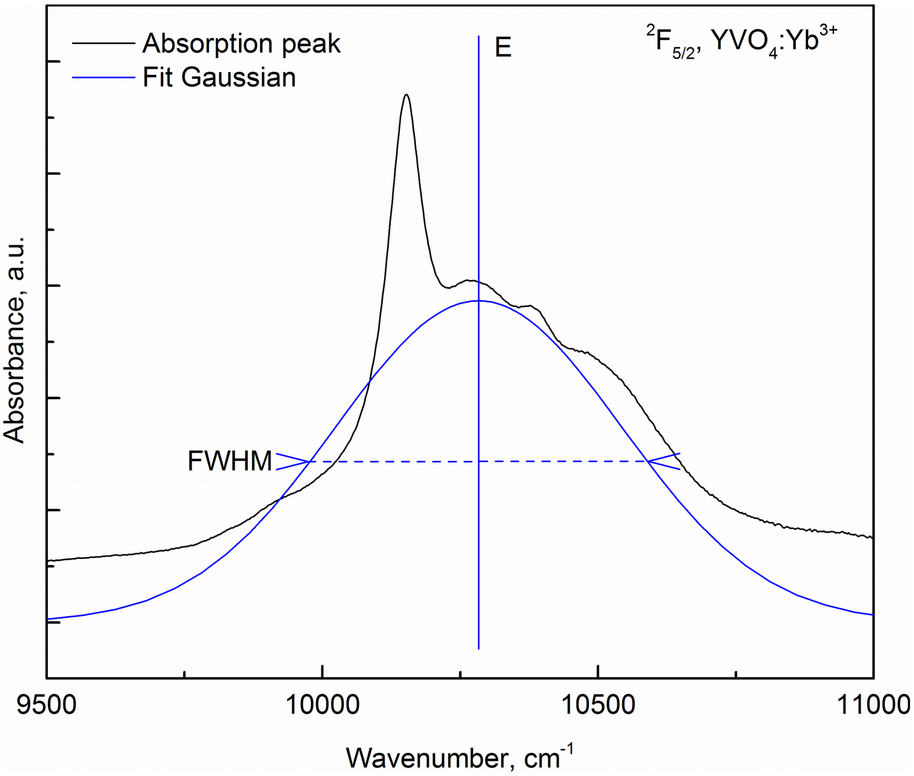

Fig. 62. Gaussian fitting of the YVO$_4$:Yb^{3+} $^2F_{7/2} \rightarrow {}^2F_{5/2}$ absorption peak

In particular, the spectral widths of the initial state of acceptor and the final state of donor were used. The respective data were obtained from the optical absorption measurements of YVO$_4$:Yb^{3+} and YVO$_4$:Er^{3+}. The whole-manifold peaks were fitted using single Gaussian curves [226]. Using such method, the centroid positions (energies of the levels) and full-width at half-maximum (FWHM) of the peaks were found. Consequently, the data were used in Eq. 5.3.23, where γ_D and γ_A were equal to the respective FWHMs and the centroids were used to calculate the energy differences. The procedure is illustrated in Fig. 62, where the $^2F_{5/2} \rightarrow {}^2F_{7/2}$ Yb^{3+} absorption peak is shown together with the fit curve.

Spectral width of the energy level manifolds in Ln^{3+} is quite small. Consequently, the energy mismatch (Δ) between the donor and acceptor transition energies above 1500 cm^{-1} leads to a very small value of the spectral overlap factor. The (Yb^{3+}: $^2F_{5/2} \rightarrow {}^2F_{7/2}$; Er^{3+}: $^4I_{13/2} \rightarrow {}^4F_{9/2}$) and (Er^{3+}: $^4I_{11/2} \rightarrow {}^4I_{15/2}$, Er^{3+}: $^4I_{13/2} \rightarrow {}^4F_{9/2}$) transitions are characterized by such large energy mismatches. The transitions might occur, however, if they were assisted by a phonon emission. In the simplest case, only one phonon is involved and the energy mismatch is reduced by the respective phonon energy. Here, the assumed initial level of the acceptor was a virtual level located one phonon energy above the regular initial level of the acceptor. The virtual level was thermally populated. From Boltzmann distribution, the respective rate would be [226]:

$$W_{phon.} = W_0 \exp\left(\frac{-E_{phon.}}{kT}\right) \tag{5.3.24}$$

where $E_{phon.}$ is the highest phonon energy available in YVO$_4$, 891 cm^{-1} [151]; W_0 is the energy transfer rate calculated as a regular rate (without the phonon assistance) from Eqs. (5.3.1-7) using spectral overlap factor F obtained for the energy difference Δ reduced by the value of $E_{phon.}$ [226].

5.3.5. The effective energy transfer rate by numerous different donor-acceptor distances

The ω_{dd}, ω_{dq}, and ω_{qq} rate components depend on the material and transition characteristics only and do not depend on the distance between the interacting species. In order to get the rates of energy transfer according to the respective mechanisms, ω_{dd}, ω_{dq}, and ω_{qq} should be multiplied by the distance to the respective power [226]. In a solid crystalline material, there are multiple sites suitable for the Ln^{3+} dopant ions. Consequently, the donor-acceptor distance is variable. Both species can be randomly distributed in the structure. In order to estimate the energy transfer rates, the elementary rates corresponding to all of the possible distances should be taken into account. As the crystal structure and the possible positions of Ln^{3+} are known, it is possible to construct a set of interatomic distances present in the structure. The dopant ions were assumed to occupy the Y sites in the tetragonal YVO$_4$. Thus, Y-Y distances were considered. The energy transfer rates tend to decay very fast as the donor-acceptor distance increases. Thus, distances larger than 15 Å were not considered.

As a crystal is a virtually infinite structure, it is impossible to count all of the interatomic distances in it. Alternatively, a supercell can be used. As the question requires only short distances to be counted, the supercell has to be just large enough for that. In this study, a supercell of I4$_1$/amd (*a*,*b*=7.1183 Å, *c*=6.2893 Å) tetragonal YVO$_4$ (t-YVO$_4$) was used [226]. A periodic boundary condition was applied, that is, the shortest line segment connecting two positions was not necessarily located within the supercell; in some cases, the shortest line segment was crossing the supercell wall. However, it must be noted, that the proportions of the number of the line segments might depend on the supercell size. A series of the t-YVO_4 supercells comprising of $n \times n \times n$ unit cells, with $n = 3, 4, 5, 6, 7, 8$ and 9 was analyzed [226]. It was found that for 5×5×5 supercells or larger, the occupation numbers for distances smaller than 15 Å are the same [226]. Consequently, the 5×5×5 supercell was selected for further studies. The supercell contained 500 formula units of YVO_4. In such a supercell, substitution of 10 Y^{3+} ions with Er^{3+} corresponds to 2% content of dopant. The number of Yb^{3+} ions was equal to 2 (0.4%), 5 (1%), 10 (2%), 20 (4%), 30 (6%) and 40 (8%) ions per supercell [226].

Assuming the set R_i of distances as known, Eqs. (5.3.2-7) can be used to calculate and sum up the elementary rates. The total rate should be equal to the sum of elementary rates normalized according to the dopant ions concentration. However, the powers of R can be summed up instead of doing the elementary rates summation. The following equations are the same for the electric dipole-dipole (*dd*), dipole-quadruple (*dq*) and quadruple-quadruple (*qq*) mechanism and are thus generalized: *mm* stands for *dd*, *dq* of *qq*, while the corresponding values of m are –6, –8 and –10, respectively.

$$W_{mm} = \sum_i W_{mm}(R_i) = \sum_i \omega_{mm} R_i^m = \omega_{mm} \sum_i R_i^m \tag{5.3.25}$$

Due to the crystal symmetry, some of the R_i values might repeat. Consequently, the R_i set can be replaced with two sets: the R_j set, that contains each R value only once and the a_j set, such that each R_j value occurs in the R_i set a_j times. Next, the total rate can be expressed as:

$$W = \sum_{mm,m} \left(\omega_{mm} \sum_j a_j R_j^m \right) \tag{5.3.26}$$

$$\sum_j a_j = N_{Yb} N_{Er} \tag{5.3.27}$$

where the second equation is the normalization condition. N_{Er} and N_{Yb} are the amounts of Er^{3+} and Yb^{3+} ions in a supercell [226]. Clearly, there are $N_D \cdot N_A$ line segments that connect N_D of donor ions to N_A of acceptor ions. The calculations of optional Er-Er energy transfer rates were made using a different formula, namely $N_{Er} \cdot (N_{Er} - 1)/2$ – according to the number of line segments connecting N_{Er} points [226].

5.3.6. The set of rate equations

A photoluminescence system can be described by a set of energy levels and a set of transitions between the levels. The levels are characterized by their populations. The process occurring at particular level such as excitation, emission, relaxation or energy transfer depend on the level population. Some of the processes are linear. The rates of the linear processes (in units of energy per second) are linear functions of (normalized) population of the corresponding (initial) level. The linear processes include multiphonon relaxation and photon emission. Some processes are nonlinear and depend on populations of two participating levels. Namely, in the Ln-Ln energy transfer processes, the rate depends on the populations of initial (excited) state of donor and initial (ground) state of acceptor. The observable features of the system such as luminescence lifetimes and intensities depend on the energy flow balance in a given system. This kind of balance can be described by a set of rate equations showing the particular level population changes in time. The equations include the terms populating the levels and the terms depopulating them. The respective signs are plus and minus, respectively. A sum of these two types of terms is the time derivative of the level population.

According to the energy level scheme (Fig. 61), the following set of rate equations was constructed:

$$\begin{aligned}\frac{d\eta_1}{dt} = -\Phi\eta_1 + \frac{1}{\tau 2}\eta_2 + W_{52}\eta_2\eta_3 + W_{62}\eta_2\eta_4 + W_{72}\eta_2\eta_5 - W_{25}\eta_1\eta_5 - W_{26}\eta_1\eta_6 \\ -W_{27}\eta_1\eta_7\end{aligned} \tag{5.3.28}$$

$$\frac{d\eta_2}{dt} = -\frac{d\eta_1}{dt} \tag{5.3.29}$$

$$\frac{d\eta_3}{dt} = \frac{1}{\tau_4}\eta_4 - W_{52}\eta_2\eta_3 + W_{25}\eta_1\eta_5 + (W_{65}\eta_4\eta_5 + W_{75}\eta_5\eta_5) \tag{5.3.30}$$

$$\frac{d\eta_4}{dt} = -\frac{1}{\tau_4}\eta_4 + W_5\eta_5 - W_{62}\eta_2\eta_4 + W_{26}\eta_1\eta_6 - (W_{65}\eta_4\eta_5) \tag{5.3.31}$$

$$\begin{aligned}\frac{d\eta_5}{dt} = -W_5\eta_5 + W_6\eta_6 + W_{52}\eta_2\eta_3 - W_{72}\eta_2\eta_5 - W_{25}\eta_1\eta_5 + W_{27}\eta_1\eta_7 \\ - (W_{65}\eta_4\eta_5 + 2W_{75}\eta_5\eta_5)\end{aligned} \tag{5.3.32}$$

$$\frac{d\eta_6}{dt} = -W_6\eta_6 + W_7\eta_7 + W_{62}\eta_2\eta_4 - W_{26}\eta_1\eta_6 + (W_{65}\eta_4\eta_5) \tag{5.3.33}$$

$$\frac{d\eta_7}{dt} = -W_7\eta_7 + W_{72}\eta_2\eta_5 - W_{27}\eta_1\eta_7 + (W_{75}\eta_5\eta_5) \tag{5.3.34}$$

where W_{ij} are the energy transfer rates from level j to level i, W_i are the non-radiative decay rates from level i, τ_i is the radiative lifetime of level i, and Φ is the pump rate [226]. Optional Er-Er enegy transfer processes are represented by the terms in brackets.

The fourth-order Runge-Kutta numerical method with an adaptive integration step [26,57] was used to solve the above equations [226]. In this method, the level populations are changed step-wise by the respective sum of populating and depopulating rates. An original software by Prof. R.L. Longo [248,250,251] was used to perform the solution procedure. Appropriate modifications to the software were made in order to include the non-linear terms. In particular, the rate equations (5.3.28-34) were introduced into the subroutine responsible for calculating the function to be integrated during the current step [226]. The timestep was defined by the fastest-decaying level and was equal to the time required for the population of the level to decrease down to 1/e of its current value [226]. The initial step was equal to the lowest rate reciprocate. The initial population of level 3 (Er^{3+} ground state) was set to 1, while the population of level 1 (Yb^{3+} ground state) was set to 0.2, 0.5, 1, 2, 3 or 4, according to the amount of the Yb^{3+} dopant and the Yb:Er ratio [226].

5.3.7. The transitions rates, experimental and calculated

The rates of radiative and non-radiative transitions [226], the spectral widths and peak positions as well as the calculated total energy transfer rates corresponding to transitions between the levels of Er^{3+} and Yb^{3+} [226], are shown in Tables 11-13. Note that the rates of the linear processes were considered to be independent of the amount of Yb^{3+} dopant.

The Yb-to-Er energy transfer process populating level 5 and the respective back-transfer were characterized by the highest rates. It can be explained by the small energy differences corresponding to the transitions. The rate of the energy transfer process populating level 7 of Er^{3+} (second excitation) was also high, while the energy difference was also low. It is interesting that the former process was less-intense than the latter, despite the smaller energy difference. Here, the effect of transition electric dipole properties (expressed via the matrix elements [228]) was observed.

Table 11. The properties of Yb^{3+} and Er^{3+} manifolds in YVO_4, obtained via single-Gaussian fitting of the experimental absorption peaks

Level	Centroid, cm^{-1}	FWHM, cm^{-1}
Yb^{3+} $^2F_{5/2}$	10256	610
Yb^{3+} $^2F_{7/2}$	0*	-
Er^{3+} $^4F_{7/2}$	20452	310
Er^{3+} $^4S_{3/2}$	18325	70
Er^{3+} $^4F_{9/2}$	15207	310
Er^{3+} $^4I_{11/2}$	10157	280
Er^{3+} $^4I_{13/2}$	6573	270
Er^{3+} $^4I_{15/2}$	0*	-

*Assumed

The phonon assistance was used for the transitions (Yb^{3+}: 2→1, Er^{3+}: 4→6) and (Er^{3+}: 5→3, Er^{3+}: 4→6). The respective energy differences were reduced by the t-YVO_4 phonon energy. However, the reverse processes (energy transfer with phonon absorption, initial energy smaller than the final) were neglected as highly unlikely to happen [12,226]. Such an approach resulted in a very low rate of the back-transfer from level 7 (Er^{3+}: 7→5, Yb^{3+}: 1→2). Thus, the back-transfer was much less efficient that the respective direct transfer. This fact was considered to be the reason for high green-to-red ratio of the upconversion emission peaks in the studied material [226].

Table 12. The radiative and non-radiative rates in $YVO_4:Yb^{3+}$ and $YVO_4:Er^{3+}$, experimental

Transition	Levels	Rate, s^{-1}
Yb^{3+}: $^2F_{5/2} \rightarrow {}^2F_{7/2}$ (radiative)	Yb^{3+}: 2→1	3571
Er^{3+}: $^4S_{3/2} \rightarrow {}^4F_{9/2}$ (non-radiative)	Er^{3+}: 7→6	111111
Er^{3+}: $^4F_{9/2} \rightarrow {}^4I_{9/2}$* (non-radiative)	Er^{3+}: 6→5	175439
Er^{3+}: $^4I_{11/2} \rightarrow {}^4I_{13/2}$ (non-radiative)	Er^{3+}: 5→4	31250
Er^{3+}: $^4I_{13/2} \rightarrow {}^4I_{15/2}$ (radiative)	Er^{3+}: 4→3	455

Two processes populate the red-emitting level 6, namely, the relaxation of level 7 and energy transfer process (Yb^{3+}: 2→1, Er^{3+}: 4→6) from Yb^{3+}. The latter is a function of level 4 population, which is populated exclusively by the relaxation of level 5. Despite higher energy difference, the rate of back transfer from level 6 is even higher than the rate of the respective direct process taking into account the values of the corresponding doubly reduced matrix elements [226].

Table 13. The calculated energy transfer rates (corresponding to 8% of Yb^{3+}) and the energy mismatch conditions in $YVO_4:Yb^{3+}$, Er^{3+}

Transition	Levels	Rate, s^{-1}	Energy mismatch, cm^{-1}
Yb^{3+}: $^2F_{5/2} \rightarrow {}^2F_{7/2}$, Er^{3+}: $^4I_{11/2} \rightarrow {}^4F_{7/2}$	Yb^{3+}: 2→1, Er^{3+}: 5→7	6347	39
Yb^{3+}: $^2F_{5/2} \rightarrow {}^2F_{7/2}$, Er^{3+}: $^4I_{13/2} \rightarrow {}^4F_{9/2}$	Yb^{3+}: 2→1, Er^{3+}: 4→6	118	1622 (731*)
Yb^{3+}: $^2F_{5/2} \rightarrow {}^2F_{7/2}$, Er^{3+}: $^4I_{15/2} \rightarrow {}^4I_{11/2}$	Yb^{3+}: 2→1, Er^{3+}: 3→5	41303	99
Er^{3+}: $^4S_{3/2} \rightarrow {}^4I_{11/2}$, Yb^{3+}: $^2F_{7/2} \rightarrow {}^2F_{5/2}$	Er^{3+}: 7→5, Yb^{3+}: 1→2	0.02	2088
Er^{3+}: $^4F_{9/2} \rightarrow {}^4I_{13/2}$, Yb^{3+}: $^2F_{7/2} \rightarrow {}^2F_{5/2}$	Er^{3+}: 6→4, Yb^{3+}: 1→2	401	1622
Er^{3+}: $^4I_{11/2} \rightarrow {}^4I_{15/2}$, Yb^{3+}: $^2F_{7/2} \rightarrow {}^2F_{5/2}$	Er^{3+}: 5→3, Yb^{3+}: 1→2	40545	99
Er^{3+}: $^4I_{11/2} \rightarrow {}^4I_{15/2}$, Er^{3+}: $^4I_{11/2} \rightarrow {}^4F_{7/2}$	Er^{3+}: 5→3, Er^{3+}: 5→7	1.7	138
Er^{3+}: $^4I_{11/2} \rightarrow {}^4I_{15/2}$, Er^{3+}: $^4I_{13/2} \rightarrow {}^4F_{9/2}$	Er^{3+}: 5→3, Er^{3+}: 4→6	189	1523 (632*)

*Photon-assisted

5.3.7. The dependence of the energy transfer rates on the donor-acceptor distance

The energy transfer rates by the three electric multipolar mechanisms (*dd*, *dq* and *qq*) decrease with increasing donor-acceptor distance. The different powers of R in the corresponding equations result in different decrease rates. For instance, the *qq* mechanism is the fastest decaying with the distance. On the other hand, this mechanism corresponds to the highest energy transfer rate, under other conditions the same. As a result, different portions of energy are transferred by the mechanisms at different donor-acceptor distances. At the shortest possible donor-acceptor distance in YVO_4 (3.9 Å), the *qq* mechanism is responsible for over 98% of energy transfer, while the corresponding value is only about 77% at about 14 Å. At this point, about 1% and 22% of energy transfer occur via *dd* and *dq* mechanisms respectively. This estimations were made for W_{52} (Yb-to-Er; Er^{3+}: $^4I_{15/2} \rightarrow {}^4I_{11/2}$) [226].

5.3.8. *The dynamical simulations*

Three different types of simulations were used to study the evolution of energy transfer in YVO_4:Yb^{3+},Er^{3+} in time [226]. They were chosen to model different properties of the material. In the first series, a continuous excitation regime was applied. In this kind of excitation, the pump power was constant (10 s^{-1}), while the rate equation solution procedure was continued until the equilibrium values of the level populations were obtained. The dependence of level 7 population on the amount of Yb^{3+} dopant was studied. The amount of Yb^{3+} dopant was represented by the initial population of level 1 (Yb^{3+} ground state). The results were compared to the experimental data on the green upconversion intensity. The intensity of emission is a linear function of level population. For Ln^{3+}, it can be calculated if the full (forced electric dipole plus dynamic coupling contributions) Ω_λ parameters are known. On the other hand, as the Ω_λ are usually obtained via fitting to the experimental data, the intensity calculations would include the error produced by the Ω_λ fitting. Moreover, the data on populations are enough to compare the trends [226].

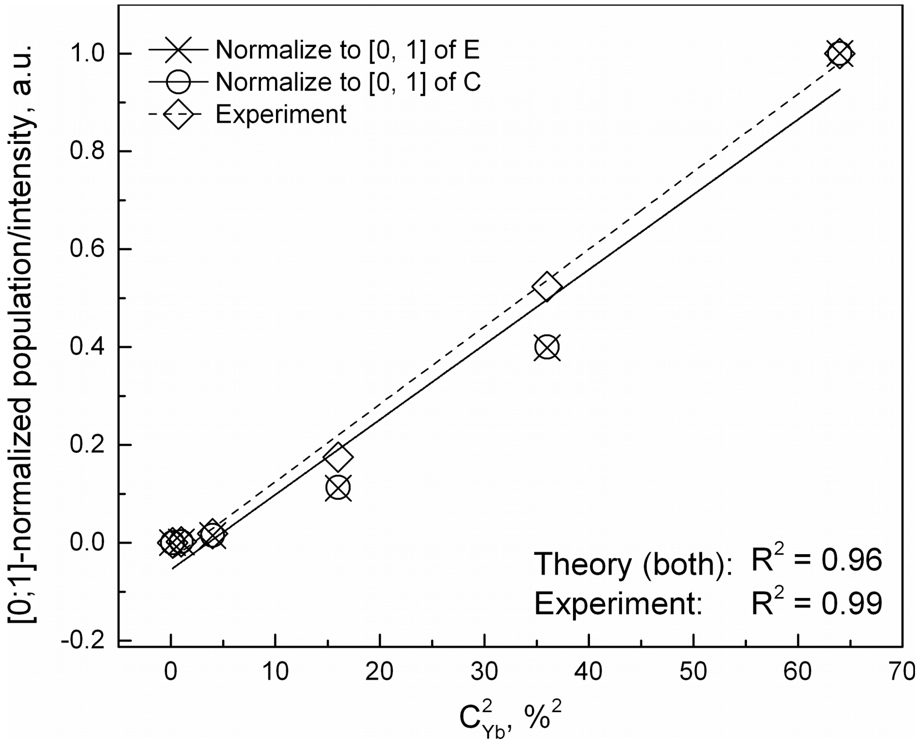

Fig. 63. The dependence of normalized population of the emitting level 7 (calculated) and the normalized green upconversion emission intensity (experimental) on the amount of Yb^{3+}

Similarly, the populations may be used instead of intensities in double-logarithmic intensity vs. pump power plots [226]. The latter are used to describe the amount of excitation photons participating in the upconversion emission [227]. The slopes of log(I) and log(η) dependencies on log(Φ) would be the same and both would describe the amount of excitation photons [226].

In Fig. 63, normalized values of the experimental green emission intensities and the theoretical level 7 populations population are presented as functions of the Yb^{3+} concentration squared. Apparently, both showed the same linear trend. The trend of the experimental intensity was characterized by the value of R^2 equal 0.99. The R^2 of the theoretical population trends was 0.96, for both results obtained with or without Er-Er energy transfer processes. It was concluded that the overall dependence of the upconversion emission intensity on the amount if Yb^{3+} dopant was represented correctly by the simulation [226].

The goal of the second type of simulations was to find out the number of excitation photons required to achieve the upconversion emission. Continuous excitation mode was used in this case, and several separate simulations with different pump power values were performed. The dependencies of the logarithm of the emitting levels population upon the logarithm of the pump power were determined [226]. As the intensity is a linear function of the population, the slopes of the logarithm of the population and of the logarithm of the intensity with respect to the logarithm of the pump power should be the same [226].

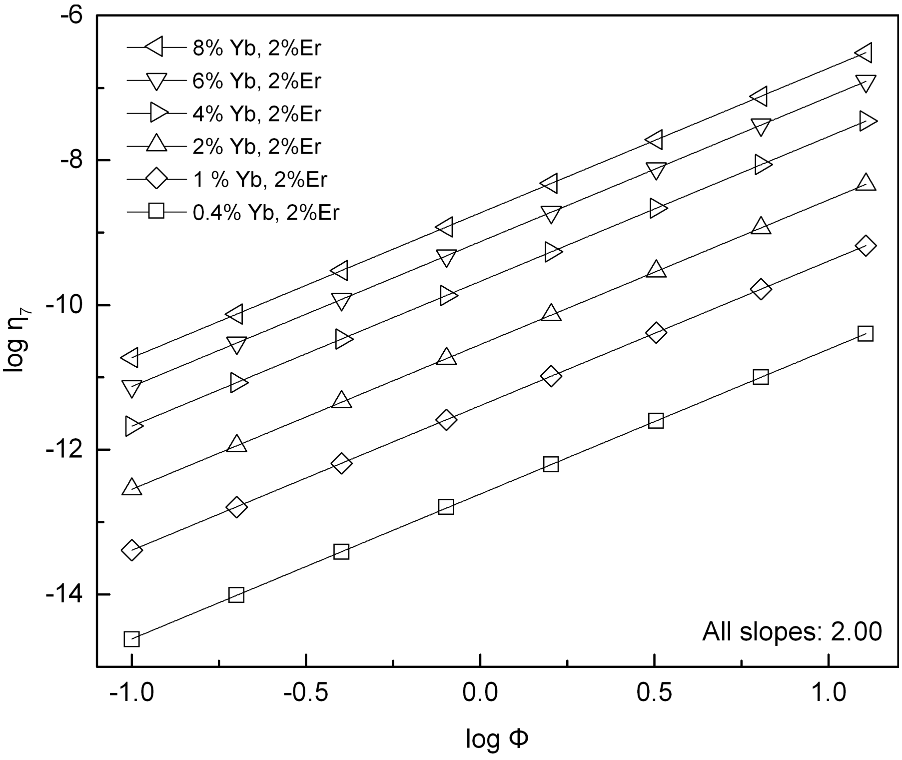

Fig. 64. The log(η) vs. log(Φ) plots of $YVO_4:Yb^{3+}, Er^{3+}$, calculated

The pump rate ranged from 0.1 to 12.8 s^{-1} in a geometric progression with a common ratio of 2. The dependence of the logarithm of the population upon the logarithm of the pump power was linear for all of the Yb^{3+} concentrations considered (Fig. 64). The slopes of fit lines were equal 2.00 [226]. Extending the sequence of the pump power values beyond 12.8 s^{-1} resulted in increase of nonlinearities. The plot in Fig. 64 concerns the logarithms of populations of level 7 and was obtained with the Er-Er energy transfer processes. The plots describing the same dependence of population of level 6 were very similar to those presented in Fig. 64 and were not shown. The slopes of fit lines are a bit different, varying between 2 (8% Yb^{3+}) and 1 (0.4% Yb^{3+}) [226]. As the population of level 6 was very low at low pump rates, the respective results were considered unreliable (numeric solution artefacts were noticeable, while in some cases the level converged with negative population). The same observation applied to the results of simulations performed without the Er-Er energy transfer. The plots were essentially similar and were not shown. The effect of Er-Er energy transfer in this case was considered negligible [226].

The experimental amount of photons required for the upconversion emission (deduced from the double-logarithm plot slopes) was 1.98 and 1.90 for green and red emission, respectively. Apparently, the results of theoretical calculations and the experiment agree on the number of photons, that is two.

In the third kind of simulation, a pulsed excitation mode was used. The intention was to investigate the behavior of the system after a short excitation pulse. The whole theoretical setup remained the same, with two exceptions. The pump rate was set to zero, while some of the level 1 population was transferred to level 2. In other words, the initial population level 2 was non-zero, while the population of level 1 was reduced by the respective value. Thus, this type of simulation was characterized by the initial excitation, expressed in % of Yb^{3+} ground state population. Consequently, the particular values of initial populations of levels 1 and 2 depended on the amount of Yb^{3+} dopant.

After the equation solution procedure was started, the population of level 2 went down, while the other level populations displayed a rise and decay pattern. Eventually, level 1 population approached almost the default value (0.2, 0.5, 1, 2, 3 or 4, depending on Yb^{3+} amount), level 3 approached unity while the others approached zero (within the degree of numerical method accuracy).

The rise and decay pattern curves (both experimental and theoretical) were fitted using a pulse function (5.3.35). In Eq. 5.3.35, t_1 is the rise time and t_2 is the decay time. The fitting was performed with the OriginPro 9 software, by a two-step procedure. In the first step, the offsets y_0 and x_0 were fixed at their initial guess values and the fitting was allowed to converge. Skipping this step resulted in a convergence failure. Next, the offsets were allowed to vary and the following fitting procedure started with the values of amplitude A and lifetimes derived in the first step [226].

$$y = y_0 + A\left(1 - \mathrm{e}^{-(x-x_0)/t_1}\right)\mathrm{e}^{-(x-x_0)/t_2} \tag{5.3.35}$$

The use of both small and large values of the initial excitation (0.1 – 10%) resulted in an agreement with experiment acceptable for this order-of-magnitude-precise model. For instance, for the green upconversion luminescence, the rise time of YVO_4:2%Er^{3+}, 4%Yb^{3+} sample was 20 μs. The simulation on the same sample with 0.1% excitation and Er-Er energy transfer taken into account resulted in 32 μs rise time, while the simulation with excitation of 10% resulted in the rise time of 37 μs [226]. The proportions of theoretical and experimental rise times of the samples with different amounts of Yb^{3+} were similar. The wide range of excitation did not have any dramatic effect on the rise times. These features demonstrate that the proposed model of the energy levels and energy transfer processes combined with the new approach to determine the effective rates and the numerical solution of the rate equations provides a precise and robust methodology for a complete description of upconversion processes in crystal matrices. [226]. Another conclusion here is that the effect of Er-Er processes is negligibly small in this case.

Table 14. The rise times (μs) of level 7 population (effective level of Er^{3+}: $^4F_{7/2}$, $^2H_{11/2}$, $^4S_{3/2}$ in YVO_4:Yb^{3+}, Er^{3+}) theoretical and experimental [226]

	Excitation, %	4% Yb^{3+}	6% Yb^{3}	8% Yb^{3}
With Er-Er ET	0.1	32	25	17
	0.5	36	24	16
	1	37	21	16
	5	38	21	16
	10	37	21	15
Without Er-Er ET	0.01	34	26	17
	0.1	34	24	16
	1	36	21	16
	5	36	21	16
	10	36	21	15
Experiment		20	9	6

5.3.8. Temporal dependencies of the level populations

During the numerical solution of the rate equations, the evolution of level populations in time was recorded and can be visualized. In Fig. 65, the curves correspond to the continuous excitation, while the plots in Fig. 66 visualize the results of simulations in pulsed excitation regime. Both were made for the sample of 8% Yb^{3+}. The data points were normalized in the [0;1] range by their peak amplitudes [226]. In all cases, the curves corresponding to the simulations with the Er-Er energy transfer processes taken into account overlap perfectly the curves corresponding to the simulations without these processes.

In Fig. 65, the first 10 ms of the continuous mode simulation are shown (the equilibrium is not reached yet). Overlapping curves illustrate the increase in the populations of levels 2 and

5. They increase almost synchronously due to the highly efficient Yb-to-Er transfer from level 2 to level 5 (Yb^{3+}: $^2F_{5/2} \rightarrow {}^2F_{7/2}$, Er^{3+}: $^4I_{15/2} \rightarrow {}^4I_{11/2}$). The populations of levels 6 and 7 increased a bit slower and only after the populations of levels 2 and 5 had reached some noticeable value: the energy transfer process populating level 7 depends strongly on the population of level 5, while the energy transfer to level 6 depends on the population of level 4 (Eq. 33) [226]. The important notion here is that the level 4 population increases much slower than the populations of levels 6 and 7. It is not surprising, as level 4 is populated mostly by the relaxation of level 5 at a relatively low rate (Er^{3+}: $^4I_{11/2} \rightarrow {}^4I_{13/2}$). Level 6 is populated by both energy transfer, in which level 4 is the initial level of the acceptor (Yb^{3+}: $^2F_{5/2} \rightarrow {}^2F_{7/2}$, Er^{3+}: $^4I_{13/2} \rightarrow {}^4F_{9/2}$), and level 7 relaxation (Er^{3+}: $^4S_{3/2} \rightarrow {}^4F_{9/2}$). The latter is characterized by a higher rate and apparently is more important for the level 6 population. The populations of levels 1 and 3 (ground levels) were decreasing due to an increase in the higher level populations.

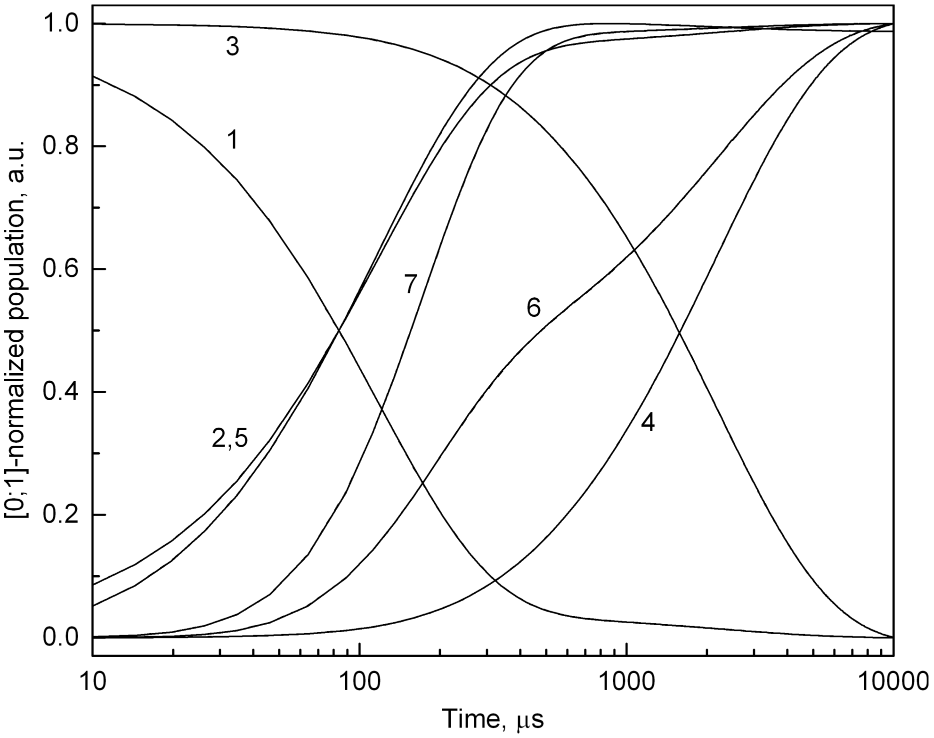

Fig. 65. The evolution of the populations of the energy levels in time, continuous excitation

The pulsed mode excitation dynamics curves (Fig. 66) provide further information about the energy transfer upconversion in question. The initial excitation was 5%. Rapid decays of levels 2 and 3 caused by the Yb-to-Er energy transfer are noticeable. The populations of levels 5, 7 and 6 reach short-lasting (tens of μs) peaks one by one, in the presented order. This is a nice illustration of the two-step upconversion: at first, level 5 is populated; then the upper levels are populated via the following energy transfer processes [226]. Additionally, the peak population of level 6 is reached shortly after the level 7 peak and significantly before the level 4 peak [226], This observation confirms the conclusion about the sources of level 6 population. Despite the Yb-to-Er energy transfer, the relaxation of level 7 is a much more important excitation source. After the excitation pulse, Yb^{3+} loses energy and eventually returns to its ground state, which can be seen as an increase in the population of level 1 [226]. Similarly, the population of level 3 would reach its initial value at the end of the simulation (not visible in the presented plot).

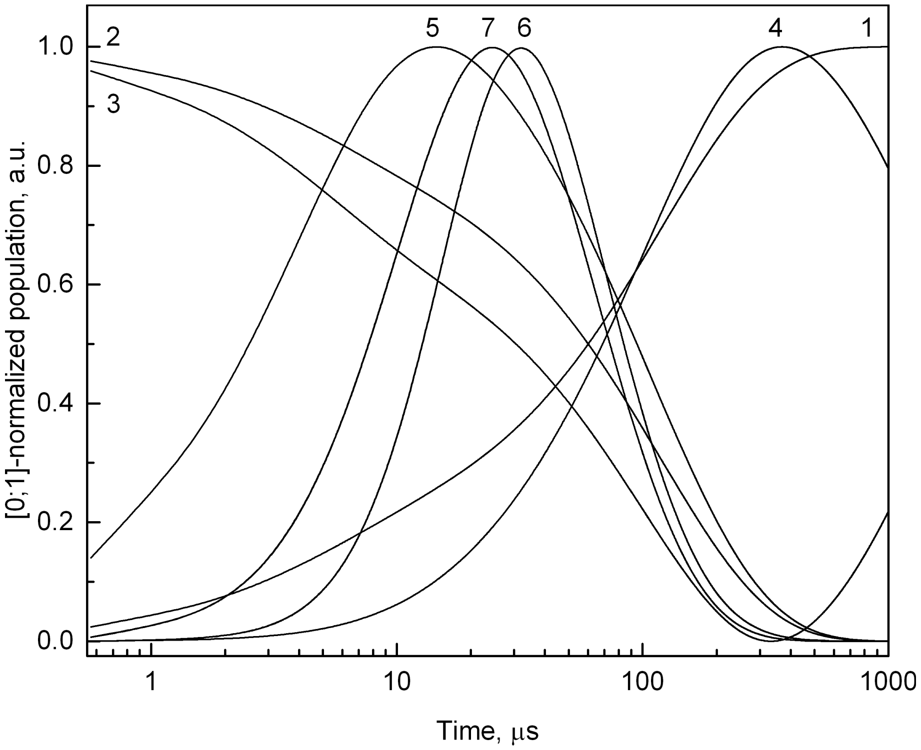

Fig. 66. The evolution of populations of the energy levels in time, pulsed excitation

5.4. Studies of possible interactions of dopant ions in the $YVO_4:Ln^{3+}$ luminophores

Although the modeling of structure of Ln-doped material does not provide spectroscopic properties directly, it might provide insights on the photoluminescence-related aspects. One of them is achieved when assuming that the dopant ions may not necessarily be simply randomly distributed in the matrix crystal. What if the dopant ions interact somehow and tend to locate close to one another? This factor might affect the energy transfer rates and, consequently, the photoluminescence efficiency of the material. Crystal structure of the matrix material suggests a particular set of Ln-Ln distances that would affect the energy transfer rates between these Ln ions located at RE ions sites. Assuming a simple random (equiprobable) distribution of dopant ions among the available crystallographic sites, it is relatively simple to take into account the multiple energy transfer pathways (see section 5.3 and Ref. [226] for details). If, however, the dopant ions tend to keep close to one another, the proportions of these distances would differ from those suggested by the simple distribution. As a result, the effective energy transfer rates will be affected accordingly. Thus, the location of activator ions in respect to one another has a direct effect on the energy transfer rates and thus, the photoluminescence properties of the material. However, the significance of the effect is clearly unknown, while the answer to the above question is unclear. This aspect might appear significant. Surprisingly, the studies on possible agglomeration of dopant ions have been scarce recently. There is some experimental evidence that such agglomeration might happen [252–256]. In particular, dopant ions may occur as pairs at neighboring sites more often than it is suggested by a simple statistical distribution. The respective computational studies are missing.

In this section, an attempt was made to check the effect of the distance between the dopant ions on the electronic energy of the system. A very simple approach was used: several Ln^{3+} ions were located at the Y sites of YVO_4 supercells treated as periodic structures and the effect of the distances between the ions on the systems' energy was studied. The idea is the same as the one used in the previous sections: while spectroscopy suggests a preference of one of the La sites in SLB by the Tb^{3+} dopant ions, the computations show that the dopant ions at one site or another cause differences in total energies of the respective structure. If a more compact location of dopant ions in the structure resulted in an energy decrease (in respect to the structure with homogeneous location of dopant ions), the agglomeration of dopant ions should be considered probable. In this section it was shown that the shorter the distance between the dopant ions, the lower the energy. Such a result suggests that the structures in which the dopant ions are agglomerated are thermodynamically more stable than those with more distant ion locations. The approach, however, does not suggest any mechanism of formation of one structure or another.

Two types of computations were performed. The first approach used semi-empirical computations by the Sparkle/PM6 [37,38,214] method for 2×2×2 supercell of YVO_4. The Y^{3+} ions were substituted by La, Eu and Lu ions. The overall procedure was similar to that described in section 5.2 with randomly-substituted input structures and steepest-descent relaxation of lattice vectors. In this study, one hundred random input structures were created per each amount of dopant. The amounts of dopant used were 2, 4, 8, 12 and 16 ions per the supercell. The aim of this part of the study was to find out if there are any effects of the distance between the dopant ions on the properties of the system. Although such calculations provided interesting preliminary results, they were found to be unreliable to provide any strong evidence of the effect. Consequently, the calculations were repeated using DFT. The DFT computations were performed with the use of CASTEP code (Projector Augmented Wave, PAW [51], or simply *plane wave* DFT) and the Perdew-Burke-Ernzerhof (PBE) [222] generalized gradient approximation (GGA) exchange-correlation functional. The calculation was a BFGS [257,258] geometry optimization with the fractional coordinates of atoms constrained (only lattice vectors were being relaxed). The first attempt was to reproduce the calculation performed with the semi-empirical method. The result was found to be close to the one provided by the semi-empirical computations. On the other hand, the result was found to be not clear enough, while the computations were lacking quality (relatively low plane wave cutoff energy was used) and were time-consuming due to numerous and large input structures. Thus, a new approach was applied in this study. The alternative idea was to use small supercells (1×1×3, for instance) and only two ions of dopant per a supercell. In this case, larger cutoff energy may be used as the system is small, and the computation should run faster.

5.4.1. The YVO_4 supercells

Several model systems of YVO_4 were used in this study. All of them were supercells of tetragonal yttrium vanadate (t-YVO_4). Structural data from [259] (provided by the Crystallography Open Database [260–262]) were used. A unit cell was replicated along the principal axis to form the supercells. The supercells were marked as a×b×c, where a, b and c indicate, how many times a unit cell was replicated by the respective axes x, y and z. The 2×2×2 supercell (8 unit cells), 1×8×1 (8 unit cells), 1×1×3 (3 unit cells), 1×3×1 (3 unit cells) and 3×1×1 (3 unit cells) supercells were created.

Two kinds of Y-by-Eu substitution were applied to the supercells in order to create doped structures corresponding to YVO_4:Eu^{3+}. To the 2×2×2 supercell, a random substitution procedure was applied [27,210]. It was necessary as there are too many options to put several dopant ions among the 32 available positions of Y^{3+} to take them all into account. Thus, for the random substitution, the appropriate number of Y ions were selected randomly from the structure and substituted by Eu^{3+} ions. This procedure was repeated dozens of times producing supercells with different layouts of the two dopant ions. In case of the small supercells (1×1×3, 1×3×1, 3×1×1), no randomization was used. One of the substituted positions was the most proximate to the small face of the supercell, while the other ones were substituted one by one producing five structures for the 1×1×3 and 1×3×1 supercells and eight structures for 3×1×1 supercell.

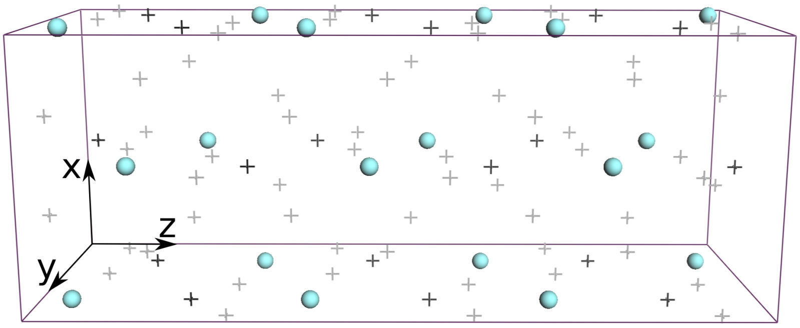

Fig. 67. The 1×1×3 supercell of YVO_4; Y is displayed as the spheres, V as the black crosses and O as the gray crosses

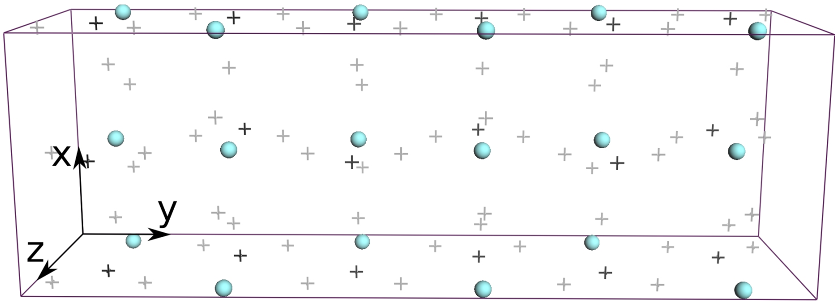

Fig. 68. The 1×3×1 supercell of YVO_4; the atoms are styled in the same fashion as in Fig. 67

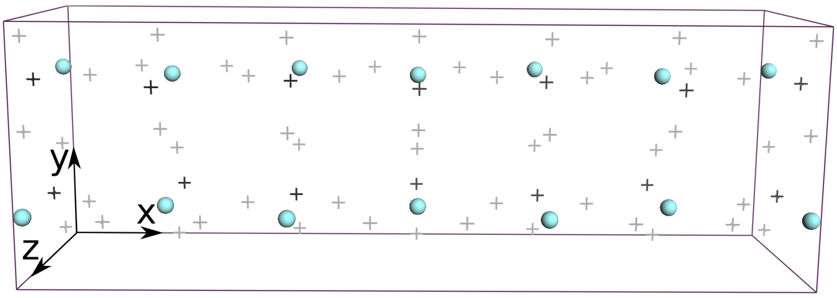

Fig. 69. The 3×1×1 supercell of YVO_4; the atoms are styled in the same fashion as in Fig. 67

These supercells contain twelve Y^{3+} ions each, which should have produced 11 different substitutions for each of them. However, as the DFT computations kept failing if the dopant ions were placed at the supercell wall (that is, if any of the fractional coordinates was either 0 or 1), the respective structures were excluded.

In 1×8×1 supercell, two dopant ions were located symmetrically with respect to the supercell center. Starting with the furthermost positions, each subsequent structure contained the dopant ions closer to each other. Note, that 1×8×1 supercell was not shown as it is too long and narrow. The idea about its structure can be grasped from the image of 1×3×1 supercell (1×8×1 supercell is similar but longer, Fig. 68).

One of the reasons for selecting YVO_4 as the studied system, was a rich set of distances between the Y^{3+} positions available in this material. The effect of mutual location of dopant ions on the energy transfer rates between them is only significant if the distances between the ions are relatively short. As the Ln-Ln energy transfer rates decay very fast with the donor-acceptor distance [226], they become very small at about 10-15 Å. Even in a relatively small 2×2×2 supercell, there are 11 possible Y-Y line segments shorter than 15 Å. This offers a possibility to get more data points in the energy as a function of Ln-Ln distance plot.

5.4.2. Semi-empirical calculations on dopant ions agglomeration in $YVO_4:Ln^{3+}$

The semi-empirical computations used the 2×2×2 YVO_4 supercell and the random substitution procedure. After the lattice vector optimization was finished, the total energies from every modeled structure were obtained. In MOPAC2012, the total energy is a sum of nuclei repulsion and electron energies.

In order to find out, if the dopant ions tend to locate close to each other (agglomerate) or not, some quantitative description of dopant's mutual location is required. In case of more than two dopant ions, a statistical approach to the distances between them was applied. For a given number of dopant ions n, there would be $N=n(n-1)/2$ line segments connecting them. The length of these line segments were collected separately for each particular randomly doped structure. Of the sets of collected distances, minimum, maximum, mean, standard deviation, variance and mean absolute deviation were calculated. The correlations between these statistical values and total energy of the respective structure were analyzed using Pearson correlation. The data sets were analyzed separately for each number of dopant studied.

Among the statistical characteristics of dopant ions mutual location, namely, minimum, maximum, mean, standard deviation, variance and mean absolute deviation of the distances between them, only the mean distance has shown any significant correlation with the total energy.

Fig. 70 depicts plots of total energy of $YVO_4:Eu^{3+}$ 2×2×2 supercell (computed with Sparkle/PM6) as a function of mean distance between the dopant ions. Every point represents a single randomly generated structure. Although the points were noticeably distributed, both linear fit and Pearson correlation coefficient was obtained for every particular amount of dopant. A very clear linear correlation between the mean distance and the total energy of the system was concluded. The list of particular correlation coefficients for different number of dopant ions is shown in Table 15.

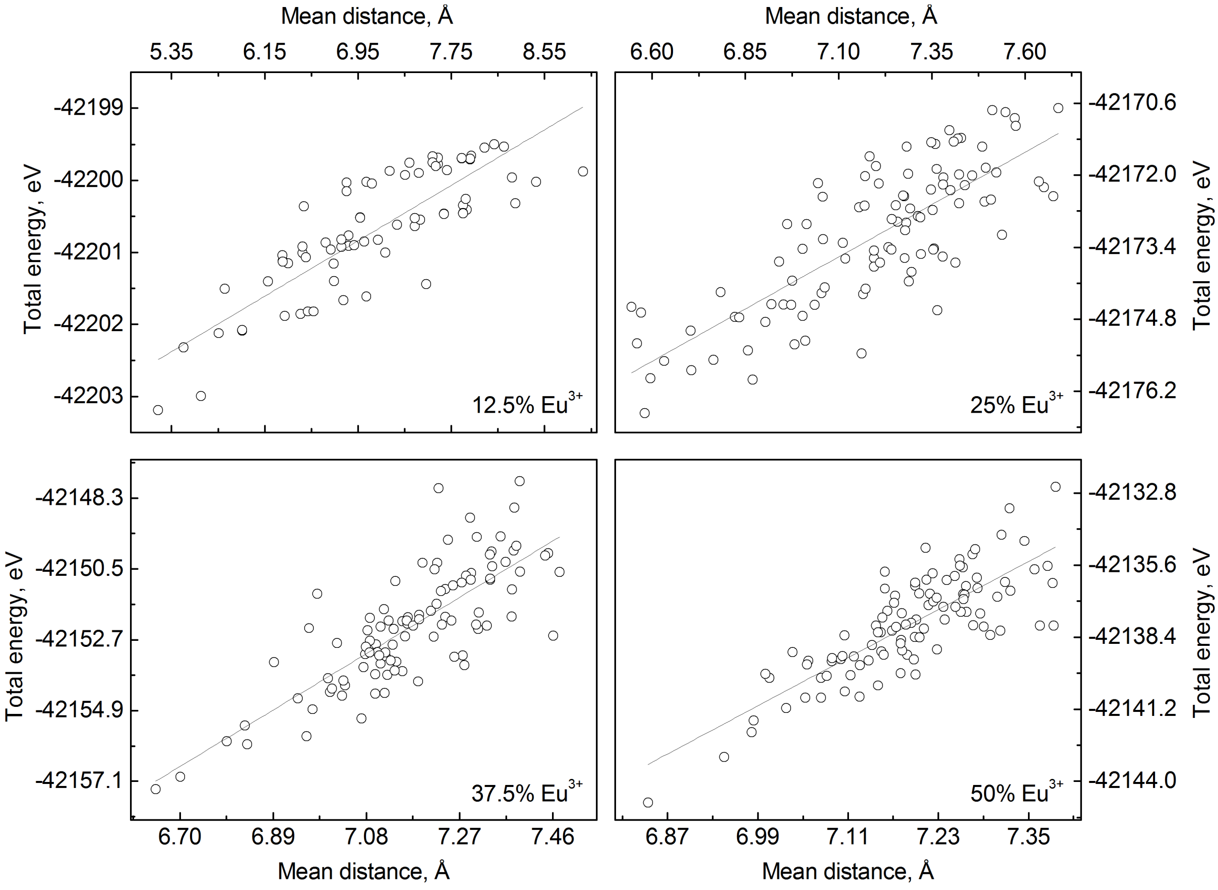

Fig. 70. Plots of total energy of YVO_4:La^{3+} 2×2×2 supercell (computed with Sparkle/PM6) as a function of the mean distance between the dopant ions

Table 15. Correlation coefficients between total energy and mean distance between the dopant ions in YVO_4:Ln^{3+}

	YVO_4:Eu^{3+}	YVO_4:La^{3+}	YVO_4:Lu^{3+}
Amount of dopant	Sparkle/PM6	PM6	PM6
0.125	0.854	0.851	-0.640
0.25	0.794	0.879	-0.672
0.375	0.798	0.868	-0.573
0.5	0.809	0.792	-0.620

As seen from Table 15, Pearson correlation coefficients characterizing the semi-empirical results were rather high. In particular, the total energies of YVO_4:Eu^{3+} obtained using the Sparkle/PM6 approach correlate positively with the mean distance between the dopants (Pearson correlation coefficient ~0.8-0.85). Larger mean distance corresponds to higher total energy. Here, a preliminary conclusion can be made. Since every quantum system tends to lower its energy, it is probable, from the thermodynamical point of view, that YVO_4:Eu^{3+} system would prefer lower energy configuration, that is one of those in which mutual location of dopant atoms is denser.

It is to be noted, however, that Y^{3+} ions of PM6 parametrization and basis functions for electrons were substituted by Eu^{3+} ions represented as Sparkles (basically, a point charge with no electrons [263]). Thus, the computed effect might be a result of the interacting Sparkles. To exclude the possible effect of Sparkle model on the results, the computations on $YVO_4:La^{3+}$ and $YVO_4:Lu^{3+}$ using PM6 model without Sparkle were performed. PM6 model contains usual parametrization for both La^{3+} and Lu^{3+}, treating them as 5d metals. In fact, neither of them is a good replacement for Eu^{3+}. The only purpose was to check, if the observed dependence takes place irrespectively of Sparkle use.

Clearly, the correlation was still present for both $YVO_4:La^{3+}$ and $YVO_4:Lu^{3+}$. For $YVO_4:La^{3+}$ it was even stronger than for $YVO_4:Eu^{3+}$, confirming the idea that more compact location of dopant ions (shorter mean distance) might result in a lower total energy of the system. Although the result was the opposite for $YVO_4:Lu^{3+}$, it does not disprove the result for $YVO_4:Eu^{3+}$; it only shows that Sparkles were not the reason for the observed effect.

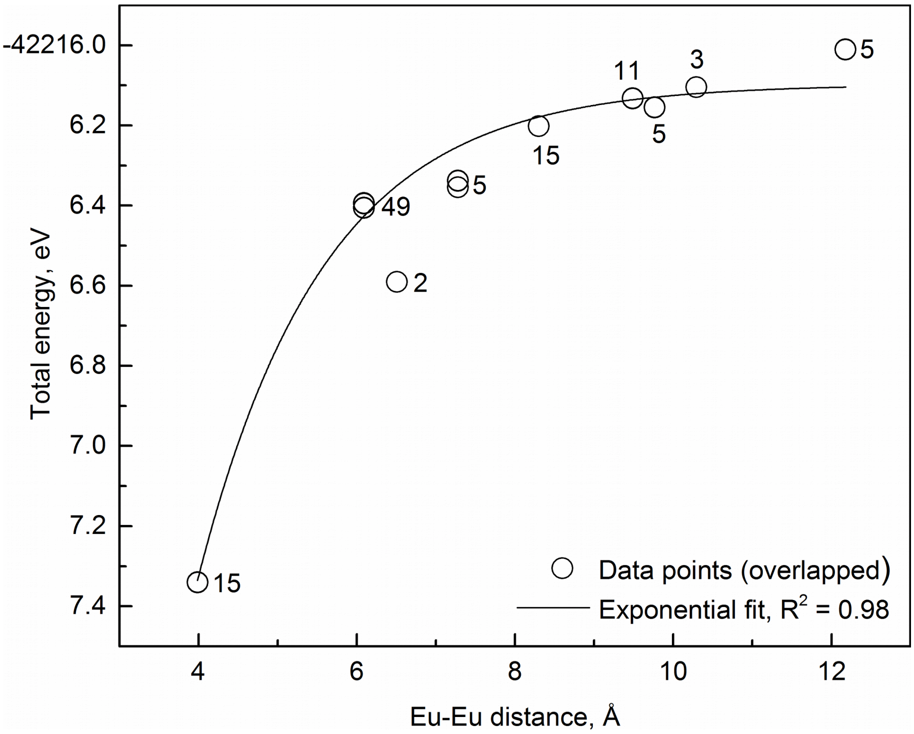

Fig. 71. A plot of total energy of $YVO_4:Eu^{3+}$ 2×2×2 supercell (computed with Sparkle/PM6) as a function of distance between the dopant ions

Unlike the results of computations for the YVO_4 2×2×2 supercell with more than four Eu^{3+} ions, the data points representing the energies of the systems with two Eu^{3+} ions form non-linear plot as a function of the Eu-Eu distance. The plot of this type was fitted with a simple exponential dependence:

$$y = y_0 + A\mathrm{e}^{-(x-x_0)/\tau} \tag{5.4.1}$$

where A is amplitude (negative), e is Euler's number, τ is a parameter and x_0 and y_0 are offsets.

An apparent decrease in the total energy with decreasing Eu-Eu distance was noticed (Fig. 71). It can be concluded at this point, that more dense packing of the dopant ions within the matrix material results in a decrease in the total energy of the $YVO_4:Eu^{3+}$ system. Consequently, there might be a tendency of dopant ions to agglomerate, that is to occupy neighboring positions in the crystal.

Most of the data points in Fig. 71 are overlapping. Different input structures with different particular positions occupied by Eu^{3+} ions are likely to have the same energy if the Eu-Eu distance is the same. The numbers of the overlapping points are indicated.

On the one hand, the result of this semi-empirical modeling is quite promising. It agrees well with the idea of the study. On the other hand, semi-empirical computations are not sophisticated enough for this kind of study. The Sparkle model represents the Ln^{3+} cations as point charges. Consequently, the electrons of Eu^{3+} are missing. Moreover, the electron correlation is missing in PM6.

Summarizing, due to the above mentioned inconsistencies, the results of Sparkle/PM6 modeling were considered as only preliminary. A logical next step was to repeat the study using *ab initio* DFT. PBE is a functional which permits computation of both exchange and correlation interactions as function of electron density and its gradient. Of course, all of the 4th shell electrons were taken into account in the plane-wave computation.

5.4.3. DFT calculations on dopant ions agglomeration in $YVO_4:Ln^{3+}$

In the DFT computations, only two ions of Eu^{3+} were introduced into each supercell. This approach results in only one Eu-Eu distance, which simplifies the computations (no statistics was required). A Projector Augmented Wave [51] (PAW, or simply plane-wave) DFT code, CASTEP [52,264], (within the Materials Studio package) was used. Again, only lattice vectors of the studied supercells were relaxed. Fractional coordinates and lattice angles were constrained. A variant of BFGS geometry optimization method from CASTEP [258] with fixed basis quality was used.

General Gradient Approximation (GGA) Perdew-Burke-Ertzenhoff (PBE) [222] exchange-correlation functional was used. The systems were treated as spin-polarized and open-shell (“fix occupancy” feature was disabled). The initial number of unpaired electrons in the system was 12, provided by two Eu^{3+}. All of the computations were performed employing the Pulay mixing in the self-consistent field achievement (SCF) procedure with convergence window of 3. The computations were performed using ultrasoft effective core potential in the reciprocal space representation. The finite basis set correction was performed automatically via pre-optimization single point energy calculations with the cutoff energies of $E - 10$ eV, $E - 5$ eV and E, where E (eV) is the plane wave cutoff energy of the calculation. The plane wave energy cutoff was equal 430, 550 and 600 eV in case of the 2×2×2, 1×8×1 and 1×1×3/1×3×1/3×1×1 supercells, respectively. The convergence threshold (energy) was equal $1 \cdot 10^{-6}$ eV for the 2×2×2 and 1×8×1 supercells or $5 \cdot 10^{-7}$ eV for the 1×1×3/1×3×1/3×1×1 supercells. The charge mixing amplitude was set to 0.5 in all cases. The spin mixing amplitude was equal 0.5 for the 1×8×1 supercell and 2.0 for the other ones. The charge and spin density mixing g-vectors were equal to 1.5 Å^{-1}. For 2×2×2 and 1×8×1 supercells, the BFGS convergence thresholds by energy, force, displacement and stress were equal to $1 \cdot 10^{-5}$ eV/atom, 0.03 eV/Å, $1 \cdot 10^{-3}$ Å and 0.05 GPa, respectively. These same parameters for the computations for 1×1×3/1×3×1/3×1×1 supercells were equal $5 \cdot 10^{-6}$ eV/atom, 0.01 eV/Å, $5 \cdot 10^{-4}$ Å and 0.02 GPa.

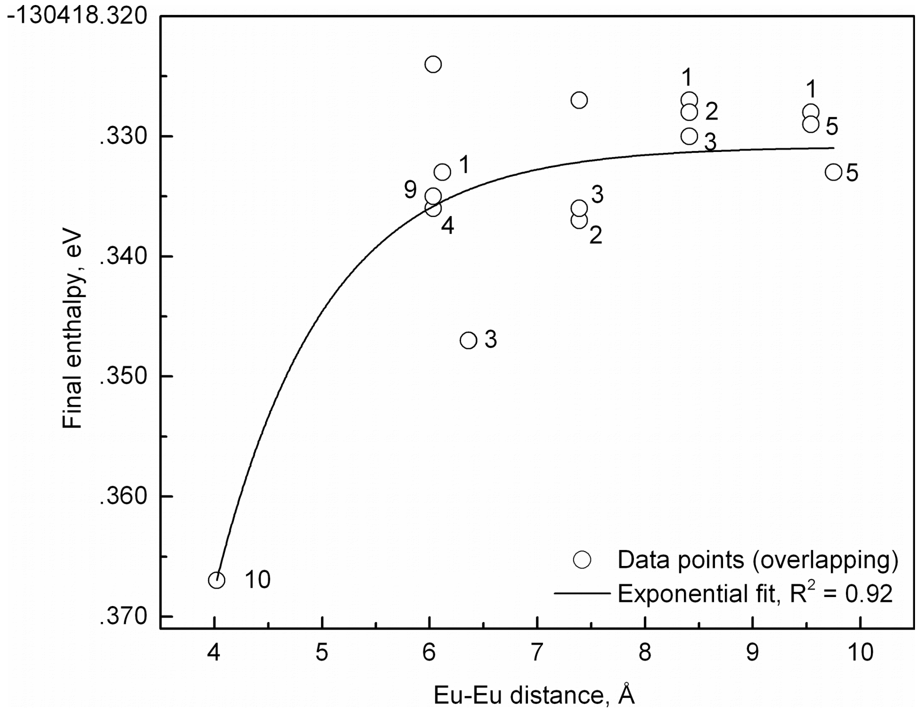

Fig. 72. A plot of the enthalpies of $YVO_4:Eu^{3+}$ 2×2×2 supercell (computed with PAW/PBE) as a function of distance between the dopant ions

Since the ionic radii of Eu^{3+} and Y^{3+} are close (eight-coordination, 1.066 and 1.019 Å, respectively) [2], no distortions at the proximity of dopant ion were modeled. In other words, the unperturbed unit cell was used to construct the supercells and no further changes (except for the lattice vector lengths) were introduced.

The first attempt of the DFT study was a simple repetition of the Sparkle/PM6 calculations. There were basically two exceptions. The amount of input structures was reduced to 50, while the dopant ions were not placed at the supercell wall. The BFGS final enthalpy from the computations was used as a thermodynamic characteristic instead of the total energy. The obtained plot of the final enthalpy vs. Eu-Eu distance (Fig. 72) is pretty much similar to the one obtained with the Sparkle/PM6 results (Fig. 71).

Similarly as above, an exponential fit was applied to the data points in Fig. 72. A conclusion can be drawn that the shorter Eu-Eu distance corresponds to the lower enthalpy of the system. Such dependence can be considered as confirmation of the initial idea that dopant ions might agglomerate.

The next step was to clarify the dependence shown in Fig. 72. The idea was to create a system in which no random substitution was required. Here, linear supercells were considered to be a good option. At first, a search for the critical distance of the studied interaction was performed. For this purpose, an unusual 1×8×1 supercell was used.

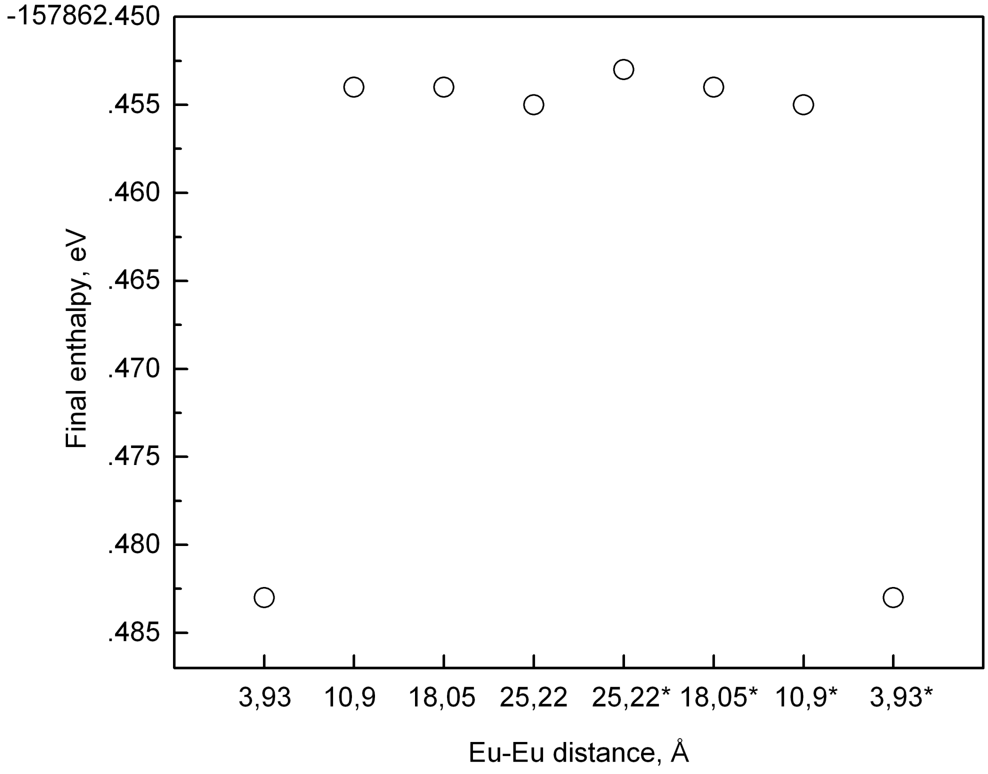

Fig. 73. A plot of the enthalpies of $YVO_4:Eu^{3+}$ 1×8×1 supercell (computed with PAW/PBE) as a function of distance between the dopant ions; the * marked values correspond to structures other than those corresponding to the unmarked values; the distances are the same because of the PBC

In the 1×8×1 supercell, there are 32 positions of Y, of which 16 are located at the supercell wall. Another 16 form a zig-zag line through the middle of the supercell. The same zig-zag line of Y positions is seen in Fig. 68 (the 1×3×1 supercell). These latter positions were used for the substitution, that started with the two closest positions at the supercell center. In the subsequent step the next two positions to each side were used. Finally, the two furthermost positions were substituted, resulting in a total of 8 structures in which the distances between the Eu^{3+} ions varied between 3.93 and 25.22 Å (optimized values). It is to be noted that in the first four cases, the Eu-Eu line segment is located inside the supercell, while in the next four structures, the shortest Eu-Eu line segment pierces through the smallest face of the supercell to its reflection at the periodical boundary. The computation results are presented in Fig. 73.

The first conclusion is that PBC does not have any significant effect. That is, there was no much difference in the final enthalpy values between the cases when the Eu-Eu line segment crossed the supercell wall and when it did not. Then, the interaction of interest was relatively short-ranged: the values of enthalpy for proximate location of Eu^{3+} ions (3.93 Å) were clearly smaller than those corresponding to distant location (10.9+ Å). The latter data points fluctuated a bit.

The subsequent step was aimed at obtaining more data points for the Eu-Eu distances from the range 4-10 Å. For this purpose, smaller supercells of three unit cells of YVO_4 were used, namely, 1×1×3, 1×3×1 and 3×1×1 supercells (Fig. 67-69).

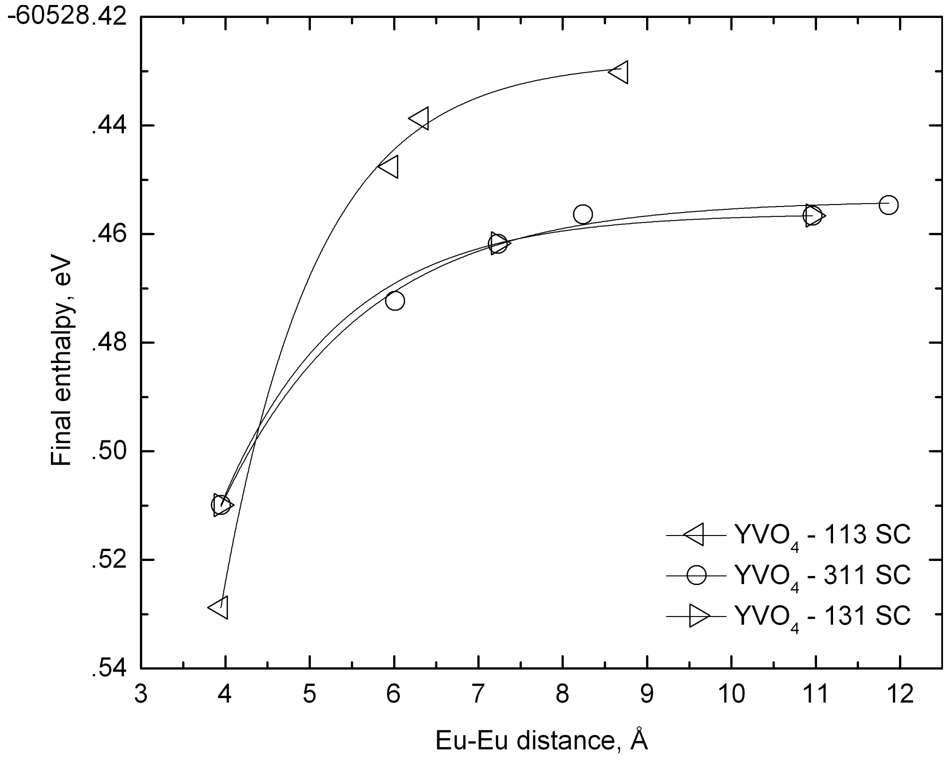

Fig. 74. Plots of the final enthalpies of $YVO_4:Eu^{3+}$ 1×1×3, 1×3×1 and 3×1×1 supercells (computed with PAW/PBE) as a function of distance between the dopant ions

In these small supercells, one of the Eu^{3+} ions was located at the Y^{3+} site at the smallest face of the supercells, while one of the other Y^{3+} sites was substituted by the second Eu^{3+} ion (sites in the supercell wall were excluded). The results of computations are presented in Fig. 74.

The data points were fitted with an exponential function, which resulted in high values of

R^2. A tendency of exponential decrease in the enthalpy with decreasing Eu-Eu distance is very clear in this case.

The enthalpy difference between the systems with furthermost location of the dopant ions and the systems with their proximate location was about 0.03 eV for 2×2×2 (two Eu^{3+} ions) and 1×8×1 supercells and about 0.1 eV for 1×1×3, 1×3×1 and 3×1×1 supercells. Thus, it was roughly proportional to the number of Eu^{3+} ions per number of all ions in the supercell. Both 2×2×2 and 1×8×1 supercells were composed of 8 unit cells of YVO_4, while the small supercells were composed of 3 unit cells. All of the supercells were doped with two ions of Eu^{3+}. Consequently, the concentration of Eu^{3+} in the small supercells was 2.67 times higher, which was roughly the proportion of the enthalpy differences. Also note, that these values were by a few orders of magnitude higher, then the SCF convergence threshold ($1 \cdot 10^{-6}$, $5 \cdot 10^{-7}$ eV).

The computations resulted in lattice vector values that were similar but not identical. For 2×2×2 and 1×8×1 supercells, the values did not show any systematic dependence on the Eu-Eu distance and were rather randomly varied. For 1×1×3, 1×3×1 and 3×1×1 supercells, the lengths of *a* and *b* lattice vectors increased a bit with increasing Eu-Eu distance, while the *c* lattice vector decreased a bit. However, the dependences were not clear. The data on the variations of the lattice vectors are collected in Table 16.

Table 16. The variation in the lattice vector lengths (calculated) of YVO_4 supercells doped with two Eu^{3+} ions

	Lattice vector *a*			Lattice vector *b*			Lattice vector *c*		
Supercell	Value, Å	±, Å	±, %	Value, Å	±, Å	±, %	Value, Å	±, Å	±, %
2×2×2	14.777	0.0008	0.006	14.777	0.0008	0.006	12.723	0.0010	0.008
1×8×1	7.161	0.0006	0.009	57.525	0.0042	0.007	6.386	0.0004	0.006
1×1×3	7.233	0.0011	0.015	7.233	0.0010	0.014	18.972	0.0027	0.014
1×3×1	7.233	0.0003	0.005	21.698	0.0005	0.002	6.324	0.0002	0.003
3×1×1	21.698	0.0010	0.004	7.233	0.0005	0.007	6.324	0.0003	0.005

Summarizing, an apparent decease in the system's energy/enthalpy with decreasing Eu-Eu distance was found using semi-empirical and *ab initio* DFT calculations. As long as the shorter distance corresponds to the lower energy/enthalpy, the dopant ions might show a tendency to agglomerate. The described phenomenon was short-ranged. It means it might have some effect on photoluminescence of the material – if the latter is somehow dependent on the Ln-Ln energy transfer rates.

6. Concluding remarks

In the presented study, several tasks have been completed. A series Ln^{3+}-doped photoluminescent materials based on mixed borates of alkaline earths and rare earths metal ions were prepared. In particular, $M_3RE_2(BO_3)_4:Ln^{3+}$ (M = Ca, Sr, Ba, RE = Y, La, Gd, Ln^{3+} = Eu^{3+}, Tb^{3+}, Dy^{3+}) were studied. Materials of this type have not been known before as nanophosphors. According to the obtained results, such materials can be successfully synthesized by the wet-chemistry sol-gel Pechini route (with citric acid and ethyleneglicol as co-reagents). The addition of Eu^{3+}, Tb^{3+}, and Dy^{3+} dopants to the studied materials results in intense red, green and white emission (under UV excitation), respectively. Several bands are present in the excitation spectra of these phosphors, namely charge transfer band (Eu^{3+}-doped samples) in the range of 200-300 nm and high-spin f-d band (Tb^{3+}-doped samples) in the range of 200-260 nm as well as f-f bands (300-400 nm). The f-f excitation bands of Tb^{3+} and Dy^{3+}-doped samples can be used for light electric diode excitation in near ultraviolet and blue range. Thus, the phosphors can be potentially applied in LED-based light sources. Another option was tuning the emission properties (color) by the chemical composition of the matrix material. This feature might be useful if a correction of emission color is required.

Another important part of this work was devoted to the computational studies focused on scarcely investigated structural aspects of RE-based luminophores, such as the effects of dopant addition of the crystal structure of the matrix material, the effects of crystal structure of the matrix on energy transfer processes and dopant ions clustering (agglomeration). In particular, both semi-empirical and *ab initio* DFT quantum-chemical computations were used to study the influence of doping on lattice parameters of crystalline materials. In such computations, multiple structures with dopant ions at different randomly selected positions were used. Only lattice vector lengths were relaxed while the positions of atoms in fractional coordinates remained constrained. It was found out that an increase in the Tb^{3+} dopant content resulted in a gradual decrease in the crystal cell dimensions of such materials as $Sr_3La_2(BO_3)_4$ and CeF_3. Most likely, this is a manifestation of substitution of larger La^{3+} and Ce^{3+} ions with smaller Tb^{3+} ions. Both semi-empirical and DFT computations resulted in good agreement with the experiment producing only several percent of error in the crystal cell dimensions predictions. Moreover, such computational studies were used to analyze the two crystallographically inequivalent La sites (both of C_1 point symmetry) in $Sr_3La_2(BO_3)_4$. It was found out that if the dopant ions are located at La1 sites, the resulting system is characterized by lower electronic energy then the one obtained by doping La2 sites. As lower energy means higher system stabilization, La1 might be preferred by the dopant ions, from the thermodynamic point of view. This result corresponds to the results of photoluminescence lifetime measurements of such system. $Sr_3La_2(BO_3)_4$:Tb^{3+} exhibits emission from mostly one type of emission center at lower doping rate, while a higher doping rate results in observations of the emission from two types of centers. A probable interpretation is that at lower doping rate the preferred site is occupied by the dopant ions, while at higher doping rate the less-preferred site also gets occupied as there is much smaller proportion of the preferred sites available.

In this work, a solution to the problem of calculation of energy transfer rates between the Ln^{3+} ions in solids was proposed. The resonance energy transfer has a great importance in defining the materials photoluminescence efficiency. A (virtually infinite) crystal offers various positions suitable for dopant ions. Consequently, there are numerous line segments connecting the corresponding points. A solution allowing computation of the effective rate over various pathways on the basis of the matrix material crystal structure was proposed. The proportional amounts of different donor-acceptor distances in a solid material were calculated using a large supercell. Then the elementary rates corresponding to the donor-acceptor distances were summed up with respect to the proportional amount of the respective distance in the population. Such an approach was applied to analyze the energy transfer processes in the YVO_4:Yb^{3+}, Tb^{3+} system. The system was characterized by a set of rate equations describing temporal dependencies of the system's energy level populations. The set was solved using numerical forth-order Runge-Kutta algorithm. Continuous and pulsed excitation modes were simulated. The characteristics of emitting level populations evolution in time (lifetimes) as well as number of excitation photons per one emitted photon were calculated and compared to experimental value. Considering the quality of results, the model was considered to be successful. Moreover, the proposed approach can be easily applied to any other kind of energy transfer processes in any Ln^{3+}-based materials.

Finally, the effort to analyze the problem of inhomogeneity of dopant ions distribution in the structure of the matrix compound was made. In particular, it is not known precisely if dopant ions locate as close to one another as possible, or as far from one another as possible, or are distributed in a simple random fashion. Meanwhile, the co-location of the dopant ions is of key importance for energy transfer and cross-relaxation processes, as both depend on the distance between the interacting species. The suggestion about the simplest case of equiprobable occurrence of a dopant ion at any RE position disregarding the distance to the neighboring dopant ions might be true, but might as well not. Experiments suggest that some inhomogeneities of dopant ions location might exist. In this study, a computational approach based on semi-empirical and DFT computations was proposed. Several Ln^{3+} ions were located in Y positions of YVO_4 supercell. Next, the dependence of the electronic energy of such a structure on the distance between the dopant ions was analyzed. Note that the original crystal structure remained unperturbed, while the lattice vectors were relaxed. Proximate or distant Y positions were selected and substituted with the dopant ions in order to create the analyzed structures. It was found out that shorter distance (that is, more dense dopant ion packing, clustering) corresponds to a lower energy, and thus to higher stabilization. In other words, the geometry with agglomerated dopant ions can be more preferable from the thermodynamical point of view.

7. List of the Figures

8. List of the Tables

9. Publications of the author

1. A.A. Shyichuk, S. Lis, *J. Rare Earths* **29** (2011) 1161–1165.
2. A. Shyichuk, S. Lis, *Mater. Chem. Phys.* **140** (2013) 447–452.
3. A. Shyichuk, S. Lis, G. Meinrath, *J. Rare Earths* **32** (2014) 248–253.
4. A. Shyichuk, M. Runowski, S. Lis, J. Kaczkowski, A. Jezierski, *J. Comput. Chem.* **36** (2015) 193–199.

10. References

[1] F.H. Spedding, Handbook on the Physics and Chemistry of Rare Earths, Elsevier B.V., 1978.

[2] R.D. Shannon, *Acta Crystallogr. Sect. A* **32** (1976) 751–767.

[3] S. Gai, C. Li, P. Yang, J. Lin, *Chem. Rev.* **114** (2014) 2343–2389.

[4] S. Lis, *J. Alloys Compd.* **341** (2002) 45–50.

[5] G. Liu, B. Jacquier, Spectroscopic Properties of Rare Earths in Optical Materials, 2005.

[6] G.F. de Sá, O.L. Malta, C. de Mello Donegá, A.M. Simas, R.L. Longo, P.A. Santa-Cruz, E.F. da Silva, *Coord. Chem. Rev.* **196** (2000) 165–195.

[7] S. Lis, M. Elbanowski, B. Mąkowska, Z. Hnatejko, *J. Photochem. Photobiol.* **150** (2002) 233–247.

[8] P. Dorenbos, *J. Phys. Condens. Matter* **15** (2003) 8417–8434.

[9] O.L. Malta, *J. Non. Cryst. Solids* **354** (2008) 4770–4776.

[10] T. Förster, *Ann. Phys.* **437** (1948) 55–75.

[11] D.L. Dexter, *J. Chem. Phys.* **21** (1953) 836–850.

[12] F. Auzel, *Chem. Rev.* **104** (2004) 139–173.

[13] G. Lakshminarayana, E.M. Weis, A.C. Lira, U. Caldiño, D.J. Williams, M.P. Hehlen, *J. Lumin.* **139** (2013) 132–142.

[14] L. Chen, Y. Jiang, S. Chen, G. Zhang, C. Wang, G. Li, *J. Lumin.* **128** (2008) 2048–2052.

[15] F. Ermeneux, C. Goutaudier, R. Moncorgé, Y. Sun, R. Cone, E. Zannoni, E. Cavalli, M. Bettinelli, *Phys. Rev. B* **61** (2000) 3915–3921.

[16] J.H. Van Vleck, *J. Phys. Chem.* **41** (1937) 67–80.

[17] G. Racah, *Phys. Rev.* **61** (1942) 186–197.

[18] B.R. Judd, *Phys. Rev.* **127** (1962) 750–761.

[19] G.S. Ofelt, *J. Chem. Phys.* **37** (1962) 511–520.

[20] B.M. Walsh, Advances in Spectroscopy for Lasers and Sensing, Springer Netherlands, Dordrecht, 2006.

[21] R.D. Peacock, *Struct. Bond.* **22** (1975) 83–122.

[22] B. Walsh, N. Barnes, B. Di Bartolo, *J. Appl. Phys.* **83** (1998) 2772 –2787.

[23] C.K. Jørgensen, B.R. Judd, *Mol. Phys.* **8** (1964) 281–290.

[24] O.L. Malta, L.D. Carlos, *Quim. Nova* **26** (2003) 889–895.

[25] O.L. Malta, H.J. Batista, L.D. Carlos, *Chem. Phys.* **282** (2002) 21–30.

[26] D. Young, Computational Chemistry: A Practical Guide for Applying Techniques to Real World Problems, John Wiley & Sons, 2001.

[27] A. Shyichuk, M. Runowski, S. Lis, J. Kaczkowski, A. Jezierski, *J. Comput. Chem.* **36** (2015) 193–199.

[28] E.H. Lieb, B. Simon, *Commun. Math. Phys.* **53** (1977) 185–194.

[29] C.C.J. Roothaan, *Rev. Mod. Phys.* **23** (1951) 69–89.

[30] T. Sommerfeld, *J. Chem. Educ.* **88** (2011) 1521–1524.

[31] M.J.S. Dewar, E.G. Zoebisch, E.F. Healy, J.J.P. Stewart, *J. Am. Chem. Soc.* **107** (1985) 3902–3909.

[32] G.B. Rocha, R.O. Freire, A.M. Simas, J.J.P. Stewart, *J. Comput. Chem.* **27** (2006) 1101–1111.

[33] J.J.P. Stewart, *J. Comput. Chem.* **10** (1989) 209–220.

[34] J.J.P. Stewart, *J. Comput. Chem.* **10** (1989) 221–264.

[35] J.J.P. Stewart, *J. Comput. Chem.* **12** (1991) 320–341.

[36] J.J.P. Stewart, *J. Mol. Model.* **10** (2004) 155–164.

[37] J.J.P. Stewart, *J. Mol. Model.* **13** (2007) 1173–213.

[38] J.J.P. Stewart, *J. Mol. Model.* **14** (2008) 499–535.

[39] J.J.P. Stewart, *J. Mol. Model.* **19** (2013) 1–32.

[40] J.J.P. Stewart, MOPAC Manual: Parameters, http://openmopac.net/manual/parameters.html.

[41] A.V.M. de Andrade, N.B. da Costa, A.M. Simas, G.F. de Sá, *J. Alloys Compd.* **225** (1995) 55–59.

[42] R.O. Freire, G.B. Rocha, A.M. Simas, *J. Braz. Chem. Soc.* **20** (2009) 1638–1645.

[43] A.M. Simas, R.O. Freire, G.B. Rocha, Cerium (III) Complexes Modeling with Sparkle / PM3, in: Comput. Sci. – ICCS 2007. Lect. Notes Comput. Sci., Springer Berlin Heidelberg, 2007: pp. 312–318.

[44] R.O. Freire, A.M. Simas, *J. Chem. Theory Comput.* **6** (2010) 2019–2023.

[45] D.A. Rodrigues, N.B. da Costa, R.O. Freire, *J. Chem. Inf. Model.* **51** (2011) 45–51.

[46] M.O. Rodrigues, N.B. da C. Júnior, C.A. de Simone, A.A.S. Araújo, A.M. Brito-Silva, F.A.A. Paz, M.E. De Mesquita, S.A. Júnior, R.O. Freire, *J. Phys. Chem. B* **112** (2008) 4204–4212.

[47] P. Hohenberg, W. Kohn, *Phys. Rev.* **136** (1964) B864–B871.

[48] W. Kohn, L.J. Sham, *Phys. Rev.* **140** (1965) A1133–A1138.

[49] P.W. Ayers, R.G. Parr, *Indian J. Chem. A* **53** (2014) 929–931.

[50] R. Peverati, D.G. Truhlar, *Philos. Trans. A. Math. Phys. Eng. Sci.* **372** (2014) 20120476.

[51] P.E. Blöchl, *Phys. Rev. B* **50** (1994) 17953–17979.

[52] M.D. Segall, P.J.D. Lindan, M.J. Probert, C.J. Pickard, P.J. Hasnip, S.J. Clark, M.C. Payne, *J. Phys. Condens. Matter* **14** (2002) 2717–2744.

[53] C.K. Duan, P.A. Tanner, *J. Phys. Chem. A* **114** (2010) 6055–6062.

[54] M.F. Reid, C.-K. Duan, H. Zhou, *J. Alloys Compd.* **488** (2009) 591–594.

[55] H.U. Liusen, W.E.N. Jun, X.I.A. Shangda, Y.I.N. Min, *J. Rare Earths* **28** (2010) 899–902.

[56] L. Hu, M.F. Reid, C. Duan, S. Xia, M. Yin, *J. Physics. Condens. Matter.* **23** (2011) 045501.

[57] J.D.L. Dutra, T.D. Bispo, R.O. Freire, *J. Comput. Chem.* **35** (2014) 772–775.

[58] M.G. Brik, M. Nazarov, M.N. Ahmad Fauzi, L. Kulyuk, S. Anghel, K. Sushkevich, G. Boulon, *J. Alloys Compd.* **550** (2013) 103–108.

[59] M.G. Brik, N.M. Avram, A.S. Gruia, *Opt. Mater.* **35** (2013) 1772–1775.

[60] M.G. Brik, *J. Phys. Condens. Matter* **25** (2013) 345802.

[61] C.-G. Ma, M. Trevisani, F. Piccinelli, K. V Ivanovskikh, M. Bettinelli, M.G. Brik, *J. Phys. Condens. Matter* **25** (2013) 165503.

[62] L. Ning, L. Zhang, L. Hu, F. Yang, C. Duan, Y. Zhang, *J. Phys. Condens. Matter* **23** (2011) 205502.

[63] J. Luis, Z. Barandiarán, L. Seijo, *J. Lumin.* **145** (2014) 808–817.

[64] P.A. Tanner, C.S.K. Mak, N.M. Edelstein, K.M. Murdoch, G. Liu, J. Huang, L. Seijo, Z. Barandiara, *J. Am. Chem. Soc.* **125** (2003) 13225–13233.

[65] S. Tsukamoto, H. Mori, H. Tatewaki, E. Miyoshi, *Chem. Phys. Lett.* **474** (2009) 28–32.

[66] L.-S. Hu, J. Wen, M. Yin, S.-D. Xia, *Chinese Phys. B* **21** (2012) 017801.

[67] W.-X. Ji, W. Xu, W.H.E. Schwarz, S.-G. Wang, *J. Comput. Chem.* **36** (2015) 449–458.

[68] Y. Kowada, K. Ogasawara, *J. Non. Cryst. Solids* **356** (2010) 2454–2457.

[69] M. Hatanaka, S. Yabushita, *Chem. Phys. Lett.* **504** (2011) 193–198.

[70] D.A. Pantazis, F. Neese, *J. Chem. Theory Comput.* **5** (2009) 2229–2238.

[71] T. Grzyb, M. Runowski, A. Szczeszak, S. Lis, *J. Phys. Chem. C* **116** (2012) 17188–17196.

[72] A. Kar, S. Kundu, A. Patra, *ChemPhysChem* **16** (2015) 505–521.

[73] P. Kulpinski, M. Namyslak, T. Grzyb, S. Lis, *Cellulose* **19** (2012) 1271–1278.

[74] J. Zhou, Z. Liu, F. Li, *Chem. Soc. Rev.* **41** (2012) 1323–1349.

[75] Y. Yang, Q. Zhao, W. Feng, F. Li, *Chem. Rev.* **113** (2013) 192–270.

[76] J. Yao, M. Yang, Y. Duan, *Chem. Rev.* **114** (2014) 6130–6178.

[77] X. Wang, H. Chang, J. Xie, B. Zhao, B. Liu, S. Xu, W. Pei, N. Ren, L. Huang, W. Huang, *Coord. Chem. Rev.* **273-274** (2014) 201–212.

[78] L. Zhang, M. Yin, H. You, M. Yang, Y. Song, Y. Huang, *Inorg. Chem.* **50** (2011) 10608–10613.

[79] R.M. Petoral, F. Söderlind, A. Klasson, A. Suska, M.A. Fortin, N. Abrikossova, L. Selegård, P.O. Käll, M. Engström, K. Uvdal, *J. Phys. Chem. C* **113** (2009) 6913–6920.

[80] M. Ahrén, L. Selegård, F. Söderlind, M. Linares, J. Kauczor, P. Norman, P.-O. Käll, K. Uvdal, *J. Nanoparticle Res.* **14** (2012) 1006.

[81] Z. Wei, L. Sun, C. Liao, J. Yin, X. Jiang, C. Yan, S. Lü, *J. Phys. Chem. B* **106** (2002) 10610–10617.

[82] J. Zhao, Z. Lu, Y. Yin, C. McRae, J. a Piper, J.M. Dawes, D. Jin, E.M. Goldys, *Nanoscale* **5** (2013) 944–52.

[83] Z.-G. Wei, L.-D. Sun, C.-S. Liao, X.-C. Jiang, C.-H. Yan, *J. Mater. Chem.* **12** (2002) 3665–3670.

[84] C.H. Kim, I.E. Kwon, C.H. Park, Y.J. Hwang, H.S. Bae, B.Y. Yu, C.H. Pyun, *J. Alloy. Compd.* **311** (2000) 33–39.

[85] A. Szczeszak, T. Grzyb, B. Barszcz, V. Nagirnyi, A. Kotlov, S. Lis, *Inorg. Chem.* **52** (2013) 4934–40.

[86] D. Errandonea, A. Muñoz, J. Gonzalez-Platas, *J. Appl. Phys.* **115** (2014) 10–13.

[87] L. Guerbous, M. Seraiche, O. Krachni, *J. Lumin.* **134** (2013) 165–173.

[88] R. Velchuri, B.V. Kumar, V.R. Devi, G. Prasad, D.J. Prakash, M. Vithal, *Mater. Res. Bull.* **46** (2011) 1219–1226.

[89] C.W.E. Van Eijk, *Nucl. Instruments Methods Phys. Res. Sect. A Accel. Spectrometers, Detect. Assoc. Equip.* **460** (2001) 1–14.

[90] S. Ekambaram, K.C. Patil, M. Maaza, *J. Alloys Compd.* **393** (2005) 81–92.

[91] J. Zhang, Y. Wang, Z. Zhang, X. Peng, Y. Jiang, H. Li, *Mater. Res. Bull.* **44** (2009) 953–955.

[92] A. Lakshmanan, R.S. Bhaskar, P.C. Thomas, R.S. Kumar, V.S. Kumar, M.T. Jose, *Mater. Lett.* **64** (2010) 1809–1812.

[93] R. Arun Kumar, R. Dhanasekaran, *J. Cryst. Growth* **318** (2011) 636–641.

[94] Z. Weidong, Z. Xiying, X. Tian, L.Z.X. I, Y.Z. B, Z. Chunlei, H.X.R. Ijz, *J. Rare Earths* **2** (2006) 1–4.

[95] X. Cui, W. Zhuang, X. Zhang, T. Xia, Z. Long, Z. Yu, C. Zhao, X. Huang, *J. Rare Earths* **24** (2006) 719–723.

[96] X. Li, Y. Wang, *J. Rare Earths* **28** (2010) 361–364.

[97] Z. Leng, N. Zhang, Y. Liu, L. Li, S. Gan, *Appl. Surf. Sci.* **330** (2015) 270–279.

[98] H. Zhang, J. Chen, H. Guo, *J. Rare Earths* **29** (2011) 822–825.

[99] L. Huili, Z. Jing, M. Lei, Z. Qitu, *J. Rare Earths* **25** (2007) 34–36.

[100] S. Ye, F. Xiao, Y.X. Pan, Y.Y. Ma, Q.Y. Zhang, *Mater. Sci. Eng. R Reports* **71** (2010) 1–34.

[101] Y. Wang, G. Zhu, S. Xin, Q. Wang, Y. Li, Q. Wu, C. Wang, X. Wang, X. Ding, W. Geng, *J. Rare Earths* **33** (2015) 1–12.

[102] C.K. Lin, M.L. Pang, M. Yu, J. Lin, *J. Lumin.* **114** (2005) 299–306.

[103] F.-S. Chen, C.-H. Hsu, C.-H. Lu, *J. Alloys Compd.* **505** (2010) L1–L5.

[104] R.S. Yadav, A.C. Pandey, *J. Alloys Compd.* **494** (2010) L15–L19.

[105] K.Y. Jung, *Phys. B Condens. Matter* **405** (2010) 3195–3199.

[106] S.S. Yi, J.C. Kim, D.W. Kim, R. Balakrishnaiah, S.H. Kim, K. Jang, H.S. Lee, B.K. Moon, J.H. Jeong, *Thin Solid Films* **518** (2010) 6163–6167.

[107] M. Tukia, J. Hölsä, M. Lastusaari, J. Niittykoski, *Opt. Mater.* **27** (2005) 1516–1522.

[108] J. Lin, Y. Huang, J. Zhang, X. Ding, S. Qi, C. Tang, *Mater. Lett.* **61** (2007) 1596–1600.

[109] Y. Ru, Q. Jie, L. Min, L. Guoqiang, *J. Eur. Ceram. Soc.* **28** (2008) 2903–2914.

[110] Z. Ren, C. Tao, H. Yang, *J. Mater. Sci. Mater. Electron.* **19** (2008) 319–321.

[111] G.V. Lokeswara Reddy, L. Rama Moorthy, P. Packiyaraj, B.C. Jamalaiah, *Opt. Mater.* **35** (2013) 2138–2145.

[112] C.H. Yang, G.F. Yang, Y.X. Pan, Q.Y. Zhang, *J. Fluoresc.* **19** (2009) 105–109.

[113] E.C. Fuchs, C. Sommer, F.P. Wenzl, B. Bitschnau, A.H. Paulitsch, A. Mühlanger, K. Gatterer, *Mater. Sci. Eng. B Solid-State Mater. Adv. Technol.* **156** (2009) 73–78.

[114] C.H. Yang, Y.X. Pan, Q.Y. Zhang, *Mater. Sci. Eng. B Solid-State Mater. Adv. Technol.* **137** (2007) 195–199.

[115] L. van Pieterson, M.F. Reid, A. Meijerink, *Phys. Rev. Lett.* **88** (2002) 067405.

[116] G. Jia, P.A. Tanner, C.K. Duan, J. Dexpert-Ghys, *J. Phys. Chem. C* **114** (2010) 2769–2775.

[117] H.G. Giesber, J. Ballato, W.T. Pennington, J.W. Kolis, *Inf. Sci. (Ny).* **149** (2003) 61–68.

[118] J. Ma, Q. Wu, Y. Chen, Y. Chen, *Solid State Sci.* **12** (2010) 503–508.

[119] R. Cong, T. Yang, Z. Wang, J. Sun, F. Liao, Y. Wang, J. Lin, *Inorg. Chem.* **50** (2011) 1767–1774.

[120] B. Moine, J. Mugnier, D. Boyer, R. Mahiou, S. Schamm, G. Zanchi, *J. Alloys Compd.* **323-324** (2001) 816–819.

[121] C. Mansuy, J.M. Nedelec, C. Dujardin, R. Mahiou, *Opt. Mater.* **29** (2007) 697–702.

[122] H. Zhu, L. Zhang, T. Zuo, X. Gu, Z. Wang, L. Zhu, K. Yao, *Appl. Surf. Sci.* **254** (2008) 6362–6365.

[123] B. Yan, C. Wang, *J. Alloys Compd.* **462** (2008) 147–152.

[124] X. Cui, W. Zhuang, Z. Yu, T. Xia, X. Huang, H. Li, *J. Alloys Compd.* **451** (2008) 280–285.

[125] C. Yang, P. Yang, W. Wang, J. Wang, M. Zhang, J. Lin, *J. Colloid Interface Sci.* **328** (2008) 203–10.

[126] Y. Zhang, Y. Li, *J. Alloys Compd.* **384** (2004) 88–92.

[127] J. Pan, Z. Lin, Z. Hu, L. Zhang, G. Wang, *Opt. Mater.* **28** (2006) 250–254.

[128] Y. Zhang, Z. Lin, L. Zhang, G. Wang, *Opt. Mater.* **29** (2007) 543–546.

[129] C. Tu, Y. Wang, Z. You, J. Li, Z. Zhu, B. Wu, *J. Cryst. Growth* **265** (2004) 154–158.

[130] Y. Wang, C. Tu, Z. You, J. Li, Z. Zhu, B. Wu, *Opt. Mater.* **29** (2006) 257–261.

[131] Y. Ji, Y. Wang, J. Cao, Z. You, Y. Wang, C. Tu, *J. Alloys Compd.* **509** (2011) 9753–9757.

[132] Y. Wei, C. Tu, G. Jia, Z. You, H. Wang, F. Yang, X. Lu, J. Li, Z. Zhu, Y. Wang, *Solid State Commun.* **140** (2006) 230–235.

[133] P. Ma, Z. Lin, G. Wang, *Opt. Mater.* **29** (2007) 1553–1556.

[134] S. Sun, J. Xu, Q. Wei, F. Lou, Y. Huang, F. Yuan, L. Zhang, Z. Lin, J. He, G. Wang, *J. Alloys Compd.* **632** (2015) 386–391.

[135] L. Zhou, J. Huang, L. Yi, M. Gong, J. Shi, *J. Rare Earths* **27** (2009) 54–57.

[136] L.G. Jacobsohn, K.B. Sprinkle, S.A. Roberts, C.J. Kucera, T.L. James, E.G. Yukihara, T.A. Devol, J. Ballato, *J. Nanomater.* **2011** (2011) ID523638.

[137] T. Grzyb, S. Lis, *J. Rare Earths* **27** (2009) 588–592.

[138] M. Runowski, S. Lis, *J. Alloys Compd.* **597** (2014) 63–71.

[139] T. Grzyb, M. Runowski, K. Dąbrowska, M. Giersig, S. Lis, *J. Nanopart. Res.* **15** (2013) 1958.

[140] A. Szczeszak, T. Grzyb, Z. Śniadecki, N. Andrzejewska, S. Lis, M. Matczak, G. Nowaczyk, S. Jurga, B. Idzikowski, *Inorg. Chem.* **53** (2014) 12243–12252.

[141] W. Ryba-Romanowski, *Cryst. Res. Technol.* **38** (2003) 225–236.

[142] Y. Liang, P. Chui, X. Sun, Y. Zhao, F. Cheng, K. Sun, *J. Alloys Compd.* **552** (2013) 289–293.

[143] B. Yan, X.Q. Su, *Opt. Mater.* **29** (2007) 547–551.

[144] B. Yan, X. Su, K. Zhou, *Mater. Res. Bull.* **41** (2006) 134–143.

[145] M. Sobczyk, *Mater. Lett.* **88** (2012) 86–88.

[146] F. Wang, X. Xue, X. Liu, *Angew. Chem. Int. Ed. Engl.* **47** (2008) 906–909.

[147] L. Chen, G. Liu, Y. Liu, K. Huang, *J. Mater. Process. Technol.* **198** (2008) 129–133.

[148] L.R. Singh, R.S. Ningthoujam, *J. Appl. Phys.* **107** (2010) 6–11.

[149] H. Zhu, H. Hu, Z. Wang, D. Zuo, *Nanoscale Res. Lett.* **4** (2009) 1009–1014.

[150] Y. Wang, S. Wang, Z. Wu, W. Li, Y. Ruan, *J. Alloys Compd.* **551** (2013) 262–266.

[151] A. Sanson, M. Giarola, B. Rossi, G. Mariotto, E. Cazzanelli, A. Speghini, *Phys. Rev. B* **86** (2012) 214305.

[152] Y. Wu, D. Ding, S. Pan, F. Yang, G. Ren, *J. Alloys Compd.* **509** (2011) 366–371.

[153] X. Zhang, X. Qiao, H.J. Seo, *Curr. Appl. Phys.* **11** (2011) 442–446.

[154] H. Liang, H. Lin, G. Zhang, P. Dorenbos, Q. Su, *J. Lumin.* **131** (2011) 194–198.

[155] G. Ju, Y. Hu, H. Wu, Z. Yang, C. Fu, Z. Mu, F. Kang, *Opt. Mater.* **33** (2011) 1297–1301.

[156] H. Takahashi, A. Unemoto, K. Amezawa, T. Kawada, *Solid State Ionics* **192** (2011) 275–278.

[157] B. Han, J. Zhang, Y. Lü, *J. Am. Ceram. Soc.* **96** (2013) 179–183.

[158] L. Yang, L. Zhou, Y. Huang, Z. Tang, *Mater. Res. Bull.* **46** (2011) 239–243.

[159] J. Plewa, T. Jüstel, *J. Therm. Anal. Calorim.* **88** (2007) 531–535.

[160] M. Ren, J.H. Lin, Y. Dong, L.Q. Yang, M.Z. Su, *Chem. Mater.* **11** (1999) 1576–1580.

[161] X. Zhang, L. Zhou, Q. Pang, M. Gong, *Opt. Mater.* **36** (2014) 1112–1118.

[162] G. Chadeyron, M. El-Ghozzi, R. Mahiou, a Arbus, J.C. Cousseins, *J. Solid State Chem.* **128** (1997) 261–266.

[163] H. Xu, W. Zhuang, X. Wen, R. Liu, Y. Hu, T. Xia, *J. Rare Earths* **28** (2010) 701–704.

[164] X. Guo, Y. Wang, J. Zhang, *J. Cryst. Growth* **311** (2009) 2409–2417.

[165] L. Yang, L. Zhou, X. Chen, X. Liu, P. Hua, Y. Shi, X. Yue, Z. Tang, Y. Huang, *J. Alloys Compd.* **509** (2011) 3866–3871.

[166] J. Zhang, M. Yang, H. Jin, X. Wang, X. Zhao, X. Liu, L. Peng, *Mater. Res. Bull.* **47** (2012) 247–252.

[167] L. Yang, L. Zhou, Y. Huang, Z. Tang, *Mater. Chem. Phys.* **131** (2011) 477–484.

[168] Y. Gao, F. Yang, W. Han, Q. Fang, Z. Xu, *Mater. Res. Bull.* **51** (2014) 13–18.

[169] Z. Xu, C. Li, Z. Cheng, C. Zhang, G. Li, C. Peng, J. Lin, *CrystEngComm* **12** (2010) 549.

[170] L. Wang, L. Shi, N. Liao, H. Jia, P. Du, Z. Xi, L. Wang, D. Jin, *Mater. Chem. Phys.* **119** (2010) 490–494.

[171] J.C. Zhang, Y.H. Wang, X. Guo, *J. Lumin.* **122-123** (2007) 980–983.

[172] X. Jiang, L. Sun, C. Yan, *J. Phys. Chem. B* **108** (2004) 3387–3390.

[173] S. Hosokawa, M. Inoue, *Chem. Lett.* **38** (2009) 1108–1109.

[174] J.M. Nedelec, *J. Nanomater.* **2007** (2007) ID36392.

[175] A. Szysiak, L. Lipińska, W. Ryba-Romanowski, P. Solarz, R. Diduszko, A. Pajaczkowska, *Mater. Res. Bull.* **44** (2009) 2228–2232.

[176] A. Szczeszak, K. Kubasiewicz, T. Grzyb, S. Lis, *J. Lumin.* **155** (2014) 374–383.

[177] T. Grzyb, S. Lis, *Inorg. Chem.* **50** (2011) 8112–8120.

[178] D. Boyer, G. Bertrand-Chadeyron, R. Mahiou, a. Brioude, J. Mugnier, *Opt. Mater.* **24** (2003) 35–41.

[179] C. Qin, L. Qin, G. Chen, T. Lin, *Mater. Lett.* **106** (2013) 436–438.

[180] H. Shen, S. Feng, Y. Wang, Y. Gu, J. Zhou, H. Yang, G. Feng, L. Li, W. Wang, X. Liu, D. Xu, *J. Alloys Compd.* **550** (2013) 531–535.

[181] C. Badan, O. Esenturk, A. Yilmaz, *Solid State Sci.* **14** (2012) 1710–1716.

[182] W. He, J. Zhang, L. Wang, Q. Zhang, *J. Rare Earths* **27** (2009) 231–233.

[183] S.S. Yao, L.H. Xue, Y.W. Yan, *Curr. Appl. Phys.* **11** (2011) 639–642.

[184] K. Patil, S.T. Aruna, S. Ekambaram, *Curr. Opin. Solid State Mater. Sci.* **2** (1997) 158–165.

[185] Z. Leng, L. Liu, L. Li, S. Gan, *Colloids Surfaces A Physicochem. Eng. Asp.* **463** (2014) 1–7.

[186] R.S. Yadav, R.K. Dutta, M. Kumar, A.C. Pandey, *J. Lumin.* **129** (2009) 1078–1082.

[187] B.L. Cushing, V.L. Kolesnichenko, C.J.O. Connor, **104** (2004) 3893–3946.

[188] B. Fultz, J.M. Howe, Transmission Electron Microscopy and Diffractometry of Materials (Third Edition), 2007.

[189] G. Hölzer, M. Fritsch, M. Deutsch, J. Härtwig, E. Förster, *Phys. Rev. A* **56** (1997) 4554–4568.

[190] A.L. Patterson, *Phys. Rev.* **56** (1939) 978–982.

[191] A. Monshi, *World J. Nano Sci. Eng.* **02** (2012) 154–160.

[192] H.M. Rietveld, *J. Appl. Crystallogr.* **2** (1969) 65–71.

[193] L. Lutterotti, S. Matthies, H. Wenk, *IUCr Newsl. CPD* **21** (1999) 14–15.

[194] H.R. Wenk, S. Matthies, L. Lutterotti, *Mater. Sci. Forum* **157-162** (1994) 473–480.

[195] H. Chen, C. Ferrari, M. Angiuli, J. Yao, C. Raspi, E. Bramanti, *Carbohydr. Polym.* **82** (2010) 772–778.

[196] M.P. Pechini, Method of preparing lead and alkaline earth titanate and niobates and coating method using the same to form a capacitor, U.S. Patent 3330697, 1967.

[197] A. Szczeszak, T. Grzyb, S. Lis, R.J. Wiglusz, *Dalt. Trans.* **41** (2012) 5824–5831.

[198] A.A. Shyichuk, S. Lis, *J. Rare Earths* **29** (2011) 1161–1165.

[199] P. Packiyaraj, P. Thangadurai, *J. Lumin.* **145** (2014) 997–1003.

[200] G. Blasse, *J. Solid State Chem.* **2** (1970) 27–30.

[201] K. Binnemans, C. Görller-Walrand, *J. Rare Earths* **14** (1996) 173–180.

[202] Y. Ruan, Q. Xiao, W. Luo, R. Li, X. Chen, *Nanotechnology* **22** (2011) 275701.

[203] C.A. Kodaira, H.F. Brito, O.L. Malta, O.A. Serra, *J. Lumin.* **101** (2003) 11–21.

[204] A. Shyichuk, S. Lis, *Mater. Chem. Phys.* **140** (2013) 447–452.

[205] P. Pascuta, L. Pop, S. Rada, M. Bosca, E. Culea, *J. Mater. Sci. Mater. Electron.* **19** (2007) 424–428.

[206] J. Lu, F. Guo, J. Chen, *J. Cryst. Growth* **314** (2011) 157–162.

[207] J. Lin, D. Sheptyakov, Y. Wang, P. Allenspach, *Chem. Mater.* **16** (2004) 2418–2424.

[208] 47 CFR §73.682 - TV transmission standards, .

[209] D.S. Zang, J.H. Song, D.H. Park, Y.C. Kim, D.H. Yoon, *J. Lumin.* **129** (2009) 1088–1093.

[210] A. Shyichuk, S. Lis, G. Meinrath, *J. Rare Earths* **32** (2014) 248–253.

[211] Python programming language, http://python.org.

[212] R.O. Freire, E. V. do Monte, G.B. Rocha, A.M. Simas, *J. Organomet. Chem.* **691** (2006) 2584–2588.

[213] M.A.M. Filho, J.D.L. Dutra, G.B. Rocha, R.O. Freire, A.M. Simas, *RSC Adv.* **3** (2013) 16747–16755.

[214] R.O. Freire, A.M. Simas, *J. Chem. Theory Comput.* **6** (2010) 2019–2023.

[215] J.J.P. Stewart, General description of MOPAC, http://www.openmopac.net/manual/index.html.

[216] J.D.C. Maia, G.A. Urquiza Carvalho, C.P. Mangueira, S.R. Santana, L.A.F. Cabral, G.B. Rocha, *J. Chem. Theory Comput.* **8** (2012) 3072–3081.

[217] G. Kresse, J. Hafner, *Phys. Rev. B* **47** (1993) 558–561.

[218] G. Kresse, J. Furthmüller, *Comput. Mater. Sci.* **6** (1996) 15–50.

[219] G. Kresse, J. Furthmüller, *Phys. Rev. B* **54** (1996) 11169–11186.

[220] G. Kresse, J. Hafner, *Phys. Rev. B* **49** (1994) 14251–14269.

[221] A.I. Liechtenstein, V.I. Anisimov, J. Zaanen, *Phys. Rev. B* **52** (1995) R5467(R).

[222] J. Perdew, K. Burke, M. Ernzerhof, *Phys. Rev. Lett.* **77** (1996) 3865–3868.

[223] K. Klier, P. Novák, a. C. Miller, J. a. Spirko, M.K. Hatalis, *J. Phys. Chem. Solids* **70** (2009) 1302–1311.

[224] T. Grzyb, M. Runowski, A. Szczeszak, S. Lis, *J. Solid State Chem.* **200** (2013) 76–83.

[225] J.J.P. Stewart, A Note on Thermochemistry (MOPAC), http://openmopac.net/manual/thermochemistry.html.

[226] A. Shyichuk, S.S. Câmara, A.N. Carneiro Neto, I.T. Weber, L.A.O. Nunes, S. Lis, R.L. Longo, O.L. Malta, *J. Lumin.* **(**submitted**)** (2015).

[227] M. Pollnau, D. Gamelin, S. Lüthi, H. Güdel, M. Hehlen, *Phys. Rev. B* **61** (2000) 3337–3346.

[228] W.T. Carnall, H.M. Crosswhite, Energy level structure and transition probabilities in the spectra of the trivalent lanthanides in LaF_3. Tables, diagrams., Argonne, IL (United States), 1978.

[229] T. Kushida, *J. Phys. Soc. Japan* **34** (1973) 1318–1326.

[230] J. Mulak, *J. Mod. Phys.* **2** (2011) 1373–1389.

[231] G. te Velde, F.M. Bickelhaupt, E.J. Baerends, C. Fonseca Guerra, S.J.A. van Gisbergen, J.G. Snijders, T. Ziegler, *J. Comput. Chem.* **22** (2001) 931–967.

[232] C. Fonseca Guerra, J.G. Snijders, G. te Velde, E.J. Baerends, *Theor. Chem. Accounts Theory, Comput. Model. (Theoretica Chim. Acta)* **99** (1998) 391–403.

[233] A.D. Becke, *Phys. Rev. A* **38** (1988) 3098–3100.

[234] C. Lee, W. Yang, R.G. Parr, *Phys. Rev. B* **37** (1988) 785–789.

[235] D.P. Chong, *Mol. Phys.* **103** (2005) 749–761.

[236] D.P. Chong, E. van Lenthe, S. Van Gisbergen, E.J. Baerends, *J. Comput. Chem.* **25** (2004) 1030–1036.

[237] E. Van Lenthe, E.J. Baerends, *J. Comput. Chem.* **24** (2003) 1142–56.

[238] E. van Lenthe, A. Ehlers, E.-J. Baerends, *J. Chem. Phys.* **110** (1999) 8943.

[239] E. van Lenthe, E.J. Baerends, J.G. Snijders, *J. Chem. Phys.* **101** (1994) 9783.

[240] E. van Lenthe, E.J. Baerends, J.G. Snijders, *J. Chem. Phys.* **99** (1993) 4597.

[241] A.J. Freeman, J.P. Desclaux, *J. Magn. Magn. Mater.* **12** (1979) 11–21.

[242] J.M. Enoch, V. Lakshminarayanan, G. Li, C. MacDonald, V.N. Mahajan, E. Van Stryland, Handbook of Optics, Third Edition Volume IV: Optical Properties of Materials, Nonlinear Optics, Quantum Optics (set):, McGraw Hill Professional, 2009.

Montgomery, Jr., T. Vreven, K.N. Kudin, J.C. Burant, J.M. Millam, S.S. Iyengar, J. Tomasi, V. Barone, B. Mennucci, M. Cossi, G. Scalmani, N. Rega, G.A. Petersson, H. Nakatsuji, M. Hada, M. Ehara, K. Toyota, R. Fukuda, J. Hasegawa, M. Ishida, T. Nakajima, Y. Honda, O. Kitao, H. Nakai, M. Klene, X. Li, J.E. Knox, H.P. Hratchian, J.B. Cross, V. Bakken, C. Adamo, J. Jaramillo, R. Gomperts, R.E. Stratmann, O. Yazyev, A.J. Austin, R. Cammi, C. Pomelli, J.W. Ochterski, P.Y. Ayala, K. Morokuma, G.A. Voth, P. Salvador, J.J. Dannenberg, V.G. Zakrzewski, S. Dapprich, A.D. Daniels, M.C. Strain, O. Farkas, D.K. Malick, A.D. Rabuck, K. Raghavachari, J.B. Foresman, J. V. Ortiz, Q. Cui, A.G. Baboul, S. Clifford, Gaussian03, revision B.04.

[244] A. Bergner, M. Dolg, W. Küchle, H. Stoll, H. Preuß, *Mol. Phys.* **80** (1993) 1431–1441.

[245] M. Kaupp, P.V.R. Schleyer, H. Stoll, H. Preuss, *J. Chem. Phys.* **94** (1991) 1360.

[246] M. Dolg, H. Stoll, H. Preuss, *J. Chem. Phys.* **90** (1989) 1730.

[247] R. Reisfeld, C.K. Jørgensen, Lasers and Excited States of Rare Earths, Springer Berlin Heidelberg, Berlin, Heidelberg, 1977.

[248] O.L. Malta, F.R. Gonçalves e Silva, R.L. Longo, *Chem. Phys. Lett.* **307** (1999) 518–526.

[249] W.H. Press, S.A. Teukolsky, W.T. Vetterling, B.P. Flannery, Numerical Recipes: The Art of Scientific Computing, Cambridge University Press, 1990.

[250] R.A.S. Ferreira, M. Nolasco, A.C. Roma, R.L. Longo, O.L. Malta, L.D. Carlos, *Chemistry* **18** (2012) 12130–12139.

[251] R.L. Longo, F.R. Gonçalves e Silva, O.L. Malta, *Chem. Phys. Lett.* **328** (2000) 67–74.

[252] B. Viana, B. Bellamy, D. Gourier, S. Jandl, *Opt. Mater.* **13** (2000) 427–437.

[253] H. Fuks, S.M. Kaczmarek, L. Macalik, B. Macalik, J. Hanuza, *Opt. Mater.* **31** (2009) 1883–1887.

[254] D. Simons, D. Gourier, *J. Phys. Chem. Solids* **60** (1999) 555–565.

[255] T. Chakraborty, C. Meneghini, G. Aquilanti, S. Ray, *J. Phys. Condens. Matter* **26** (2014) 196001.

[256] K. Gofryk, M. Pan, C. Cantoni, B. Saparov, J.E. Mitchell, A.S. Sefat, *Phys. Rev. Lett.* **112** (2014) 1–5.

[257] N.I.M. Gould, S. Leyffer, An introduction to algorithms for nonlinear optimization, in: J.F. Blowey, A.W. Craig, T. Shardlow (Eds.), Front. Numer. Analyis, Springer Verlag, 2003: pp. 109–197.

[258] B.G. Pfrommer, M. Cote, S.G. Louie, M.L. Cohen, *J. Comput. Phys.* **131** (1997) 233–240.

[259] B.C. Chakoumakos, M.M. Abraham, L.A. Boatner, *J. Solid State Chem.* **109** (1994) 197–202.

[260] S. Gražulis, D. Chateigner, R.T. Downs, A.F.T. Yokochi, M. Quirós, L. Lutterotti, E. Manakova, J. Butkus, P. Moeck, A. Le Bail, *J. Appl. Crystallogr.* **42** (2009) 726–729.

[261] S. Gražulis, A. Daškevič, A. Merkys, D. Chateigner, L. Lutterotti, M. Quirós, N.R. Serebryanaya, P. Moeck, R.T. Downs, A. Le Bail, *Nucleic Acids Res.* **40** (2012) D420–D427.

[262] R.T. Downs, M. Hall-Wallace, *Am. Mineral.* **88** (2003) 247–250.

[263] R.O. Freire, G.B. Rocha, A.M. Simas, *Inorg. Chem.* **44** (2005) 3299–3310.

[264] S.J. Clark, M.D. Segall, C.J. Pickard, P.J. Hasnip, M.I.J. Probert, K. Refson, M.C. Payne, *Z. Kristallogr.* **220** (2005) 567–570.